Universitat de València
DEPARTAMENT DE FÍSICA ATÒMICA
MOLECULAR I NUCLEAR

Beam size and very low emittance with a Multi-OTR system in ATF2

DOCTORAT EN FÍSICA
JAVIER ALABAU GONZALVO

Supervisors:
Ángeles Faus Golfe
Javier Resta López

Febrer de 2013

Abstract

ATF is a Damping Ring built to create very low emittances and ATF2 is a Beam Delivery System and a Final Focus prototype for a future e^+e^- Linear Collider. In the frame of these experiments 4 OTR monitors have been installed in the Extraction line from ATF in order to perform emittance reconstruction with high statistics and to do fast coupling correction for the beam tuning. The single OTR design, the hardware and the software to control the 4 devices are presented, as well as the algorithms to measure the beam size, reconstruct the emittance and correct the coupling. The performance of the device is analyzed and systematic measurements are shown. The Multi-OTR system is validated as a reliable and fast emittance reconstruction device with future applications.

Dra. ANGELES FAUS GOLFE, Científic Titular del Consejo Superior de Investigaciones Científicas (CSIC),
Dr. JAVIER RESTA LÓPEZ, Investigador Juan de la Cierva (JdC), Institut de Física Corpuscular (IFIC),

CERTIFIQUEM:

Que la present memòria *Beam size and very low emittance measurements with a Multi-OTR system in ATF2* ha estat realitzada baix la nostra direcció en el Departament de Física Atòmica Molecular i Nuclear de la Universitat de València per Javier Alabau Gonzalvo i constitueix la seua Tesi Doctoral.

I per a que així conste, firmem el present Certificat.

Firmat: Angeles Faus Golfe

Firmat: Javier Resta López

Contents

Resum

L'estudi de la física més enllà del model estàndard exigeix col·lisionadors de partícules que exploren les escales del TeV. L'LHC al CERN hauria de donar les primeres respostes i l'existència del bosó de Higgs, del qual ja hi ha indicis sòlids, és una d'elles però tambe l'origen del sabor de quarks i leptons, la possible supersimetria, o la unificació de les interaccions fonamentals. Actualment hi ha un consens en la comunitat de física d'altes energies de que la pròxima generació d'acceleradors després d'LHC ha de ser un col·lisionador e^+e^- que treballe en un rang d'energies entre 0.5-5 TeV. La col·lisió e^+e^- té avantatges respecte a la d'hadrons i partícules compostes perquè són partícules puntuals, amb la qual cosa les reaccions esdevenen molt netes i ben definides als detectors des del punt de vista de background. D'altra banda, com que són partícules puntuals l'energia està totalment disponible, al contrari que els hadrons on hi ha una energia que lliga els quarks. El col·lisionador ha de ser per força linial, perquè la potència perduda per radiació sincrotró a eixes energies es tan gran que forçaria l'anell a tenir circumferències de l'ordre de centenars de kilòmetres per a reduir l'energia perduda fins al punt que les cavitats de radiofrequència pogueren compensarla. Per tant l'única opció realista és construir un col·lisionador linial. Açò però implica haver de lidiar amb una màquina que no reutilitza el feix i on cada bunch col·lisiona només una volta. Contant amb açò, per a poder tenir luminositats equivalents a aquelles dels col·lisionadors circulars s'ha de pressionar la tècnica per tal de disminuir el tamany dels paquets de partícules per a tenir una densitat més alta, cosa que ens obliga, a més a més, a controlar millor la posició del feix per tal de fer-los col·lisionar.

Per a investigar la creació de feixos de baixa talla i la preservació i control d'aquestos fins al punt d'interacció naixen ATF i ATF2. ATF és un Damping Ring amb la funció de crear baixes emitàncies verticals (12 pm·rad de valor nominal). L'emitància és un paràmetre relacionat amb la qualitat del feix, és una constant del moviment (mentre no hi haja acceleració) que dóna compte de l'area que el feix ocupa en l'espai fàsic, des d'un punt de vista estadístic, i que és determinant entre altres coses en el tamany transversal d'aquest. ATF2 és un prototip de beam delivery system i final focus amb paràmetres equivalents (amb una escala menys ambiciosa) als dels projectes futurs de col·lisionadors e^+e^- que té la funció de demostrar la possibilitat de transportar el feix extret d'ATF fins al punt d'interacció preservant la qualitat d'aquest i d'enfocar-lo fins a 37 nm controlant la seua posició al nivell del nanòmetre. D'altra banda serveix també com a test facility per a un esquema d'enfoc al punt d'interacció que corregeix la cromaticitat de forma local.

Provar nova tecnologia útil per als futurs col·lisionadors i entrenar als que hauran de ser els operadors d'aquestes mèquines són també objectius d'ATF i ATF2.

Dins del marc d'ATF2 la mesura de l'emitància a l'extracció del feix del Damping Ring és crucial per a determinar si aquesta esta fent-se de manera òptima o si hi ha alguna font de creixement de l'emitància. També aquesta mesura es important per al tuning de la màquina, és a dir, per a optimitzar el rendiment de l'accelerador i portar-lo als valors de disseny amb les condicions d'error reals. ATF2 incorpora una secció de diagnostic amb dispersió nula per tal de realitzar aquestes i altres mesures. A banda de la mesura de l'emitancia, per al tuning d'ATF2 és necessari corregir l'acoblament (coupling) transversal. De fet, degut a l'extracció del feix des d'ATF o a possibles errors en l'alineament dels quadrupols de la línia, el feix que és inicialment pla pot presentar un angle en el pla transversal que cal corregir per tal d'augmentar l'eficàcia de la col·lisió i per tant la luminositat. Aquesta correcció es fa mitjançant un sistema de quatre skew quadrupoles (electroimans quadrupolars rotats 45°) que, amb les intensitats correctes desacoblen el feix. Per a tal efecte és necessari també tenir mesures de les dimensions del feix i reconstrucció de l'emitància posteriors als skew quadrupoles.

Fins ara, aquestes mesures de l'emitància i correccions de l'acoblament, havien estat realitzades amb un sistema de Wire Scanners amb bons resultats. Utilitzant 3 o més beam size monitors i coneguent l'òptica entre ells és possible reconstruir l'anomenada beam matrix, que descriu el feix, i d'aquesta obtenir l'emitància. De tota manera, el sistema de Wire Scanners presentava alguns desavantatges que calia solventar. Primerament el temps de mesura dels Wire Scanners és gran en comparació al temps entre paquets, açò comporta que la talla es mesura sobre diferents bunches integrant d'aquesta manera el jitter (variacions en la posició del feix degudes a vibracions de qualsevol tipus al llarg de l'accelerador i el sistema d'alimentació d'aquest) i per tant sobreestimant el tamany del feix. D'altra banda, el fet de que mesurar una sola volta la talla del feix fóra un procés llarg comportava que la reconstrucció de l'emitància poguera durar fins a una hora i que la correcció de l'acoblament (on es fan series de mesures de l'emitància) poguera durar fins a un shift de 8 hores sencer, temps en el qual les condicions de la línia poden haver canviat subtilment. Calia aleshores un sistema de mesura de la talla del feix que fóra ràpid i que mesurara un únic bunch cada vegada.

Els OTR monitors introdueixen una pel·lícula metàl·lica anomenada target en la direcció del feix de tal manera que quan este la travessa té lloc el fenòmen de radiació de transició, radiació que es produeix quan una particula carregada travessa la interfície entre dos medis amb diferent constant dielèctrica. Esta llum s'emet en la direcció especular a la d'incidencia del feix i és recollida per un sistema òptic que la projecta sobre un sensor CCD. D'aquesta manera es pot tenir una imatge instantània de la talla transversal del paquet de partícules. Quatre OTR monitors han estat insatal·lats a la línia d'extracció d'ATF2 per a realitzar mesures de l'emitància i correccions de l'acoblament així com altres estudis.

El disseny dels OTR del sistema està basat en un OTR que hi havia instal·lat en la línia prèviament. El nou disseny incorpora certes millores respecte al vell, com ara mecanismes de protecció per a la càmera CCD i sistemes per a la cal·libració d'aquesta o la disminució del tamany total que ocupa en la línia. Tot el sistema està controlat remòtament mitjançant Epics, un software de control que serveix com a primera capa de comunicació entre el hardware i l'usuari. El Graphic User Interface ha estat programat amb Matlab i es comunica amb EPICS via labCA, una interfície entre ambdós llenguatges, i permet controlar el sistema en profunditat per a fer mesures, cal·libració, protecció de la màquina, etc.

L'algoritme de reconstrucció de l'emitància ha sigut estudiat per a identificar certes situacions en les que donava solucions no físiques i per a obtenir les condicions que l'óptica ha de complir per tal de tenir solucions úniques. Mesures de l'emitància s'estan fent de manera rutinària amb bons resultats. El procés complet de mesura té una duració inferior al minut. El Multi-OTR system ha estat utilitzat per a fer investigacions relatives al creixement de l'emitància en el moment de l'extracció del feix i en la pròpia línia d'ATF2.

L'acoblament s'està corregint amb mesures realitzades per els Multi-OTR. Una correcció d'aquest dura menys de mitja hora, comparada amb les 8 hores dels Wire Scanners. A més, una rutina del tipus response-matrix per a automatitzar el procés s'ha instal·lat i fa la correcció en menys d'un minut. Aquesta correcció, però, necessita unes certes condicions del feix que no es donen sempre i, per tant, en el pitjor dels casos s'ha de recórrer al mètode manual.

Altres mesures s'han fet amb els OTR com ara obtenir la beam energy spread (dispersió d'energia del feix) amb resultats satisfactoris.

El sistema Multi-OTR serà crucial en el futur pròxim per a poder assolir els objectius d'ATF2, especialment el que s'ha d'adreçar a finals de 2012 i 2013, que és la creació d'un feix al punt d'interacció de 37 nm de talla vertical.

El Multi-OTR té, a més, altres aplicacions potencials a ATF2. Existeix encara un creixement residual de l'emitància que s'ha d'investigar i els OTR poden ajudar a trobar la font. Com que és possible també mesurar la posició del paquet respecte al sistema de referència de la pròpia càmera es aleshores també possible fer estudis que incloguen el jitter com a paràmetre. Altres aplicacions inclouen la possibilitat d'estudiar la variació de l'emitància per a diferents condicions del feix, experiments d'estudi de metalls per al target del OTR, etc.

El Multi-OTR també té aplicacions fora d'ATF2. Existeix la possibilitat d'utilitzar el sistema a un futur col·lisionador linial, subjecta a estudis sobre la supervivència dels materials del target per a les intensitats i els tamanys dels feixos. El sistema es podria utilitzar al mode single-bunch a les fases d'start-up i comissioning de la màquina, per exemple a la secció Ring To Main Linac.

Es conclou, per tant, que el Multi-OTR queda validat com a instrument de recon-

strucció de l'emitància amb alta velocitat de mesura i amb un potencial per a realitzar altres funcions com ara la correcció de l'acoblament o la caracterització del jitter, i que presenta aplicacions per als futurs col·lisionadors e^+e^- .

Summary of the thesis

The high energy particle physics lives one of the most exciting moments in his history, facing challenges that will advance the understanding of the deepest laws of nature. There are reasons to expect new physics lying beyond the standard model, including dark matter and neutrino mass and some hints point that this new physics should be found at accessible energy scales.

High energy particle colliders are the primary tools to discover these basic bricks that build our universe and to study the forces inter-playing between them. Nowadays, the state-of-the-art in particle colliders is represented by the Large Hadron Collider (LHC) in CERN, the world's largest and highest-energy particle accelerator. It is a ring able to collide two proton beam at 7 TeV per nucleon (lead ions can be collided as well) with the aim of allowing physicists to test different theories of particle physics and high-energy physics, and particularly the existence of the hypothesized Higgs boson and of the large family of new particles predicted by super-symmetry. At the very moment of writing this work results from 4th July 2012 announce that to 5-sigma confidence level a new boson in the region around 126 GeV was observed [1]. Whether this new particle is the Higgs boson or not only further experiments can say.

Inside the particle physics community it is a general consensus that after the LHC the next high energy accelerator should be a linear e^+e^- collider. It has to be e^+e^- because of the point-like nature of these particles which provide a cleaner environment than that of the hadrons and it has to be linear because of the fact that synchrotron radiation losses at such high energies make a circular light-lepton collider practically impossible.

In such a single pass machine a higher effort has to be made in pushing the knowledge and technology forward in order to reach luminosity levels comparable to that of circular colliders. Beams with high intensity and very small transverse sizes are to be collided against each other. The quality of the beam plays a role in the luminosity maximization and among other challenges very low emittance beams have to be delivered to the Interaction Point (IP) preserving their quality and control in the positioning. Some test facilities have been built to test and demonstrate new techniques and in particular the Accelerator Test Facility (ATF) in KEK is a Damping Ring (DR) with the lowest vertical emittance of $4\,pm \cdot rad$ [2, 3] until 2002. The current value for the lowest achieved emittance comes from the Swiss Light Source and claims to be lower than $3\,pm \cdot rad$ [4]. ATF2 is a Final Focus system (FFS) prototype built to study the feasibility of the Local Chromaticity Correction scheme [5]. In this context reliable and fast emittance measurements after the

extraction of the beam from the ATF DR are needed.

For the purpose of measuring the emittance after the DR a system of four Optical Transition Radiation (OTR) monitors has been installed in 2010 in the Extraction line of ATF2 (EXT line) in order to complement the measurements made with a set of five Wire Scanners (WS) already installed in the EXT line of ATF2 since 2000. This thesis presents the so called Multi-OTR system from its very first concept and explains the design, the hardware construction and installation, the software implementation in the ATF2 Control System, calibrations and settings and finally the beam size and emittance measurements and some other applications as coupling correction and energy spread measurement.

This work is organized as follows:

A brief introduction on the status and future of the high energy colliders is presented in Chapter 1.

ATF2 is revised in more detail in Chapter 2, with special emphasis in the diagnostic devices installed and the R&D projects the accelerator hosts.

The Chapter 3 is devoted to the Multi-OTR project itself. After the basics of a general OTR monitor, the motivation and layout of the Multi-OTR project for ATF2 is explained. Finally the whole design is shown, the elements of a single OTR monitor and the system that connects and controls all together are described in detail as well as the software specially developed for the project.

In Chapter 4 it is presented the single OTR beam size measurement and how the software obtains the relevant information from the beam image. Simulations and comparisons with the model are presented as well as calibration tasks.

Chapter 5 is related to the proper emittance reconstruction and how the information of the four OTRs is put together in order to reconstruct the beam matrix and hence the 2D and 4D emittance. Studies on a full 4-D emittance and a discussion on eventual non-positive values when reconstructing the beam matrix are also presented. Simulations, measurements and comparison with the model are also shown.

Some applications and studies of the Multi-OTR system are discussed in Chapter 6, specially the automatic coupling correction as well as energy spread measurements performed with the system.

Finally, some conclusions are drawn in Chapter 7.

Chapter 1

Introduction

1.1 The future of high energy colliders

High energy particle accelerators are nowadays the most important element to study the fundamental particles within our Standard Model and to explore any new physics beyond it. The highest-energy collider, the Large Hadron Collider (LHC), built for this purpose during the last decade works in the TeV region. The evolution of the particle accelerators growing at about one order of magnitude each decade is foreseen by the so-called Livingston plot.It is, however, not sure for how long will stand this exponential trend or if the curve will soon come to a saturation. In any case the next step in the high-energy accelerators will depend on the results and eventual discoveries given by the LHC.

CMS and ATLAS lasts results seem to indicate that nature has chosen a standard model-like Higgs. In this case measuring its characteristics other than the mass, as decay width, CP properties, spin or branching ratios with a better accuracy than a few percent and correlating them with top studies and electroweak physics will require some future collider[6]. Although there are some LHC upgrades such as the SLHC or the LHeC which could improve the accuracy of the measurements and some innovative proposals such as muon colliders it is a consensus between particle physics community that the next high energy accelerator will be an e^+e^- Linear Collider (LC).

1.1.1 LHC: The present

The LHC is the highest-energy hadron accelerator so far. It is, in short, a storage ring built in CERN in the existing 27 km circumference Large Electron Positron collider (LEP) tunnel that collides two proton beams with about 2800 bunches per beam and 1×10^{11} protons per bunch at 14 TeV center of mass energy with a collision frequency of 40 MHz, and consists in eight regions with a straight section in each one where, in four of them, the beams are collided against each other. The collision points host four experiments, namely: ATLAS and CMS (for general purpose experiments), LHCb (for CP violation studies in B meson decays) and ALICE (for heavy-ions physics and quark-gluon plasma experiments). The peak luminosity will be $10^{34} cm^{-2} s^{-1}$. The other remaining four straight sections are

dedicated to the acceleration (RF cavities), cleaning of the beam and beam dump. The beams are guided by means of about 1200 superconducting dipole magnets with 8.3 T nominal field cooled down to 1.9 K with super-fluid helium. In primary operation mode the LHC collides proton beams however LHC is able to collide lead ions at center of mass energy of about 1200 TeV. Detailed information can be found in [7].

LHC is the last of a chain of accelerators which were in turn previous CERN energy frontier accelerators. After the proton source the beam goes into the Linac2 where it reaches 50 MeV and then it is injected into the Proton Synchrotron Booster (PSB) for a ramp of the energy up to 1.4 GeV, after that in the Proton Synchrotron (PS) the proton beam energy is raised to 26 GeV and the last step is the Super Proton Synchrotron (SPS) where the beam reaches the 450 GeV for LHC final injection.

In order to have more statistics for low cross section events the luminosity will need to be increased. An upgrade of the machine called Super LHC (SLHC) is envisaged and will mean a factor 10 in the luminosity. Other upgrades are proposed such as the LHeC which would transform the collider into a electron-ion facility.

At the moment of the writing results from 4th July 2012 announce that to 5-sigma confidence level a new boson in the region around 126 GeV has been observed by ATLAS and CMS independently. This fact will surely reopen the discussion of the next step in high energy accelerators and will more likely reaffirm the linear e^+e^- collider option.

1.1.2 Why colliding e^+e^- and why linearly?

Historically the last discoveries made by a hadron collider have been followed by accurate measurements with a light lepton collider. In fact after the $W^\pm$ and Z^0 bosons discovery in the SPS the LEP was used to make precise measurements of their properties. Leading with point-like particles, electron colliders have and excellent experimental accuracy to permit even the discovering of new phenomena. Moreover, since protons are composed objects the center-of-mass energy of the single elementary particle involved in the collision in the LHC cannot be precisely determined. The absence of precise knowledge of a collision's initial conditions makes the analysis of the data very challenging. On the other hand, electrons and positrons are elementary, so e^+e^- colliders can be used to determine parameters with a much higher precision than proton ones, with very well defined initial states and lower background in the detectors because of the fact that no strong interactions are present but only electroweak.

The LHC has the capacity to discover new physics and new particles, specially those created in high quantity in proton-proton collisions. Assuming that a potential Higgs has been discovered further experimental analysis needs to be done to tell whether its properties are consistent with the Standard Model. In order to do this studies and specially in case the experiment reveals nonstandard properties more complete and precise studies are needed. ATLAS and CMS could also detect a Z' gauge boson at 5 TeV and the squarks and gluinos predicted from super-symmetry even at 2.5 TeV or new particles associated with extra spatial dimensions whose characteristics are to be unequivocally determined

with precision. To identify a potential super-partner, couplings to other partners and spins are to be found for an accurate machine. Studies showing the central importance of an e^+e^- collider and are summarized in [8]. In some scenarios even new phenomena can be hidden to LHC but an e^+e^- collider could detect them and bring new questions and maybe answers to light.

The technical problem of colliding electrons against positrons at very high energies in a ring is the loss of energy due to Synchrotron Radiation (SR). It is well known that a charged particle emits radiation when it is accelerated. This radiation can be negligible when it comes from longitudinal acceleration, but when the trajectory is bent the energy-loss per revolution comes to be

$$\Delta E \sim \frac{\beta^3\gamma^4}{\rho^2} \sim \frac{E^4}{\rho^2 m^4}, \tag{1.1}$$

where ρ is the bending radius and it has a dependence on the inverse of the fourth power of the particle mass. It is therefore much more higher for light electrons than for protons or heavy particles. This lost energy per SR has to be restored by the Radio Frequency (RF) accelerating structures in order to be able to have the beam circulating and this turns to be the major restriction to the circular e^+e^- collider, in addition to the fact that a high radiation power would hit the accelerator itself. In order to compensate this effect the Eq. (1.1) suggests to make grow the accelerator bending radius. Following this suggestion and assuming no drastic advance in the technology, if one scales the previous LEP ring, which was 27 km circumference and 200 GeV CM energy obtains, for a TeV scale collider, a circumference of 675 km long, which means an about 200 km diameter ring and reveals itself at first sight completely unfeasible. Then the LC is the option to avoid this SR energy loss.

But life is not simple for LCs. Luminosity is one of the main challenge. The instantaneous luminosity is defined as

$$L = \frac{N^+N^-f}{4\pi\sigma_x\sigma_y}H_D, \tag{1.2}$$

where $N^{\pm}$ is the charge per bunch of each colliding beam, f is the collision frequency, σ_x and σ_y are the horizontal and vertical beam sizes and H_D represents the so called disruption enhancement factor to take in consideration the fact that beams with opposite charges tend to focus one to each other and is defined as the ratio of the effective luminosity to the geometrical luminosity

$$H_D = \frac{L}{L_0} = \frac{\sigma_x\sigma_y}{\sigma_{x,eff}\sigma_{y,eff}} \tag{1.3}$$

.

The luminosity enhancement factor is not calculable analytically because the dynamics of the beam-beam interaction is non-linear. It is however a function of the so-called disruption parameter which quantifies the beam-beam effects and represents the relative change in the impact parameter while crossing the opposite bunch

$$D_{x,y} \equiv \frac{\sigma_z}{f_{x,y}} = \frac{2r_e N_b \sigma_z}{\gamma \sigma_{x,y}(\sigma_x + \sigma_y)} \tag{1.4}$$

,
with σ_z the bunch length, r_e the classical electron radius and γ the relativistic parameter.

In a circular collider one stores the beams and can re-use them for hours, the frequencies reaching up to the MHz level but a linear accelerator is a single-pass machine, the electron and positron bunches are accelerated and collided only once and therefore the frequency is lower (tens of kHz for the current projects). If one wants to have comparable luminosities to the rings it is then mandatory to improve the beam size and intensities and the control over them. As the beam size decreases a higher positioning and control in order to make both beams collide becomes mandatory.

The principle of a linear accelerator based on alternating fields was proposed by Ising and Wideroe in the first quarter of the last century: the particles would be accelerated by RF fields. Nowadays we use accelerating structures where a set of discs with an iris in the center to let the beam pass are located normal to the axis of a waveguide tube. The arrangement of these structures acts as a band pass filter which only permits the propagation of electromagnetic waves of a certain frequency. By choosing the proper shape and geometric dimensions of the cavity the frequency of the waves can be tuned and therefore their phase velocity can be matched to the particles velocity [9]. Obviously the structure can only accelerate particles on the positive period of the wave and as a consequence the beam has to be bunched.

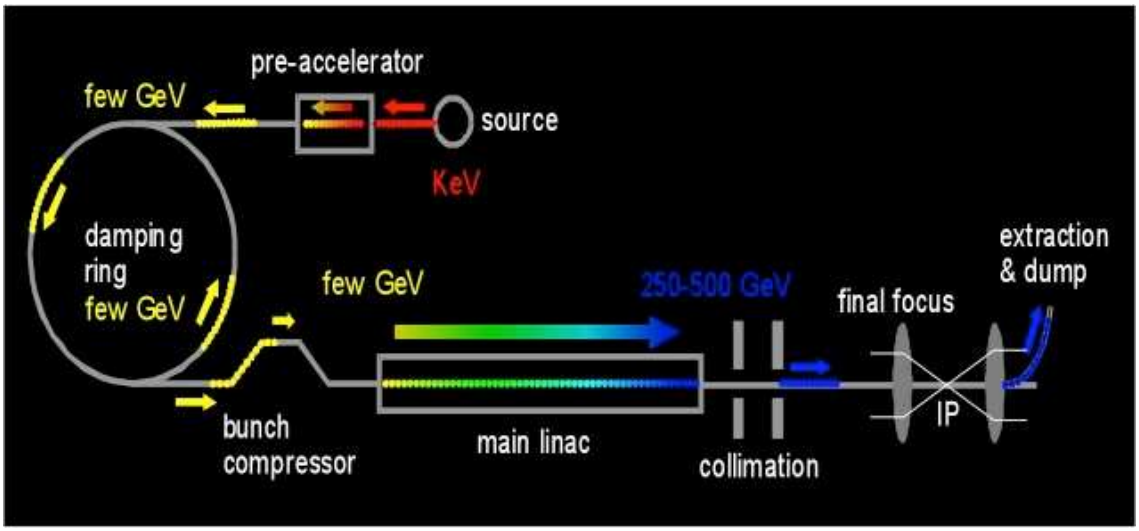

Figure 1.1: General layout of a LC not in scale.

The general layout for a LC is shown in Figure 1.1 does not vary much in its main parts whatever the project [10, 11]. The first part of the collider is the generation and injection of the beam. The electrons are created in thermionic guns while the positrons are generated through pair production. Since the LC is constantly injecting bunches the source has

to be delivering the beam at its maximum rate. After an acceleration up to 150GeV and bunching the beam has low energy and high emittance, it is cooled in the DR. In this storage rings the momentum is damped by SR while the longitudinal component is preserved by accelerating structures, therefore the transverse emittance is lowered until it reaches an equilibrium. The minimum emittance achievable in the DR is a crucial parameter because it is a lower limit for the rest of the collider and specially for the emittance at the IP. After the DR the beam naturally comes out extremely flat, this is an advantage for luminosity enhancement, see Eq. (1.2), and minimizes the beamstrahlung disruption parameter in the IP, see Eq. (1.4), responsible for an energy spread which introduces uncertainties in the collision energy. Once the emittance has been lowered in the DR the beam is injected into the main linac to be accelerated to the nominal energy previous to the collision. The acceleration principle uses RF waves loaded into structures and the beam is timed so that it only feels an accelerating field in the longitudinal direction. Apart from the RF cavities the linac has FODO cells (an arrangement of focusing and defocusing quadrupoles with the net effect of focusing the beam), dipole correctors and Beam Position Monitors (BPMs). This is the longer part of the accelerator. After the acceleration of the beam comes the so-called Beam Delivery System (BDS) with the function of deliver the beam to the IP with the best quality. It is composed of a collimation section where the particles with position or energy out of a certain limits are eliminated in order to protect the Final Focus (FF) quadrupoles and lower the background in the detector, a chromatic correction section composed of sextupoles with the scope of correct the aberrations introduced by the FFS, which is a set of very strong quadrupoles in different configurations that focus the beam to the smallest size in the IP. After that the detectors will reconstruct and measure all the parameters in the collision event and the beam will be dumped away in order to eliminate any background and optimize some parameters in the collision.

1.1.3 ILC and CLIC

There are two projects of a high-energy high-luminosity e^+e^- LC, namely the International Linear Collider (ILC) and the Compact Linear Collider (CLIC).
The ILC is based on superconducting acceleration technology while CLIC acceleration is based on a two-beams scheme. The two collaborations agree that the ILC technology is presently more mature and less risky than that of CLIC. There are plans to demonstrate the feasibility of CLIC technology and to reduce the associated risk in the future. The ILC collaboration will focus on consolidation of the technology for global mass production. Both collaborations consider it essential to continue to develop both technologies for the foreseeable future.

ILC

Until 2004 there were four proposals of Future Linear Collide (FLC) working in parallel (CLIC, JLC/GLC, NLC and TESLA). In this year some of the institutes related to R&D for LCs decided to join their efforts in order to build what would be called ILC. In the next years the basic parameters of the machine were decided and the ILC Reference Design

Report was published in 2007 [12, 13]. The main accelerating technology is based in the previous TESLA project [14], having a gradient of 31 MV/m with superconducting RF (SRF) cavities at 1.3 GHz. In fact this is the primary cost driver of the project. The ILC design mass-center energy is 500 GeV and the luminosity is $2 \times 10^{34} cm^{-2} s^{-1}$.

Fig. 1.2 shows schematically the layout of the accelerator. It has about 15000 SRF cavities working at 2 K. The two main linacs measure 11.3 km long, making a total length for the whole collider of 31 km (in the 1 TeV energy upgrade where the linacs have to twice the length the whole complex measures around 50 km).

The electron beam generation is made by means of a thermionic gun while the production of positrons is made by an undulator parallel to the electron linac. In fact, after a pre-acceleration the electrons go through an undulator radiating 10 MeV synchrotron photons. This photons collide with a titanium-alloy target and create e^+e^- pairs from where the positron beam is separated. The vertical emittance is reduced up to five orders of magnitude in the DRs with wiggler magnets and RF cavities in their straight sections. After that and before the entrance of the main linac a bunch compressor reduces the bunch length a factor of 40 in order to fulfill the linac requirements. Now the main linacs accelerates the bunches from 15 GeV to 250 GeV with RF units containing 26 cavities each one. There are 278 of these units for positrons and 282 for electrons, more in the last case to compensate the energy lost in the undulator. Each RF unit has also a quadrupole to create a FODO lattice, a BPM and a superconducting horizontal and vertical corrector magnet in order to control the trajectory and preserve the emittance. The main linac follows the earth curvature. The BDS is in charge of collimation and aberration corrections and focus the beam at the IP. The beams collide at a certain angle, this 14 mrad angle prevents the interaction with new bunches and makes easier to eliminate the used beam. The beam is kicked by the so-called crab cavities in order to counter-cancel this angle to maximize the luminosity by making the bunches interact with no collision angle. Two detectors with a complex push-pull system are projected.

Each one of these parts has technical challenges associated with the very tight requirements and constrains. The main challenges are related to achieving the very high gradients in the main linac and the small beam sizes in the IP but the ILC pushes the state-of-the-art in several fields and technical parts.

CLIC

An important work has been carried out at CERN the last decades in order to study the possibility of a LC to complement LHC results. The CLIC [15, 16] would collide e^+e^- in a range of energies of 0.5-5 TeV, optimized for 3 TeV and a luminosity of $10^{34}-10^{35}\ cm^{-2}s^{-1}$. The value for the accelerating gradient in CLIC is 100 MV/m with a frequency of 12 GHz [17], this allows the total length to be called compact having in account the energies to be reached and comparing with other LC projects. In fact, the length for the 3 TeV option will be about 34 km. Fig. 1.3 shows the layout of the accelerator.

The high gradient at CLIC is achieved by the use of very high RF frequencies. The

Acronym	Purpose	Host Lab	Organized trough
ATF	DR	KEK	ATF Collaboration
CesrTA	DR	Cornell	Cornell
STF	Main Linac	KEK	KEK
TTF/FLASH	Main Linac	DESY	TESLA Collaboration, DESY
ILCTA-NML	Main Linac	FNAL	Fermilab
ATF2	BDS	KEK	ATF Collaboration

Table 1.1: Main active ILC test facilities.

ILC SRF cavities cannot operate to this high gradients and therefore room temperature traveling wave structures have been chosen. In order to provide enough RF power a novel design of acceleration is being tested. In this method the needed power to load the RF structures in order to accelerate the so-called main beam comes from a secondary electron beam with high current and high frequency called drive beam. The drive beam, parallel to the main beam, is decelerated by means of the Power Extraction and Transfer Structures (PETS), the RF power is extracted and transferred to the main beam via waveguides. This is the most characteristic feature of the CLIC project. The drive beam is generated with a thermionic gun, bunched and accelerated with conventional low-frequency structures. Once it is accelerated to 2.4GeV its frequency is multiplied and thus the beam compressed in the delay loops and Combiner Rings (CR in Fig. 1.3). The positron main beam starts with 10 MeV electrons accelerated to 2 GeV and directed to a positron target. The two main beams are guided through a series of DRs to the bunch compressor and transfer lines to the main linacs where their energy reaches 1.5 TeV. The other structures as the BDS and FFS are similar to those described for the ILC.

1.1.4 The ILC beam test facilities

Beam Test Facilities are required for critical technical demonstrations, including accelerating gradient, precision beam handling and beam dynamics. They serve also to train scientific and engineering staff and regional industry. There are mainly three test purposes:

- Demonstration of high-gradient high-power superconducting accelerator assembly and operation.
- Demonstration of the generation and preservation of very low emittances.
- Instability studies such as electron cloud and their mitigation [18].

Table 1.1 shows the ILC test facilities identifying the purposes related to each one. In the following we describe briefly the TTF/FLASH and CesrTA facilities. ATF and ATF2 will be described in chapter 2.

	XFEL	ILC RDR Design	TTF/FLASH 9 mA
Bunch charge (nC)	1	3	3
Bunch number	3250	2625	2400
Pulse length (μm)	650	970	800
Current (mA)	5	9	9
Gradient (MV/m)	23.4	31.5	30

Table 1.2: TTF/FLASH 9 mA parameters and comparison with ILC and XFEL values.

TTF/FLASH 9 mA

To demonstrate the industrialization of the SRF technology and its application in a linear accelerator, the European X-Ray Laser Project (XFEL) is under construction at DESY (Hamburg) since 2007. In the operating light source at DESY the linac of TTF/FLASH is the only electron linac nowadays able to work near the reference gradient and nominal beam parameters of ILC.

The goals of the experiment called TTF/FLASH 9 mA are among others to demonstrate for long pulses at full beam loading the bunch-to-bunch beam energy uniformity and for pulse-to-pulse the beam energy stability and to identify the potential problems that could limit the operation at such high gradients.

Table 1.2 shows the performance of TTF/FLASH compared to XFEL and ILC.

The Low Level RF (LLRF) system is one of the main keys in TTF/FLASH. It has the role of stabilizing the amplitude and phase of high power 1.3 GHz RF field in the linear accelerator. This stabilization is done by measuring the field changes in the cavity, calculating the error, comparing with a set point and applying a closed loop (feedback) or open loop (feed-forward) active control algorithms [20].

CesrTA

After the 10 GeV e^+e^- collider called CESR at Cornell, CesrTA was built to be used as a DR test facility for the ILC. It is able to work either with electrons or positrons and it has twelve superconducting wigglers at zero dispersion and therefore it is a unique facility to study the effects of the Electron Cloud (EC) in a regime near the ILC specifications [18]. There are mainly three fields of research: First of all the low emittance tuning which includes the development of tuning tools in order to reach the 20 pm low emittances and to demonstrate the low emittance operation for a positron ring. Second the instrumentation and diagnostics which involves the development of diagnostic instrumentation to handle ultra low emittances for tuning and correction and for the beam characterization and research in diagnostic techniques to characterize the EC and its impact in the beam dynamics. Last the EC characterization and mitigation including to characterize the EP build-up in zones with drifts, dipoles, quadrupoles and wigglers and validate techniques to mitigate it, to characterize the effects of the EC in beam dynamics, emittance growth and instabilities, in a low emittance regime near to ILC parameters and to validate the simulation codes of the EC in ILC-like regimes, to ensure the reliability of the simulations

made for ILC.

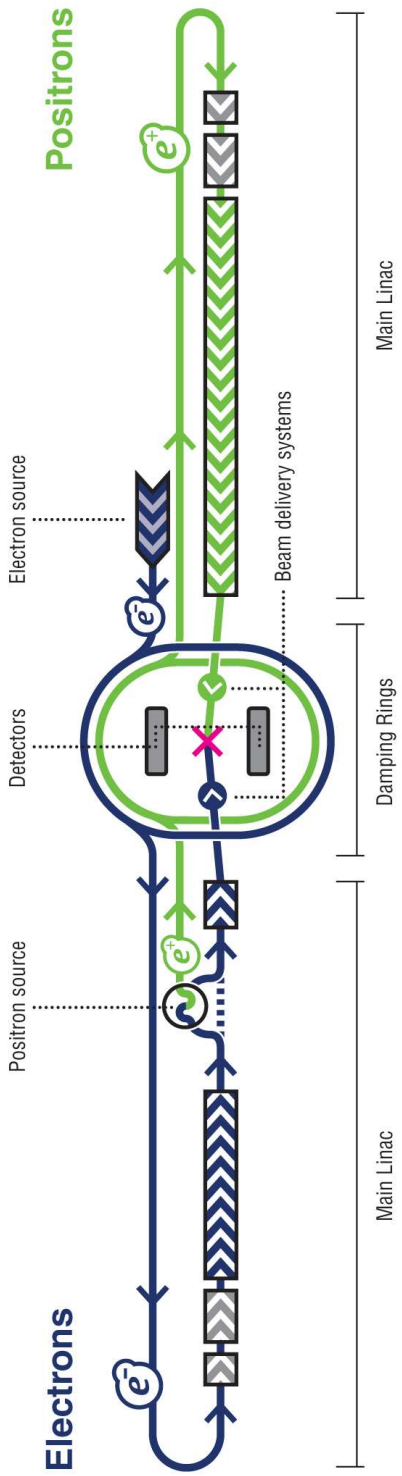

Figure 1.2: Simplified layout of the ILC not to scale. Total length is 30∼50 km.

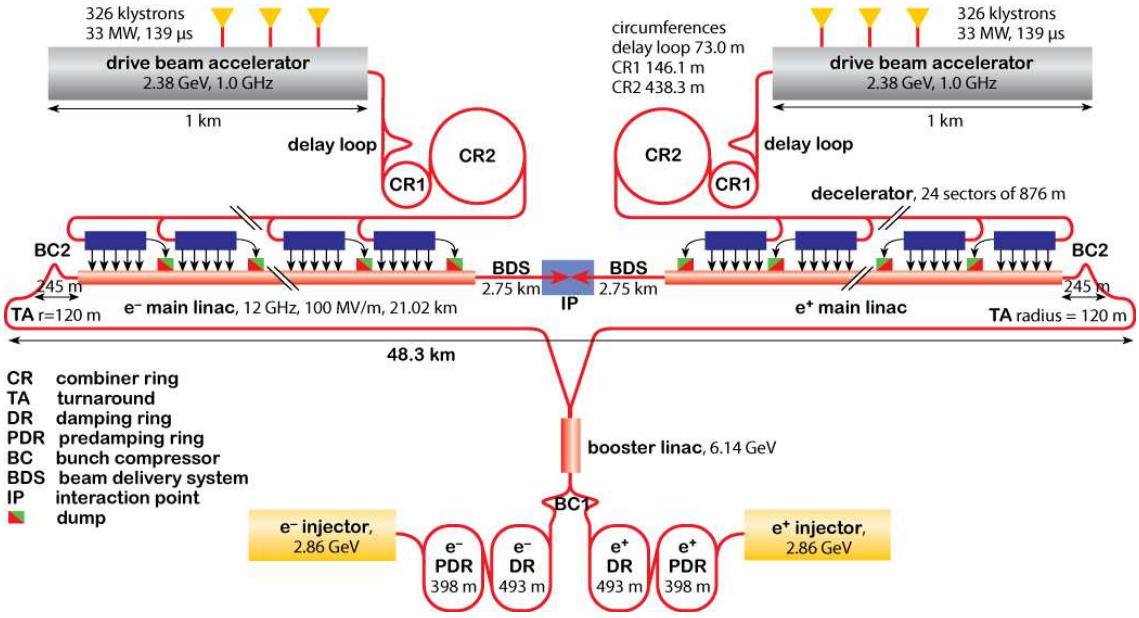

Figure 1.3: Simplified layout of the CLIC project not to scale. In the upper part is the drive beam generation while in the half lower part is the main beam generation and acceleration.

Chapter 2

The Accelerator Test Facility ATF2

2.1 Introduction

ATF is a 1.3 GeV DR with a configuration similar to the ILC DR built at KEK, Tsukuba, which started to operate in 1997 with the goal of creating extremely small emittance beams. The design value was achieved in 2001 [19, 3].

After the beam generation in the photo-cathode, the beam is accelerated in a 90 m linac with an average gradient of 26 MV/m powered by 10 klystrons of 80 MW peak power. The DR is a 138 m circumference race-track with two straight sections. 5 trains of 20 bunches can be stored at a time. The fast pulse kicker magnet for extraction and injection pulses the magnetic field in 350 ns on the flat top and then the beam is extracted by a septum magnet working in DC. In order to minimize the pulse-by-pulse orbit fluctuation in the extraction a double kicker is used. Any eventual fluctuation caused by noise in the first extraction kicker is compensated by the second kicker downstream, both kickers are driven by the same signal source [21]. The typical bunch structure coming out from the DR is a 10^{10} electrons bunch with a 1.56 Hz frequency in single bunch (up to a maximum of 2×10^{10} electrons at 3 Hz) and for multi-bunch there exist two options depending whether a conventional kicker is used (1$\sim$3 bunches with 154 ns spacing) or the fast kicker (1$\sim$30 bunches train with 308 ns spacing) [22].

The very low emittance is generated in the DR. The horizontal emittance is determined by the magnet position, the magnetic field and the beam orbit while the vertical emittance is determined by the coupling strength to the horizontal orbit depending on the magnet alignment and the orbit correction. In order to align the magnets the mounting table has a very precise adjustment system. For the magnet field to be controlled a calibration system based on Beam Based Alignment (BBA) is used, measuring the response of the beam itself using the 96 high-resolution BPMs along the DR.

Nowadays the major part of the ATF time is dedicated to ATF2 but still some studies are carried out for DR issues, specially the BBA procedure and fast kicker beam extraction studies [24].

ATF2 is a BDS with a Local Chromatic Correction FFS scheme installed right after the ATF DR extraction and will be discussed in detail in next section.

2.2 Motivation and purposes

The primary challenge for a future linear e^+e^- accelerator is to collide extremely small beams in order to increase the luminosity and to make it comparable to the circular collider case. To make this collision possible three issues arise, namely:

- to create the very small emittance beam,
- to preserve the good quality during acceleration and transport and
- to focus the beam down in order to make it collide.

The first item is accomplished by the ATF DR and the last two items are the challenges faced by ATF2 [19], a BDS built at KEK, Tsukuba, after the ATF DR provided with a scaled-down version of the ILC FFS. The ATF2 is an international collaboration from institutes all over three continents it is considered as a model of organization of a large scale project such as the ILC. Training and transfer of knowledge are also promoted since it is crucial to strengthen the accelerator community and to prepare them for the management of the ILC. A layout of the whole complex is shown in Fig. 2.1.

The ATF2 main parameters [26] are summarized in Table 2.1. In the Table the optical focal point is named IP only by analogy with the linear collider, since ATF2 is half a collider. The value of β_y^* has been chosen so that it leads to a similar chromaticity than the ILC one. L^* is the distance from the last FF quadrupole to the IP.

There are two main goals of ATF2 named Goal 1 and Goal 2 which are planned to be achieved sequentially:

- Goal 1: To obtain the design vertical beam size at the IP which is 37 nm and
- Goal 2: to stabilize it at the nanometer level.

At the moment of writing this thesis the work is focused on accomplishing the Goal 1.

To test the Local Chromaticity Correction (LCC) scheme is one of the main purposes of ATF2. Chromatic aberrations has to be corrected since the beam has a natural energy spread and hence particles with different energies are focused into different positions along the beam-line. In a "traditional" FFS the chromaticity correction is done non-locally by dedicated sections equipped with sextupoles placed in dispersive regions and paired with a minus identity transformation between them in order to compensate for the aberrations generated by the sextupoles themselves. In fact, the sextupoles produce a focusing proportional to the distance from their center. If they are placed in a high-dispersion zone then this focusing would be proportional to the energy. This model is sub-optimal since it has intrinsic limitations to the bandwidth and it is high sensitive to any disturbance between the sources of chromaticity. Moreover its length makes it difficult to scale to higher

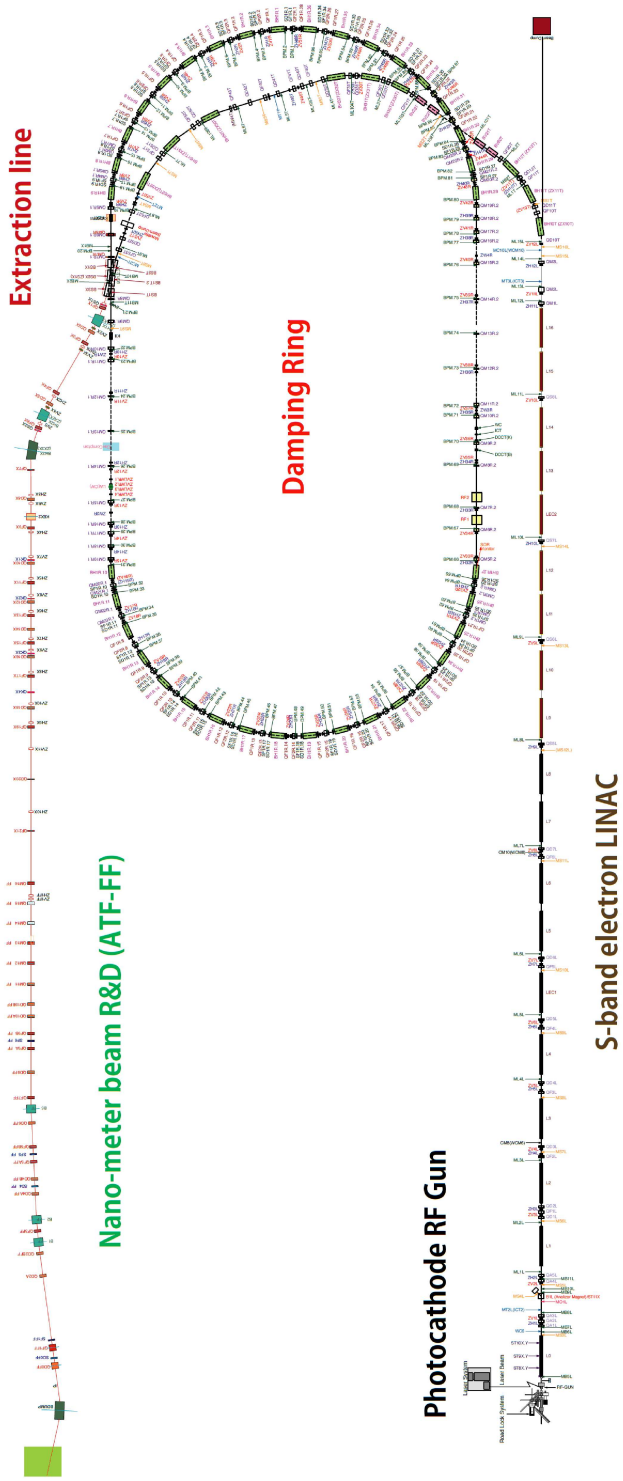

Figure 2.1: Layout of the ATF/ATF2 complex with the highlight of the main parts.

Parameter	ATF2	ILC	CLIC
Beam energy [GeV]	1.3	250	1500
L^* [m]	1	3.5-4.5	3.5
$\gamma\epsilon_x$ [m rad]	5×10^{-6}	1×10^{-5}	6.6×10^{-7}
$\gamma\epsilon_y$ [m rad]	3×10^{-8}	4×10^{-8}	2×10^{-8}
β_x^* [mm]	4	21	6.9
β_y^* [mm]	0.1	0.4	0.07
η'^* [rad]	0.14	0.0094	0.00144
σ_E [%]	~ 0.1	~ 0.1	~ 0.3
Chromaticity	$\sim 1 \times 10^4$	$\sim 1 \times 10^4$	$\sim 5 \times 10^4$
Number of bunches	1-3 (goal 1)	~ 3000	312
Number of bunches	3-30 (goal 2)	~ 3000	312
Bunch population	$1 - 2 \times 10^{10}$	2×10^{10}	3.7×10^9
σ_y^* [nm]	37	5.7	0.7

Table 2.1: ATF2 parameter comparison with ILC and CLIC values.

energies. The LCC scheme is being tested at ATF2 and corrects the chromaticity locally by interleaving two sextupoles with the final doublet quadrupoles and a bend upstream to generate dispersion [5]. In order to cancel the geometric aberrations, two more sextupoles upstream in the non dispersion region are required as can be seen in Fig. 2.2.

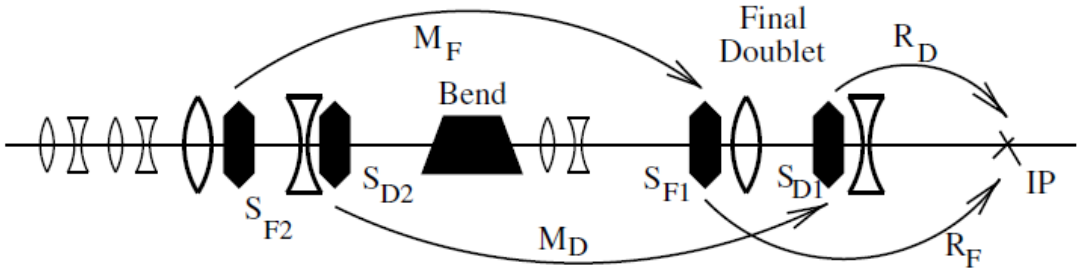

Figure 2.2: Optical layout of the Local Chromaticity Correction FFS.

The horizontal kick (dx'_Q) a particle with an energy variation δ receives by a quadrupole of infinitesimal length ds and strength K_Q in a dispersive region can be written [23]:

$$dx'_Q = (\delta - 1)K_Q x ds = (-K_Q x_0 - K_Q D_x \delta + K_Q \delta x_0 + K_Q \delta^2 D_x) ds, \qquad (2.1)$$

where $x = x_0 + D_x\delta$, the first two terms being the focusing of the beam and the third and fourth terms are the chromaticity and second order chromaticity contributions.

The horizontal kick (dx'_S) a particle receives by a focusing sextupole of infinitesimal length ds and strength K_S is approximated by [23]:

$$dx'_S = K_S \left[\frac{1}{2}(x^2 - y^2)\right] ds = K_S \left[-\frac{1}{2}y^2 + \frac{1}{2}(x_0^2 + D_x^2\delta^2 + 2x_0 D_x \delta)\right] ds, \tag{2.2}$$

using again $x = x_0 + D_x\delta$, with the second term corresponding to the geometric aberration, the third and fourth to the chromaticity in first and second order. Assuming that the β-function does not change significantly between the sextupole and the near quadrupole, if one sets the sextupole strength to $K_S = \frac{K_Q}{D_x}$ the chromaticity is corrected at first and half of the second order. To correct the second order half of the chromaticity must be generated upstream in a non dispersive region doubling the overall chromaticity and the sextupoles strength are doubled. The pure geometric aberration (δ-independent terms) must be canceled by using a pair of sextupoles upstream in phase with the ones in the FD with a -I transformation between them but in a non-dispersive region.

This scheme leads to a better performance FFS, shorter and thus cheaper and suitable to be scaled to higher energies.

It is important for the accomplishment of the ATF2 Goals to generate and maintain a stable and well aligned orbit through EXT line and the FFS for two reasons: the background and the beam quality. In fact, the monitor at the IP (IPBSM, see section 2.4.3) requires a good ratio signal-to-noise. It was found a strong correlation between the noise level and the amplitude of the orbit. The halo-generated background could be maintained in an acceptable level if the beam centroid was keep within the $500\mu m$ from the center of the magnets. The first part of the beam tuning is then to perform BBA. Alignment techniques using the beam itself and the magnet movers or dipole correctors and reading the measurements of the downstream BPMs are used. After calibration and alignments of the BPMs the beam is passed through the magnetic centers of the EXT line and FFS magnets using a '1-to-1' style steering algorithm in two steps. First correcting in the EXT line using the 25 horizontal and vertical dipole correctors. Then the orbit in the FFS is steered flat using the magnet mover and the BPMs on them. The dispersion in the EXT line is measured previously by changing the DR energy and corrected with quadrupoles horizontally, and vertically with a "sum knob" with skew quadrupoles in order not to add coupling [27]. Coupling is corrected with an orthogonal knob of four skew quadrupoles and the measurements from the Multi-OTR system or with the WS. The tuning of the IP vertical beam size in order to cancel any remaining aberrationis done by iterating quasi-orthogonal knobs moving the five FFS sextupoles [25].

2.3 General layout

ATF2 extends over 90 m beyond the DR and is equipped with 7 dipoles, 49 quadrupoles, 5 sextupoles, 4 skew-sextupoles and 25 corrector magnets. The layout of ATF2 can be seen in more detail in Fig. 2.3 and the design optics are shown in Fig. 2.4. There are mainly two parts: the first one is the EXT line which comprises the extraction of the DR with the kicker and the septum. The second main part of ATF2 is the FFS itself which includes an initial section for matching and tuning with quadrupoles and sextupoles and the final

doublet (FD) composed by two quadrupoles and two sextupoles. Each quadrupole and sextupole at the FFS is provided with a mover system which moves with a high degree of precision the magnet in three axis (horizontal, vertical and roll) in order to counter thermal drift and long-period ground motion and which is used as well to calibrate the high precision BPMs. The quads and dipoles in the main parts of the FFS were designed and built in purpose for ATF2. However some magnets including those in the FD were re-used from SLAC's Final Focus Test Beam (FFTB). Future upgrade proposed for the FD as a superconducting magnet [28] or a permanent magnet FD [29] are proposed.

Along ATF2 and in the IP there are installed R&D projects of beam instrumentation such as BPMs or a feedback system some of them used to tune the machine. The development of these devices is crucial to reach the ATF2 Goals and they will be presented in detail in the next section.

2.4 The diagnostics in ATF2

Along ATF2 and specially in the diagnostic section of the EXT line an R&D effort in beam diagnostics is being made. This will make possible the achievement of the main goals of ATF2. The the main devices for this purpose are:

- Beam Feedback: Intra-train fast feedback (FONT)
- Beam Position Monitors:
  - Cavity BPMs
  - IP BPM
- Beam Size Monitors:
  - Laser interference fringe monitor at the IP (IPBSM)
  - Pulsed laser wire scanner (LW)
  - Solid wire scanners (WS)
  - Optical transition radiation monitor (Multi-OTR)

The ongoing projects are presented in detail in the following subsections and their location in ATF2 can be seen in Fig. 2.5.

2.4.1 FONT project

In order to maintain the high luminosity in a FLC it is necessary to ensure the collision of the beams with high precision. ATF2 Goal 2 aims for a control of the beam position in the IP at the nanometer level. The beam stability depends on the ground motion, mechanical vibrations of the elements, electrical noise in magnets, etc. The FONT (Feedback On Nanosecond Timescales) project is a position and angle fast feedback for electron and

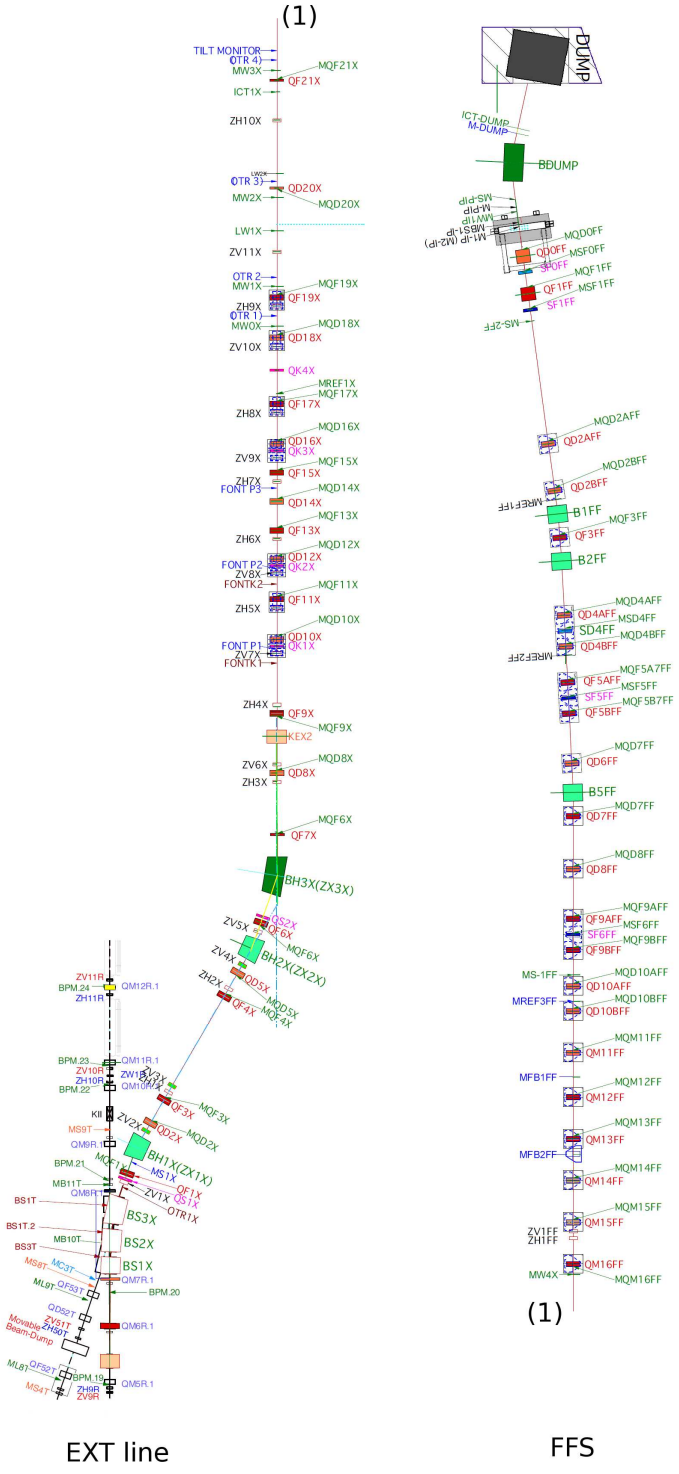

Figure 2.3: Layout of ATF2 divided in the two main parts, namely the EXT line and the FFS.

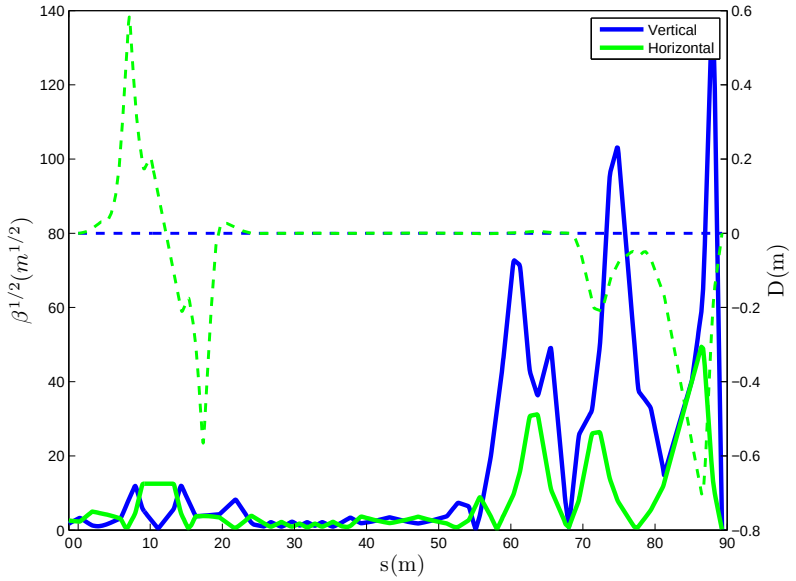

Figure 2.4: Optical Twiss parameters for ATF2.

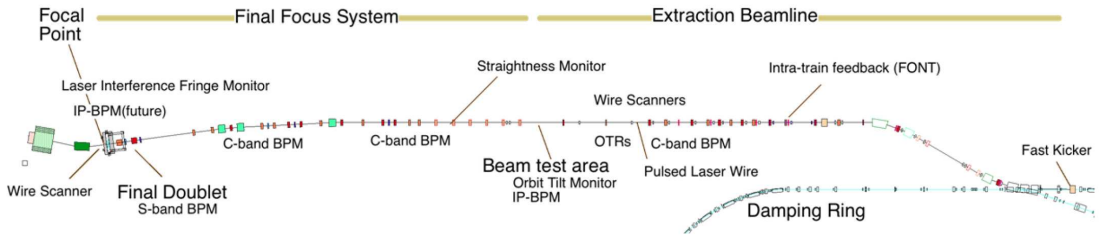

Figure 2.5: Main beam diagnostics and feedback projects installed in ATF2.

positron beams of a FLC. The project is based in John Adams Institute (JAI), Oxford, and the current version FONT5 is being tested in the EXT line at ATF2.

FONT works by measuring the position of the electron bunch with BPMs. This signal is processed by the electronics, after that the feedback signal is sent to the kicker, which corrects for the next bunch trajectory. For a given angle and position three feedback BMPs and two kickers are used to measure the position and to deflect the bunches respectively.

To correct a bunch position and angle is necessary to measure the previous bunch. This fact makes the bunch-to-bunch correlation one of the main limitations of the FONT correction. The uncorrelated jitter is the factor that limits the correction and this is related to the BPMs resolution. It has been shown that for a sub-micron correction the BPM has to have a resolution better than $1\mu m$ [30].

Another issue in such a fast feedback is the latency of the electronic system, limiting the number of bunches that can be corrected. In order to perform a proper correction the

feedback latency has to be less than the bunch spacing, which is 154 ns for the 3-bunch operation mode of ATF2, 369 ns for the 3000 bunches and 185 ns for the 6000 bunches operation mode of the ILC. The FONT5 latency has been measured to be 135 ns which makes the device suitable to correct in the mentioned cases.

FONT has demonstrated a reduction of a 2.1 μm initial jitter to 0.4 μm and 0.8 μm for the second and third bunch jitter respectively. the third jitter value corresponds to an extrapolated jitter of 2.6 nm at the IP [31].

The vibration of the FD quadrupoles is one of the most important jitter sources at the IP. The vertical displacement of these magnets causes roughly the same displacement of the IP beam position. The intra-train IP feedback can be considered as the last line of defense against such a jitter. A feedback version for the IP is in progress [32]. Fig. 2.6 shows the diagram of this feedback.

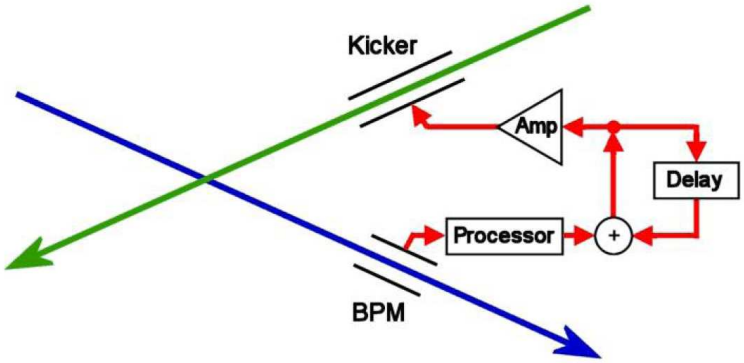

Figure 2.6: Diagram of the IP feedback system.

2.4.2 Cavity BPMs

When a beam passes through a cavity creates an electromagnetic field oscillations. The mono-polar mode is always excited but the dipole modes, which are not present when the beam passes through the exact center of the cavity, are excited if it is off-centered. The larger the offset from the center of the cavity, the stronger is the excitation. Both excited modes are shown in Fig. 2.7 in a general case. From all oscillating modes the first dipole mode TM110 is used for beam position monitoring. Its signal in the beam-pipe region has a linear dependence on the bunch displacement. The excited modes are coupled from the cavity by four symmetrically arranged feedthroughs: two for x and two for y position detection [19].

In particular in ATF2 three different types of cavity BPMs with different designs are installed (C-band and S-band Q-BPMs and IP-BPM). In order to maintain the orbit in the center of the magnetic field to avoid undesirable kicks the so called Q-BPMs are used all along ATF2. On the other hand the IP-BPM is placed in the FD in order to measure

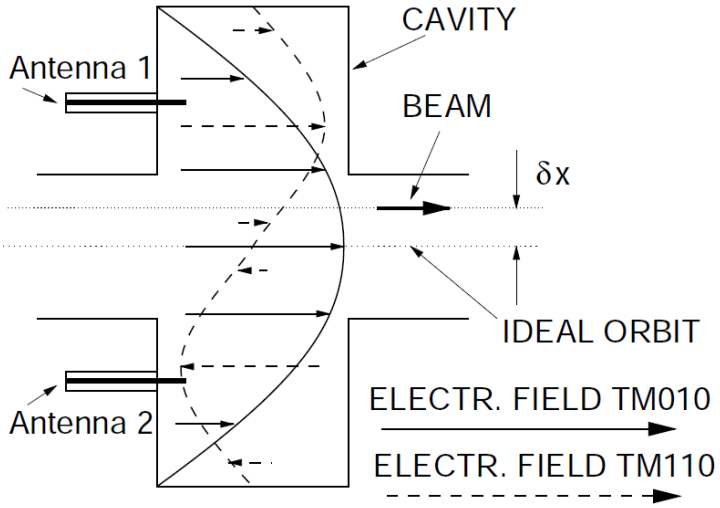

Figure 2.7: Basic scheme of the cavity BPM principle.

the transverse beam stability for the focal point. An ultra-high resolution special design is needed for this purpose.

Q-BPM

To measure the beam orbit and maintain the beam size with feedback the beam-line magnets are equipped with sub-micron resolution cavity BPMs known as Q-BPMs. Fig. 2.8 shows the circular design while Fig. 2.9 shows the installation near the quadrupole. In the diagnostic, matching and FF and at exception of the final doublet magnets, there are 35 C-band (6.4 GHz) cavity BPMs. In the FD they have to be larger due to the fact that the beam size before the IP is enlarged and thus they are a scaled S-band (2.9 GHz) version. The resolution for these monitors is expected to be better than 200 nm [31].

The entire BPM system has been operating successfully since 2009. A study of the best achievable resolution yielded a value of 27 nm for a bunch charge of $\sim 0.3 \times 10^{10}$ electron per bunch.[33]

IP-BPM

The IP-BPM needs to have the best possible resolution in order to measure the position jitter at the focal point at the nanometer level. In the IP we have a very flat vertical beam where the vertical jitter will be lower than the horizontal one, hence it is crucial to suppress the cross-talk between the two planes. The IP-BPMs are a rectangular shape monitor working in C-band and with a target resolution of 2 nm. They have been installed and operated but need further work to realize their full resolution potential at the IP. [33]

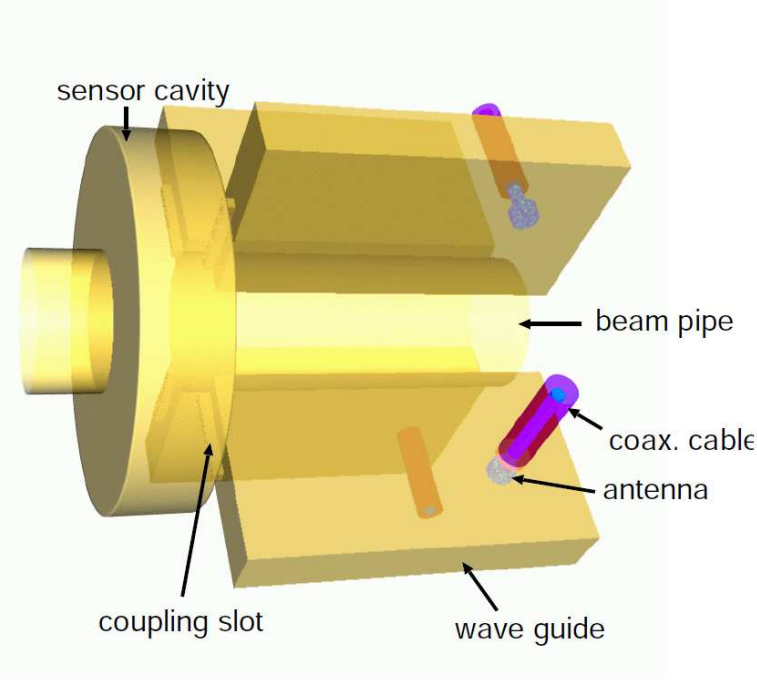

Figure 2.8: 3D view of the circular C-band BPM.

2.4.3 IPBSM

Unlike a collider, where the collision itself provides information about the sizes and how the colliding beam overlap in the case of ATF2, being a single beam line there is no real IP and thus the beam size needs to be directly measured. A laser interferometer based beam size monitor also called Shintake monitor is used for that purpose. The IPBSM is an improvement of an old monitor installed in SLAC's FFTB in the 90s [19].

The Shintake monitor is based in a laser interference fringe pattern that creates a split laser divided in two photon beams, made intersect in the IP. When the electron beam passes through the pattern the inverse Compton scattering takes place. A dipole located after the IP separates the electron beam from the Compton gamma rays. Fig. 2.10 shows the layout of the ATF2 IPBSM.

If the beam size is small compared to the fringe pitch then the number of scattered photons has a large variation depending whether the beam interferes with the peak or with the valley of the fringe. If the fringe and the beam size are comparable then the beam will interact with peak and valley at the same time and the number of photons will not vary too much. The modulation depth is defined as:

$$M = \frac{N_{max} - N_{min}}{N_{max} + N_{min}}, \tag{2.3}$$

with both N the maximum and minimum number of photons when the relative position

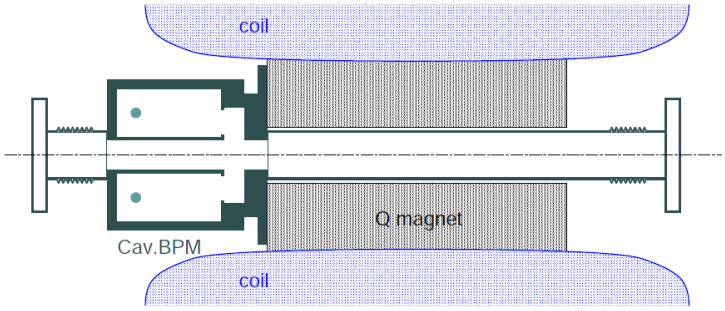

Figure 2.9: Detail of the location of a C-BPM in the ATF2 quadrupole.

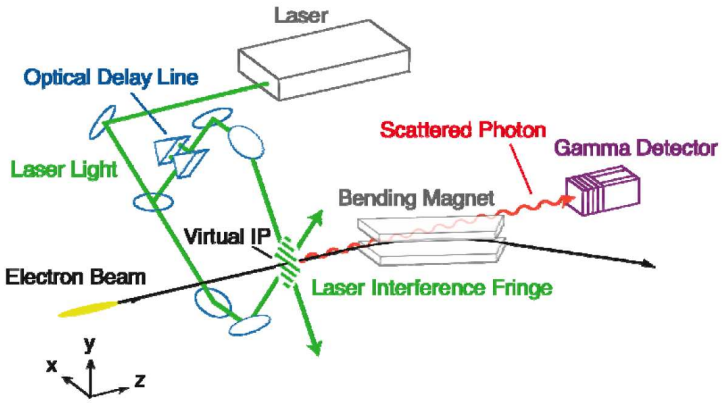

Figure 2.10: Basic scheme of the Shintake monitor working principle.

between the beam and the fringe pattern is moved. M can be also written as

$$M = |cos\theta| \cdot exp[-2(k_y\sigma_y)^2], \tag{2.4}$$

with θ the crossing angle between both lasers, k_y the wave number of the interference fringe in vertical and σ_y the vertical electron beam size, which we are looking for. An example of a measurement is shown in Fig. 2.11.

The position of the interference fringe relative to the electron beam is changed by modifying the relative phase between the two lasers, which is done with an optical delay line that changes the path length of only one of the photon beams [34]. At ATF2 there are different angle configuration in order to measure a range of sizes, namely 174°, 30°and a variable mode with range 8°∼2°. The different configurations with the respective measurable sizes are summarized in Table 2.2. The monitor is capable of measuring beam sizes from 6 μm up to 25 nm with a resolution better than 10% [35].

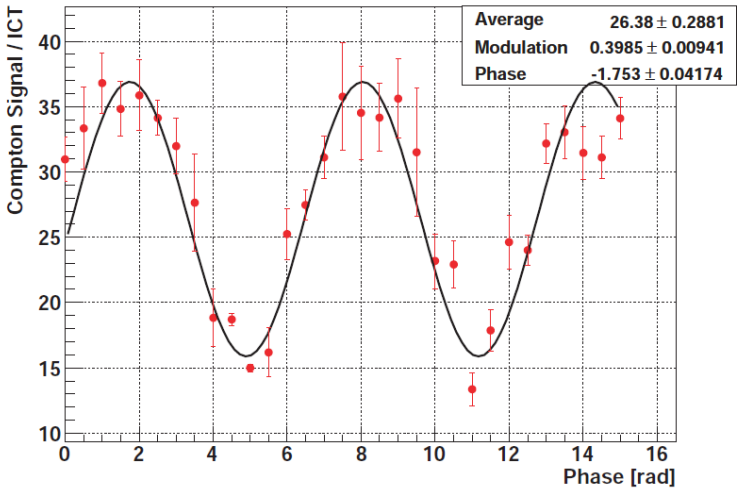

Figure 2.11: Example of a real Shintake beam size measurement.

Crossing angle (°)	Fringe pitch d (μm)	Measurable size σ_y (nm)
174	0.266	$25 \sim 100$
30	1.028	$100 \sim 360$
8	3.81	$360 \sim 1400$
2	15.2	$1400 \sim 6000$

Table 2.2: Shintake monitor size measurement possibilities depending on the laser crossing angle.

2.4.4 Laser Wire

In the ILC with the high intensities and small beam sizes the transverse beam diagnostics has to be made by means of laser-based devices. Laser wires for the sizes of the order of a few microns and Shintake monitor for the sizes of the tenths of the nanometer order. The first use in HEP of such a laser wire device was at the Stanford Linear Collider (SLD) in the 1996. More recently in ATF DR a laser wire has been used and a high-power pulsed laser system is operational in PETRA [19].

The laser wire uses a high-power beam laser very well focused in order to scan across the electron beam and detecting downstream the inverse Compton scattered photons as a function of the relative position between the electron beam and the laser. The number of photons being scattered are proportional to the overlap between both laser and electron beams. The basic layout can be seen in Fig. 2.12. The laser spot size has to be very well determined in order to measure with precision the electron beam size.

Assuming a gaussian spatial density for the electron and for the photon beams and considering that the laser dimensions do not vary along the electron beam the number of

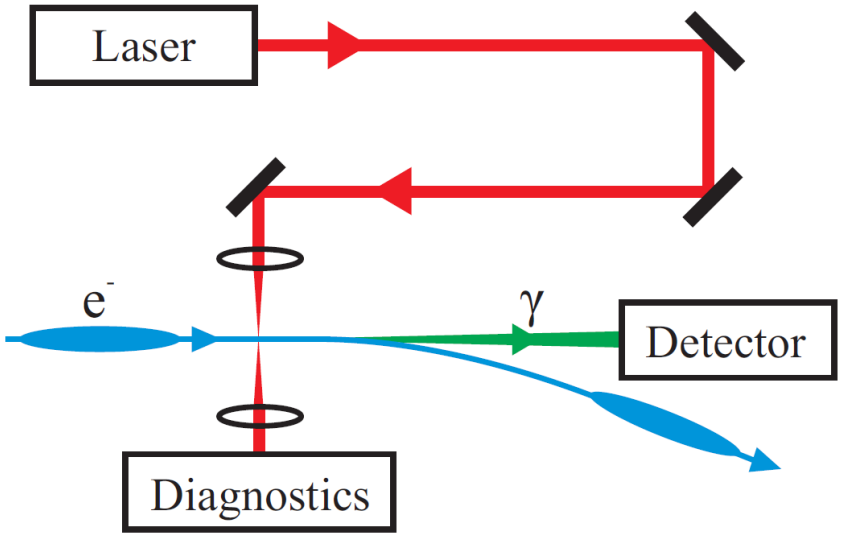

Figure 2.12: Laser wire basic diagram.

scattered photons is given by:

$$\langle N_\gamma \rangle = N_e P_L C exp\left(-\frac{(y_L - y_e)^2}{2\sigma_c^2}\right), \tag{2.5}$$

where the sub-indexes e and L represent the electron beam and the laser respectively, N is the number of particles, P_L is the laser power, y is the vertical position of the beam, C is a normalization constant and σ_c is the quadrature sum of both beam sizes $\sigma_c = \sigma_L^2 + \sigma_e^2$. The vertical electron beam size is then indirectly measured.

The laser wire has been upgraded and it is under commissioning but the previous one demonstrated a minimum RMS electron beam size of $4.8 \pm 0.3 \mu m$. The goal of the upgrade is to measure beam electron sizes of about 1 μ m. Nowadays the laser has a transverse size of around $\sigma_L \sim 2\mu m$. The laser system produces a 167 ps long pulses of 150 mJ at the ATF2 repetition frequency, which is 1.56 Hz. It is focused to the IP with the electrons using a fused-silica lens. The laser is scanned along the electron beam moving the vacuum chamber, i.e., the silica lens. The scattered photons with a maximum energy of about 28 MeV are separated from the electrons by means of a dipole magnet, then they are detected with a lead layer that produces e^+e^- pairs which in turn create Cerenkov radiation in an Aerogel layer and are guided to a photomultiplier in order to measure the signal [36]. Fig. 2.13 shows the minimum measured convoluted size of $\sigma_c = 8.0 \pm 0.3 \mu m$.

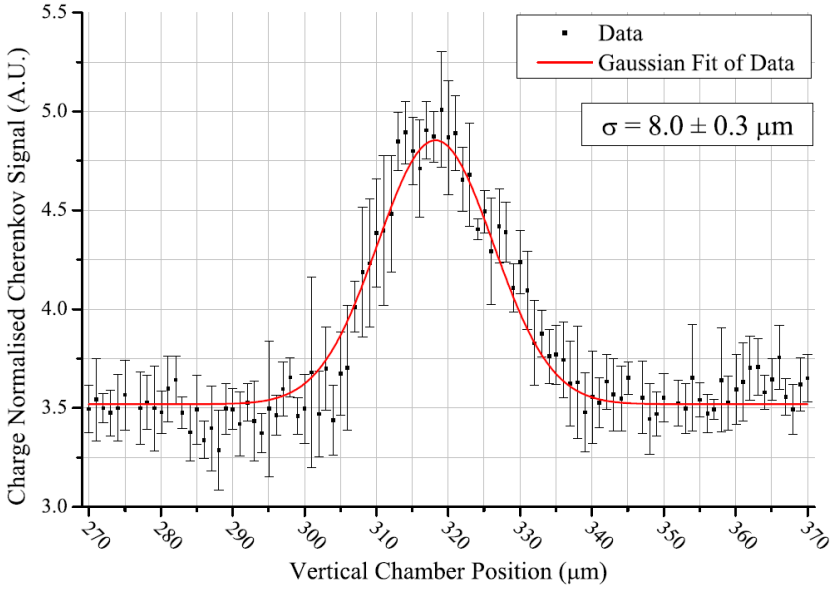

Figure 2.13: Example of a LW raw measurement.

2.4.5 Wire Scanners

In order to measure the extracted beam size and to reconstruct the emittance and be able to correct coupling for beam tuning purposes, 5 Wire Scanners (WS) were installed in ATF2. The principle of such a beam size measurement monitor is to move a wire across the beam while measuring the signal which is proportional to the number of particles of the beam interacting with the wire. It is therefore and invasive method. The observed signal are mostly gammas from the bremmsstrahlung process. The precision of a WS is dominated by the precision in the positioning of the wire and the precision in the measured signal. It interesting to maintain the wire as small as possible although there are methods of deconvolution to take in account the error introduced by the finite size of the wire. Moreover deformations and damage of the material are another source of errors [37].

WS in the EXT line

The ATF2 design of the WS is shown in Fig. 2.14. Five of this WS are installed in the dispersion-free diagnostic section between quadrupole magnets in order to use the measured beam sizes to calculate the beam emittance and correct coupling. The scanning speed is around 30 seconds per profile, being so slow in order to gain precision not distorting the wire shape while scanning. The pulse-to-pulse stability is important for this kind of monitor in order to reduce the size overestimation due to the integration of the jitter. The position jitter is estimated in $2.4 \sim 4.4 \mu m$ in the region. In each WS stage there is a $50 \mu m$

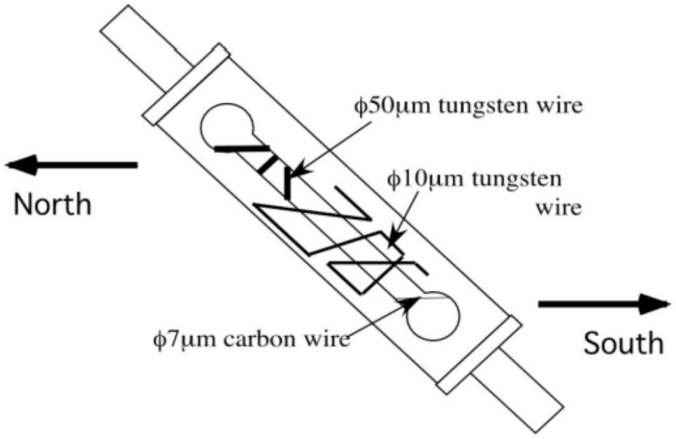

Figure 2.14: WS stage with the two different wires.

diameter gold plated tungsten wire in the x, y and 45°directions and a $10\mu m$ diameter gold plated tungsten wire in the x, y, 45°and 10°directions. The whole moves in the 45°direction and thus it measures the three axis with a single movement. The resolution is between 10 and 20μ m [38]. An emittance measurement can take up to an hour and a coupling correction lasts an entire 8-hour shift. A picture of a WS as installed in the ATF2 line is shown in Fig. 2.15.

Post-IP WS

In addition to the Shintake monitor in the IP there were installed a $10\mu m$ tungsten wire in 2009 [39] 40 cm after the focal point and a $5\mu m$ carbon wire in 2011 [25] 41.5 cm downstream of the focal point in order to measure the beam sizes during the initial tuning with resolutions of $2.5\mu m$ and $1.25\mu m$ respectively. When these WS are used the optics is adjusted in order to shift the waist to this post-IP location. The bremmstrahlung photons produced by the interaction of the beam with the material are measured with a Cerenkov detector which is placed downstream after a bending magnet to separate the electron beam. The finite size of the wire and the measured dispersion value is taken in account in order to indirectly measure the beam size.

2.4.6 Multi-OTR

The Multi-OTR project is a four OTR monitor system installed in the diagnostics section of the EXT line of ATF2. An OTR monitor is based on the transition radiation effect, a light cone emitted when the charged particle crosses a metallic interface. This light is emitted in a specular fashion so the device can focus it in a CCD camera. Whereas the WS measurements require many pulses, often with an overestimation of the beam size

Figure 2.15: WS as installed in ATF2. The stage moves in 45°direction.

due to beam position and intensity jitter, and can take up to half a minute to complete a beam size measurement and several minutes to measure the emittance; the OTRs are able to take many fast and single-bunch measurements and therefore to measure the emittance with high statistics in less time. This thesis is devoted to the Multi-OTR project in ATF2 and therefore a detailed description of the monitor itself, setup, installation, calibration and measurements will be found in the further chapters.

Chapter 3

The Multi-OTR project

3.1 OTR Beam Size Monitor

In electron and in high energy proton accelerators the beam profile can be measured using the electromagnetic radiation called Optical Transition Radiation (OTR) emitted when the beam intercepts a thin metallic foil. This section describes with the OTR phenomenon and how to take profit of it in order to measure beam sizes in an OTR beam profile monitor.

3.1.1 Optical Transition Radiation

The Transition Radiation (TR) phenomenon was predicted by Frank and Ginzburg in 1945 [40].The TR can be seen as a second order Cerenkov effect, because it is produced by a charge passing through an interface of two media with different dielectric constants or, more generally, when crossing a medium with inhomogeneities.

A visual interpretation of the effect is to consider the pass of a charged particle from the vacuum to a high conductivity metal, which is an ideal mirror, as shown in Fig. 3.1. From the electromagnetism it is known that the field of a charge in the described geometry is the sum of the field of the charge q moving in the vacuum in the absence of mirror plus a charge $-q$ (named commonly image charge) moving in the mirror in the direction of q. As soon as the charge q crosses the boundary it finds itself in a medium with high conductivity, it is unable to produce any field in the vacuum and consequently $-q$ is lost. For this fact, from the point of view of the observer it is as if a pair of charges q and $-q$ would annihilate each other in the vacuum producing radiation [41].

The TR can be then understood considering the electromagnetic field that a moving particle carries with it. These fields are media dependent and so they have to reorganize themselves when the particle approaches and crosses the interface. In this reorganizing process some parts of the fields turn into emitters of TR.

The angular distribution of the radiation is explained by the "phase coherence" argument given by Jackson [42]. In the case of particle passing from the vacuum to a medium the driving fields of the incident particle penetrate the medium as the particle approaches to the surface. In order to have considerable TR, coherent superposition of the fields in

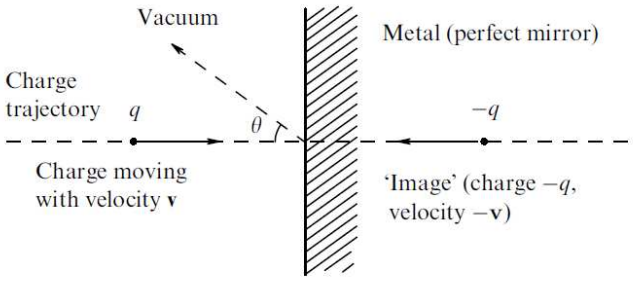

Figure 3.1: Scheme of the TR emission in the image charge interpretation.

different places in the medium has to be present. This happens by assuming that the product of the driving fields and the generated wave does not change in phase too much in the region and results in the condition for appreciable TR:

$$\sqrt{\epsilon(\omega)} \cdot \gamma \cdot \theta \leq 1, \tag{3.1}$$

with γ the Lorentz factor, θ the emission angle of the radiation with respect to the beam axis, ϵ being the dielectric constant of the medium and ω the frequency of the radiation. The characteristic angular distribution of the TR is then a cone of aperture $\theta \sim 1/\gamma$.

In the case of a charge moving from a medium with dielectric constant ϵ to the vacuum with dielectric constant unity the spectral intensity, I_f, of the forward emitted radiation in the frequency range $d\omega$ and into a solid angle $d\Omega$ is given by [43]:

$$\frac{d^2 I_f}{d\omega d\Omega} = \frac{e^2\beta^2}{\pi^2 c} \frac{\sin^2\theta\cos^2\theta}{(1-\beta^2\cos^2\theta)^2} \cdot \left| \frac{(\epsilon-1)(1-\beta^2-\beta\sqrt{\epsilon-\sin^2\theta})}{(\epsilon\cos\theta+\sqrt{\epsilon-\sin^2\theta})(1-\beta\sqrt{\epsilon-\sin^2\theta})} \right|^2. \tag{3.2}$$

For relativistic electrons where $\beta \to 1$ and in the case where $|\epsilon| > 1$ the third term in (3.2) tends to be 1. This can be noted from Eq. (3.1) where $\theta << 1$ and then it is possible to use the approximation $\sin^2\theta \approx 0$ and $\cos\theta \approx 1$. The simplification of the other terms is easier to see by defining $x = \beta\cos\theta \approx 1$:

$$\frac{x^2}{(1-x^2)^2} = \frac{1}{(1+\frac{1}{x})^2(1-x)^2} \approx \frac{1}{4(1-x)^2}, \tag{3.3}$$

and so Eq. (3.2) comes to be

$$\frac{d^2 I_f}{d\omega d\Omega} = \frac{e^2}{4\pi^2 c} \frac{\sin^2\theta}{(1-\beta\cos\theta)^2} \approx \frac{e^2}{\pi^2 c} \frac{\theta^2}{(\theta^2+\gamma^{-2})^2}, \tag{3.4}$$

where it has been used the small angle approximation and $\beta \approx 1 - 1/(2\gamma^2)$.

When the charge passes from the vacuum to the medium the backward emission is obtained by simply changing β for $-\beta$ in Eq. (3.2). In the limits where $\beta \to 1$ and $|\epsilon| > 1$

now the third term takes the form of a Fresnel reflection term, which is not strange due to the fact that the backward emission comes from the waves which are not able to propagate in the material medium and are reflected in the boundary. By simplifying as done in the forward radiation formula, now the backward radiation takes the form:

$$\frac{d^2 I_b}{d\omega d\Omega} = \frac{e^2}{\pi^2 c} \left| \frac{\sqrt{\epsilon} - 1}{\sqrt{\epsilon} + 1} \right|^2 \frac{\theta^2}{(\theta^2 + \gamma^{-2})^2}. \tag{3.5}$$

Note that the radiated energy does not depend on the frequency ω, i.e., the whole spectrum in covered. This is valid up to the plasma frequency of the metal, which is for most metals in the deep UV at about 10 eV [47]. Fig. 3.2 shows the peaked angular behavior of this distribution. Note the amplification factors in the plot for the lower γ values and the fact that the peaks are located at $\theta \sim 1/\gamma$.

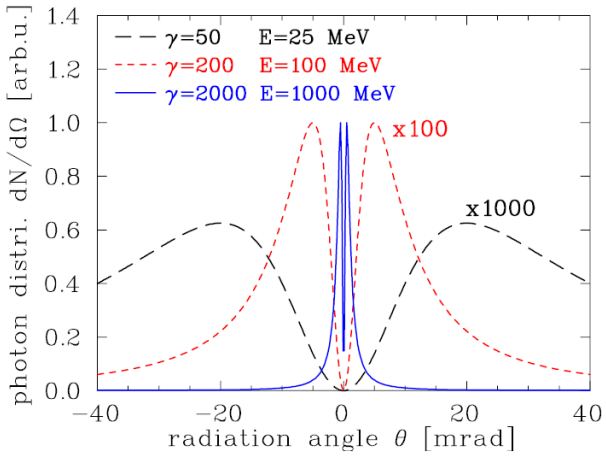

Figure 3.2: Angular distribution of the emitted TR light for different incoming particle energies [47]. (Note the amplification in two of the lines)

These formulae are valid for normal incidence of the electron beam. For the case of optical frequencies in metals and for relativistic electrons the treatment of the oblique incidence can be simplified and it reduces to the equations shown above. The forward OTR does not depend on the incidence angle and it is emitted in the beam direction while the backward is emitted in the specular direction, i.e. in an angle equal to the incidence angle with respect to the normal of the surface. The importance of a high Lorentz factor can be seen in the Fig. 3.3, which shows the evolution of the backward OTR emission angle when gamma grows higher.

3.1.2 OTR beam profile monitor

The application of the OTR phenomenon in beam diagnostics was suggested by Wartski [44] and realized by Bosser in the middle 80s [45]. The basic scheme of an OTR monitor

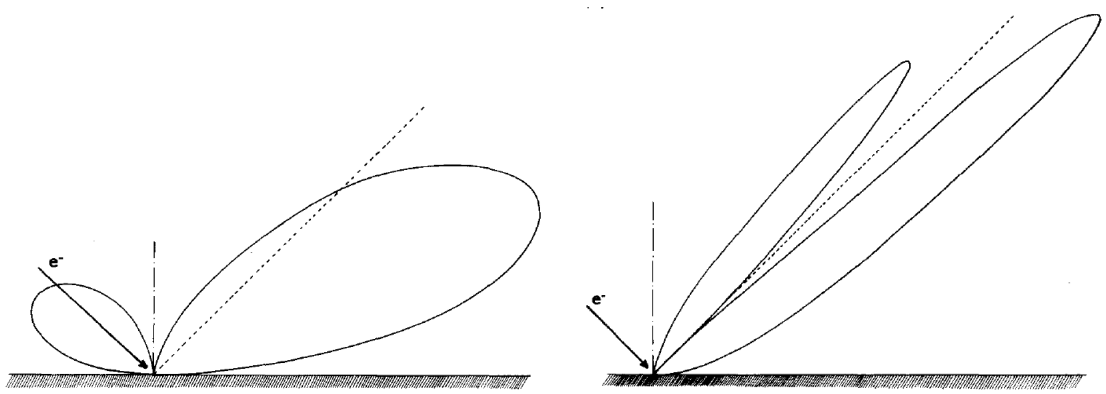

Figure 3.3: Sketch of the TR emission when the particle hits not normal to the surface. In the left non relativistic while in the right relativistic electrons [44].

has normally the same features. A metallic foil is inserted to intercept the beam and a CCD camera registers the emitted light. The target is normally inserted at 45° with respect to the beam path so that the light is emitted orthogonal to the beam pipe and can be collected by an optical system. Since it is normally outside the pipe it is necessary to have a vacuum sealed window to let the radiation pass through. The scheme of an OTR measurement can be seen in Fig. 3.4.

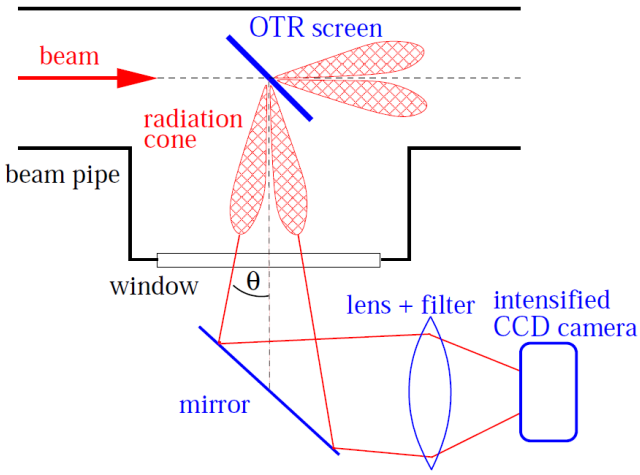

Figure 3.4: Typical setup of an OTR monitor.

The target foil is made of some metal or Mylar/Kapton[1] with metallic coating and is normally less than a μm thick. Due to optical imaging reasons one wants the aperture

[1]Mylar and Kapton are commercial dielectric polymers widely used for scientific purposes due to their high mechanical and thermal stability.

angle of the radiation cone to be small and since the intensity peak of the light is emitted at an angle $\theta \approx 1/\gamma$ then the OTR monitors are limited to particle beams with reasonably high energy [46], i.e $\gamma \gg 1$. In our case this angle is equal to 0.4 mrad.

With respect to the classical scintillator screen which normally is about 1 mm thick, the OTR light can be obtained with very thin foils, with considerably less scattering of the beam particles and thus less increase of the emittance. The number of photons does not depend on the thickness of the foils, and therefore it is possible to use very thin targets which are less invasive due to the low scattering probability and can be used in high power beams because the lost energy is low in low Z materials. Moreover, it is based in a classic electrodynamics process and there is a linearity between the number of OTR photons and the number of particles in the beam and that, assuming gaussian beams, allows to adjust a gaussian to the image in order to infer the beam size.

The Multi-OTR system has the ability to measure very small beam sizes and emittances. In addition, these profile monitors can be used for other purposes, such as dispersion and energy spread measurements. For example, in the CLIC test facility CTF3 OTRs are used to measure the drive beam energy spread. In CTF3 setup, for low beam energies there is no problem in imaging the beam, whereas for higher beam energies the light cone generated off the center can may escape the image system partially or entirely in what is called the vignetting effect. Studies on diffusive and parabolic targets may be seen in [48]. In the XFEL context in TTF/FLASH at DESY, four OTRs are used for emittance, dispersion and energy spread measurements. In FLASH the peak charge per bunch is around 10^{-9} C (6×10^9 electrons per bunch), which is comparable to the ATF2 charge. In FLASH the RF pulse repetition rate is almost one order of magnitude higher than in ATF2, with 7200 bunches per train, which imposes severe constraints for the OTR screens in terms of damage issues. Therefore, pulse kicker magnets are installed in order to deflect only a bunch to be analyzed by off-axis OTR screens [49]. Further away from the colliders field, in the proton line of the T2K long base-line neutrino oscillation experiment an OTR has been installed to measure the proton beam position and width [50]. One of the key issues in such a harsh environment near the pions and kaons production target is an optical system capable of transporting the light over a large distance out of this environment to a lower radiation area where it is possible to operate a camera to capture this light.

3.2 Multi-OTR in ATF2 EXT line

In the frame of ATF2 four OTR beam profile monitors have been installed in the EXT line and are fully operative and working. The Multi-OTR project was put in context in Chapter 2 and will be detailed in this and next Section in more depth.

3.2.1 Motivation

In the frame of ATF2 being a FFS prototype to test the Local Chromaticity Correction scheme and in order to fulfill the two ATF2 Goals, reliable and fast emittance measure-

ments after the extraction of the beam from the ATF DR are needed.

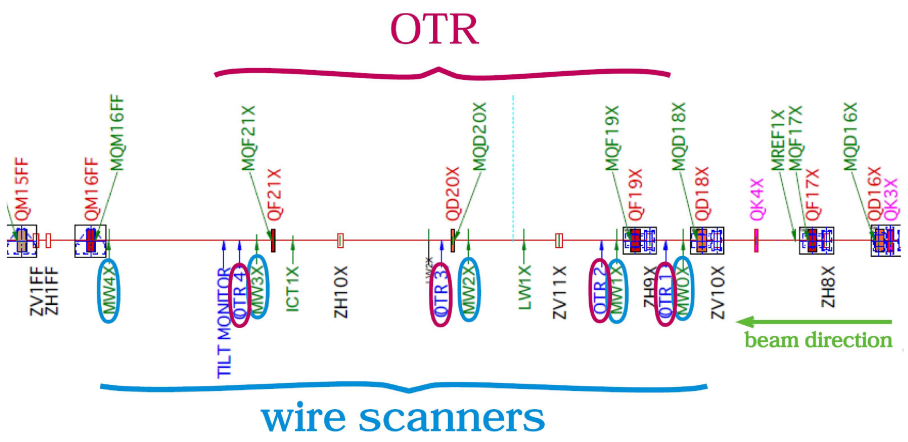

Figure 3.5: Layout of the ATF2 diagnostics section of the EXT line where the WS and the Multi-OTR system are located, the beam going from right to left.

As was explained in Section 2.4.5 five WS were installed in 2000 for the emittance reconstruction and have been used successfully over the years, however these devices present some issues that was interesting to be addressed:

- Due to the fact that a profile measurement takes around 30 seconds to be made the measurement is integrated over several bunches and therefore there is a contribution to the beam size coming from the bunch-to-bunch jitter. This results in an overestimation of the beam size.

- The long measurement time for one single profile means that an emittance measurement, where at least three WS stations have to operate and some measurements for each one are necessary in order to determine an statistical error, can take near half an hour to be completed. Moreover, if one wants to correct the beam coupling this measurement time is multiplied by normally four skew quadrupoles and some emittance measurements per skew in order to fit a parabola, which means an entire 8-hour shift has to be used with the only purpose of correcting the coupling.

In the past, there was an OTR installed at the beginning of the EXT line which served for many purposes including measuring the beam size and emittance parameters from the ATF DR [51] and which doesn't exist anymore. This device served later to the Multi-OTR designing. The aim was to install a faster single-shot device able to measure the beam emittance with high statistics, giving a low error and a good understanding of emittance jitter. In fact, the Multi-OTR ameliorates the WS listed issues. First, since the ATF2 bunch repetition rate (in single bunch mode) is 1.56 Hz, the CCD camera can be timed so

that it captures only one single-bunch image and therefore no overestimation of the beam size due to jitter happens. Second, an emittance measurement lasts less than a minute and the coupling can be corrected in less than 30 minutes.

Moreover, locating the Multi-OTR system near the WS would permit to compare and validate the results of both monitor systems being a definitive test of the OTRs as a small emittance diagnostic device. The Multi-OTR provides also measurement for coupling correction using the four skew quadrupole knob. This system can help as well in future studies such as emittance growth after the DR extraction, and could be used in eventual jitter studies.

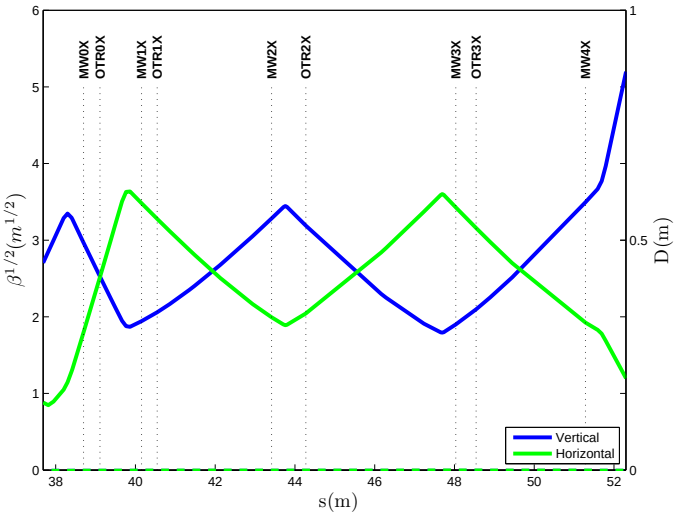

Figure 3.6: Optics in the Multi-OTR region. The solid line represents the Twiss beta function while the dashed line shows the dispersion function. The position is referenced to the beginning of the EXT line.

3.2.2 Location

The location of the four OTRs is important for the proper work of the system and has to be chosen carefully. In order to make a comparison with the WS the OTR system has been located near them using the available space in the beam line. Fig. 3.5 shows the layout of both systems as installed in ATF2 EXT line. In ATF2 the WS are labeled as $MWiX$ with i from 0 to 4 while the OTRs are labeled $OTRiX$ with i from 0 to 3.

The OTRs are installed in between FODO cells in a zero dispersion region. Fig. 3.6 shows the optics in the diagnostics section where the Multi-OTR and the WS are located. Both the phase advance between the OTRs and the phase advance between the WS are selected to make possible emittance measurements by not looking at the same phase in different monitors. Phase advances between the devices are shown in Fig. 3.7.

In the old single OTR installed in the EXT line the small beam sizes (20 μm horizontal per 12 μm vertical) arriving at the device damaged the copper target (a single 7.5×10^9

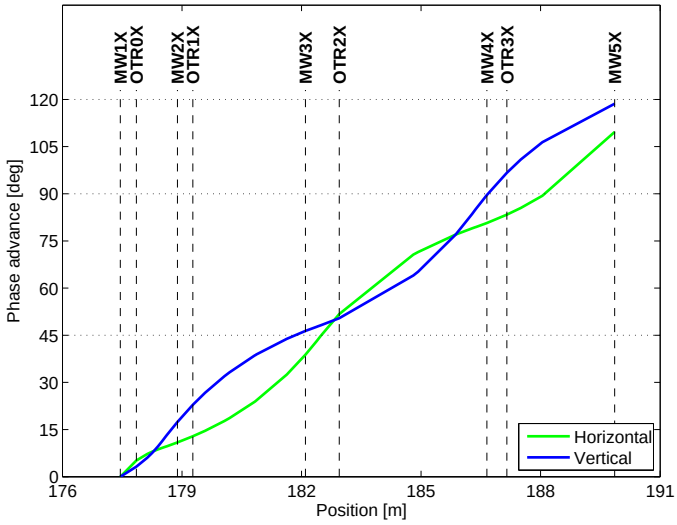

Figure 3.7: Phase advances between the OTRs and WS. The position being one DR turn plus the EXT line.

electrons bunch at 1.3 GeV [51]). The optics are then to be selected in order not to go under a minimum beam size that leaves the target undamaged. In the Multi-OTR system the targets are in safe margin in nominal single bunch ATF2 operation. Fig. 3.8 show the beam spots and the vertical and horizontal phase spaces in each of the four OTR locations.

3.3 Design and construction

The four OTR monitors are custom designed on purpose for the project. Technical features of their design, construction and installation are related in this Section.

3.3.1 Hardware development

The 4 OTR monitors installed in the EXT line are based on the design of the previous one labeled as $OTR1X$ which was placed near one of the WS in order to compare them and to demonstrate that this device could measure the small beam sizes that would be found after a linear collider DR. It was also used to evaluate target materials for the currents and spot sizes most likely to be encountered. After that, the device was used for other purposes such as, for example, experimental studies on the vertical emittance growth after the DR beam extraction [56].

A picture of the old design can be seen in Fig. 3.9. Although this design was used to build the new Multi-OTR monitors taking profit of the previous experience it presented some issues that were improved in the newer version:

- As the device was built step by step by adding new functionalities on the existing

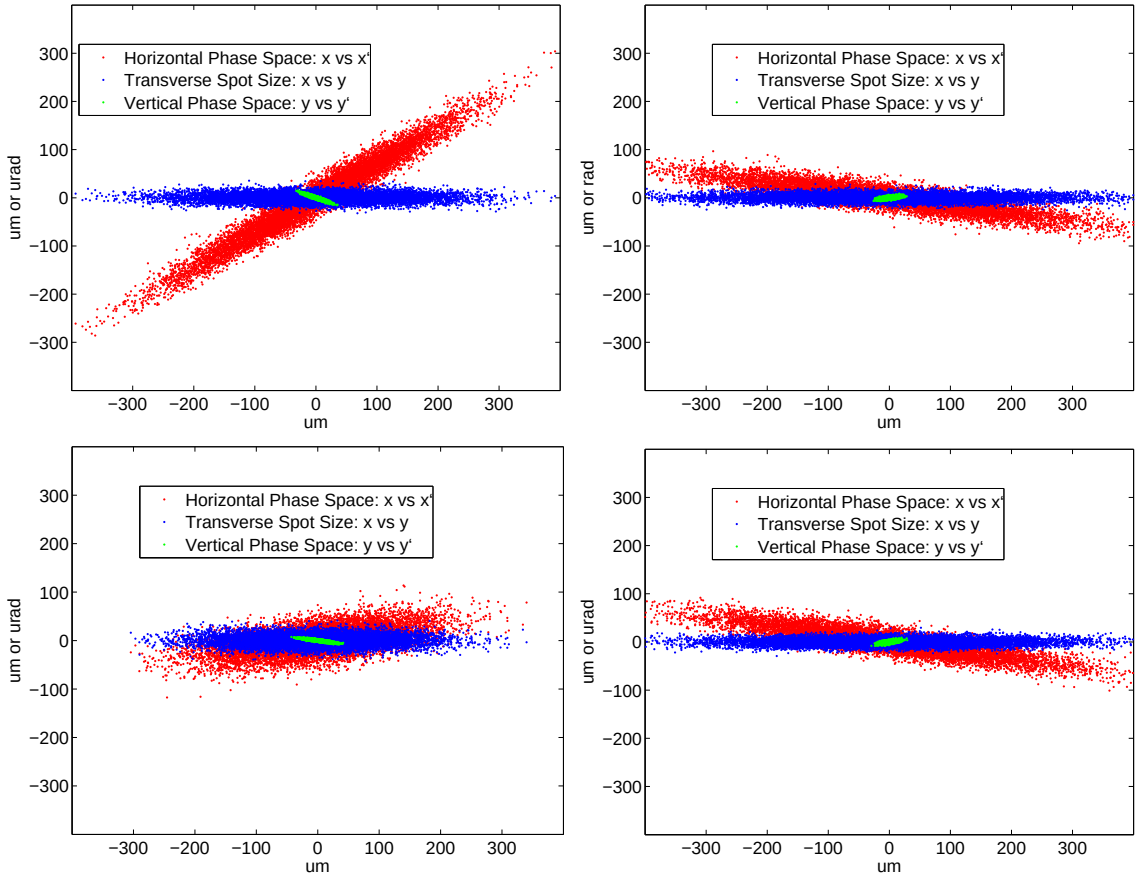

Figure 3.8: Transverse beam size and transverse phase spaces in each of the four OTR locations. OTR 0 and 1 in the first line and OTR 2 and 3 in the second one.

structure it ended to be an evolved patchwork rather than an optimized design. Because of this reason it took up a lot of space in the beam line.

- The target actuator was placed on the bottom being a source of interference problems with the supporting structure.
- Since the targets were rather thick the glass lens was darkened because of the radiation and the camera suffered damage.
- The small beam sizes arriving at the device damaged the copper target. Therefore, as explained in previous section, the placement of the new OTRs where the beam sizes were over a certain minimum had to be studied. New materials need to be tested as well.

Fig. 3.10 shows a general overview of the new OTR design and Fig. 3.11 shows it as installed in ATF2 EXT line, the beam going from right to left. The yellow scotch covers

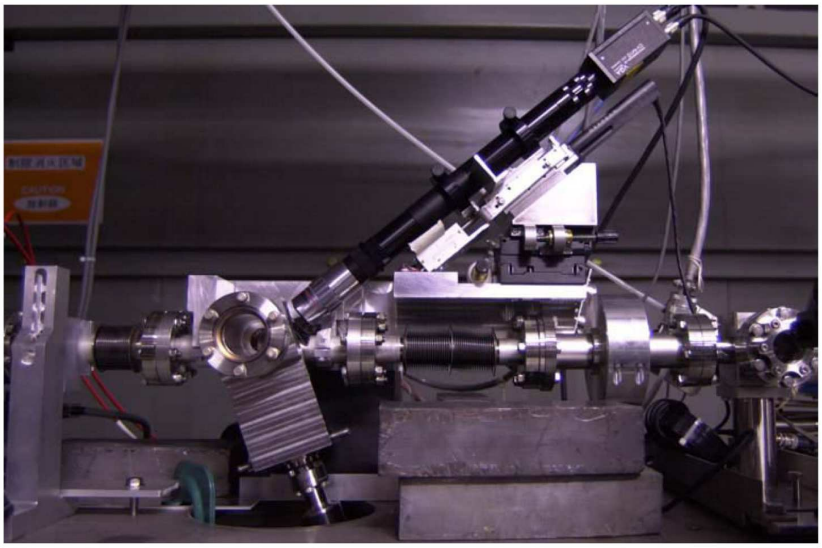

Figure 3.9: Old single OTR monitor design installed previously in the EXT line.

the main body and the side window to protect from light coming in from outside. Below it, the vertical and horizontal stepper motors are shown. From the body, in the upper-left direction is the target actuator and in the upper-right direction the optical elements. The lead shielding for preventing CCD camera damage can be seen on the left of the OTR. At the left and right sides of the body there are a couple of bellows that allows some horizontal and vertical displacement of the whole OTR system.

Optical system

In order to focus the OTR light emitted in the target onto the CCD screen, an optical system including C-Mount lenses, tubes and a mirror to protect from X-rays are used. The main lens, from M Plan Apo SL Series, is a long working distance microscope objective manufactured by Mitutoyo. This 5X objective has a numerical aperture of 0.14, and a 34 mm working distance and it is designed for use at infinite conjugate ratio (i.e. focuses a point to a parallel beam) giving a depth of field of approximately ± 7 μm. The high numerical aperture is motivated by the fact that the large angle radiation must be efficiently collected because most of the TR at high energies is emitted at large angles (this will be explained in more detail in Section 4.2). Due to the difficulty to find the beam and the fact that sometimes the spot was slightly bigger than the screen so that the measured beam size was wrong, it was decided to use a zoom system that could allow a variable Field of View. For this reason an Optem 2.0X TV Tube was installed, and together with the microscope, the whole optical system has a range of magnification factors within 1.7-0.25

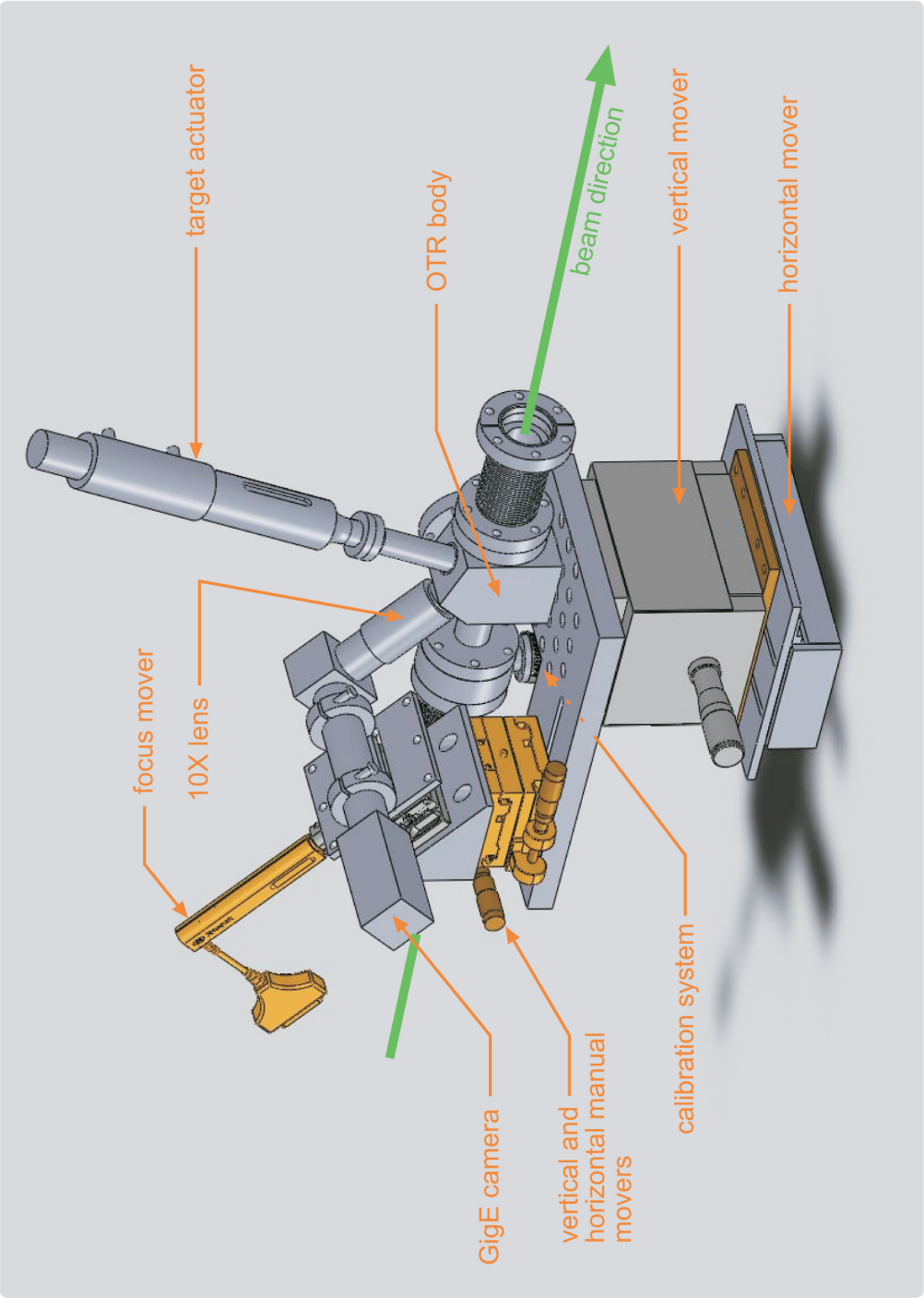

Figure 3.10: First design of the new OTR model.

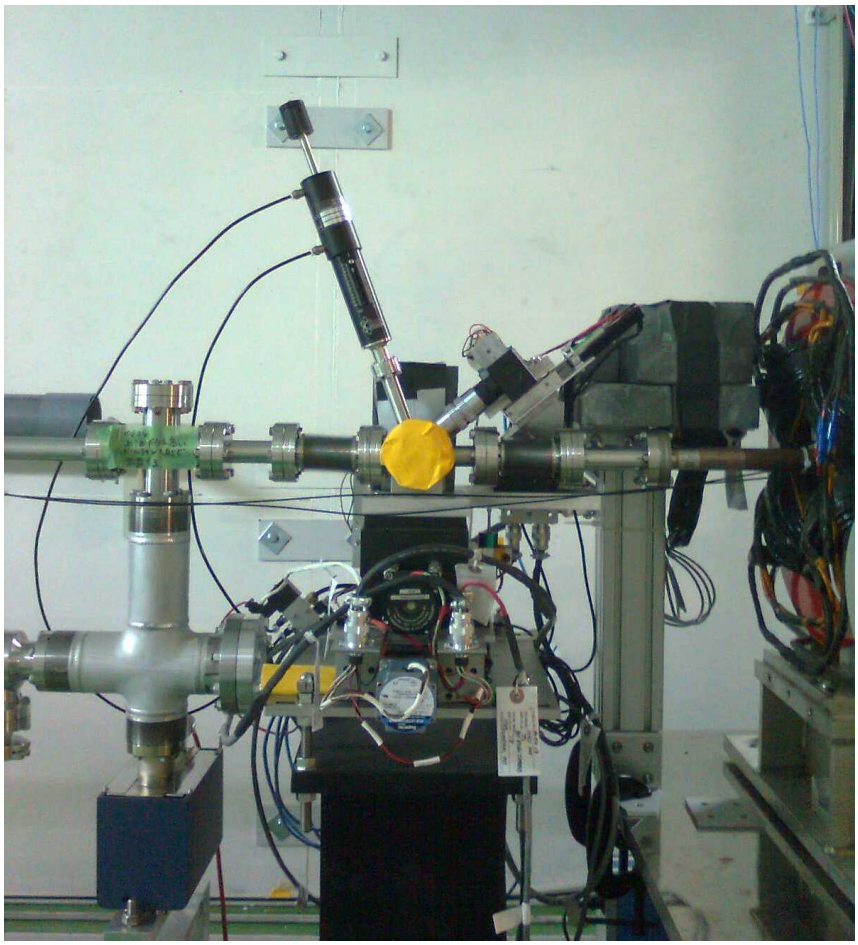

Figure 3.11: View of the new OTR design installed in the ATF2 EXT line, the beam going from right to left.

mm as stated by the manufacturer specifications.[2]. The optical system of the new OTR design includes a mirror that deflects the OTR light 90 degrees in order to place the CCD camera at one side for radiation protection.

The CCD Camera is a Prosilica GC1290, a 12 bit camera for more dynamic range (which is an improvement compared to the old design). The sensor size is the same ($1/3''$) as in the old prototype, but the pixel size now is smaller (3.75×3.75 μm) and therefore the resolution is bigger (1280×960 pixels). The camera works with Gigabit Ethernet interface (GigE), which is a standard interface introduced in 2006 for high-performance industrial cameras and assures 125 Mb/s up to at least 100 m. For synchronization the CCD is triggered from a "pre-trigger", a split, delayed copy of the trigger used to fire the

[2]This information can be found in $http://www.edmundoptics.com/imaging/imaging-lenses/zoom-lenses/7x-precision-zoom-lenses/2364$

extraction kicker at the machine repetition rate (normally 1.56Hz). Physically, this is a TTL trigger signal passed from a gate generator to the "sync-in 2" input on the camera. The gate generator allows for some fine-adjustment at the nanosecond level of the trigger signal. The CCD integration time is another setting. To set it up, the integration time is set to something large with respect to the machine repetition rate (about 0.6 s), then slowly reduce until the image disappears; move the trigger delay to put the trigger closer to the beam arrival time; reduce the integration time and iterate until the integration time is lower than 5 ms to give good signal to noise characteristics.

The optical elements are shown in Fig. 3.12. In the foreground one can see the Mitutoyo lens and the 90 degree mirror. Then, after the light is reflected, the zoom system with the zoom actuator and lastly in the very background the Prosilica CCD camera.

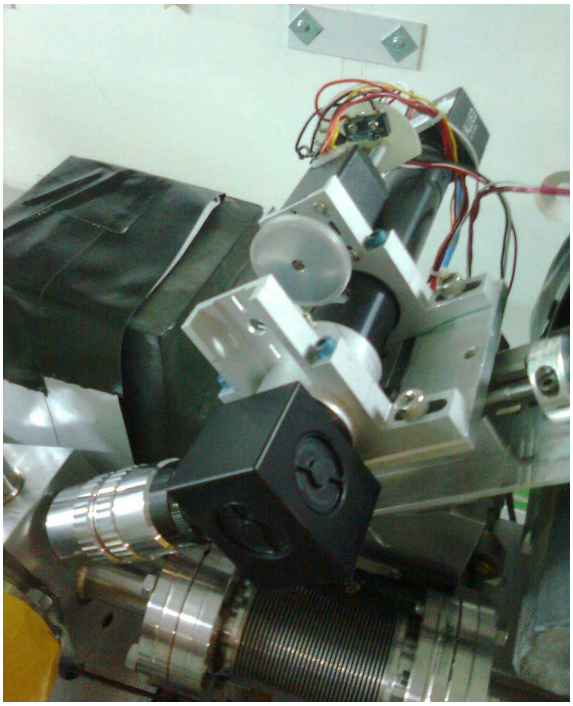

Figure 3.12: Detail of the optical elements of the single OTR.

OTR main body

The OTR body is the main part of the device around which the other components are built. It is a unique block hollowed in the center, where the passing electron beam, the metallic target and the optical elements direction have to meet. The target is inserted at 110 degrees with respect to the beam direction and therefore the optical system is placed at 40 degrees following in the light emission direction. A diagram can be seen in Fig. 3.13 (the beam going from right to left). A critical part of the design is the window between the target and the microscope, because under the distortion of its surface due to the vacuum

it can lead to wrong size measurements. From the old OTR reference [51]: *ZEMAX*[3] *calculations indicated that using a thin (less than 1 mm) window would reduce the effect of the aberrations to within our design tolerances. Mechanical calculations show that the distortion due to vacuum pressure is acceptable for a fused silica window with a diameter of less than 7 mm.* The same fused silica window was used then for the new design without any major changes. This window is installed in the body using an indium seal and an O-ring to compress the window and the seal. This whole system was problematic and the reason for vacuum leaks and required careful treatment during the installation. All in all, the new OTR body improves some issues that were present in the old design: the target actuator is built in the upper part, which causes less problems with the supporting structure and the whole footprint is reduced considerably from 55 cm to less than 30 cm.

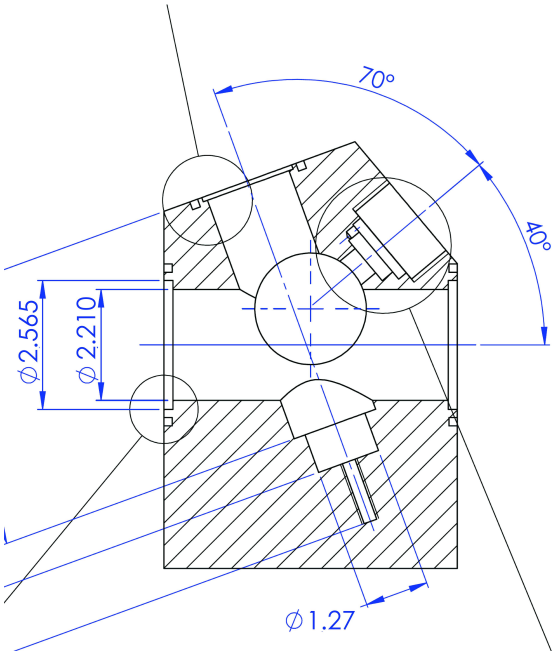

Figure 3.13: Drawing of the OTR body in whose center the electron beam, the target and the optical direction meet. Lengths in cm.

Target holder, actuator and target materials

The OTR is built in such a way that when the beam pipe is straight and the target is inside the pipe, it does not intercept the beam in normal conditions, being the last some millimeters down, as can be seen in Fig. 3.13. For this reason the whole OTR body has to be lowered, bringing the chamber closer to the beam as sketched in Fig. 3.14. Presumably due to the wake-fields generated here, some emittance growth has been lately observed. Some experiments on this topic were performed and will be treated in Section 5.3.

[3] http://www.optima-research.com/

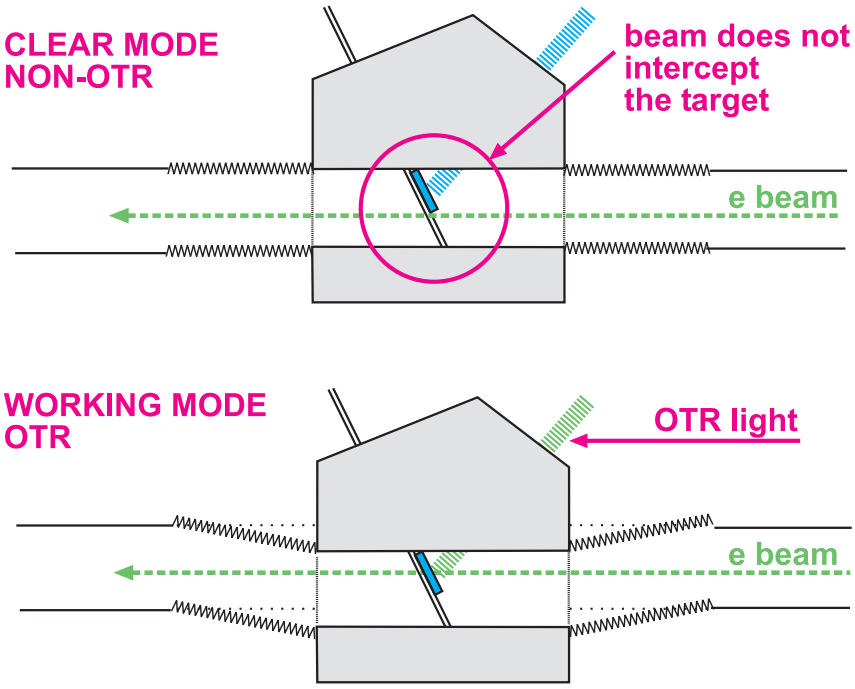

Figure 3.14: The OTR body is lowered to enable the target to intercept the beam.

In order to avoid this effect without having to redesign the whole OTR body a modification of the target holder that brings down the intersection between the optics line and the target has been proposed. The mechanical layout of the installed holder and the new proposal are shown in Fig. 3.15. While with the current design the body has to lower about 7 mm with the new proposal it has to be lowered only by 1.5 mm. The new design needs some modification in the target frame and the target holder itself to work and it is expected to be installed in February 2013 together with a new optical system of 45 mm working distance.

The target is inserted in its place by a pneumatic actuator remotely commanded. In the extreme of the rod, the target holder ends in a stainless steel ball that fits into a conical titanium receiver who ensures the target repositioning. The target holder assembly was re-designed to include a set of 10 μm tungsten wires below the target (one horizontal, one vertical and two tilted). The horizontal and vertical movers are used to scan the wires across the beam. All these features can be seen in Fig. 3.16. The spot sizes measured by these wires provide a cross check to those measured optically by the OTRs. Previous to the installation of the whole OTR in the beam-line the target has to be aligned in the axis along the actuator, it means, correct an eventual tilt that could make the emitted light hit the OTR body and not pass through the window. That is made simulating the electron beam with an upstream laser, just to see if it reflects correctly.

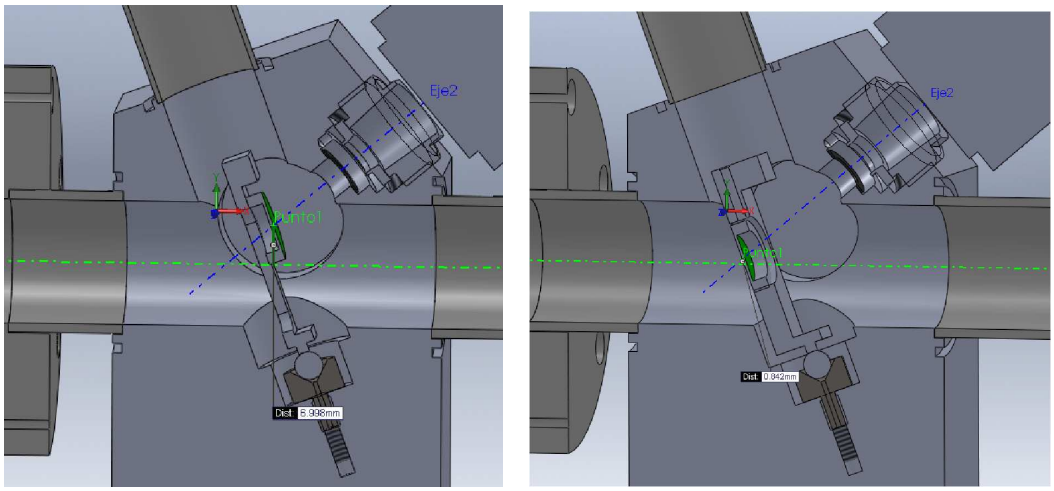

Figure 3.15: Comparison between the installed target holder (up) and the new proposal (down). The target is lowered closer to the beam position.

The old OTR was used to do some target material test which can be seen in reference [51]. Summarizing, studies were done using copper, beryllium and glassy carbon II in single and multi-bunch modes. Energy-to-break calculations were done in order to compare the experiments of damage on the targets with the theoretical prediction and the results were in accordance. Beryllium did the best with survivability although other materials like glassy carbon survived very well (albeit with reduced light output compared to metal targets) even in multi-bunch operation while copper was badly damaged after 3-4 minutes in single bunch operation with 7.5×10^9 particles and a round transverse beam size of $\sigma_r = \sqrt{\sigma_x \cdot \sigma_y} = 15.5$ μm.

However using beryllium is considered to be a nuisance, many people and institutions are extremely risk adverse, and given the poisonous effects of beryllium dust in the lungs it is very difficult to get permission to use it. It was decided to try to find another target material that would survive the single pulse charge at ATF and not pose any kind of health risk. An aluminized Mylar was used on the old OTR that was in various locations in the ATF beam line. It performed pretty well with no damage problems but with larger beam spots [52].

The first testing with the Multi-OTR was supposed to use the Mylar targets used in the old one but unfortunately what got ordered was aluminized nitrocellulose targets, which was quite unfortunate as nitrocellulose is high temperature sensitive. In fact three targets were damaged under an intensity of 4×10^9 electrons per pulse. Later on was thought to use Kapton or Polyamide material which seems to stand up quite well under current conditions. Aluminum film was tested as well. Now a four set of new targets is installed, two of them made with 2 μm aluminum and two with a 3 to 5 μm Kapton with a 0.12 μm Aluminum coating. Both materials are doing well with the current beam parameters.

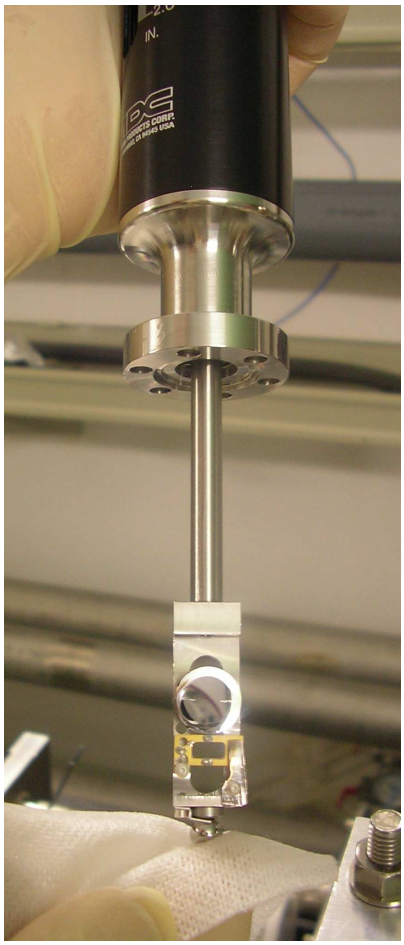

Figure 3.16: Target actuator and target holder with the metallic surface and the wires below it.

In order to estimate roughly the survivability of the materials it is important to know that for targets of very small thickness compared to the radiation length of the material (which are normally of the order of the centimeter) the charged particles deposit energy mainly by ionization. The peak of the instantaneous temperature increment due to the impact of the bunch is estimated by

$$\Delta T_{inst} = \frac{1}{C}\left(\frac{dE}{dz}\right)\frac{N_e N_b e}{2\pi\sigma_x\sigma_y}, \tag{3.6}$$

where C the heat capacity and $\left(\frac{dE}{dz}\right)$ is the stopping power of the material determined by the Bethe-Bloch formula. And N_e and N_b are the number of electrons per bunch and the number of bunches in a train respectively, and σ_x and σ_y are the bunch transverse sizes.

The limits for the temperature rise to damage the target are usually determined by melting point and the mechanical fracture temperature. The highest allowed excursion

		Cu (old OTR)	Al (Multi-OTR)	Kapton (Multi-OTR)
T_{melt}	[K]	1357	933	Does not melt
σ_{UTS}	[MPa]	210	45	172
α_T	[μK^{-1}]	16.5	23	20
C	[J/Kg $\cdot$ K]	380	900	1090
ρ	[Kg/m]	8940	2700	1420
$\frac{dE}{dz}$	[MeV $\cdot$ m^2/Kg]	0.1852	0.2040	0.2210
Y	[GPa]	110	68	2.5

Table 3.1: Mechanical and thermal properties of some target materials.

for the melting limit is defined by

$$\Delta T_{melt} = T_{melt} - T_{room}, \tag{3.7}$$

with T_{melt} the material melting point and $T_{room} = 293\ K$ the room temperature. The second limit is expressed as

$$\Delta T_{fail} = \frac{\zeta \cdot \sigma_{UTS}}{\alpha_T \cdot Y}, \tag{3.8}$$

where $\zeta \approx 2$ is an empirical factor [53], σ_{UTS} the ultimate tensile strength of the material, α_T the thermal expansion coefficient and Y the Young modulus of the material.

Generally the minimum value of both melting and fracture limit is taken as a survivability criterium for the material. These two temperature limits and the instantaneous temperature increment due to the bunch passing through the target have been calculated for the typical beam sizes to be encountered in the Multi-OTR locations ($\sigma_x \approx 110\ \mu$m and $\sigma_y \approx 15\ \mu$m) and the typical bunch intensity in ATF2 ($N_e \approx 8 \times 10^9$) for Aluminum and Kapton, and compared with the burnt Copper in the old OTR location ($\sigma_x \approx 20\ \mu$m, $\sigma_y \approx 12\ \mu$m and $N_e \approx 8 \times 10^9$ as stated in [51]). The data has been found either in the Particle Data Group [54] or in the Matweb [57], which is a renowned database for material properties. Particularly the ultimate tensile strength can have up to a 30% variation depending on the bibliography. For the stopping power the Bethe-Bloch equation has been used. The material properties are shown in Table 3.1 and the results of the study are summarized in Table 3.2. The observed mechanical damaged in the Copper is predicted while in the new Multi-OTR locations the bunch does not damage the Aluminum and Kapton targets.

For the measurement procedure of the OTR the targets are inserted sequentially one after the other. This is done because of the semi-destructive nature of the OTR monitor. In fact one can estimate the Multiple Coulomb Scattering suffered from the beam when it goes through the target material as:

$$\theta_0 = \frac{13.6[\text{MeV}]}{\beta cp}\sqrt{\frac{x}{X_0}}\left[1 + 0.038ln\left(\frac{x}{X_0}\right)\right], \tag{3.9}$$

		Cu (old OTR) $20 \times 12\ \mu m$	Al (Multi-OTR) $110 \times 15\ \mu m$	Kapton (Multi-OTR) $110 \times 15\ \mu m$
ΔT_{inst}	[K]	388	28	25
ΔT_{melt}	[K]	1064	640	Does not melt
ΔT_{fail}	[K]	231	58	6880
Damaged		Yes	No	No

Table 3.2: Comparison between the instantaneous peak temperature and the damage limits.

where X_0 is the radiation length of the material. For the 2 μm Aluminum target the scattering angle is 2.9×10^{-5} rad, while for the 2 μm Kapton it is 2.2×10^{-5} rad and for the thin Aluminum layer 0.6×10^{-5} rad. In the OTRs locations, the maximum beam angle (the second moment of the distribution) happens in the horizontal axis in the OTR0X and comes to be 8.4×10^{-5}, so the effect of the material is not negligible at all even in the better case, therefore is interesting to measure in each location at a time and take the targets out if no measurement is being done. Other installations of OTR monitors in cases of beam with bigger sizes have been done, where the four OTRs measure at a time (strictly single shot emittance measurement) and the OTR locations are chosen in order to minimize the scattering effect. This can be seen for example in reference [59].

Illumination system

An illumination system was introduced in the design in order to facilitate alignment and calibrating tasks when there is no beam. It consists in a bellow that permits the movement in and out the beam pipe of a small lamp which is subjected with a ceramic tube for isolation and feed by a feed-through BNC (see Fig. 3.17). The lamp is installed upstream of the target (right from the OTR body in the picture) and enters the beam pipe from below illuminating the target.

Movers and radiation protection

In order to find the beam spot the whole OTR needs to be movable with respect to the beam pipe. This is made vertically and horizontally by two motors and movers. The vertical mover is a Newport M-MVN120 with 12 mm run and maximum load of 24 kg moved by a Nema 23 stepper motor from National Instruments while the horizontal movement is made by an American Linear Manufacturers mover actioned by a Nema 23 stepper motor. Fig. 3.18 shows these stages installed in ATF2. The horizontal motor covers 10 μm/step and the vertical one uses a triangular wedge to convert horizontal into vertical movement and altogether covers 2 μm/step. The movers are protected both by software and by hardware. The software doesn't allow the motion over a certain position and the hard-

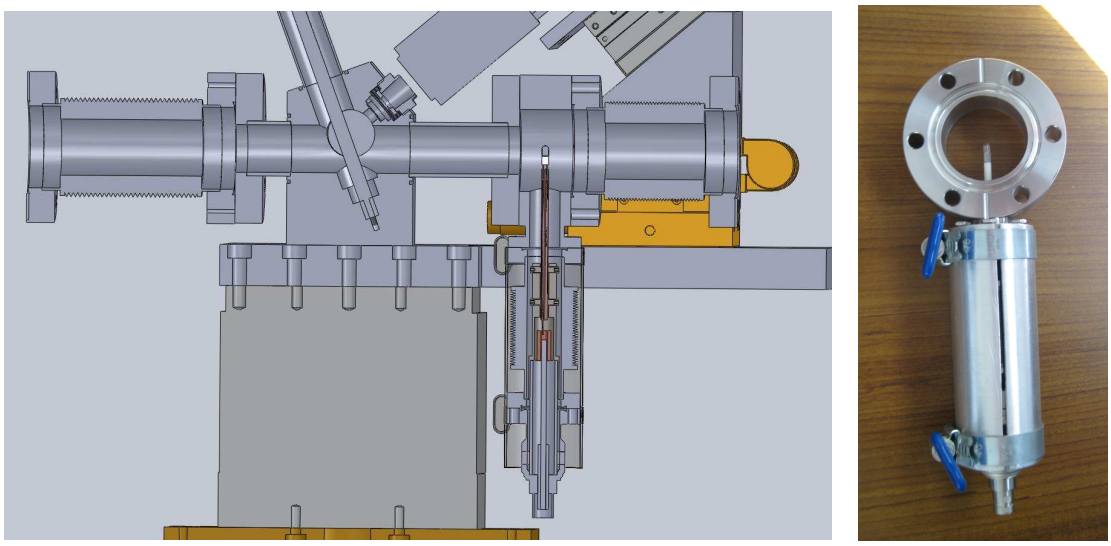

Figure 3.17: Illumination system for calibration tasks. The lamp is placed between the right bellow and the OTR main body.

ware protection is made by terms of limit switches. These switches are buttons activated when the mover exceeds a given position near the out-of-run limit and then a signal is sent to the motor to stop it. The motor is to be reset only through software using a button installed in the Multi-OTR User Interface as will be explained in the software section. In order to know the OTR position from a given reference point potentiometers are installed for each horizontal and vertical mover. These Linear Variable Differential Transformer (LVDT) can be seen in Fig. 3.19, work in the range ± 10 V and their calibration is around 2000 μm/V. The reference point is chosen to be the last place where the beam spot was found (which is called the OTR working mode position, as in the lower sketch of Fig. 3.14) and can be set pushing the appropriate button in the Multi-OTR User Interface.

Moreover, since the CCD camera is not parallel to the target and the depth of field is very small (only a few microns) the beam spot is focused on only a specific area of the target while it is out of focus in the rest of the target. The image has then to be refocused if the beam moves vertically with a remote motor. A Newport M-462-X-M stage for focus slide and a Newport CMA-25PP stepper motor are used for this purpose. Fig. 3.20 shows a picture of the focus actuator on the right side, in front of the lead bricks.

Due to an eventual peak in the intensity or due to being too much time exposed (even if the time the target can be inserted is limited by software) the target can be locally damaged and then the whole optical system needs to be movable with respect to it in order to be able to change the area of the target where the CCD is looking to. This is done by means of two manual movers. This movement is adjusted only once and only needs to

Figure 3.18: Stepper motors as installed in the line.

be readjusted in case of an eventual target damage. The stages for this purpose are the aluminum M-423 with 25 mm run and the manual micrometers SM-25 all manufactured by Newport and can be seen in the lower part of the Fig. 3.21 which shows the assembling of the OTRs out of the beam-line.

Due to the radiation eventual dead pixels appear in the CCD camera and it can be completely damaged. After a CCD was unusable due to this radiation a support for a protection shield was designed and installed, being loaded with lead protection bricks as shown in Fig. 3.21.

Connecting 4 OTRs

In order to be able to control the four OTRs each of the single motors, actuators and read-back potentiometers have to be centralized and connected to a common system accessible to issue commands and ask for readings. Fig. 3.22 shows the overview of the system.

The whole Multi-OTR control system is connected to the ATF Local Sub-net by Ethernet via the Host PC. This computer outputs just the EPICS PVs served by the Multi-OTR IOC running on its Scientific Linux 5 OS (see next section). High-level control software

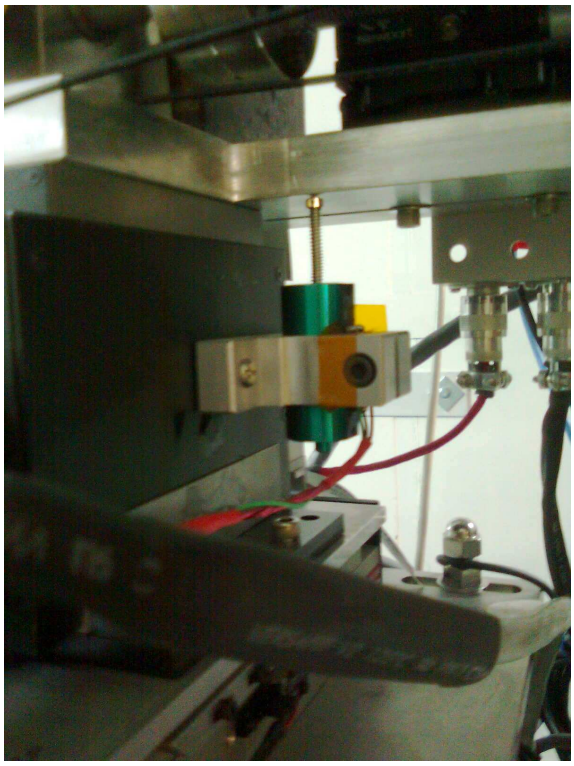

Figure 3.19: LVDT potentiometers to read the OTR position.

and analysis/processing can also optionally be performed by host PC, or another host on the ATF Sub-net. The host PC is connected as well to an 8-port GigE switch to which are connected in turn the two XPS and the four CCD cameras, all through local Ethernet connection. The Newport XPS-C8 can be seen in Fig. 3.23 (together with the zoom stepper motor driver, which was installed later) and is a universal controller for 8 channels with own IP and a Pentium IV built in. For the Multi-OTR system two of them are needed and their input and output connections are used as follows:

- 12 (of 16) motor driver cards used for OTR X and Y and camera Focus controls by means of several XPS-DRV01, a generic driver for Newport motors.
- 8 (of 72) digital outputs used for
  - 4 OTR insertion actuators.
  - 4 select relays to switch between X and Focus read-backs.
- 8 (of 8) analog inputs (14-bit, $\pm 10\ V$) used for LVDT position read-backs for X and Y stage and camera Focus.

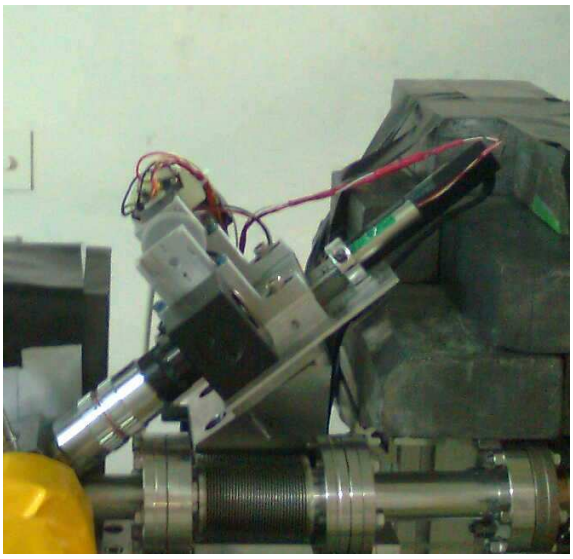

Figure 3.20: Focus system. It moves the whole optical system closer to the target or away in the 40 degree direction with respect to the beam.

It is to be noted that, because of the fact that there are only four analog inputs per XPS it was decided to use four of them for the vertical position and the other four to be shared between horizontal and focus position. For this reason four relays were installed to switch between X and Focus potentiometers, one in each OTR.

Fig. 3.24 shows the wiring of the cables in order to connect them to both XPS. All this hardware is installed outside of the tunnel, in a safe room popularly known as the "eel's bedroom" due to its long shape and can be seen in Fig. 3.25.

3.3.2 Software development

The first and lower layer of the communication between the user and the hardware is made through the Experimental Physics and Industrial Control System (EPICS). EPICS is a software environment used to develop and implement distributed control systems to operate devices such as particle accelerators, telescopes and other large experiments (see [60]). A Process Variable (PV) is a single data unit as, for example, the value of some read-back potentiometer or the steps the user may want to move on a motor. EPICS interfaces to the real world with IOCs (Input Output Controllers). These are either stock-standard PCs or VME standard embedded system processors that manage a variety of "plug and play" modules (GPIB, RS-232, IP Carrier etc.) which interface to control system instruments (oscilloscopes, network analyzers, etc.) and devices (motors, thermocouples, switches, etc.). The IOC holds and runs a database of 'records' which represent either devices or aspects of the devices to be controlled. The Multi-OTR host PC outputs just the EPICS PVs served by the Multi-OTR IOC running on its Scientific Linux 5 OS.

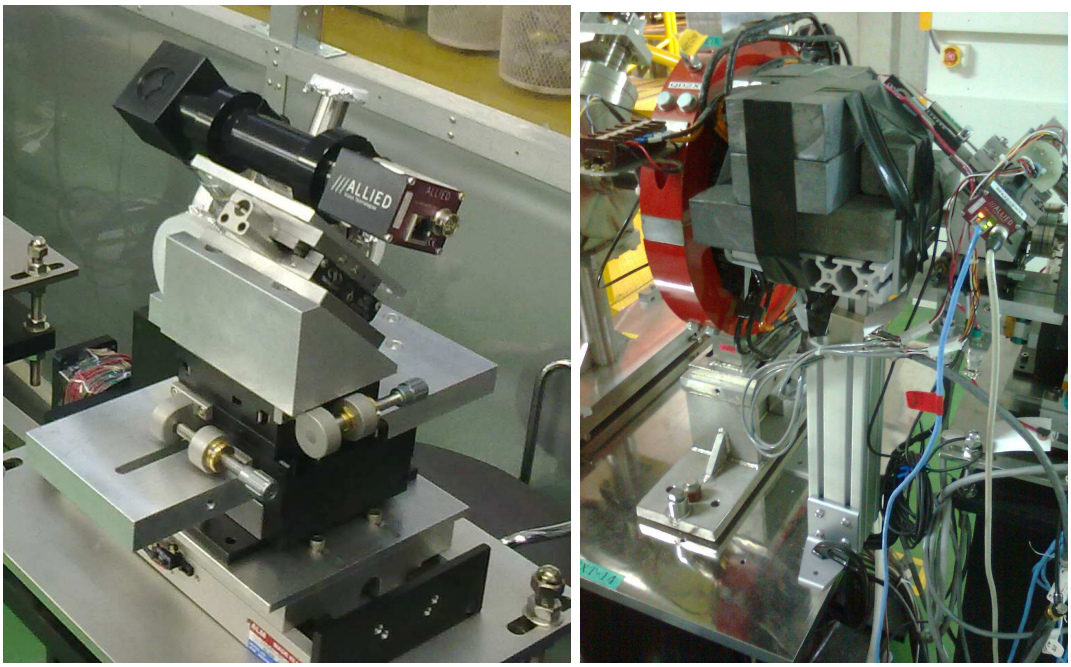

Figure 3.21: Left: Manual movers to change the relative position of the optics with respect to the whole body, being able to look at a different point in the target. Right: Lead bricks to shield the CCD camera from radiation.

The host PC broadcasts the EPICS PV's and they are then accessible within the ATF Local Sub-net. In this way the user can read the read-backs and modify the PVs to give orders to the hardware as, for example, the movers. This is made at low level by Channel Access (CA) commands. CA is a high bandwidth networking protocol, which is well suited to soft real-time applications such as scientific experiments. Any software which can speak the CA protocol can get and put values of records. In fact it is possible to use labCA, which is an EPICS CA interface for Matlab, in order to write higher level software to control the hardware in Matlab. The Graphic User Interface (GUI) allows users to perform tasks interactively through controls such as buttons and sliders and is written in GUIDE, a Matlab tool for this purpose, being for the basic functions a completely standalone program. However, some of the advanced functionalities need to get information from other sources as the near BPMs, the transfer matrices between the OTR locations as in the case of an emittance measurement or to track a simulated beam through the loaded lattice as in the case of the automatic coupling correction algorithm. This information is asked to the Flight Simulator (FS) and needs this to be running. The FS [78] is an environment for the shared development and implementation of beam dynamics code. This software exists as a 'middle-layer' between the lower-level control systems (EPICS and V-SYSTEM) and the multiple higher-level beam dynamics modeling tools (SAD, Lucretia, PLACET, MAD...). FS can automate a lot of beam tuning tasks and has a set of functionalities

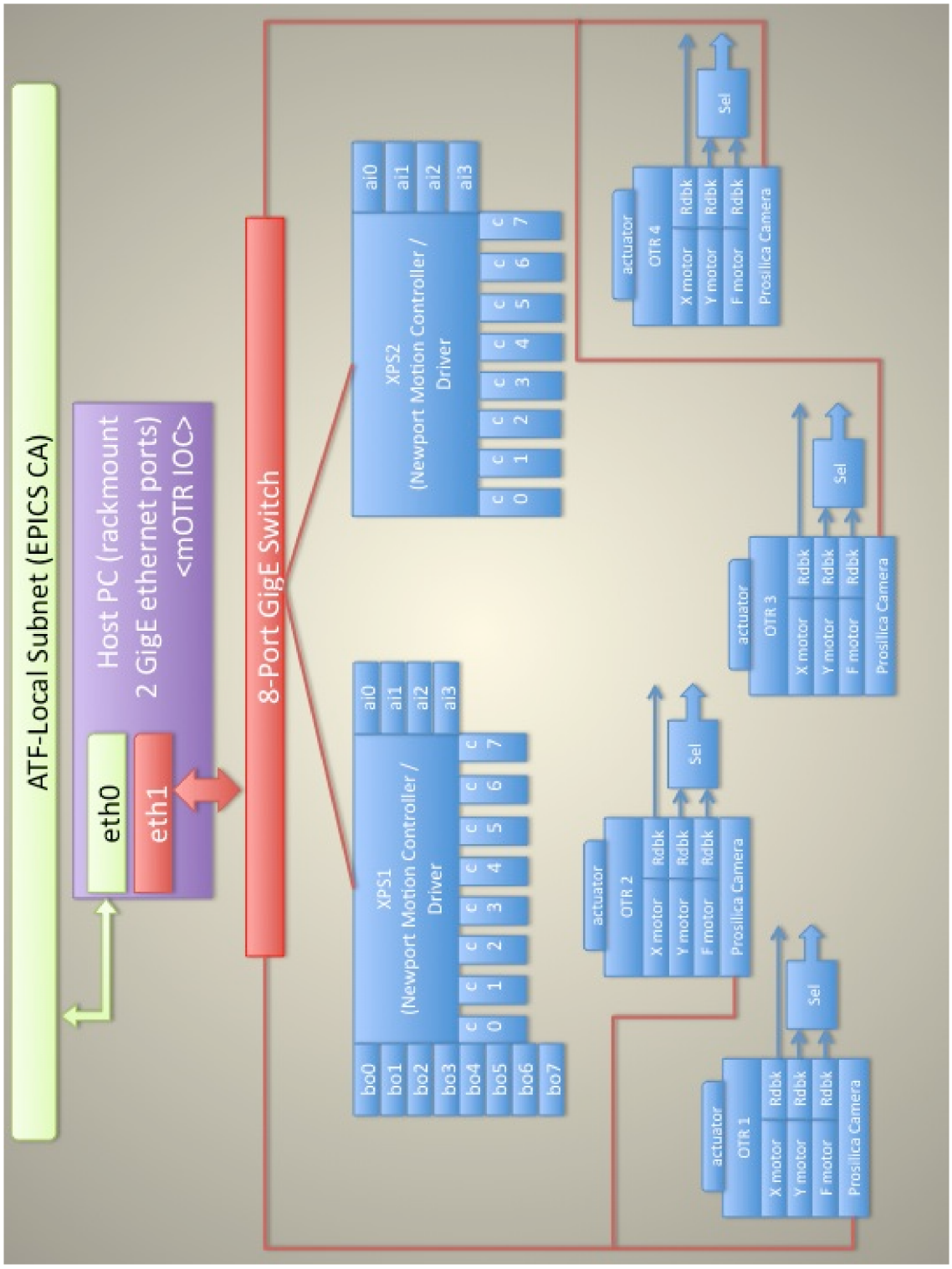

Figure 3.22: Overview of the whole Multi-OTR communications.

Figure 3.23: Multi-OTR controllers mounted in the racks. In the left the Newport XPS for motion control, in the right the zoom stepper motor driver.

and applications already written by users, such as measurements of dispersion or BPM readings. It can be used either in the ATF real machine or in simulation mode. When used in simulation or whenever it is necessary to make calculations related to beam dynamics such as tracking or transport matrix calculations it calls to Lucretia functions. Lucretia is a Matlab based toolkit for the modeling and simulation of single-pass electron transport lines. The Multi-OTR GUI is then a Matlab program which speaks via labCA to EPICS in order to control the hardware and, when necessary, calls the FS and Lucretia to perform more advanced routines which need information of other elements in the beam-line or any beam dynamics simulation.

To work with the OTRs the user can open from the ATF control room menu the Main OTR Panel whose last version is shown in Fig. 3.26. There from left to right and from up to down we find first of all the 'Emittance' button, which opens the Emittance Panel (Fig. 3.29) for emittance calculations and below this each one of this OTR buttons will open the Single OTR Panel (Fig. 3.27). Before doing an emittance measurement it is necessary to find the beam spot in each of the involved OTRs. In the central region of the Main Panel there are some indicators of the status of the system stating whether the target is in or out and the single OTR position which can be 'NonOTR' for the clear position (upper sketch on Fig. 3.14) and 'OTR' for any other position out of the clear one. Moreover the panel has indicators for the case an eventual limit is hit. Around these text screens there are some buttons for different operations such as taking all the targets out and moving all OTRs or a single one to 'NonOTR' position. For machine protection reasons one can specify how much time the target will be in and if eventually this time is exceeded the target will be automatically extracted. Since sometimes the intensity in the EXT line can be rather variable one may be interested in defining a window that ensures each emittance measurement was done within a certain range of intensities. This

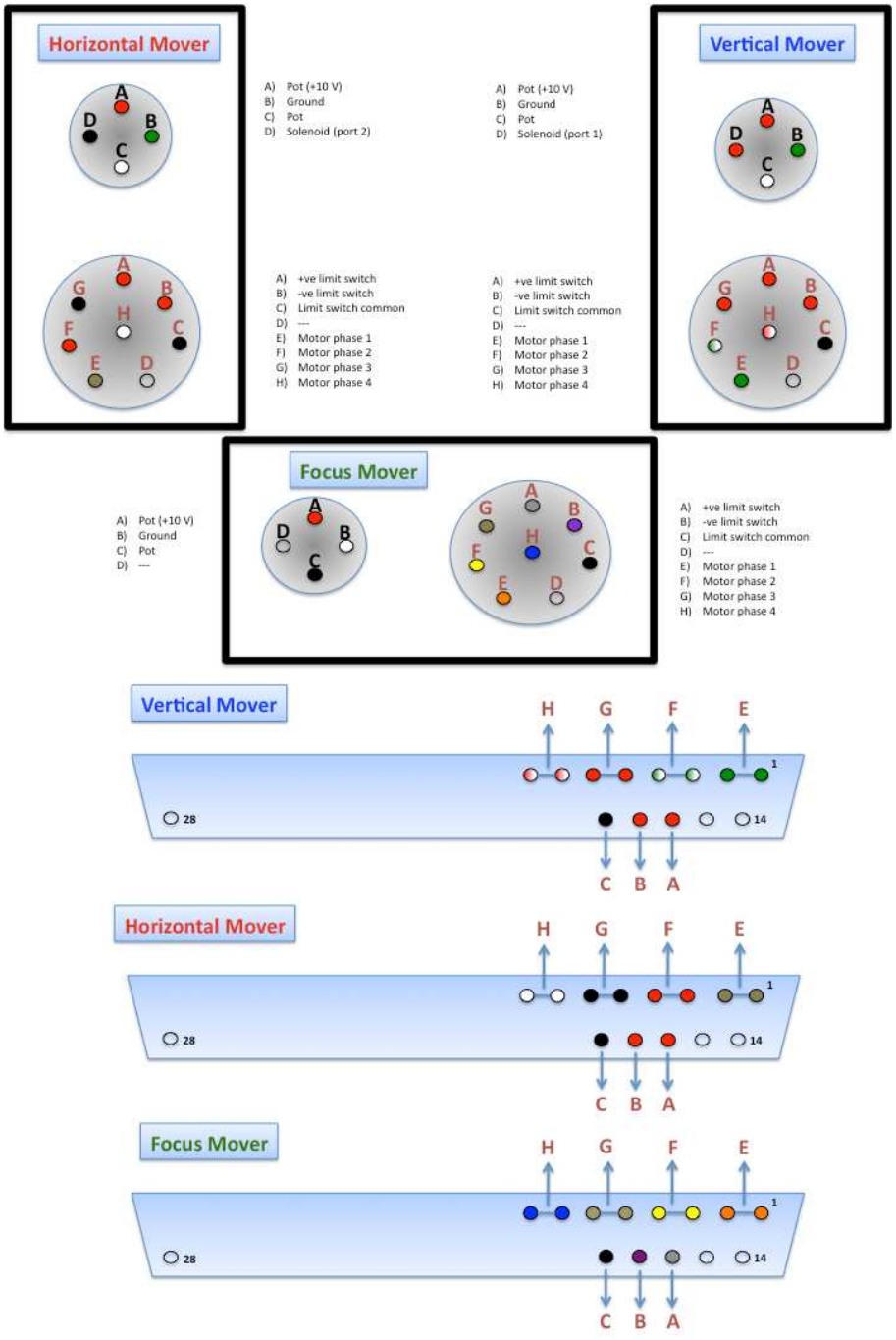

Figure 3.24: Schematics of the wiring for the XPS movers with the cable color codes.

Figure 3.25: The Multi-OTR area in the so-called "eel's bedroom" where the controllers and the host PC are located.

is made applying the cut in the upper-right part of the panel. Below it a string screen to manage errors is placed. The Get CCD Background button assumes no beam in the line and takes ten measurements with the chosen OTRs (a small window will pop up) for later image processing. The treatment of the digital image can be seen in chapter 4. Lastly, a text screen states whether the FS is running or not and a pair of buttons display some instructions to follow in case of hardware problems.

Figure 3.26: Main Panel of the Multi-OTR GUI. It is opened from the main menu in the ATF2 control room.

Single OTR Panel

When the user opens the Single OTR Panel a window pops up in front of the Main Panel. It contains information and controls for each of the OTRs as in Fig. 3.27. From the right to the left we find, in the top, a small warning for the intensity cut of the Main Panel. While it shows red no beam size measurement will be done until it turns green again. Then, the right half of the screen shows the CCD captured image, with the fitted ellipse, the horizontal and vertical projections and the 1-D gaussian that fits them, two big warnings of the target status and the OTR position as in the Main Panel, and below there is the zoom control. Moving to the left there is the Gaussian/Ellipse fitting area, where information about the measured size is shown. The first column is the measurement and the second is the statistical error, calculated over 10 pulses by default (but this number is settable in the Ave entry). Pixels or microns are selectable from the radio button. From up to down one finds the square root of the horizontal and vertical and the mixed second moments (i.e. the calculated values of the beam matrix) , the centroid position referenced to the down-left screen angle, and the projected beam sizes calculated from the 1-D gaussian fit. Below this measurement area is the mover control area with vertical, horizontal and focus absolute and relative movements and the absolute OTR position in microns (referred to the 'OTR' position, which is the last one where the beam was seen and can be reset to a new value with the proper button) and in volts, given by the LVDT read-backs. As explained in the hardware section, the horizontal and focus read-back share the same connection to the XPS and are selectable by a relay, making impossible to have simultaneously read-back in both axes. That is why there is a radio button to select one of them while the other remains disabled. Under this controls one finds some buttons to clear the limit switches in case they were pushed and down there is a Beam Presence Cut selector which controls (as the intensity cut does) whether the beam fitting is activated or not. This is needed to cut beam where the beam misses a pulse or the charge suddenly drops and the user should make sure the cut level is well above the value when there is no beam and significantly below the value when beam is present. Lastly, in the very left side of the panel, on top one finds the reference system and mode control. As explained before and in Fig. 3.14 the OTR has two main positions, the clear 'NonOTR mode' one and the so-called 'OTR mode' which is the reference. There are two buttons to move to this positions and a third button to set any current position to 'OTR' mode, in case the beam changes position. A fourth button shows the voltages of the reference 'OTR' and 'NonOTR' points for the four OTRs. Below this buttons is the target control, to take it in and out, and an option called 'integration time' which is, in seconds, the shutter speed of the CCD camera. The calibration settings button can be opened to change manually motors, potentiometers and CCD pixel size but, in case of the CCD calibration and specially when the zoom level has been changed, it is advisable to open the automatic calibration routine, which is located in the Tools drop-down menu and can be seen in Fig. 3.28. This automatic procedure moves the horizontal or vertical mover by some known distance and measures the centroid position in pixels, fitting this way a line and obtaining the calibration in microns per pixel. Going back to the Single OTR Panel, and in the left of it there is a button for a future

functionality that will calculate the expected beam position by interpolating the position in the near BPMs and will move automatically the OTR to this place but at the moment of the writing of this thesis this feature is not yet installed. Under this, the gain of the CCD camera can be set in dB and a display shows the maximum value of the signal in 12-bit in order to identify whether saturated pixels are present or not. Below, there is a warning for an eventual pixel saturation, that should be avoid in order to have a good ellipse fitting preserving a linear response of the CCD and lastly the user finds an ellipse fitting cut that defines a window around the intensity peak of the beam image in order to cut away as much noise as possible. This will be explained in more detail in section 4.1.

Emittance Panel

In the Emittance Panel (Fig. 3.29) the user can perform emittance calculations and automatic coupling corrections. In order to do that at least three OTRs need to have the beam centered, and it is preferable that the position where the beam is visible in the CCD is the reference position for the working 'OTR' mode as explained before. On top of the panel a small screen shows the different OTR images as the emittance routine takes data. Below this, the user can know which OTR and which shot is being measured at the moment. Since the data of the last measurement done is saved and accessible from the OTR software is possible to choose whether the calculation is to be made taking new data or just loading the last measurements in the 'Take New Data?' selector. 'Pulses per OTR' is the number of shots to measure for the statistical error calculation. Due to hardware problems during the runs it can be possible that an OTR is not available but the 2-D emittance can be calculated using only three OTRs and therefore a selector for which ones to use is present. Once the 'Calc Emittance' button has been pushed the emittance will be calculated in about a minute and the right half part of the window will show the results of the emittance measurement as well as the reconstructed Twiss parameters and the mismatch parameter for vertical and horizontal planes and using the projected sizes and the square root of the second moments of the distribution. More data and fitting plots can be opened with the respective buttons. Fig. 3.30 shows the window that pops up in one of the data buttons displaying the measured values with errors and in some cases the theoretical value in parentheses while Fig. 3.31 shows one of the plots showing how the measurements fit the theoretical model.

My personal contribution in the software development has been focused on the high-level controls designing, specially in the GUI and the functions it calls, such as the movement of the single OTRs, the data acquisition and treatment, the emittance reconstruction and the automatic coupling correction algorithms. The Multi-OTR software is working but in continuous status of improvement. New features such as the automatic beam finding by using the information of the other BPMs are planned to be installed.

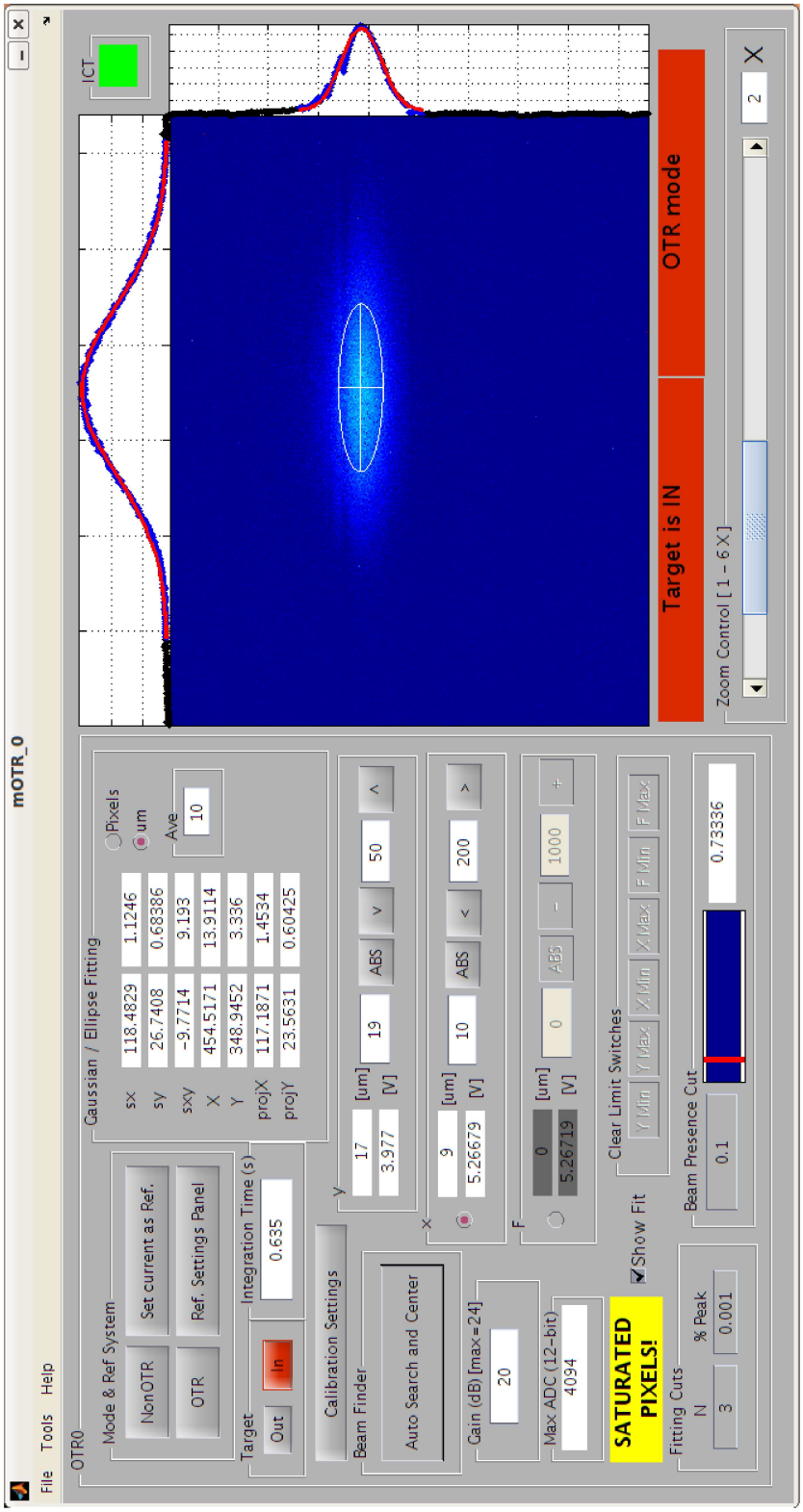

Figure 3.27: Single OTR panel showing an example of beam fitting and the main features.

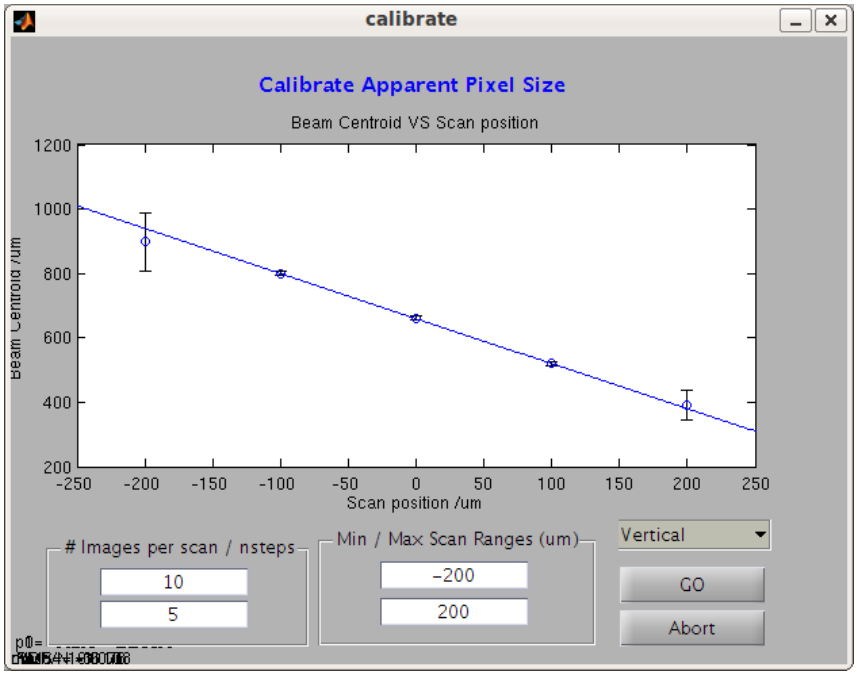

Figure 3.28: Application to auto-calibrate horizontal and vertical pixel size by moving the whole body and looking in the variation of the centroid.

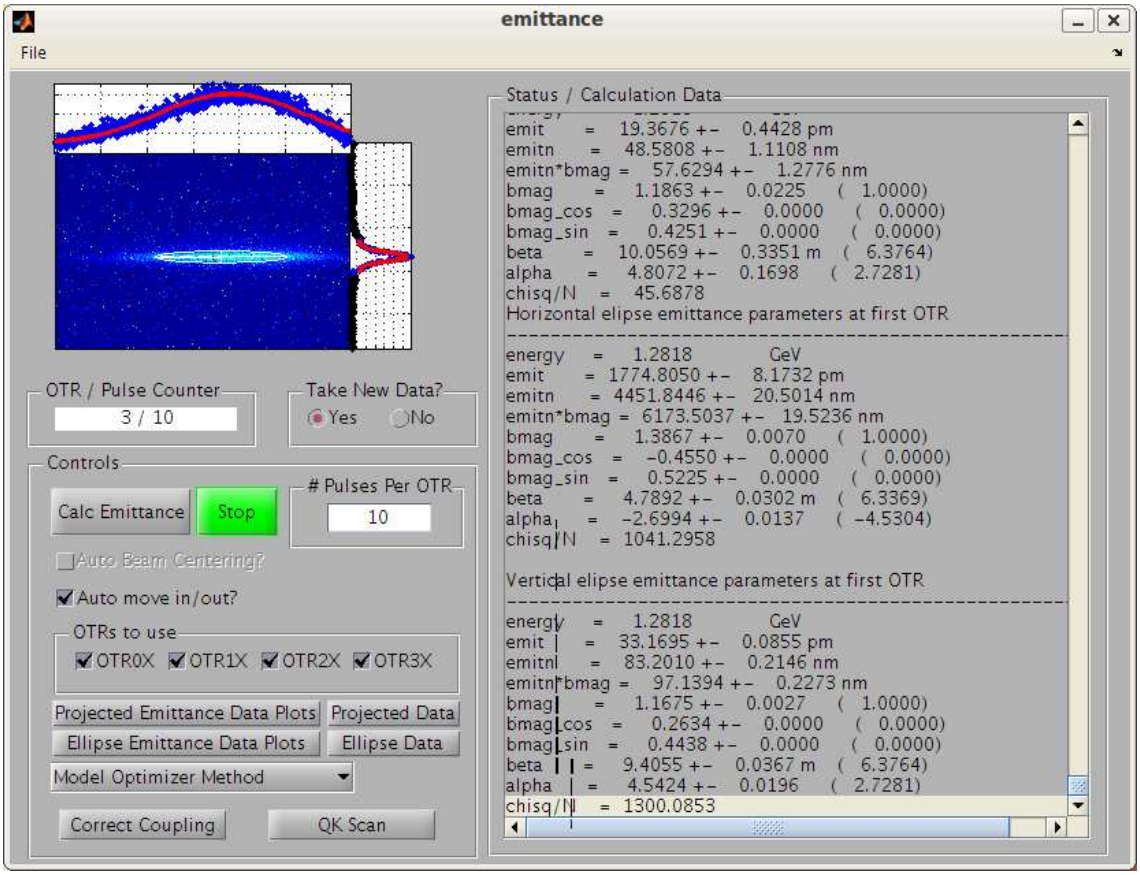

Figure 3.29: Emittance panel. It has some options for the measurement in the left part and shows the measured values in the right of the screen.

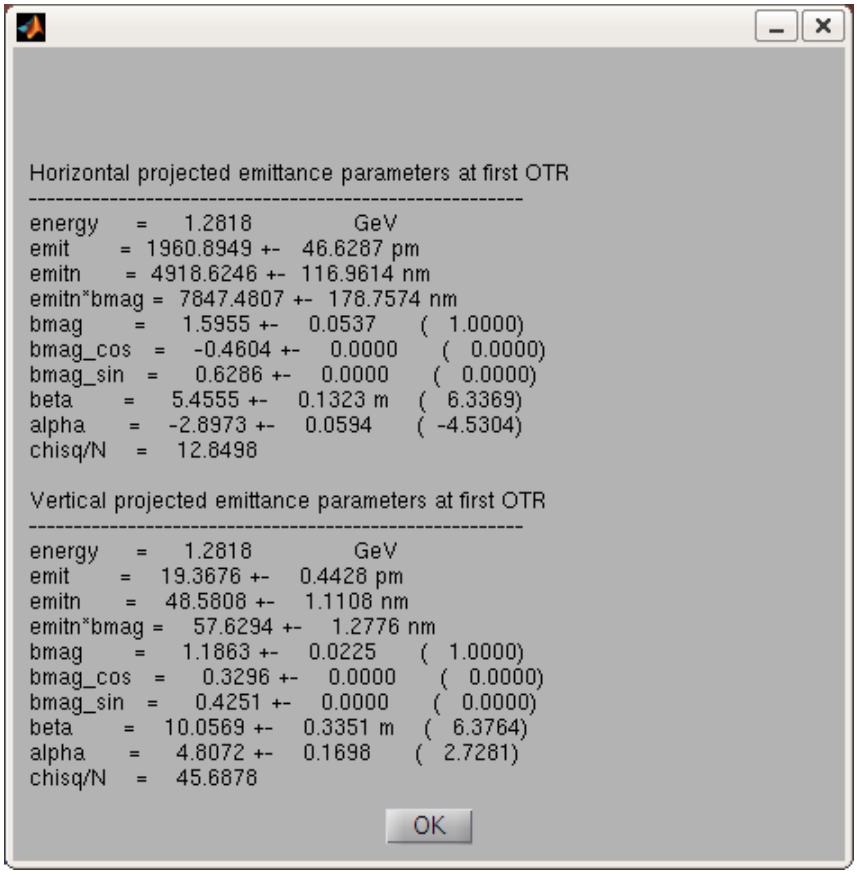

Figure 3.30: Emittance measurement values are shown in detail.

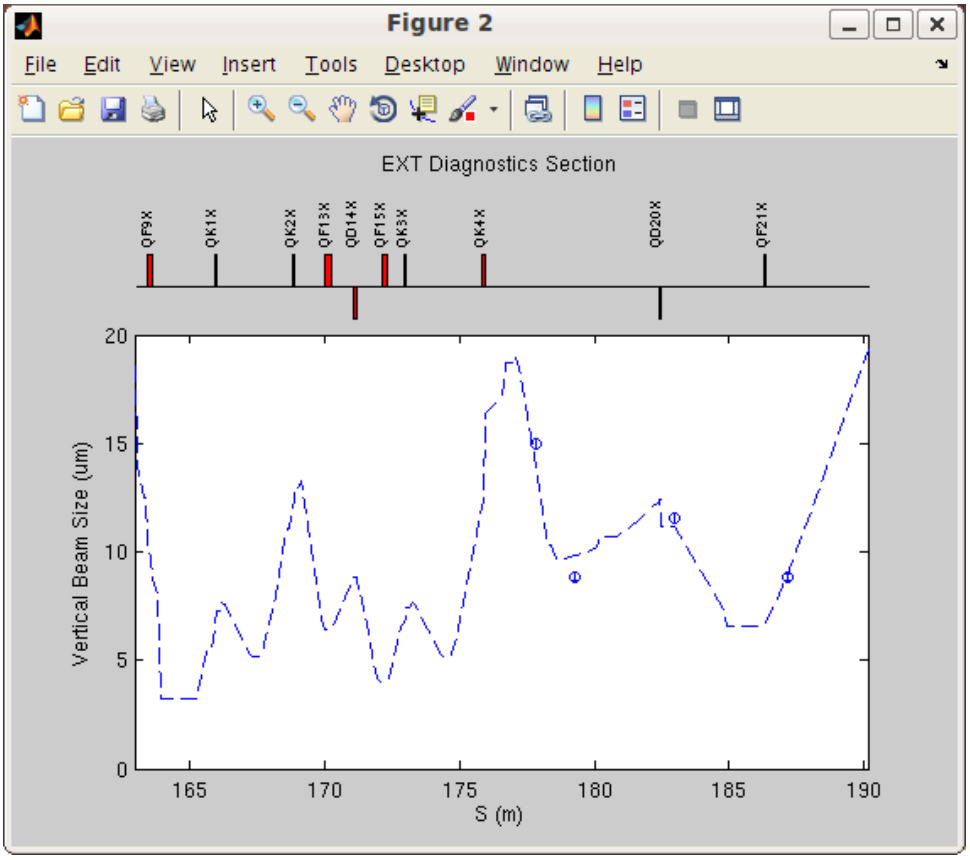

Figure 3.31: The emittance panel produces plots comparing the measurement with the model.

Chapter 4

Beam size measurements

Unlike other mono-dimensional devices such as a WS a single OTR monitor is a beam size monitor that has the ability to get a 2D shot of the beam profile. Because of this fact one can obtain from a measurement, not only the beam sizes projected onto a couple of orthogonal axis, but also the angle of the flat beam with respect to these axes. From the information given by the OTR the user is able to reconstruct the beam matrix and obtain from here further parameters such as the projected and intrinsic beam emittances or correct the coupling. As was explained in Chapter 3 an optical system collects the OTR light and projects it onto a CCD screen, converting it in a bit map. This chapter will discuss the manipulation of this information from the matrix of intensities to the final value of the intrinsic and projected beam sizes.

4.1 The ellipse fitting algorithm

As mentioned, the input for the ellipse fitting algorithm is a 1280×960 matrix representing the map of pixels where each element is a number from 0 to 4095 (the Prosilica camera has 12-bit depth). This input matrix will be called $\boldsymbol{C}^{r,f}$ where the super-indexes stand for raw and flipped meaning that the filtering and flip correction are not yet done. In order to have a beam size measurement we will make some assumptions:

- First of all we will assume that the axis of the matrix $\boldsymbol{C}^{r,f}$ of pixel intensities are aligned with the reference accelerator axis, i.e, the CCD camera is not tilted (roll alignment procedures will be explained later in this chapter).
- Second, we will also assume that the pixel size is known because a calibration has been made previously.
- Last, we will assume that the response of the camera is linear with the particle number and that the beam has a gaussian profile.

Given these assumptions the problem to be solved now is to fit an ellipse in a 2D map of intensities. The relevant steps of the data treatment are related here:

- Request the raw data (1280×960-matrix $\boldsymbol{C}^{r,f}$ with element values from 0 to 4095) from the CCD camera via labCA as explained in Section 3.3.2. Look if there are saturated pixels, i.e., matrix elements with value equal to 4095 and, if there are, display a warning message in the "Saturated Pixels" display (Single OTR Panel).

- Take out the background contribution in order to subtract the effect of eventual damaged pixels or lower other background effects. The background for each OTR monitor has been previously measured by pressing a button in the Multi-OTR Main Panel while there was no beam. This routine builds a 1280-by-960 matrix $\boldsymbol{B}$ where each matrix element is the average intensity for a given pixel over 10 measurements. The background image is subtracted from the raw matrix.

$$B_{ij} = \frac{\sum_{k=1}^{10} C_{ij_{(k)}}^{nobeam}}{10} \tag{4.1}$$

$$\boldsymbol{C}^{f} = \boldsymbol{C}^{r,f} - \boldsymbol{B} \tag{4.2}$$

- Flip the matrix horizontally in order to put the displayed image into the co-ordinate system used in the EXT line of ATF2 (i.e. positive horizontal motion is to the left, looking in the direction of the beam).

$$\underbrace{C_{ij}}_{i\in[1...1280]} = \underbrace{C_{ij}^{f}}_{i\in[1280...1]} \tag{4.3}$$

- Sum all the $\boldsymbol{C}$ values in rows, having as a result a 1280-by-1 column (the horizontal projection $\boldsymbol{P}$) and fit a one dimensional gaussian to $\boldsymbol{P}$ with a Gaussian fitting routine obtaining the amplitude scaling factor, the mean value and the standard deviation (called here respectively A_P for amplitude, μ_P and σ_P).

$$P_i = \sum_j C_{ij} \tag{4.4}$$

$$\text{Gaussian fit of } \boldsymbol{P} \longrightarrow A_P,\ \mu_P,\ \sigma_P \tag{4.5}$$

- Use A_P (the amplitude of the horizontal projected gaussian) to subtract the background by making equal zero all the $\boldsymbol{C}$ elements below a given fraction of it. How strong is this cut (i.e. which percentage of A_P will be the threshold) can be set in the Single OTR Panel in the "Fitting cuts" section and is called here cut_{A_P}.

$$\forall i,j / C_{ij} < A_P \cdot cut_{A_P} \longrightarrow C_{ij} = 0 \tag{4.6}$$

- Calculate again the horizontal projection $\boldsymbol{P}$ after the background cut.

- In order to cut the gaussian tails, the "N" input value of the "Fitting cuts" section in the Single OTR Panel (Fig. 3.26) specifies how many standard deviations will be taken in account at both sides of the gaussian peak (here "N" is called n_{σ_P}). This is done because the OTR intensity profile presents a long tailed distribution and the r.m.s values are very sensitive to these tails [63]. Apply the cut making zero all the $\boldsymbol{P}$ elements beyond n_{σ_P} standard deviations.

$$\forall i \gtrless \mu_P \pm n_{\sigma_P} \cdot \sigma_P \longrightarrow P_i = 0 \tag{4.7}$$

- Fit again new gaussian in $\boldsymbol{P}$ obtaining new values for the amplitude, mean and standard deviation (A_P, μ_P and σ_P). Take the standard deviation σ_P of this fit as the horizontal projected beam size σ_x in pixel units, convertible to microns by using the calibration factor cal_x. Calculate hor_l and hor_h, the lowest and highest element number of $\boldsymbol{P}$ at which the gaussian would be cut, using σ_P and n_{σ_P} as done in 4.7. This lower and higher horizontal limits define a window to be used in the second moment calculations.

$$\sigma_x = \sigma_P \cdot cal_x \tag{4.8}$$

$$hor_l = \mu_P - n_{\sigma_P} \cdot \sigma_P \tag{4.9}$$

$$hor_h = \mu_P + n_{\sigma_P} \cdot \sigma_P \tag{4.10}$$

- Similar to the horizontal case for the projected vertical beam size calculation, build a new $\boldsymbol{P}$ adding down each column in order to have a 1-by-960 projection, as in Eq. (4.4). Fit a gaussian to $\boldsymbol{P}$, then apply a cut in the tails of the gaussian as in Eq. (4.7), fit a new gaussian (get the new A_P, μ_P and σ_P parameters) where its standard deviation σ_P is considered the vertical beam size σ_y. Find as in the horizontal case the window to be used in the second moment calculation. ver_l will be the lower element to consider while ver_h will be the higher one.

$$\sigma_y = \sigma_P \cdot cal_y \tag{4.11}$$

$$ver_l = \mu_P - n_{\sigma_P} \cdot \sigma_P \tag{4.12}$$

$$ver_h = \mu_P + n_{\sigma_P} \cdot \sigma_P \tag{4.13}$$

- Calculate the beam matrix elements from the processed CCD data, i.e. compute the statistical second moments starting from the matrix of intensities within the horizontal and vertical tails cut window, once the background and the low intensity pixels have been taken out. Ideally the square root of the second order moment should be equal to the projected gaussian fit but it is more sensitive to the background subtraction procedure. For this reason it would be recommended to use the gaussian projection but sometimes the beam does not fit horizontally in the CCD window making the later harder to calculate.

  – The input parameters for the function are the matrix $\boldsymbol{c}$ of pixel intensities, which has been processed before and cut from $\boldsymbol{C}$ within the defined windows (it means c is a $(hor_h - hor_l)$-by-$(ver_h - ver_l)$ matrix), $\boldsymbol{x}$ a row of the horizontal position of each pixel in microns and $\boldsymbol{y}$ a column for the vertical pixel position in microns.

  – Calculate the normalization and mean values:

$$\mathcal{N} = \sum_i \sum_j c_{ij}$$

$$\overline{x} = \frac{\sum_j \sum_i x_i c_{ij}}{\mathcal{N}} \tag{4.14}$$

$$\overline{y} = \frac{\sum_j \sum_i y_j c_{ij}}{\mathcal{N}}$$

  Where the sum over i (j) indexes stands for the sum for these indexes from 1 to $hor_h - hor_l$ ($ver_h - ver_l$), i.e. over the whole c matrix dimensions.

  – Calculate the second moments and covariance:

$$< xx >= \sigma_x^2 = \frac{\sum_j \sum_i (x_i - \overline{x})^2 \cdot c_{ij}}{\mathcal{N}}$$

$$< yy >= \sigma_y^2 = \frac{\sum_j \sum_i (y_j - \overline{y})^2 \cdot c_{ij}}{\mathcal{N}} \tag{4.15}$$

$$< xy >= \frac{\sum_j \sum_i (x_i - \overline{y}) \cdot c_{ij} \cdot (y_j - \overline{x})}{\mathcal{N}}$$

- Take into account the measurement and publish results only if two conditions are given: (i) the total intensity (actually the sum of all intensities in all pixels divided by 10^8 in order to have easy-to-use numbers) has to be over a cut defined in the "Beam presence cut" window in the Single OTR Panel and (ii) if the intensity cut from the Main OTR Panel is enabled (see Figure 3.26), the beam intensity in the EXT line has to be within the defined window. This last option is motivated from the fact that the emittance has a dependence on the beam intensity and eventually it can be necessary to control that.

After the single measurement procedure the ellipse is plotted over the screen-shot and, if more than one measurement is selected (in the "Ave" entry in the Single OTR Panel or "Pulses per OTR" in the Emittance Panel), the mean and standard deviation considering past measurements are calculated. The dispersion is taken into account and quadratically subtracted from the size measurement not in the Single OTR Panel display but only when the measurement is being used for emittance calculations.

4.2 Characterization of the single device

There was some discussion during the last decade about the ultimate resolution of the OTR monitor due to self-diffraction effect. It has been said that the narrowing of the OTR emission peak at $\theta \approx 1/\gamma$ would have made impossible the measurement of the beam profile due to bad resolution imposed by diffraction. In fact, for a light beam of divergence $\Delta\theta$ the diffraction dictates a minimum resolution for a profile measurement of $\Delta b \geq \lambda/(4\pi\Delta\theta)$ where λ is the light wavelength. If one uses $\Delta\theta \approx 1/\gamma$ for a 1.3 GeV electrons and 650 nm wavelength (for simplification) the diffraction-limited resolution is $\Delta b \approx \gamma\lambda/(4\pi) \simeq$ 130 μm. But some experiments (as in reference [63]) demonstrated a better resolution of the order of the wavelength which could make possible to use transition radiation light to measure high energy beam profiles. By looking at the angular distribution of the emitted light, Eq. (3.5), it presents a long tail decreasing proportional to θ^{-2} which is much slower that, for example, that of SR. This is a particular characteristic of OTR light, at high energies the highest part of the transition radiation is emitted in the tails [62]. The minimum theoretical resolution due to diffraction effects can be calculated in a more realistic way using θ_{max}, the angular acceptance of the optical system, which is 0.14 rad in our system (from manufacturer specifications). In this case the diffraction limit resolution should not be worse [64] than $\Delta b \approx \lambda/(2\pi\theta_{max}) \approx 0.7$ μm. For our system numerical calculations were done in the past using the predicted OTR distribution and it was obtained a broadening by about 10% of a 5 μm spot by the convolution of transition radiation and diffraction [51].

This way the spatial resolution power of the OTR depends on gamma, the angular acceptance of the optics, the spatial resolution of the CCD camera, i.e. the pixel size, and the contrast sensitivity of the camera (through the modulation transfer function, which is an indicator of the contrast obtained by an image with a black and white pattern of a given spatial frequency). For the existing old OTR, the base of the Multi-OTR design, tests were done in order to know the minimum observable spot size and a 2 μm resolution was estimated [51] being it near the diffraction limit performance.

The stability of the system was tested to estimate the resolution from repeatability of measurements. Figs. 4.1 and 4.2 show an example of these tests made on monitor OTR1X. In the top of the plot the mean and standard deviation over 18 measurements is shown. In the measurements made in different moments and for the four OTRs the standard deviation of the measurements was around the 2%, never exceeding the 3%. Figure 4.3 shows a set of ten measurements done on the 29th November 2012, during the tuning campaign with similar results.

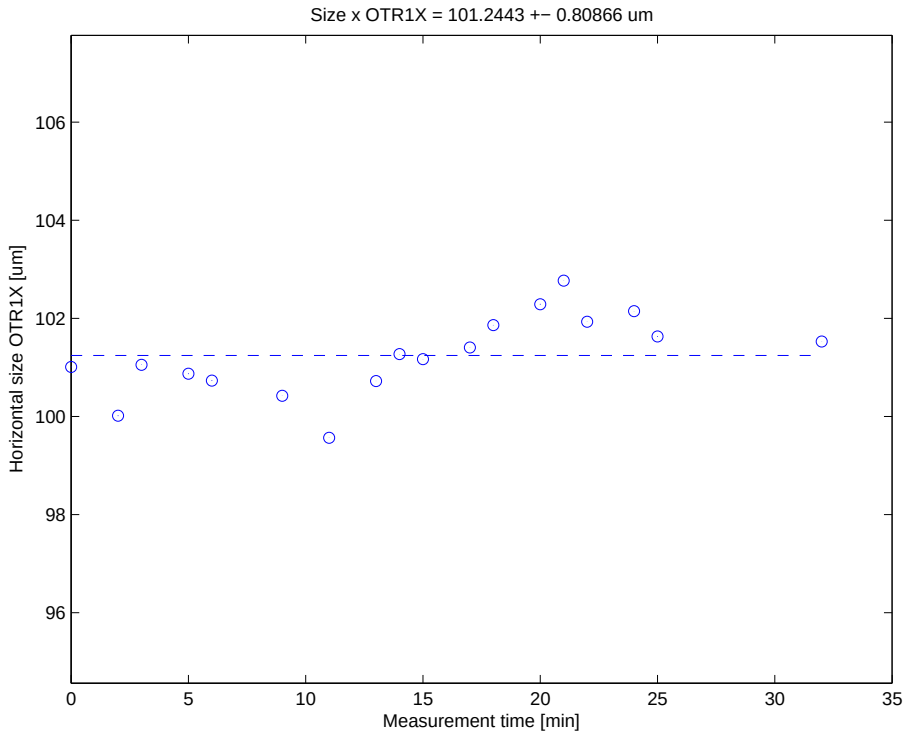

Figure 4.1: Horizontal size measured over 30 minutes for stability and resolution estimation.

The characterization of the optical system is needed for beam size measurements. The optical system is slightly at different position in each OTR and the zoom changes during the operation and it is therefore interesting to recalibrate the CCD camera often. The CCD calibration assumes that the motor movement is previously well calibrated (being 10 μm/step and 2 μm/step for the horizontal and vertical case respectively from manufacturer specifications). The procedure is done by moving independently one single motor in steps of known distance measuring at the same time the change in the ellipse centroid in pixels. This centroid position is taken as an average over a certain number of measurements in order to minimize the beam position jitter impact. As was explained in Section 3.3.2 the GUI implements a routine for auto-calibrating the CCD. A typical curve of calibration is shown in Fig. 4.4, in particular for the vertical axis of OTR2X monitor. Typical values of the calibration are around 0.5 μm/pixel.

The measurements done with the OTR monitor contain spatial information: projections are measured and ellipses fitted in order to reconstruct the beam matrix and calculate the transverse beam tilt angles for coupling correction and therefore it is important to establish accurately the axes which have to be common between the OTRs and all aligned to the accelerator axis.

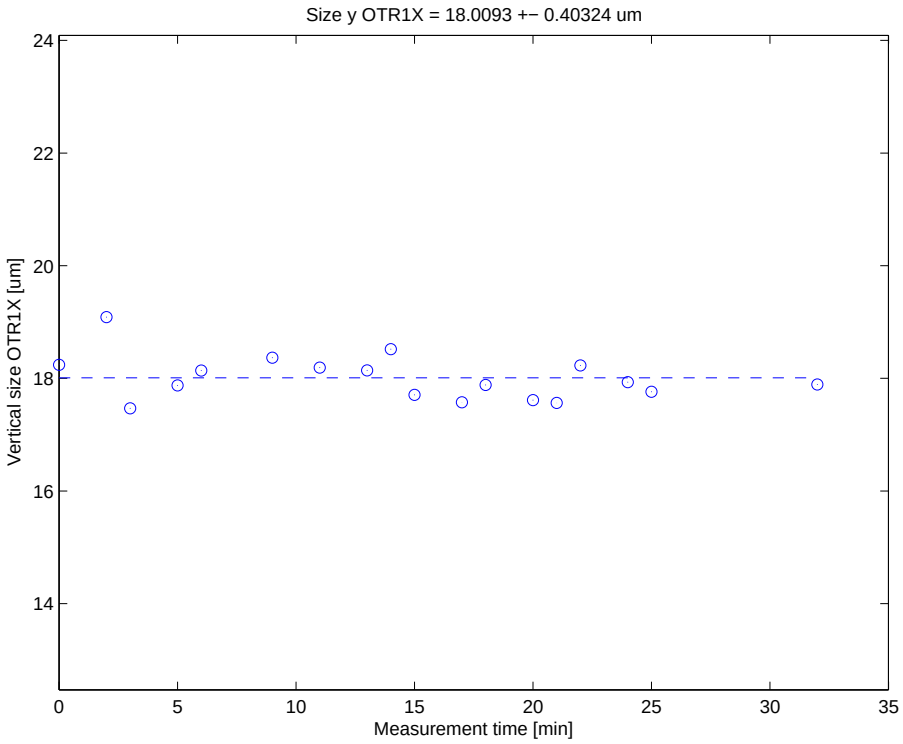

Figure 4.2: Vertical size measured over 30 minutes for stability and resolution estimation.

In order to measure the eventual rolling of the devices the beam is steered in the horizontal or vertical direction (in the accelerator axis) with an upstream corrector kicker, then the horizontal and vertical changes in the beam centroid are measured. Fig. 4.5 shows one of these measurement for OTR2X: the beam is steered horizontally and the centroid measurement is plotted versus the predicted position so, if it is well aligned the slope of the fitted blue line (*p1* parameter) must equal 1. On the other hand the vertical movement (red data points) must not change when the beam is horizontally steered if both OTR and accelerator axes coincide, as it happens. This exercise has to be done for the four OTRs to ensure that no rolling is present.

4.3 Measurements and comparison with model

Beam size measurements are needed for beam matrix reconstruction and coupling correction and are therefore routinely done with the Multi-OTR system. Figs. 4.6, 4.7 and 4.8 show screen-shots of measurements done and their comparison with the model (this information can be shown up by clicking the proper button in the Emittance Panel).

The OTRs measurements have been compared with that of the WSs and the results are in agreement, as can be seen in Fig. 4.9.

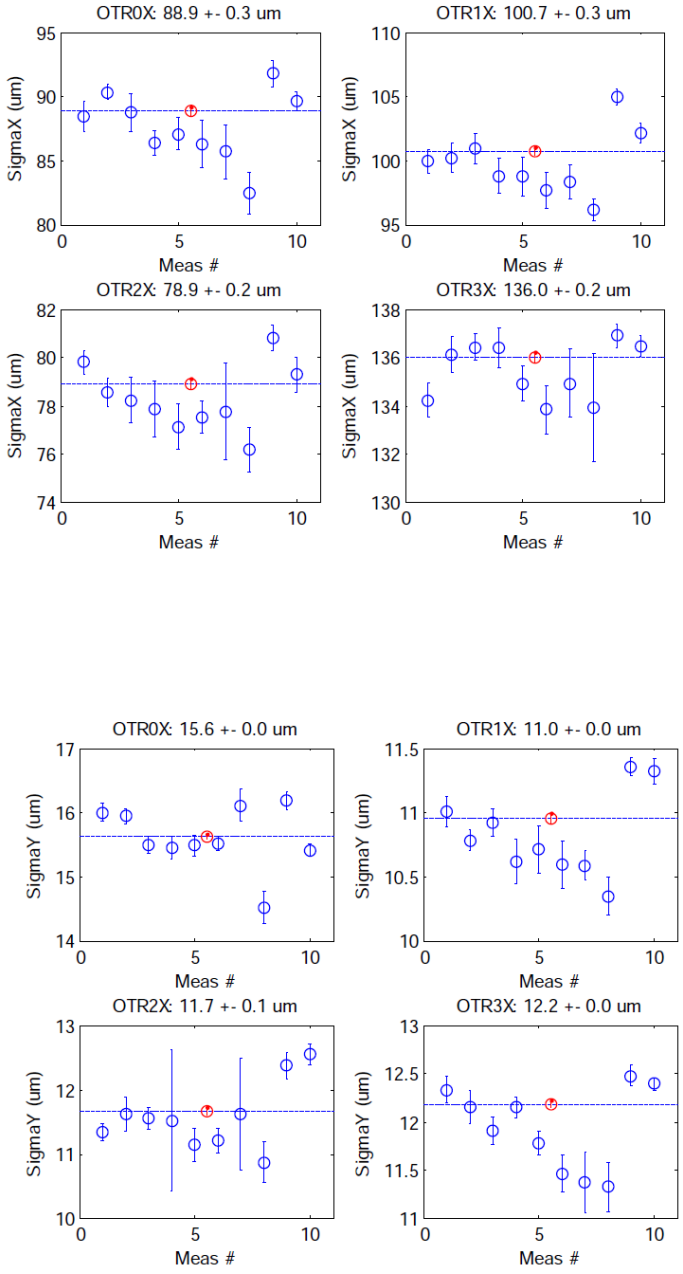

Figure 4.3: Ten consecutive OTR measurements done on 29th November 2012 with the value in red.

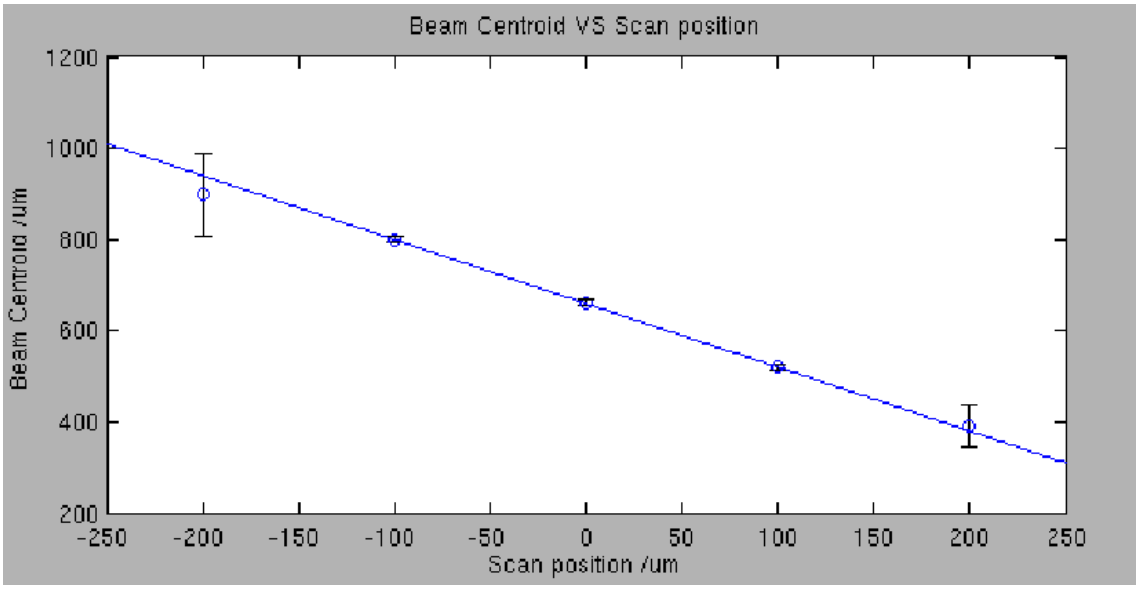

Figure 4.4: Pixel size automatic calibration plot.

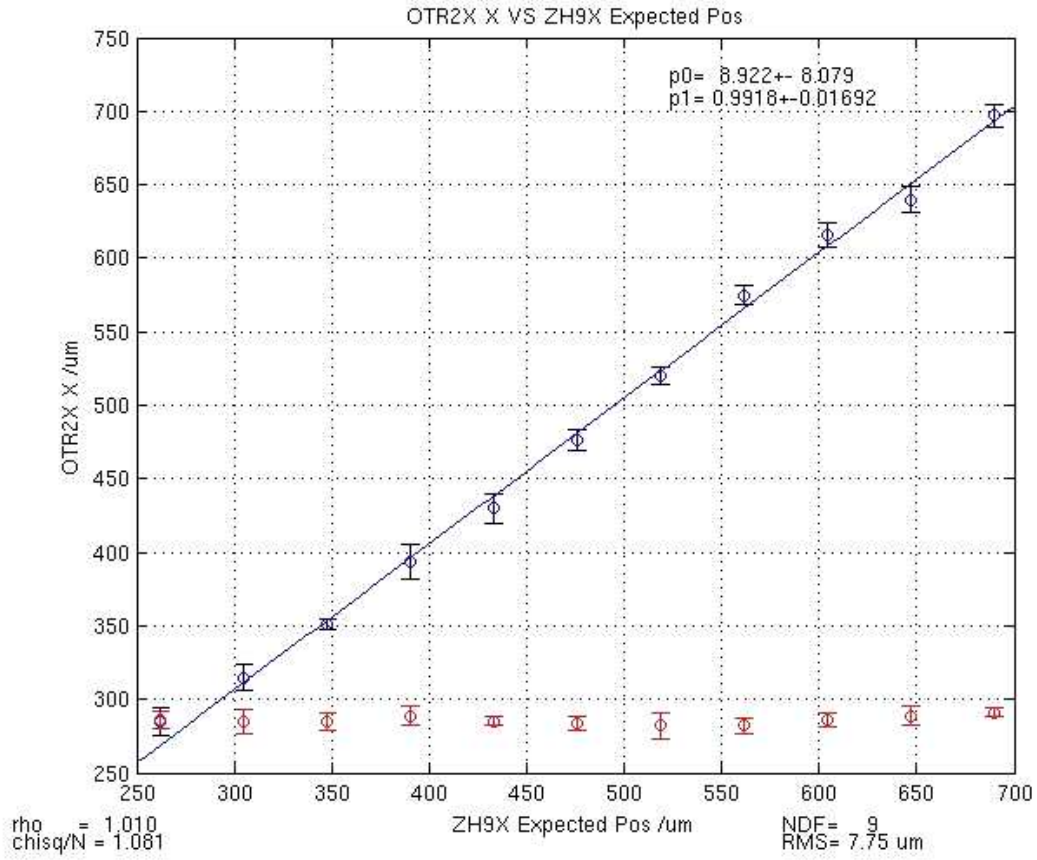

Figure 4.5: OTR2X roll measurement. In blue the horizontal beam position measurement against the expected position when the beam is steered. In red the measured vertical position remains constant.

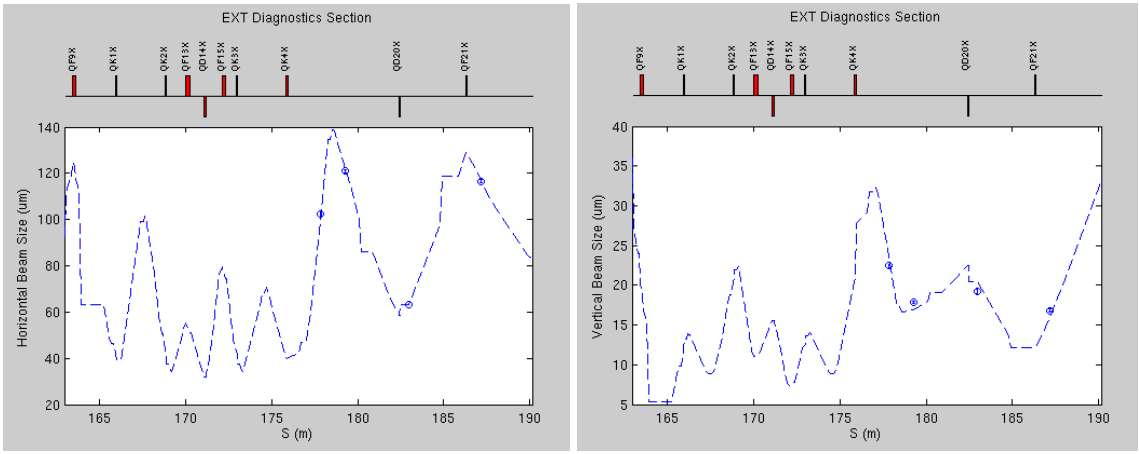

Figure 4.6: Measurement of the beam sizes and comparison with the model made on 1th December 2011.

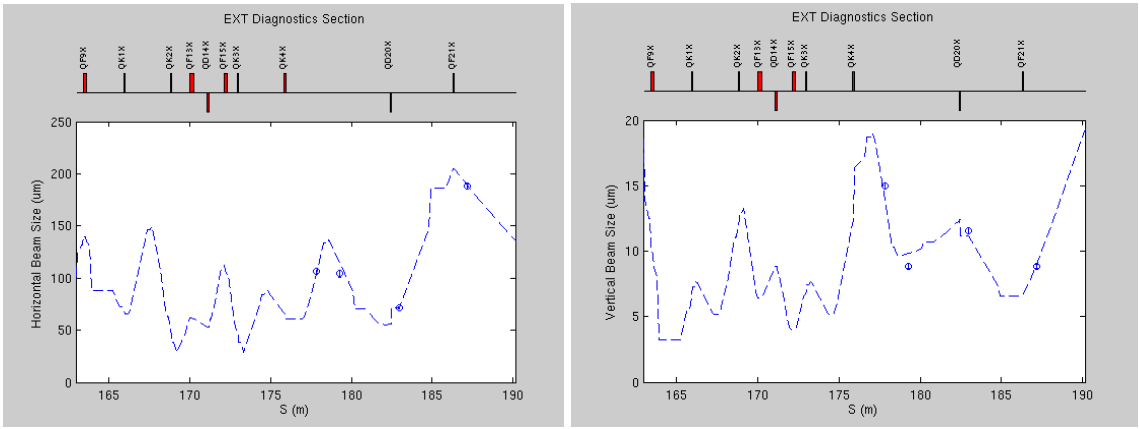

Figure 4.7: Measurement of the beam sizes and comparison with the model made on 6th March 2012.

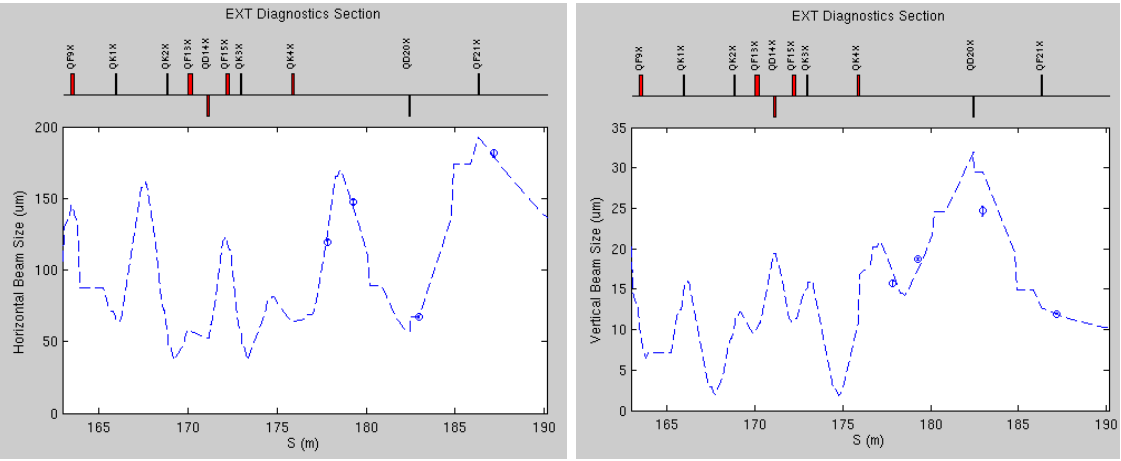

Figure 4.8: Measurement of the beam sizes and comparison with the model made on 8th March 2012.

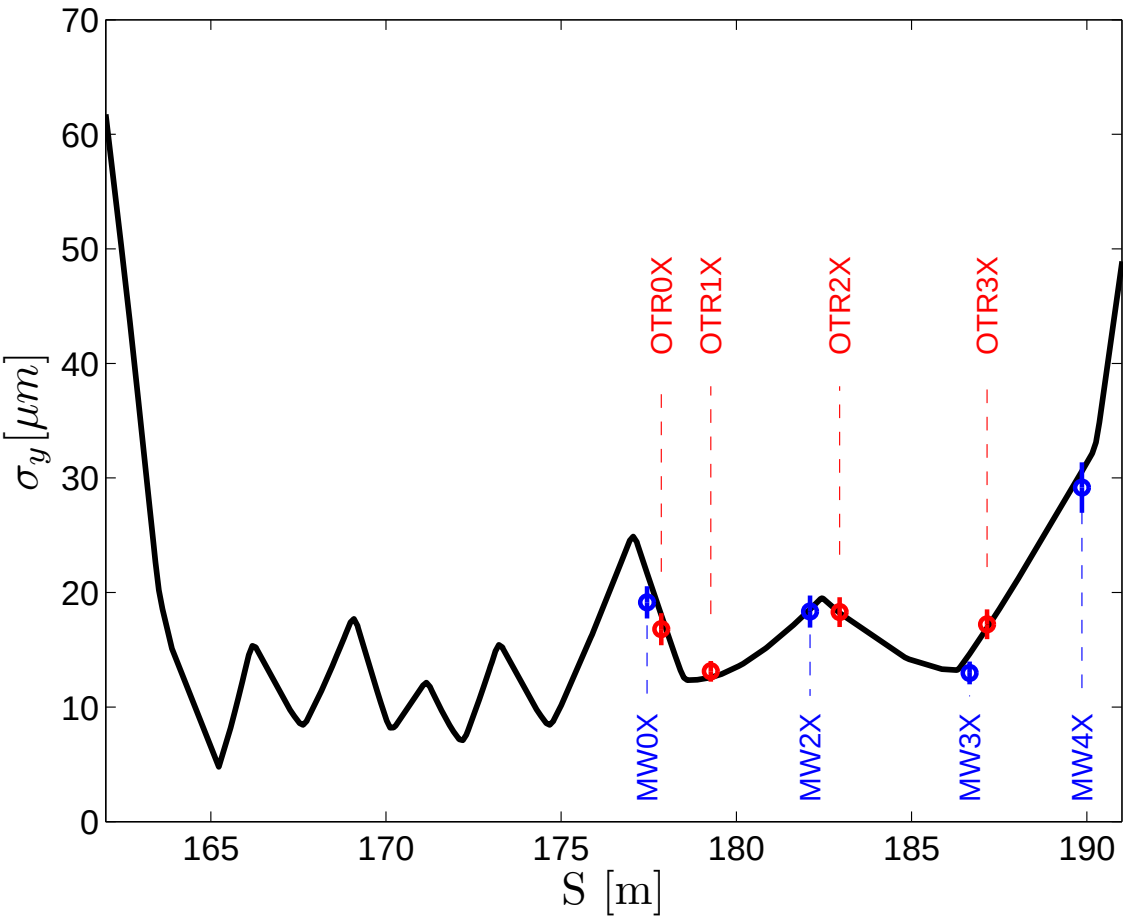

Figure 4.9: Comparison between OTR and WS measurements made on Dec. 14th 2011.

Chapter 5

Emittance measurements in ATF2

ATF is a DR prototype similar to that of the ILC built to create very small emittances, for this it is important to control the quality of the beam after the extraction of the DR to study any eventual emittance growing. ATF2 is a BDS and a FFS where the knowledge of the emittance play also a relevant role in the tuning activities. Emittance reconstruction in the EXT line is therefore crucial for different reasons. Appendix A serves as an introduction to this relevant parameter.

The ATF beam has an extremely low vertical emittance (nominally 12 pm·rad after the DR) and in order to reconstruct it beam size measurements are needed. Some difficulties are implied, specially regarding the small vertical beam sizes to be encountered. An overview of the most used emittance measurement techniques for storage rings and after them can be found in reference [65]. In the ATF DR the emittance is measured by the so called X-ray SR (XSR) beam size monitor estimating the beta function from the fitting of the beta functions among the quadrupole magnets [66].

In the past, emittance measurements in the EXT line have been carried out using the existing WS system, 4D emittance calculations were not reliable presumably due to errors in the measurements [67]. Methods based on quadrupole scans and methods based on multiple measurement locations were done, but treating the vertical and the horizontal planes uncoupled. Cross-plane coupling plays an important role in the emittance measurement and therefore, in order to reconstruct the 4D beam matrix, multiple monitors at different locations capable of tilt measurements are needed [69].

5.1 Emittance reconstruction from measured beam sizes

5.1.1 Reconstruction algorithm

In this Section the problem of reconstructing the emittance from the beam size measurements at different locations along the beam-line is addressed. The 2D (transverse) and 4D (intrinsic) emittances are obtained by numerically solving three systems of uncoupled equations. All these systems are overdetermined when the number of measurement stations is greater than three. Therefore the numerical solution leads in some cases to

unphysical results, as typically imaginary emittances. The incidence of such meaningless results usually increases if the measurements are noisy as will be seen in next Section. However some numerical rules related to the condition number of the matrices involved in these systems of equations could be used to study the conditioning of these systems [70].

An introduction to the transverse envelope beam matrix can be found in Appendix A. Here the beam matrix will be denoted by the symbols σ_i with $i = 1, 2, ..10$ in the following way:

$$\sigma = \begin{pmatrix} \sigma_1 & \sigma_2 & \sigma_3 & \sigma_4 \\ \sigma_2 & \sigma_5 & \sigma_6 & \sigma_7 \\ \sigma_3 & \sigma_6 & \sigma_8 & \sigma_9 \\ \sigma_4 & \sigma_7 & \sigma_9 & \sigma_{10} \end{pmatrix}. \tag{5.1}$$

The horizontal and vertical beam sizes are given by $\sigma_1 =< x^2 >$ and $\sigma_8 =< y^2 >$. The coupling terms: $\sigma_3, \sigma_4, \sigma_6, \sigma_7$ are zero when there is no coupling. The projected emittances (2D) ϵ_x and ϵ_y are given by:

$$\epsilon_x = \sqrt{\begin{vmatrix} \sigma_1 & \sigma_2 \\ \sigma_2 & \sigma_5 \end{vmatrix}}\ ,\ \epsilon_y = \sqrt{\begin{vmatrix} \sigma_8 & \sigma_9 \\ \sigma_9 & \sigma_{10} \end{vmatrix}}, \tag{5.2}$$

being ϵ_x and ϵ_y always positive.

The diagonalization of the beam matrix (σ) yields the intrinsic beam emittances (4D) ϵ_1 and ϵ_2 using a symplectic transformation:

$$\overline{\sigma} = S\ \sigma\ S^t = \begin{pmatrix} \epsilon_1 & 0 & 0 & 0 \\ 0 & \epsilon_1 & 0 & 0 \\ 0 & 0 & \epsilon_2 & 0 \\ 0 & 0 & 0 & \epsilon_2 \end{pmatrix}, \tag{5.3}$$

where S is the transformation matrix that make the change of coordinates. In this new system the beam matrix ($\overline{\sigma}$) is diagonalized, being ϵ_1 and ϵ_2 the eigenvalues that are degenerated and defined positive [68]. If the beam is uncoupled the intrinsic emittance equals the projected one, when coupling is present the projected emittance is larger than the intrinsic emittance. The diagonalization procedure is detailed further in Section 5.1.3.

The transformation between an initial beam matrix σ_0 to the beam matrix at a measurement point, σ_i is:

$$\sigma_i = R\ \sigma_0\ R^t, \tag{5.4}$$

where R are the linear transfer matrices between the initial point and the measurement point.

Experimentally only the horizontal σ_1 and vertical σ_8 beam sizes and the σ_3 coupling term are directly measured. We need at least ten measurements to reconstruct the ten elements of the beam matrix. The ten values could be obtained by changing the optics in a controlled manner at the location of the measurements or by measuring the beam size at different locations. In our case we will use the second method.

Let the measured values of σ_1, σ_8 and σ_3 be

$$\hat{\sigma}_1^{(i)},\ \hat{\sigma}_8^{(i)},\ \hat{\sigma}_3^{(i)}, \tag{5.5}$$

with $i = 1, 2, \ldots N$ labeling the measurement station. We can obtain from equation (5.4), assuming non-coupling transport matrices in the diagnostic section:

$$\hat{\sigma}^{(i)} = R\ \sigma_0\ R^t =$$

$$= \begin{pmatrix} R_{11} & R_{12} & 0 & 0 \\ R_{21} & R_{22} & 0 & 0 \\ 0 & 0 & R_{33} & R_{34} \\ 0 & 0 & R_{43} & R_{44} \end{pmatrix} \begin{pmatrix} \sigma_1 & \sigma_2 & \sigma_3 & \sigma_4 \\ \sigma_2 & \sigma_5 & \sigma_6 & \sigma_7 \\ \sigma_3 & \sigma_6 & \sigma_8 & \sigma_9 \\ \sigma_4 & \sigma_7 & \sigma_9 & \sigma_{10} \end{pmatrix} \begin{pmatrix} R_{11} & R_{21} & 0 & 0 \\ R_{12} & R_{22} & 0 & 0 \\ 0 & 0 & R_{33} & R_{43} \\ 0 & 0 & R_{34} & R_{44} \end{pmatrix}, \tag{5.6}$$

giving for each measurement station the following systems of equations:

$$\begin{aligned} \hat{\sigma}_1^{(i)} &= R_{11}^{2(i)}\sigma_1 + 2R_{11}^{(i)}R_{12}^{(i)}\sigma_2 + R_{12}^{2(i)}\sigma_5 \\ \hat{\sigma}_8^{(i)} &= R_{33}^{2(i)}\sigma_8 + 2R_{33}^{(i)}R_{34}^{(i)}\sigma_9 + R_{34,i}^{2(i)}\sigma_{10} \\ \hat{\sigma}_3^{(i)} &= R_{11}^{(i)}R_{33}^{(i)}\sigma_3 + R_{11}^{(i)}R_{34}^{(i)}\sigma_4 + R_{12}^{(i)}R_{33}^{(i)}\sigma_6 + R_{12}^{(i)}R_{34}^{(i)}\sigma_7 \end{aligned} \quad . \tag{5.7}$$

Introducing the matrices M_X, M_Y and M_{XY} as :

$$M_X = \begin{pmatrix} R_{11}^{2(1)} & 2R_{11}^{(1)}R_{12}^{(1)} & R_{12}^{2(1)} \\ R_{11}^{2(2)} & 2R_{11}^{(2)}R_{12}^{(2)} & R_{12}^{2(2)} \\ R_{11}^{2(3)} & 2R_{11}^{(3)}R_{12}^{(3)} & R_{12}^{2(3)} \\ \ldots & \ldots & \ldots \\ R_{11}^{2(N)} & 2R_{11}^{(N)}R_{12}^{(N)} & R_{12}^{2(N)} \end{pmatrix} \tag{5.8}$$

$$M_Y = \begin{pmatrix} R_{33}^{2(1)} & 2R_{33}^{(1)}R_{34}^{(1)} & R_{34}^{2(1)} \\ R_{33}^{2(2)} & 2R_{33}^{(2)}R_{34}^{(2)} & R_{34}^{2(2)} \\ R_{33}^{2(3)} & 2R_{33}^{(3)}R_{34}^{(3)} & R_{34}^{2(3)} \\ \ldots & \ldots & \ldots \\ R_{33}^{2(N)} & 2R_{33}^{(N)}R_{34}^{(N)} & R_{34}^{2(N)} \end{pmatrix} \tag{5.9}$$

$$M_{XY} = \begin{pmatrix} R_{11}^{(1)}R_{33}^{(1)} & R_{11}^{(1)}R_{34}^{(1)} & R_{12}^{(1)}R_{33}^{(1)} & R_{12}^{(1)}R_{34}^{(1)} \\ R_{11}^{(2)}R_{33}^{(2)} & R_{11}^{(2)}R_{34}^{(2)} & R_{12}^{(2)}R_{33}^{(2)} & R_{12}^{(2)}R_{34}^{(2)} \\ R_{11}^{(3)}R_{33}^{(3)} & R_{11}^{(3)}R_{34}^{(3)} & R_{12}^{(3)}R_{33}^{(3)} & R_{12}^{(3)}R_{34}^{(3)} \\ \ldots & \ldots & \ldots & \ldots \\ R_{11}^{(N)}R_{33}^{(N)} & R_{11}^{(N)}R_{34}^{(N)} & R_{12}^{(N)}R_{33}^{(N)} & R_{12}^{(N)}R_{34}^{(N)} \end{pmatrix}, \tag{5.10}$$

the equations (5.7) could be expressed as:

$$M_X \begin{pmatrix} \sigma_1 \\ \sigma_2 \\ \sigma_5 \end{pmatrix} = \begin{pmatrix} \hat{\sigma}_1^{(1)} \\ \hat{\sigma}_1^{(2)} \\ \hat{\sigma}_1^{(3)} \\ \dots \\ \hat{\sigma}_1^{(N)} \end{pmatrix} \tag{5.11}$$

$$M_Y \begin{pmatrix} \sigma_8 \\ \sigma_9 \\ \sigma_{10} \end{pmatrix} = \begin{pmatrix} \hat{\sigma}_8^{(1)} \\ \hat{\sigma}_8^{(2)} \\ \hat{\sigma}_8^{(3)} \\ \dots \\ \hat{\sigma}_8^{(N)} \end{pmatrix} \tag{5.12}$$

$$M_{XY} \begin{pmatrix} \sigma_3 \\ \sigma_4 \\ \sigma_6 \\ \sigma_7 \end{pmatrix} = \begin{pmatrix} \hat{\sigma}_3^{(1)} \\ \hat{\sigma}_3^{(2)} \\ \hat{\sigma}_3^{(3)} \\ \dots \\ \hat{\sigma}_3^{(N)} \end{pmatrix}. \tag{5.13}$$

The problem is reduced to that of solving three systems of uncoupled equations. In principle four measurement stations are required to reconstruct the coupled beam matrix, but one should notice that the systems (5.11) and (5.12) are then overdetermined, and unphysical results could be obtained. Limiting the number of stations to three, only the projected emittance (2D) can be reconstructed. Finally if the number of stations is greater than four, the three systems are overdetermined. The next Section studies the optics conditions in the different scenarios to get solvability of the system.

5.1.2 Unique solution conditions for the reconstruction

Vertical and horizontal sub-matrices (2D emittance)

Three measurement stations In that case one can solve the systems (5.11) and (5.12) using analytical methods. Since they have the same algebraic construction structure, we will particularize the discussion to the horizontal plane (5.11), for which the coefficient matrix is:

$$M_X = \begin{pmatrix} R_{11}^{2(1)} & 2R_{11}^{(1)}R_{12}^{(1)} & R_{12}^{2(1)} \\ R_{11}^{2(2)} & 2R_{11}^{(2)}R_{12}^{(2)} & R_{12}^{2(2)} \\ R_{11}^{2(3)} & 2R_{11}^{(3)}R_{12}^{(3)} & R_{12}^{2(3)} \end{pmatrix}. \tag{5.14}$$

As is well known the system (5.11) has a unique solution if and only of the determinant of M_X is non null. In the Appendix Section B.1 are given the matrix elements $R_{i,j}$ in terms of the Twiss parameters and the determinant of M_X is:

$$det(M_X) = 2\beta_x^{(1)}\beta_x^{(2)}\beta_x^{(3)} \sin\phi_x^{(21)} \sin\phi_x^{(31)} \sin\phi_x^{(32)}, \tag{5.15}$$

where $\phi_x^{(ij)} = (\phi_x^{(i)} - \phi_x^{(j)})$ with $ij = 1, 2, 3$ stayed for the difference of phase advances.

We obviously assume that the $\beta_x^{(i)}$ are non-null, and thus the required condition of $det(M_X)$ is that $\phi_x^{(ij)} \neq n\pi$ with n an integer for any pairs. We can see then that if and only if the independent betatron phase advance differences $\phi_x^{(ij)}$ and $\phi_y^{(ij)}$ are not integer multiple of π, the systems (5.11) and (5.12) have unique solutions and the projected emittances can be reconstructed. This result is in accordance with the rule of the optimal phase advance of π/N with N the number of measurements stations for a 2D emittance diagnostic section [87]. This rule is clear by viewing the normalized phase space as a circle with beam measurements made at π/N intervals.

Four or more measurement stations We consider now the case of $N \geq 4$ measurement stations, which lead to an undetermined system. As in the previous section we particularize for the horizontal plane, whose coefficient matrix is:

$$M_X = \begin{pmatrix} R_{11}^{2(1)} & 2R_{11}^{(1)}R_{12}^{(1)} & R_{12}^{2(1)} \\ R_{11}^{2(2)} & 2R_{11}^{(2)}R_{12}^{(2)} & R_{12}^{2(2)} \\ R_{11}^{2(3)} & 2R_{11}^{(3)}R_{12}^{(3)} & R_{12}^{2(3)} \\ R_{11}^{2(4)} & 2R_{11}^{(4)}R_{12}^{(4)} & R_{12}^{2(4)} \\ \dots & & \\ R_{11}^{2(N)} & 2R_{11}^{(N)}R_{12}^{(N)} & R_{12}^{2(N)} \end{pmatrix}, \tag{5.16}$$

associated to this matrix we construct the augmented matrix:

$$M_X^* = \begin{pmatrix} R_{11}^{2(1)} & 2R_{11}^{(1)}R_{12}^{(1)} & R_{12}^{2(1)} & \hat{\sigma}_1^{(1)} \\ R_{11}^{2(2)} & 2R_{11}^{(2)}R_{12}^{(2)} & R_{12}^{2(2)} & \hat{\sigma}_1^{(2)} \\ R_{11}^{2(3)} & 2R_{11}^{(3)}R_{12}^{(3)} & R_{12}^{2(3)} & \hat{\sigma}_1^{(3)} \\ R_{11}^{2(4)} & 2R_{11}^{(4)}R_{12}^{(4)} & R_{12}^{2(4)} & \hat{\sigma}_1^{(4)} \\ \dots & & & \\ R_{11}^{2(N)} & 2R_{11}^{(N)}R_{12}^{(N)} & R_{12}^{2(N)} & \hat{\sigma}_1^{(N)} \end{pmatrix}. \tag{5.17}$$

The Rouché-Capelli theorem establish that the system (5.11) has a unique solution $(\sigma_1, \sigma_2, \sigma_5)$ if and only if the rank of these matrices is three. From the previous subsection we can immediately see that the matrix M_X has rank 3 if and only if $\phi_x^{(ij)} \neq n\pi$ for any pair of stations.

Let us see now the conditions required in M_X^* for having rank 3. The calculation of the minors is detailed in the Appendix Section B.3 To facilitate the analysis of the minor expressions we introduce a new phase advance notation. Given that $\phi_x^{(ij)} = \phi_x^{(ik)} - \phi_x^{(jk)}$ we could introduce $N-1$ independent phase analysis that we renamed as: $\phi_x^{(21)} = \Phi_{x,1}$, $\phi_x^{(31)} = \Phi_{x,2}$ and $\phi_x^{(41)} = \Phi_{x,3} \dots$

- From (B.3) the $rank(M_X^*) \leq 3$ (all minors of order 4 of M_X^* are zero) when:
  - for the minors of order 4 of M_X^* corresponding to row combination (1, 2, 3, 4):

  - $\Phi_{x,i} = n(\pi/2)$ with n an integer and $i = 1, 2, 3$ all the independent betatron phase differences, or
  - $\hat{\sigma}_1^{(4)} = \beta_x^{(4)}/\beta_x^{(1)}\hat{\sigma}_1^{(1)} = \beta_x^{(4)}/\beta_x^{(3)}\hat{\sigma}_1^{(3)} = \beta_x^{(4)}/\beta_x^{(2)}\hat{\sigma}_1^{(2)}$ i.e. there is equivalent beam size ratio between the different measurement stations or
  - $\Phi_{x,1}$ free, $\Phi_{x,2} = n(\pi/2), \Phi_{x,3} = m(\pi/2)$ with n and m integers and $\hat{\sigma}_1^{(4)} = \beta_x^{(4)}/\beta_x^{(3)}\hat{\sigma}_1^{(3)}$, or
  - $\Phi_{x,2}$ free, $\Phi_{x,1} = n(\pi/2), \Phi_{x,3} = m(\pi/2)$ with n and m integers and $\hat{\sigma}_1^{(4)} = \beta_x^{(4)}/\beta_x^{(2)}\hat{\sigma}_1^{(2)}$, or
  - $\Phi_{x,3}$ free, $\Phi_{x,1} = n(\pi/2), \Phi_{x,2} = m(\pi/2)$ with n and m integers and $\hat{\sigma}_1^{(3)} = \beta_x^{(3)}/\beta_x^{(2)}\hat{\sigma}_1^{(2)}$
- same conditions with all the other rows combinations: (2, 3, 4, 5),... (N-3, N-2, N-1; N).

The $rank(M_X^*) = 3$ except in the case where we have: $\Phi_{x,i} = n\pi$ with n an integer and $i = 1, 2, 3, N-1$ for all the independent betatron phase differences and equivalent beam size ratio between the different measurement stations. In such a case all minors of order 3 of M_X^* are zero and the $rank(M_X^*) \leq 2$. The $rank(M_X^*) = 1$ when furthermore $\phi_x^{(10)} = n\pi$ with $n = 0, 1, 2, 3 \ldots$. Having $\Phi_{x,i} = n\pi$ with n an integer and $i = 1, 2, 3, N-1$ all the minors of order 3 and 2 of M_X are zero hence the system has **no solution**.

Being the $rank(M_X^*) = 3$ we have from the analysis of the minors of M_X:

- for the minors of order 4 of M_X^* corresponding to row combination (1, 2, 3, 4):
  - having $\Phi_{x,i} = n(\pi/2)$ with n an integer and $i = 1, 2, 3$ all the independent betatron phase differences hence the $rank(M_X) = 2$ and the system has no solution
  - having $\hat{\sigma}_1^{(4)} = \beta_x^{(4)}/\beta_x^{(1)}\hat{\sigma}_1^{(1)} = \beta_x^{(4)}/\beta_x^{(3)}\hat{\sigma}_1^{(3)} = \beta_x^{(4)}/\beta_x^{(2)}\hat{\sigma}_1^{(2)}$ i.e. there is equivalent beam size ratio between the different measurement stations hence the $rank(M_X) = 3$ and the system has **unique solution**
  - having $\Phi_{x,1}$ free, $\Phi_{x,2} = n(\pi/2), \Phi_{x,3} = m(\pi/2)$ with n and m integers and $\hat{\sigma}_1^{(4)} = \beta_x^{(4)}/\beta_x^{(3)}\hat{\sigma}_1^{(3)}$ hence if n, m and $(n-m)$ are even the $rank(M_X) < 3$ and the system has **no solution**, if n, m and $(n-m)$ are odd the $rank(M_X) = 3$ and the system has **unique solution**
  - having $\Phi_{x,2}$ free, $\Phi_{x,1} = n(\pi/2), \Phi_{x,3} = m(\pi/2)$ with n and m integers and $\hat{\sigma}_1^{(4)} = \beta_x^{(4)}/\beta_x^{(2)}\hat{\sigma}_1^{(2)}$ hence if n, m and $(n-m)$ are even the $rank(M_X) < 3$ and the system has **no solution**, if n, m and $(n-m)$ are odd the $rank(M_X) = 3$ and the system has **unique solution**
  - $\Phi_{x,3}$ free, $\Phi_{x,1} = n(\pi/2), \Phi_{x,2} = m(\pi/2)$ with n and m integers and $\hat{\sigma}_1^{(3)} = \beta_x^{(3)}/\beta_x^{(2)}\hat{\sigma}_1^{(2)}$ hence if n, m and $(n-m)$ are even the $rank(M_X) < 3$ and the system has **no solution**, if n, m and $(n-m)$ are odd the $rank(M_X) = 3$ and the system has **unique solution**

– same conditions with all the other rows combinations: (2, 3, 4, 5),... (N-3, N-2, N-1; N).

The same is valid for the vertical plane. The solution of the systems (5.11) and (5.12) give us the beam elements matrix: $\sigma_1, \sigma_2, \sigma_5, \sigma_8, \sigma_9$, and σ_{10}, the projected emittances can be calculated using equation (5.2). The conditions of solvability give us a some rules for the location of the measurement stations.

Transverse coupling sub-matrix (4D emittance)

In order to calculate the coupling terms: $\sigma_3, \sigma_4, \sigma_6$ and σ_7 from system (5.13) we have to perform at least four measurements.

Four measurement OTR stations In the case where we have four measurement station the system (5.13) give us four equations and four unknowns, and the system could be solved analytically. The Cramer's rule theorem could be applied in that case. Taken into account this rule the system has a unique solution if the coefficient matrices M_{XY} has a nonzero determinant. The coefficient matrix is given by:

$$M_{XY} = \begin{pmatrix} R_{11}^{(1)}R_{33}^{(1)} & R_{11}^{(1)}R_{34}^{(1)} & R_{12}^{(1)}R_{33}^{(1)} & R_{12}^{(1)}R_{34}^{(1)} \\ R_{11}^{(2)}R_{33}^{(2)} & R_{11}^{(2)}R_{34}^{(2)} & R_{12}^{(2)}R_{33}^{(2)} & R_{12}^{(2)}R_{34}^{(2)} \\ R_{11}^{(3)}R_{33}^{(3)} & R_{11}^{(3)}R_{34}^{(3)} & R_{12}^{(3)}R_{33}^{(3)} & R_{12}^{(3)}R_{34}^{(3)} \\ R_{11}^{(4)}R_{33}^{(4)} & R_{11}^{(4)}R_{34}^{(4)} & R_{12}^{(4)}R_{33}^{(4)} & R_{12}^{(4)}R_{34}^{(4)} \end{pmatrix}, \tag{5.18}$$

with the determinant of M_{XY} given by:

$$\begin{aligned} det(M_{XY}) = & -\tfrac{1}{8}\sqrt{\beta_x^{(1)}\beta_y^{(1)}\beta_x^{(2)}\beta_y^{(2)}\beta_x^{(3)}\beta_y^{(3)}\beta_x^{(4)}\beta_y^{(4)}} \\ & \{\cos(\Phi_{x,1} - \Phi_{x,2} + \Phi_{x,3} - \Phi_{y,1} + \Phi_{y,2} + \Phi_{y,3}) \\ & - \cos(\Phi_{x,1} - \Phi_{x,2} + \Phi_{x,3} - \Phi_{y,1} - \Phi_{y,2} + \Phi_{y,3}) \\ & - \cos(\Phi_{x,1} - \Phi_{x,2} + \Phi_{x,3} + \Phi_{y,1} + \Phi_{y,2} - \Phi_{y,3}) \\ & + \cos(\Phi_{x,1} - \Phi_{x,2} + \Phi_{x,3} + \Phi_{y,1} - \Phi_{y,2} - \Phi_{y,3}) \\ & - \cos(-\Phi_{x,1} + \Phi_{x,2} + \Phi_{x,3} + \Phi_{y,1} - \Phi_{y,2} + \Phi_{y,3}) \\ & + \cos(-\Phi_{x,1} + \Phi_{x,2} + \Phi_{x,3} - \Phi_{y,1} - \Phi_{y,2} + \Phi_{y,3}) \\ & + \cos(-\Phi_{x,1} + \Phi_{x,2} + \Phi_{x,3} + \Phi_{y,1} + \Phi_{y,2} - \Phi_{y,3}) \\ & - \cos(-\Phi_{x,1} + \Phi_{x,2} + \Phi_{x,3} - \Phi_{y,1} + \Phi_{y,2} - \Phi_{y,3}) \\ & - \cos(\Phi_{x,1} + \Phi_{x,2} - \Phi_{x,3} - \Phi_{y,1} + \Phi_{y,2} + \Phi_{y,3}) \\ & + \cos(\Phi_{x,1} + \Phi_{x,2} - \Phi_{x,3} + \Phi_{y,1} - \Phi_{y,2} + \Phi_{y,3}) \\ & + \cos(\Phi_{x,1} + \Phi_{x,2} - \Phi_{x,3} - \Phi_{y,1} + \Phi_{y,2} - \Phi_{y,3}) \\ & - \cos(\Phi_{x,1} + \Phi_{x,2} - \Phi_{x,3} + \Phi_{y,1} - \Phi_{y,2} - \Phi_{y,3})\} \end{aligned} \tag{5.19}$$

taking the expressions for the different matrix elements (see Appendix section B.1) and with $\phi_x^{(ij)} = (\phi_x^{(i)} - \phi_x^{(j)})$ with $ij = 1, 2, 3, 4$ being $\phi_x^{(32)} = \phi_x^{(31)} - \phi_x^{(21)}$, $\phi_x^{(42)} = \phi_x^{(41)} - \phi_x^{(21)}$ and $\phi_x^{(43)} = \phi_x^{(41)} - \phi_x^{(31)}$. These means that there are only three independent difference

phase advances that we renamed as: $\phi_x^{(21)} = \Phi_{x,1}$, $\phi_x^{(31)} = \Phi_{x,2}$ and $\phi_x^{(41)} = \Phi_{x,3}$. The system (5.13) will have **unique solution** when $det(M_{XY}) \neq 0$. In that case there is no direct rule between the independent betatron phase differences of the expression (5.19).

Five or more measurement stations In the case where we have five or more measurement stations the system (5.13) has more equations that unknowns, therefore the system have to be solved numerically by least square minimization for instance. In that case due to the mixing of the two planes the calculation of the minors for using the Rouché-Capelli theorem could not give us direct information about the solvability of the system.

5.1.3 Beam matrix diagonalization

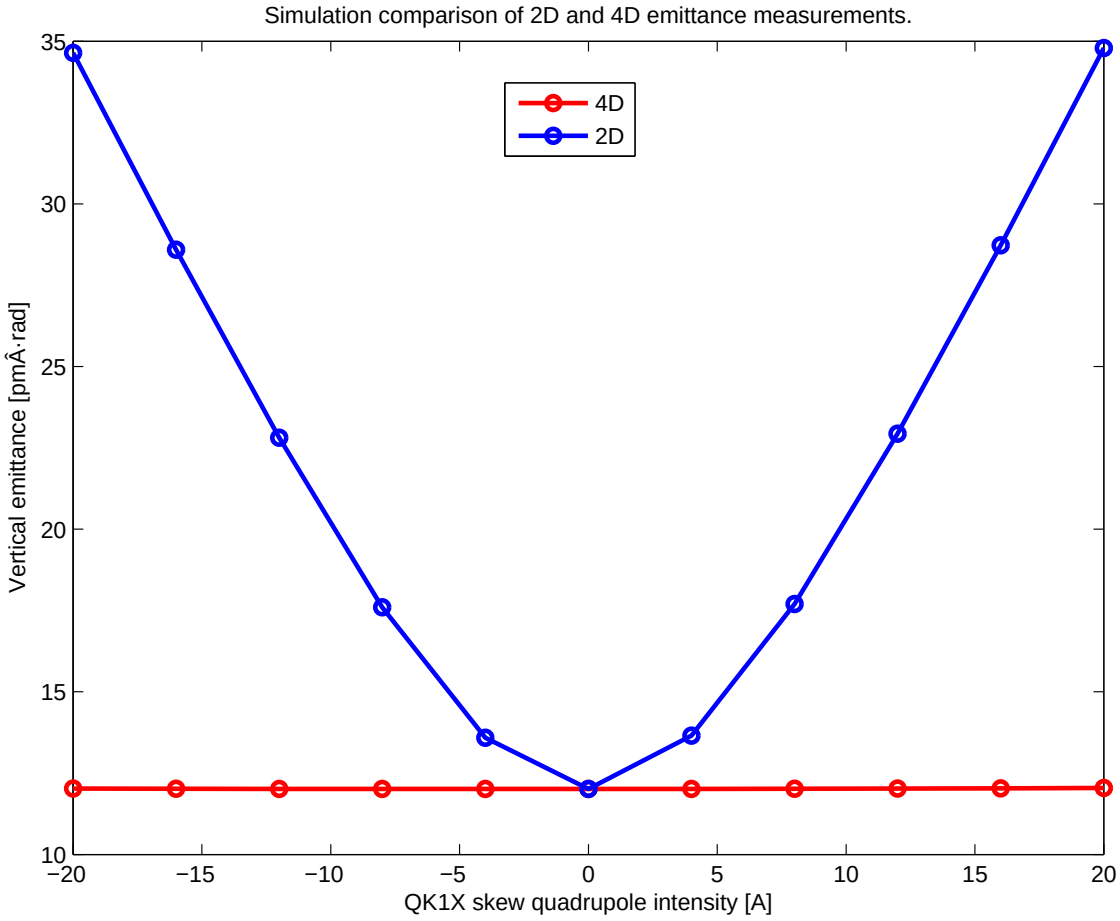

Figure 5.1: Comparison of 4D and 2D emittance reconstruction algorithms when beam coupling is increased.

Once one has reconstructed the full beam matrix, in order to obtain the intrinsic

emittances it is necessary to diagonalize it. The use of two general properties of the positive definite symmetric matrices as is the case of σ and $\overline{\sigma}$ give us a simple way to calculate the intrinsic beam emittances. If $\overline{\sigma}$ is a symmetric positive definitive matrix, we have:

1. $det(\overline{\sigma})$ is invariant $\forall R_{i,j} \in \mathbb{R}$

2. $Tr(J\overline{\sigma})^{2h}$ is invariant $\forall R_{i,j} \in \mathbb{R}$, this invariant is known as the Poincare invariant in the space of dimension $2\mathbb{N}$, being $h = 1, 2 \ldots \mathbb{N}$-1 and J defined as:

$$J = \begin{pmatrix} 0 & -1 & 0 & 0 \\ 1 & 0 & 0 & 0 \\ 0 & 0 & 0 & -1 \\ 0 & 0 & 1 & 0 \end{pmatrix} \tag{5.20}$$

Given that $\overline{\sigma} = \bar{R}\ \sigma\ \bar{R}^t$ from (5.3) we can infer from the properties 1 and 2:

$$det(\overline{\sigma}) = det(\sigma) = (\epsilon_1^2 \epsilon_2^2) \tag{5.21}$$

$$Tr(J\overline{\sigma})^2 = Tr(J\sigma)^2 = -2(\epsilon_1^2 + \epsilon_2^2). \tag{5.22}$$

The detailed demonstration of these steps can be found in the Appendix Section B.3 [71].

Using the Vieta's formula for the solutions of a quadratic equations we have from (5.21) and (5.22):

$$\chi^2 + \frac{1}{2} Tr(J\sigma)^2 \chi + det(\sigma) = 0, \tag{5.23}$$

being $\chi_1 = \epsilon_1^2$ and $\chi_2 = \epsilon_2^2$ is given by:

$$\begin{array}{l} \epsilon_{1,2} = \sqrt{\frac{1}{2}\{-\frac{1}{2}Tr(J\sigma)^2 \pm \sqrt{(-\frac{1}{2}Tr(J\sigma)^2)^2 - 4det(\sigma)}\}} = \\ \frac{1}{2}\sqrt{-Tr(J\sigma)^2 \pm \sqrt{(Tr(J\sigma)^2)^2 - 16det(\sigma)}} = \\ \frac{1}{2}\sqrt{-Tr(J\sigma)^2 \pm \sqrt{-(Tr(J\sigma)^2)^2 + 4Tr(J\sigma)^4}} \end{array} , \tag{5.24}$$

the last step in (5.24) use:

$$det(\sigma) = det(J\sigma) = \frac{1}{8}(Tr(J\sigma)^2)^2 - \frac{1}{4}Tr(J\sigma)^4, \tag{5.25}$$

with $Tr(J\overline{\sigma})^4 = Tr(J\sigma)^4 = 2(\epsilon_1^4 + \epsilon_2^4)$.

The last expression is used in the ATF control room for calculating the intrinsic emittances.

5.2 Realistic simulations

In order to compare the 2D and 4D performances simulations reconstructing both parameters have been done as a function of the intensity of a skew quadrupole (see detailed definition of this element in Section 6.1.1) upstream of the Multi-OTR system. This kind of quadrupole has an effect in coupling the horizontal and vertical planes. The 2D emittance uses the projected beam sizes not taking into account any eventual beam coupling and therefore the vertical emittance grows when the coupling is increased because the beam is flat shaped. The 4D emittance is obtained from the full beam matrix considering then any eventual coupling term in the calculation and therefore the calculated intrinsic emittance does not depend on the beam coupling. The results of the simulation can be seen in Figure 5.1.

When some measurement error is included in the simulations the method can lead to a non positive-definite beam matrix which, unlike the positive-definite matrix, can have negative eigenvalues leading to imaginary emittances as a result. This can be an issue for beam size monitors with a high measurement error and for slow measurement methods, which would need to repeat the measurement often. This is not the case of the Multi-OTR system, but however simulations of the emittance reconstruction method have been done using the nominal lattice and including errors in the beam size measurements.

Figure 5.2 shows the ratio of imaginary emittances as a function of the relative beam size measurement error. Curves are shown for the full 4D emittance and for the 2D reconstruction in the horizontal and vertical cases. The 4D vertical case is the most sensitive to error. Each point in the plot is calculated over 5000 measurements sorting randomly the measured size as

$$\sigma_{x,y} = \sigma_{x,y_{th.}} \cdot (1 + r \cdot \frac{\Delta\sigma_{x,y}}{\sigma_{x,y_{th.}}}), \tag{5.26}$$

where r is a normalized gaussian random number. For simplicity here has been assumed that the CCD camera is perfectly aligned with the accelerator axis and the initial beam has no coupling.

In order to add coupling a tilt angle was applied to the last quadrupole before the extraction of the beam and the cross-plane beam angle is measured in the extraction point. Figures 5.3 and 5.4 show the percentage of vertical imaginary emittances as a function of the beam coupling at the entrance of the EXT line and the relative measurement error in the beam sizes. Each point has been calculated over 5000 measurements. Note the error axis limits and the fact that the beam size stability measurements gave a relative error of about 2%, never exceeding the 3% (see section 4.2).

The typical cross-plane angles after the DR extraction are around 1°[72] and hence the imaginary emittance ratio in our case would be of about a 20%. In the 2D emittance reconstruction the impact in the error range of the Multi-OTR is even lower.

The same kind of simulations have been made considering only one of the 4 OTRs in order to see the influence in the rejected measurements and the results for the 4D case are shown in Figure 5.5. There can be seen that the most sensitive to error is the

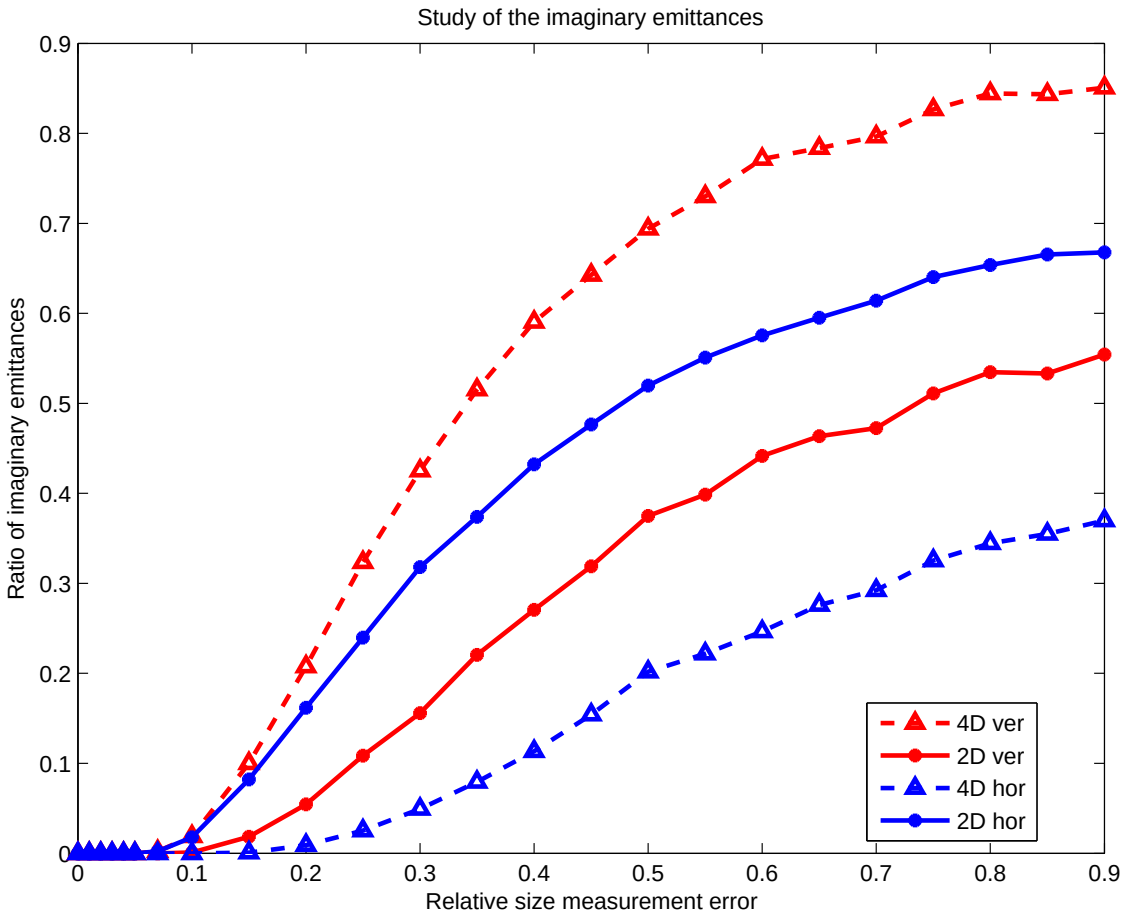

Figure 5.2: Ratio of imaginary emittances as a function of the relative measurement error.

OTR2X, which has the larger vertical β-function and is 48°away from the OTR0X. The less sensitive one is OTR1X, the one with the smallest β-function and separated 22°from the OTR0X.

Figure 5.6 shows the emittance, as the mean value over many measurements as a function of the relative measurement error. In the plot the imaginary emittances are not considered. Each point is the mean value calculated over 5000 measurements and the dotted lines are the one-sigma deviation. The dashed black line shows the input emittance of the beam. For the 2D case the curve takes a similar shape.

Taking the 2D emittances and assuming a relative error of 2% (as the stability measurements indicate) we have a distribution of vertical emittances as the one shown in Figure 5.7. In blue is shown the mean of the distribution while in red is the nominal emittance value. The relative error of these emittance measurements is 1.8%. In the next section this value is compared with the obtained from emittance stability measurements to conclude that it has good agreement.

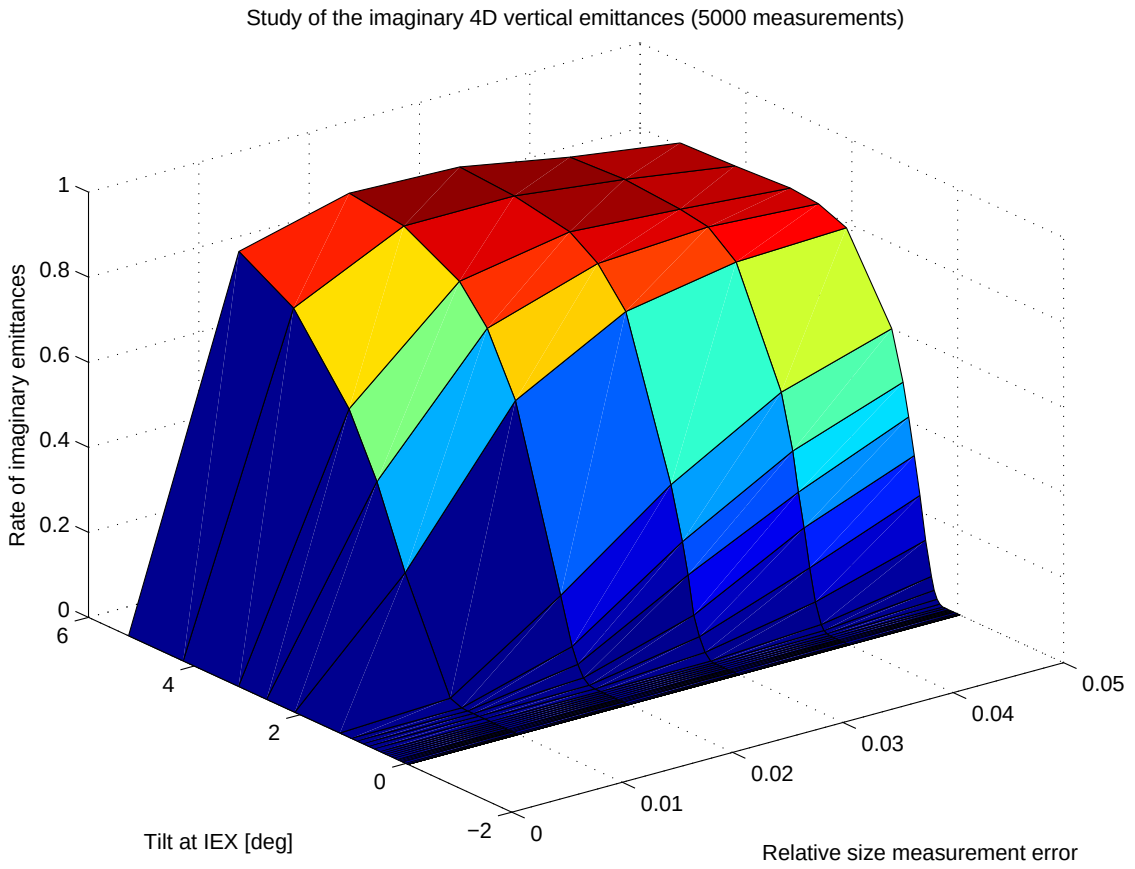

Figure 5.3: Ratio of imaginary 4D vertical emittances as a function of the beam tilt angle at the entrance of the EXT line and the relative measurement error.

5.3 Characterization of the system

The Multi-OTR emittance program, as it is installed in the ATF Control Software, calls the FS which executes the algorithm and returns back the measurements and the reconstructed emittance. The program has in account the dispersion at the OTR locations (previously measured by an existing FS routine) in order to subtract its contribution quadratically from the measured beam size. The algorithm needs as inputs the beam sizes at the OTR locations and the optics from an arbitrary point upstream, where the beam matrix will be reconstructed. In our case this point coincides with the OTR0X location.

Measurements have been done to compare the performance of both 2D and 4D emittance reconstruction methods in order to see the behavior when cross-plane coupling is introduced but have not been completely satisfactory for the 4D emittance case.The explanation of this effect should be further investigated and meanwhile 2D emittance reconstruction is routinely used with previous coupling correction (see Chapter 6) in order to make the 2D emittance coincide with the intrinsic one.

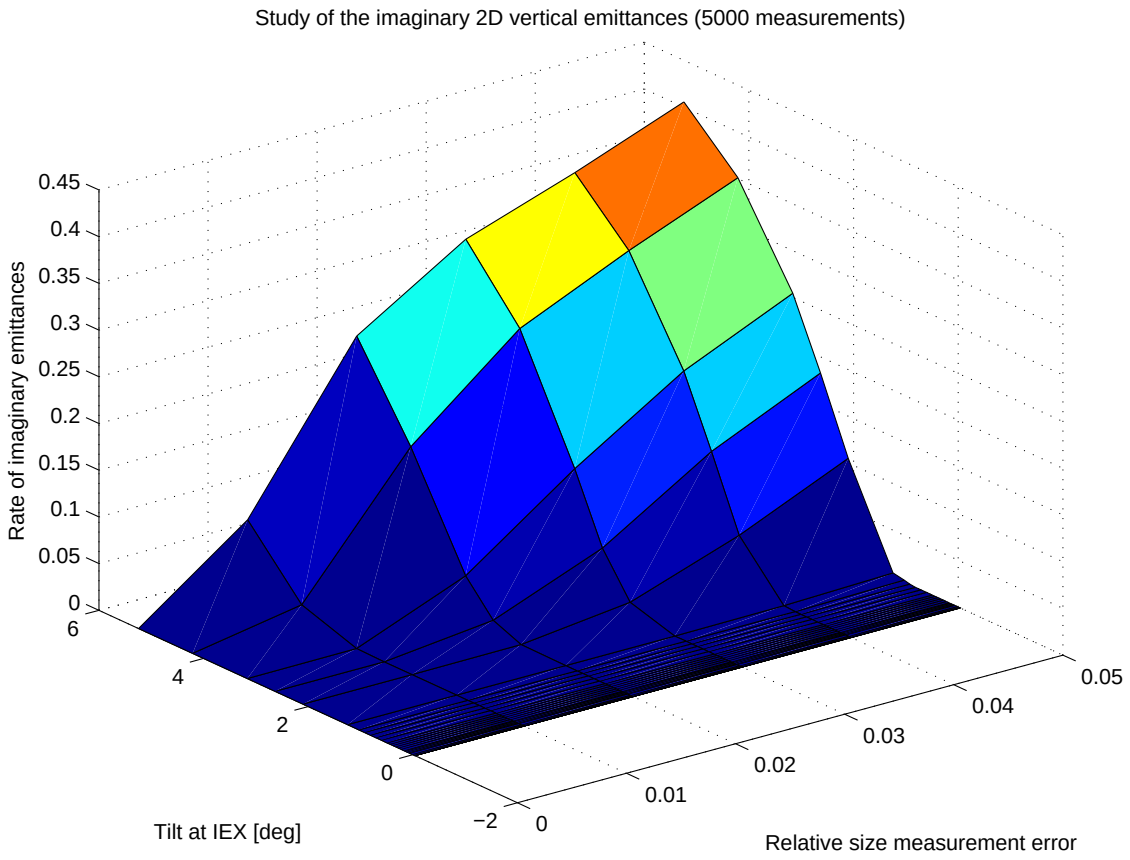

Figure 5.4: Ratio of imaginary 2D vertical emittances as a function of the beam tilt angle at the entrance of the EXT line and the relative measurement error.

Repeated measurements of the 2D emittance have been done in order to evaluate the stability and obtain an estimate of the statistical error. Figure 5.8 shows 15 measurements from 27th January 2012 in about 80 minutes. The standard deviation of the measurements is 1.5 pm·rad which means a relative error of about a 3%. This error is close to the predicted by simulations in last section. Another set of ten measurements was performed on 29th November 2012 and can be seen in Figure 5.9.

At the beginning of 2012 a growth in the beam size measurements of the last OTRs was observed. The beam size measured by a given OTR decreased when the upstream OTRs were moved to the non-measurement position (a clarifying sketch can be seen in Figure 3.14). This fact induced the idea that the measuring position of the OTRs provoked wake-fields which made the size grow downstream. An experiment measuring the size at OTR3X while moving OTR2X was done (the previous OTRs were in clear non-measurement position). In Figure 5.10 the effect on the horizontal and vertical beam size

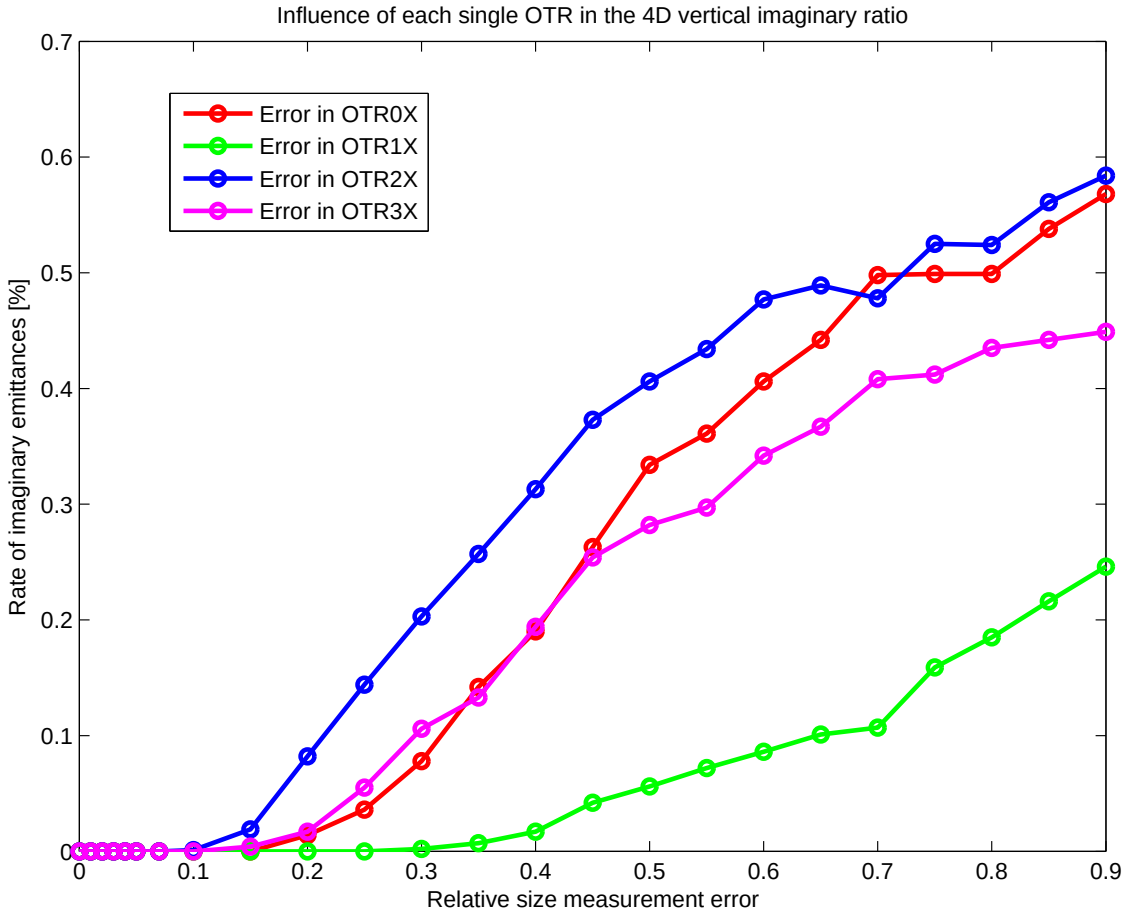

Figure 5.5: Ratio of imaginary 4D vertical emittances when only one OTR is considered to have measurement error.

of the vertical OTR1X and OTR2X positions can be seen. In the plot the position 0 corresponds to the measurement position and going to higher position means moving away from it, i.e. clearing the beam pipe. The results of the OTR2X lowering show that from 4 mm and further away the vertical beam size is lowered a 10%, which implies about a 20% decrease in the emittance. The OTR1X lowering presents a similar behaviour altough not so evident.

Among other factors, the creation of wake-fields in the OTRs themselves was useful to explain the vertical emittance growth that was observed after the DR. In fact, Figure 5.11 shows the evolution of the EXT line emittance as a function of the beam charge for different steps in the solution of the emittance growth: creation of a vertical bump to change the beam orbit, removing the second extraction kicker and solving the wake-field generation in the Multi-OTR system. As can be seen, this last step has a big influence in the emittance. The solution for the wake-field generation is done by removing the

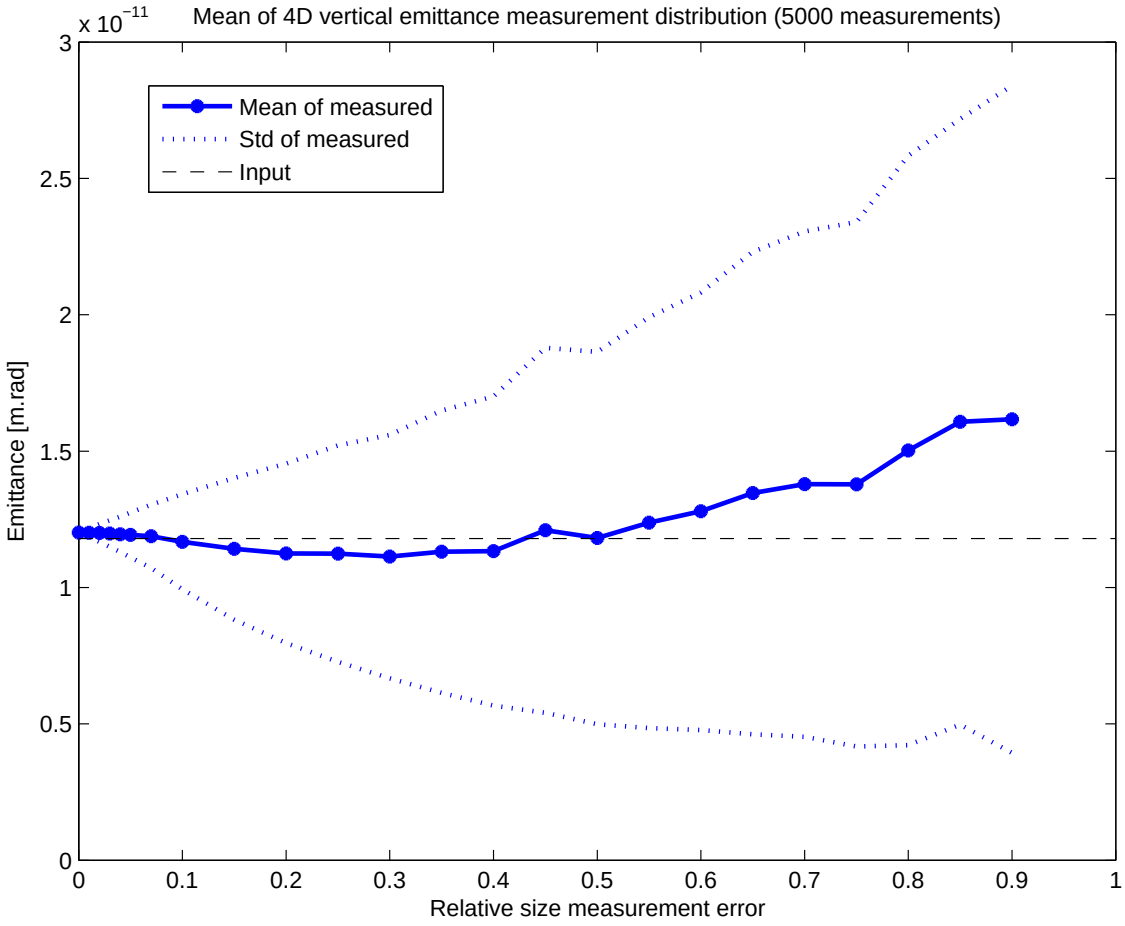

Figure 5.6: 4D emittance distribution over many measurements.

upstream OTRs in order to measure a given one. A hardware upgrade which enables to measure with all 4 OTRs in measurement position (and therefore to spare time) is under study and will imply changes the target and target holder design, as was introduced in Section 3.3.1.

5.4 Measurements

2D emittance measurements are being done since the installation of the Multi-OTR system. An example is shown in Figure 5.12. In the upper plots the beam size measurements are shown and compared with the model in order to see the agreement. The lower right window is the Emittance Panel itself and shows some information of the measurement that can be also found on the upper window. The vertical emittance comes out to be 33 pm·rad having a B_{mag} parameter of 1.17 which means an acceptable matching of the EXT line

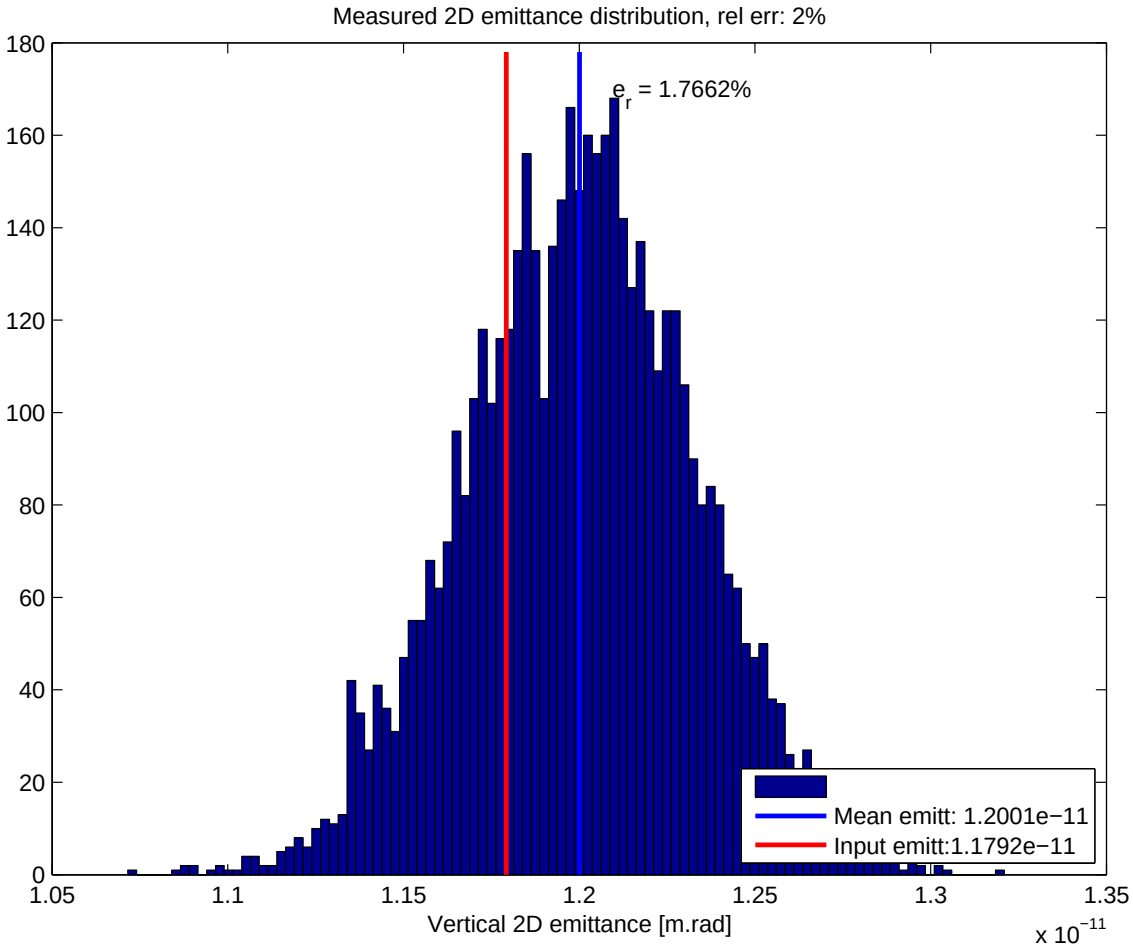

Figure 5.7: Histogram of measured emittances assuming a 2% beam size error. The relative error of the mean measured emittance with respect to the nominal one is shown.

optics with the DR extracted beam (more on this parameter in Section 6.1.5). The Twiss parameters at OTR0X are calculated from the reconstructed emittance and the measured beam sizes. Figure 5.13 shows another emittance measurement as an example.

Figure 5.14 shows measurements in the DR made by the XSR and in the EXT line made by means of the Multi-OTR system for 2011 and the first half of 2012. The lack of measurements after March 2011 is due to the Tohoku Earthquake and the two DR high measurements in June 2011 are part of the operation test after the quake. The very high emittance growth measured in the EXT line after the quake and until February 2012 was studied and partially solved as explained before (Fig. 5.11). After that the measurements are close to the DR ones but with a significant growth that should be still studied.

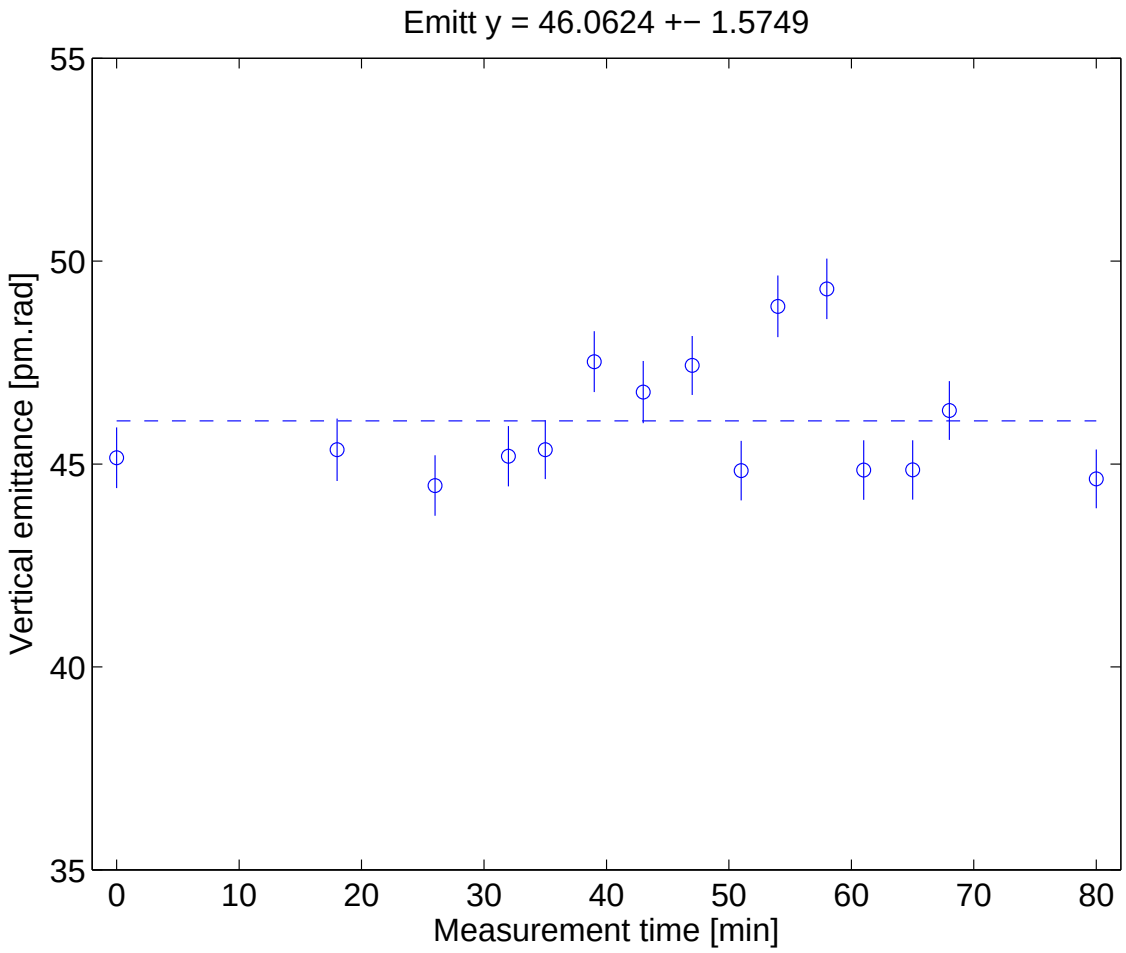

Figure 5.8: Emittance stability study. Data from 27th January 2012.

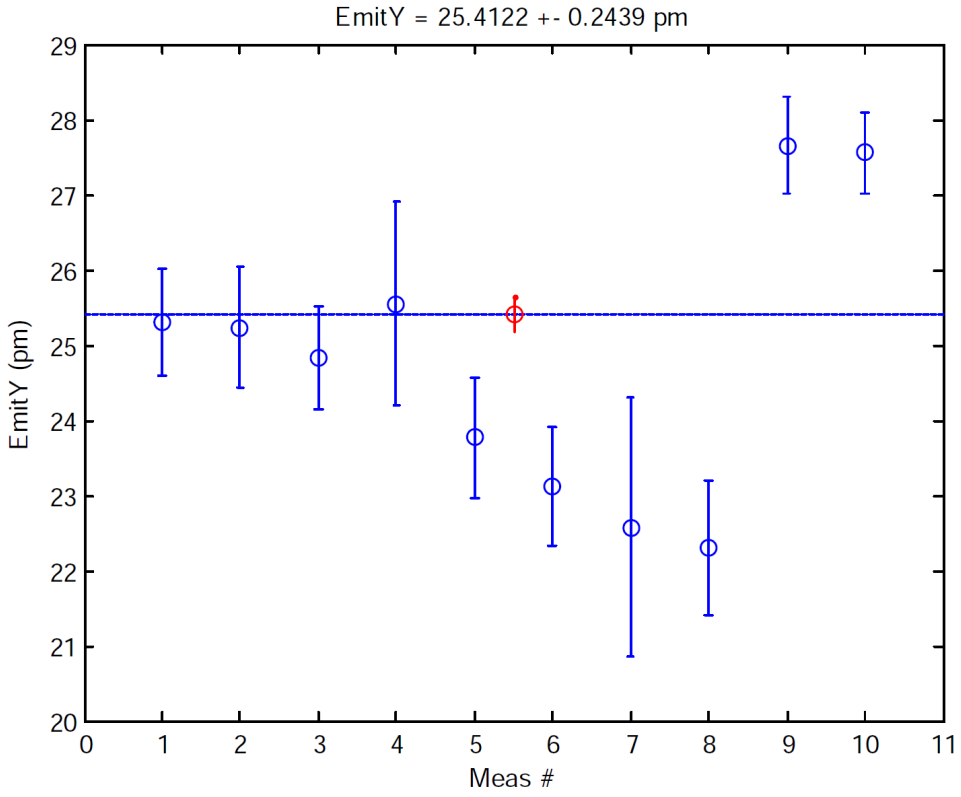

Figure 5.9: Emittance stability study. Data from 29th November 2012.

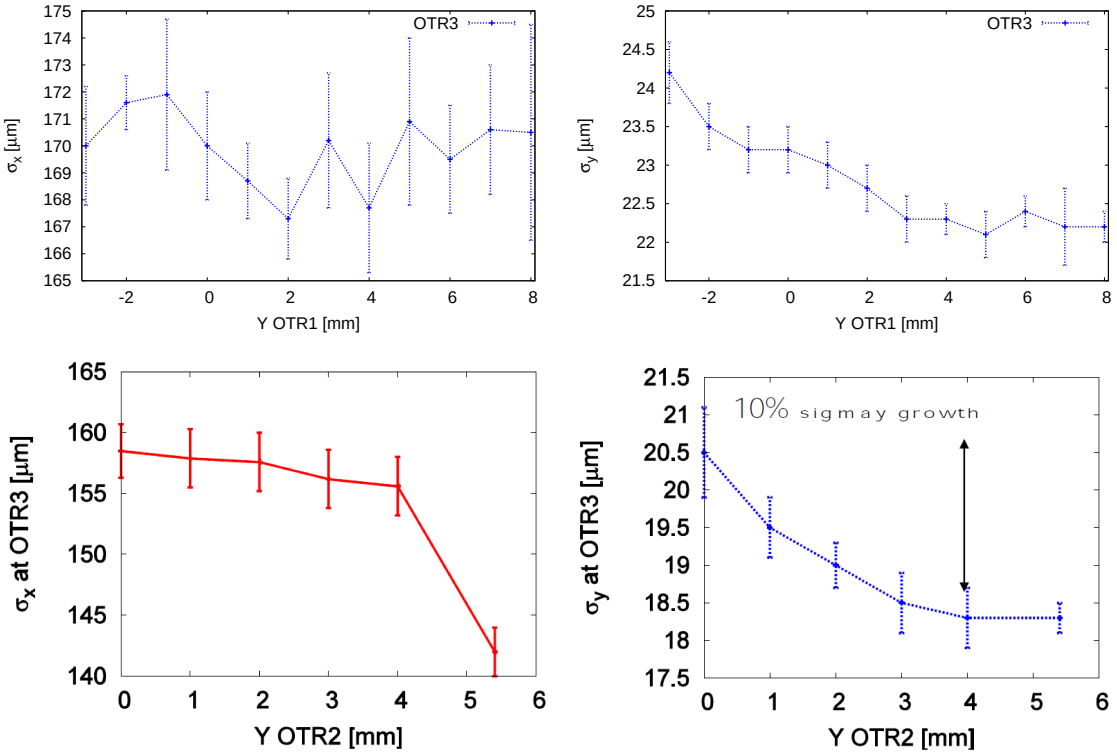

Figure 5.10: Study of the wake-field generation due to the Multi-OTR system itself. The plots below show the effect on OTR3X when OTR1X (top) and OTR2X (bottom) are lowered. Measurements taken on 13th Feb 2012.

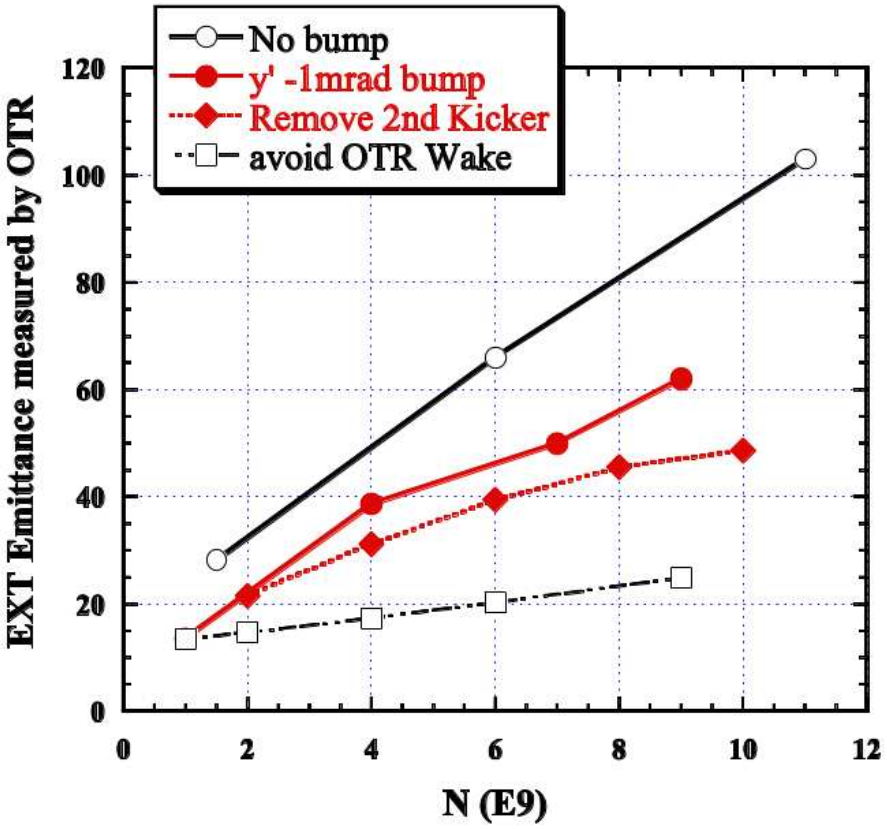

Figure 5.11: Emittance measurement in the EXT line as a function of the intensity for different steps to solve the vertical emittance growth. Courtesy of K. Kubo.

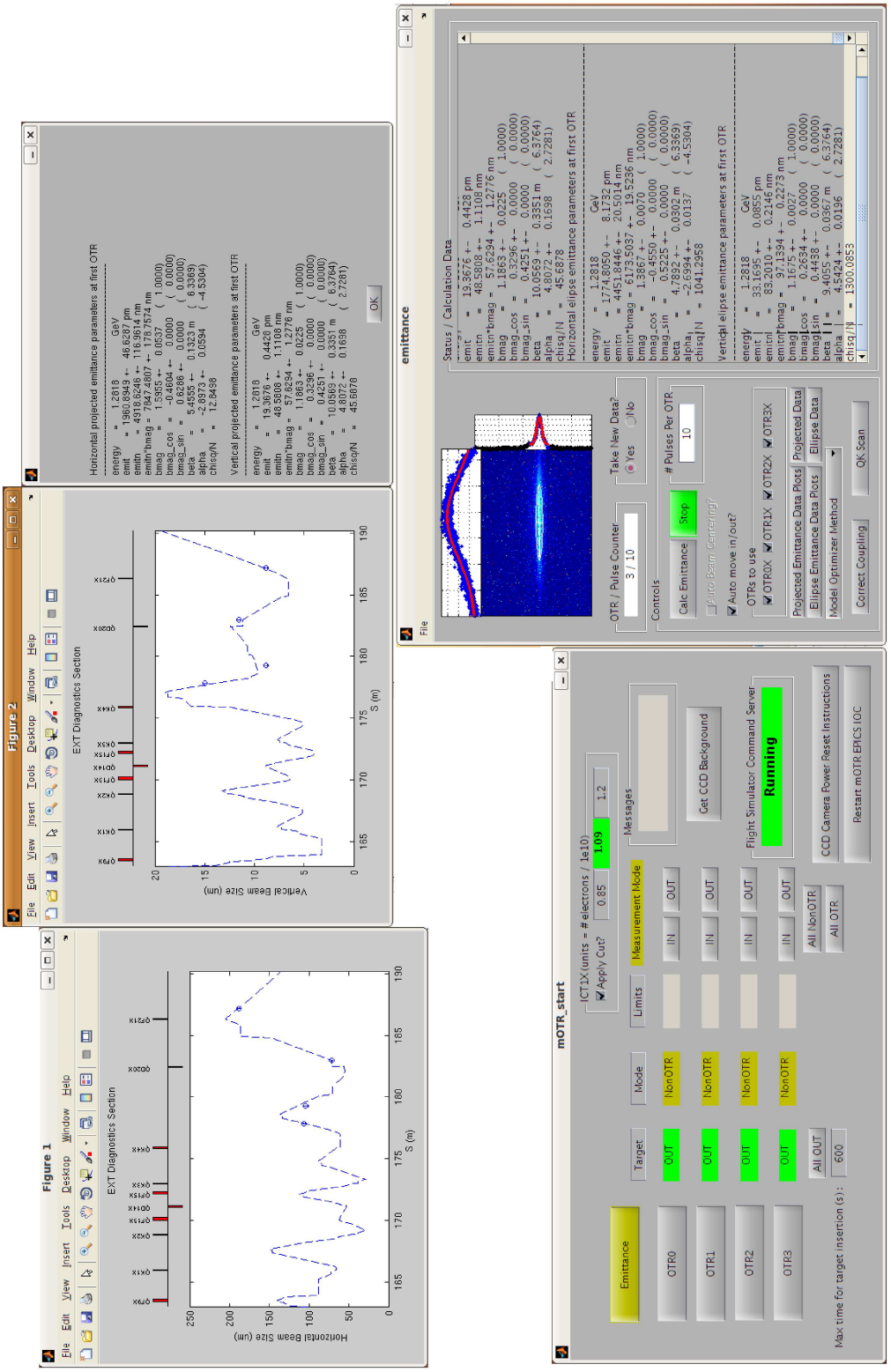

Figure 5.12: Emittance measurement performed on 8th February 2012.

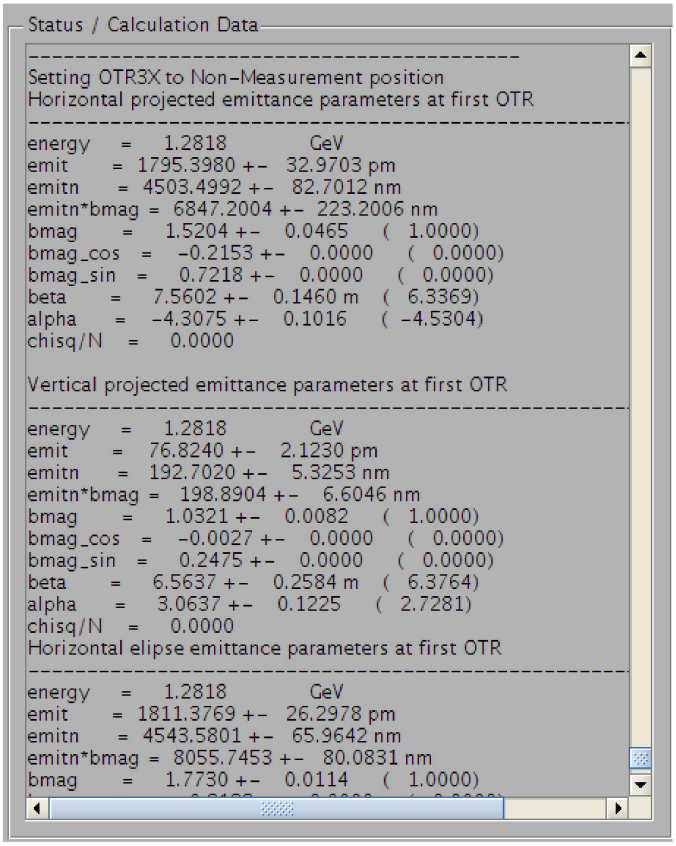

Figure 5.13: Emittance measurement performed on 6th March 2012.

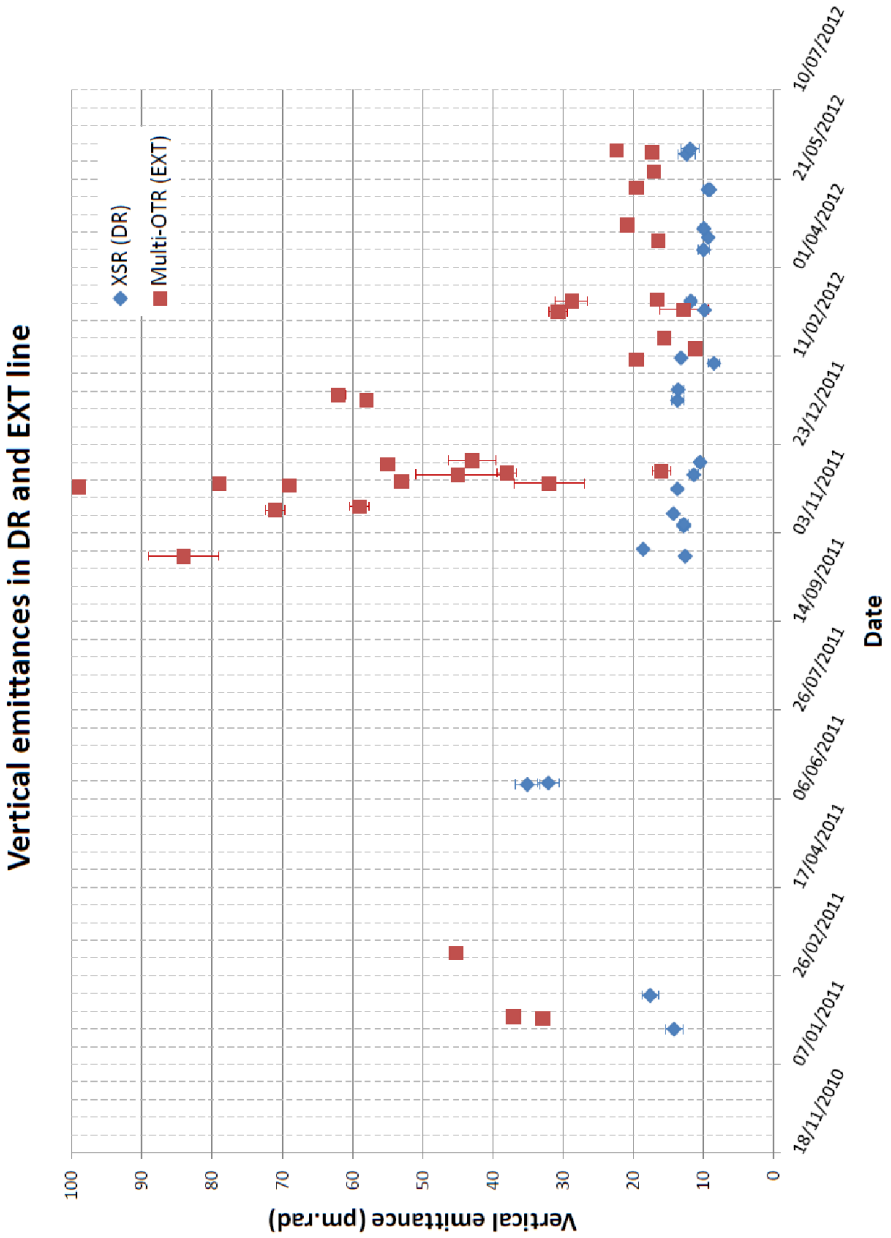

Figure 5.14: Comparison of DR and EXT line vertical emittance measurements during 2011 and half 2012.

Chapter 6

Other Multi-OTR studies

6.1 Coupling correction

6.1.1 Introduction

In the EXT line some coupling can be present due to different sources along the lattice such as roll misalignment and tilts in the quadrupole magnets and in other bending magnets, in $QS1X$ and $QS2X$ used to correct dispersion or in the extraction from the DR.

To parametrize this coupling the 4D beam matrix Σ is used. It is defined in terms of the second order moments of the phase space distribution $\Sigma_{ij} \equiv \langle x_i x_j \rangle$, where the indexes i and j run over the four phase space coordinates x, x', y and y' as

$$\Sigma = \begin{pmatrix} \langle x^2 \rangle & \langle xx' \rangle & \langle xy \rangle & \langle xy' \rangle \\ \langle xx' \rangle & \langle x'^2 \rangle & \langle x'y \rangle & \langle x'y' \rangle \\ \langle xy \rangle & \langle x'y \rangle & \langle y^2 \rangle & \langle yy' \rangle \\ \langle xy' \rangle & \langle x'y' \rangle & \langle yy' \rangle & \langle y'^2 \rangle \end{pmatrix}. \tag{6.1}$$

In the ideal case where no coupling is present the elements involving both vertical and horizontal components, i.e $\langle xy \rangle$, $\langle xy' \rangle$, $\langle x'y \rangle$ and $\langle x'y' \rangle$, will be zero and only the diagonal sub-matrices will have non-zero elements while in a real case also the coupling sub-matrix is going to have non-zero elements and thus some coupling will be present. See A for more information about the beam matrix.

The minimization of this coupling is crucial to preserve the emittance. In fact, if the beam is twisted by an angle ϕ and being the beam flat, then the vertical emittance grows by

$$\epsilon_y^2 = \epsilon_{x_0}^2 \sin^4 \phi + \epsilon_{y_0}^2 \cos^4 \phi + \epsilon_{x_0}\epsilon_{y_0} \cos^2 \phi \sin^2 \phi (\beta_x \gamma_y - 2\alpha_x \alpha_y + \beta_y \gamma_x), \tag{6.2}$$

where $\beta_{x,y}$, $\alpha_{x,y}$, $\gamma_{x,y}$ and ϵ_{x_0,y_0} are the beam Twiss parameters and initial beam emittances [73]. Assuming vertical and horizontal Twiss parameters of the same order, which is an acceptable assumption in a diagnostics section, the equation above can be approximated

by

$$\frac{\epsilon_y}{\epsilon_{y_0}} \approx \frac{\epsilon_{x_0}}{\epsilon_{y_0}} \sin^2\phi + \cos^2\phi, \tag{6.3}$$

and being in ATF the horizontal emittance around 200 times bigger than the vertical one, then a small 4 degree beam tilt leads to doubling the vertical emittance. An effort has to be made to correct even a small amount of coupling in order to maintain an acceptable level of emittance growth.

In ATF2 the coupling correction is an important step in the beam tuning procedure, which is the process of bringing the system to its design performance under realistic lattice error conditions. A coupling correction is to be made with the Multi-OTR in order to lower any eventual coupling generated in the extraction of the beam from the DR or in the EXT line. To illustrate this, figure 6.1 shows the iterative ATF2 FF tuning procedure applying different knobs, for example using skew quadrupoles in order to correct coupling or dispersion or moving spatially the sextupoles to the final scope of lowering the IP beam size to reach the 37 nm of Goal 1 (presented in 2.2). The round markers are real measurements while a green area shows the simulation over 100 machines. When the tuning knob iteration step grows, different parameters are minimized applying knobs. The order of these knobs and therefore the order of the tuning procedure was chosen by looking at which parameter contributed the most to the luminosity loss after a given minimization and selecting this parameter for the next step. As can be seen in the figure some coupling terms appear in the procedure and are to be minimized [74, 79].

In order to correct the coupling after the DR at the beginning of the EXT line, 4 skew quadrupoles are used. A skew quadrupole is a 45°tilted quadrupole that mixes both vertical and horizontal components. For our purposes, the simplest way to express the effect of such an element is in matrix notation

$$\begin{aligned} R_{skew} &\equiv R_{rot}(-45^\circ) \cdot R_{quad} \cdot R_{rot}(45^\circ) = \\ &= \begin{pmatrix} 1 & 0 & 0 & 0 \\ 0 & 1 & -kL & 0 \\ 0 & 0 & 1 & 0 \\ -kL & 0 & 0 & 1 \end{pmatrix} \end{aligned} \tag{6.4}$$

where kL is the strength of the quadrupole (assumed to be thin) and is definite positive for a horizontal-focusing element being the transfer matrix

$$R_{quad} = \begin{pmatrix} 1 & 0 & 0 & 0 \\ -kL & 1 & 0 & 0 \\ 0 & 0 & 1 & 0 \\ 0 & 0 & kL & 1 \end{pmatrix}, \tag{6.5}$$

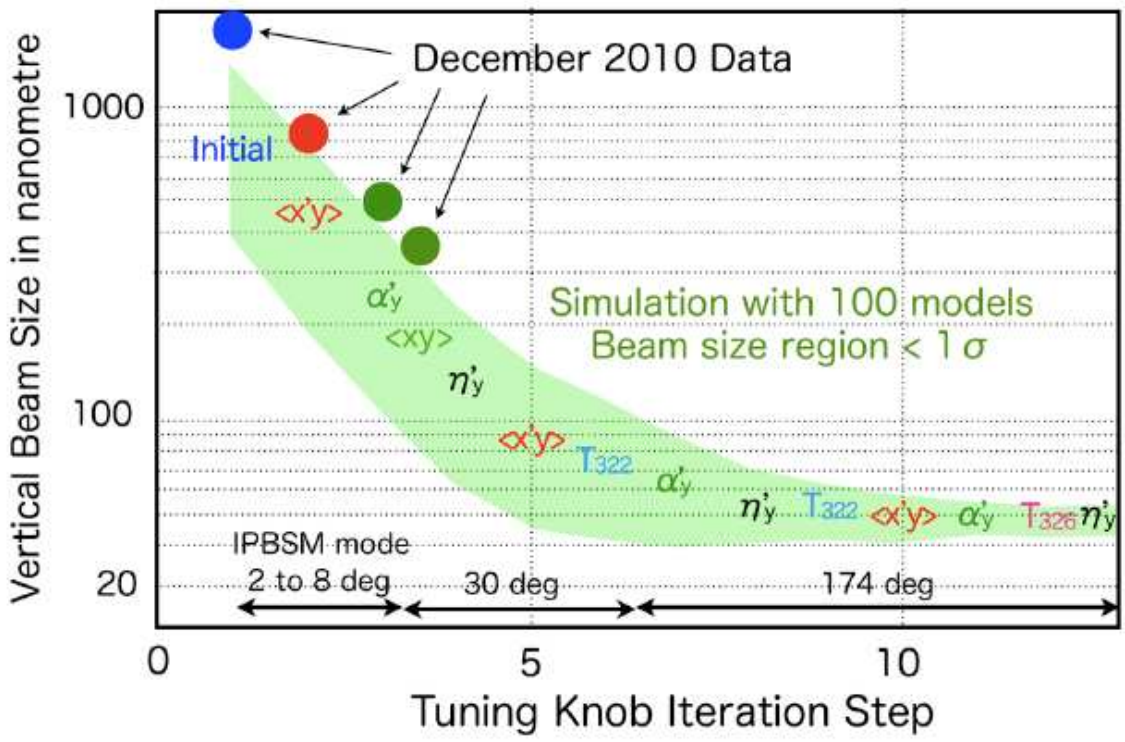

Figure 6.1: Tuning procedure to lower the beam size in ATF2 using sextupole knobs. Measurements and simulations. Courtesy of Glen White.

and R_{rot} a rotation matrix of the form

$$R_{rot}(\alpha) = \begin{pmatrix} \cos\alpha & 0 & \sin\alpha & 0 \\ 0 & \cos\alpha & 0 & \sin\alpha \\ -\sin\alpha & 0 & \cos\alpha & 0 \\ 0 & -\sin\alpha & 0 & \cos\alpha \end{pmatrix}. \tag{6.6}$$

From the structure of the result transfer matrix it is clear how the vertical and horizontal components are coupled and therefore the skew quadrupoles are usable elements to cancel the coupling terms.

In the diagnostics section of the EXT line, upstream of the Multi-OTR system, four skew quadrupoles named $QK1X$, $QK2X$, $QK3X$ and $QK4X$ are installed in a FODO lattice. Figure 6.2 shows a sketch of the diagnostics section of the EXT line highlighting the skews for coupling correction and the Multi-OTR system. The phase advances are $\Delta\mu_x = \Delta\mu_y = 90°$ between $QK1X$ and $QK2X$, $\Delta\mu_x = 180°$ and $\Delta\mu_y = 90°$ between $QK2X$ and $QK3X$ and finally $\Delta\mu_x = \Delta\mu_y = 90°$ between $QK3X$ and $QK4X$, as is shown in the figure 6.3. Due to this phase advance between them, if the first skew is able to control the xy phase, then the second controls the $x'y'$ phase, the third controls the $x'y$ phase and the fourth the xy' phase. This means that each skew quadrupole acts in a different phase and by installing them in such a location the four components of the transverse coupling can be zeroed. The skew quads in ATF2 can stand intensities in the range $I_{skew} = \pm 20\ A$ which means strengths in the range $kL = \pm 0.05\ m^{-1}$.

In this Chapter different algorithms to correct the coupling are presented first theoretically and then their performance is studied in simulations and measurements.

6.1.2 Motivation

In the past the coupling in the diagnostics section of the EXT line was corrected by means of five wire scanners (WS) scanning two skew quadrupoles [80] in intensities and trying to minimize the measured emittances (this is the reference method in ATF2 and will be explained later). As described in the Section 2.4.5 the WS presented some issues regarding a size measurement overestimation due to the fact that the wire passes through several bunches integrating the bunch-to-bunch jitter. Moreover the procedure was extremely slow and took an entire 8-hour shift due to the multiple emittance measurements that were needed. Figure 6.4 shows an example of a coupling correction done with the WS. The vertical beam size is measured for different $QK1X$ strengths and the minimum is found [81].

For the exposed reasons it was interesting to develop a faster and automated method to make this procedure lighter. Once the Multi-OTR system has been installed it has been used for this purpose. There is the possibility of using the same procedure to correct the coupling as the one used with the WS, being even in this case a less time-consuming correction. An automated coupling correction algorithm which uses a response matrix

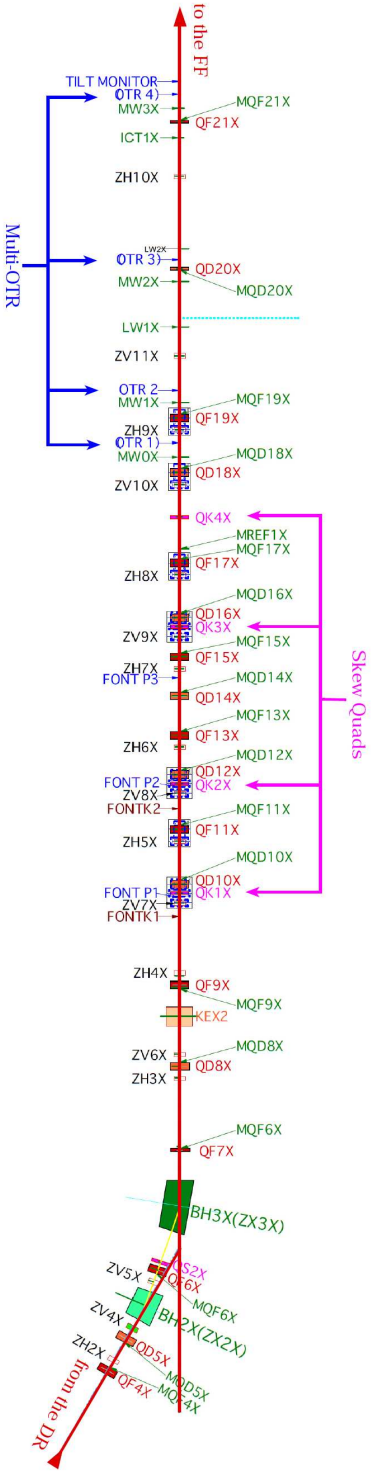

Figure 6.2: Diagnostic section of the EXT line, where the skew quadrupoles for coupling correction and the Multi-OTR system are installed. Beam direction from right to left.

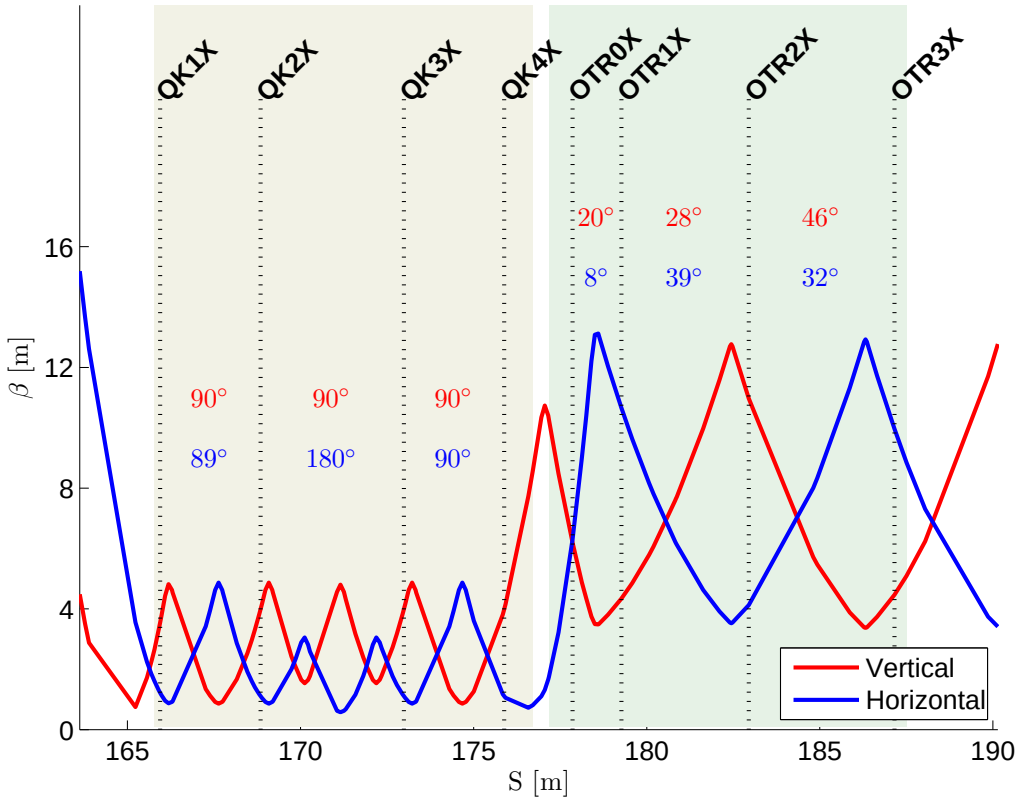

Figure 6.3: Vertical and horizontal phase advances and beta functions in the coupling correction region and in the emittance measurement region in the EXT line of ATF2.

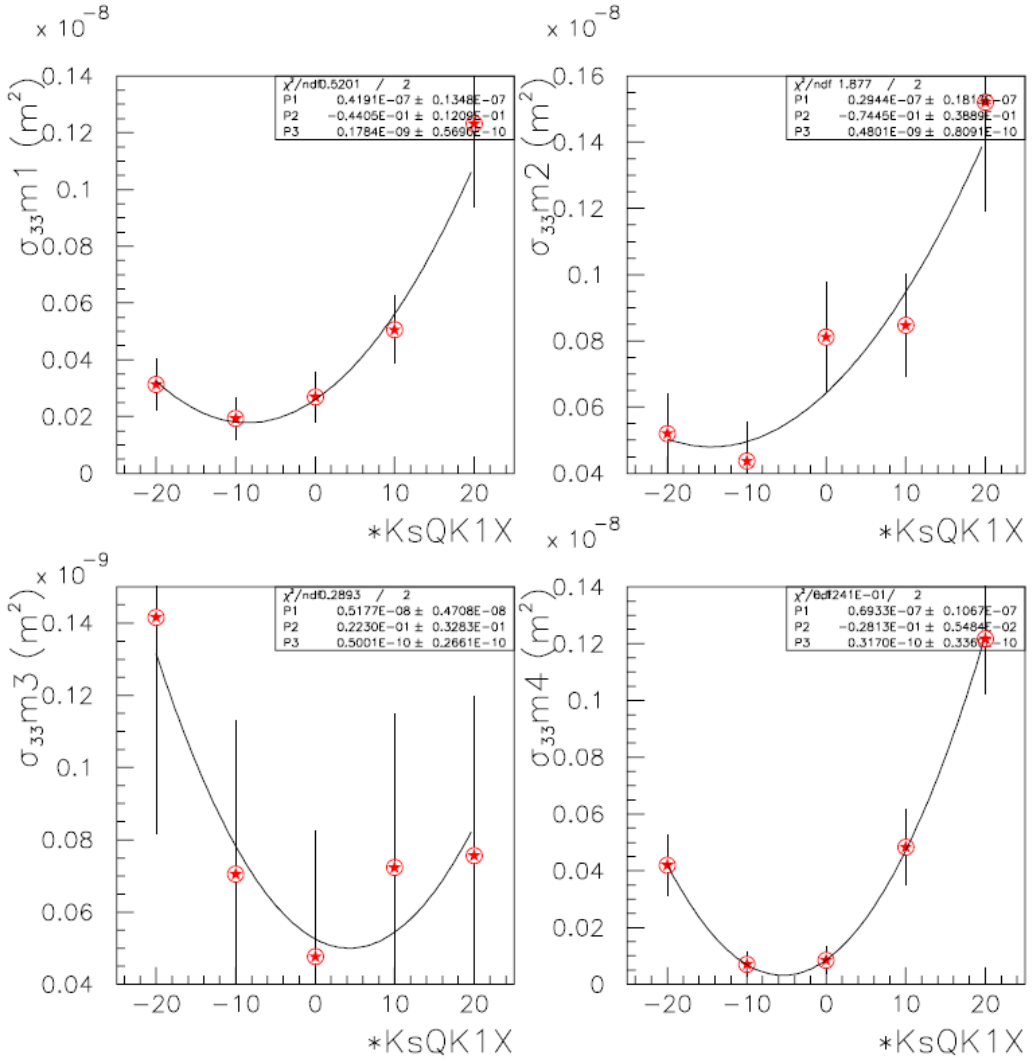

Figure 6.4: Coupling correction with the WS. Courtesy of C. Rimbault.

in order to calculate the needed strengths in the skew quadrupoles has been developed and will be explained in this Chapter. A proposal to correct the coupling using the reconstructed full 4D emittance beam matrix is also presented.

6.1.3 Algorithm comparison

The first algorithm presented is the one used normally with the WS and now being used with the OTRs and consists basically in scanning a skew quadrupole and finding the intensity that minimizes the vertical emittance. A response-matrix-like automated procedure which is installed and working under some conditions will be presented as well. Finally an algorithm that uses the information of the full 4D beam matrix is shown.

Scan method

As it happens in an non-tilted quadrupole the effect of a skew quadrupole in the beam matrix element $\langle y^2 \rangle$ (i.e. the beam size squared) after a drift space of length l behaves quadratically with kL, the strength of the skew. In fact, when one transports a beam matrix through them

$$\Sigma^{end} = R_{drift} \cdot R_{skew} \cdot \Sigma \cdot (R_{drift} \cdot R_{skew})^{\top}, \tag{6.7}$$

the vertical spatial element of Σ^{end} as a function of l and kL come to be

$$\begin{aligned} \langle y^2 \rangle^{end} \equiv \sigma_{33}^{end} &= (kL)^2 \cdot l^2 \sigma_{11} + kL \cdot 2l(l\sigma_{14} + \sigma_{13}) + \\ &\quad + l^2 \sigma_{44} + 2l\sigma_{34} + \sigma_{33} \end{aligned} \tag{6.8}$$

where the notation σ_{ij} is used for the elements of the beam matrix Σ.

Being $\langle y^2 \rangle$ directly related with the OTR measurements and due to its quadratic behavior with kL one can look for its minimization.

Experimentally this method consists in scanning each single skew quadrupole in intensities and adjust then a parabola to find the optimal intensity that minimizes either the vertical emittance or the projected vertical beam size (choosing in this case for convenience the OTR where the beam spot looks more tilted). Figure 6.5 shows a simulated parabola for a skew scan. This procedure is repeated for all the 4 skew quadrupoles one after the other. Since the effect of the skew quadrupole is a kind of rotation of the beam in the transverse plane it is easy to understand how in order to cancel the coupling, one must recover again the ideal flat non-tilted beam, which means in practice to find the minimum projected vertical emittance (i.e. the minimum projected vertical beam size).

Response matrix method

Assuming the nominal lattice one can simulate a beam passing through it and look how the OTR observable $\langle xy \rangle$ change as a single skew strength changes. When transporting

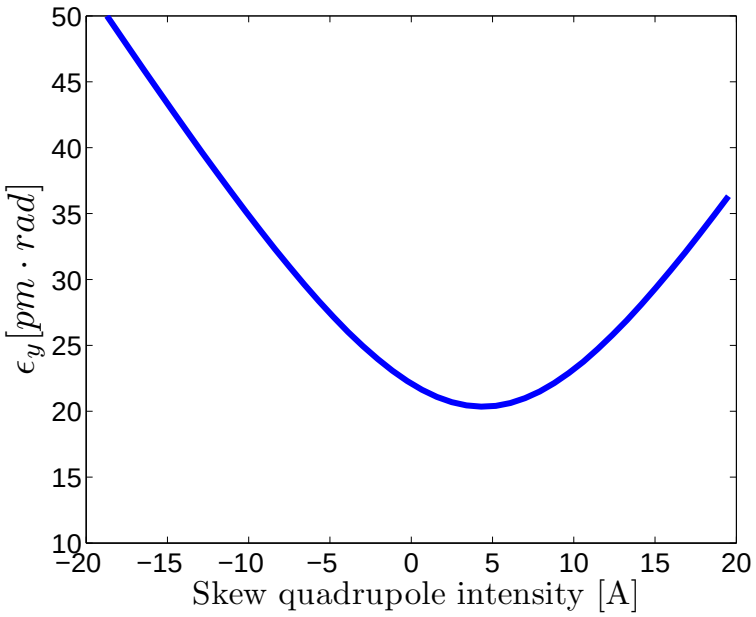

Figure 6.5: Simulation of a skew scan for coupling correction. The input beam has some initial coupling and therefore the parabola minimum is off-centered leading to an optimal intensity around 5 A.

the beam matrix through a skew quadrupole and a downstream drift space [1] as done in (6.7) the spatial coupling term comes out to be

$$\begin{aligned} \langle xy \rangle^{end} \equiv \sigma_{13}^{end} &= (kL)^2 \cdot l^2 \sigma_{13} - \\ &\quad -kL \cdot l(l(\sigma_{12} + \sigma_{34}) + \sigma_{11} + \sigma_{33}) + \\ &\quad +l(l\sigma_{24} + \sigma_{23} + \sigma_{14}) + \sigma_{13} \end{aligned} \tag{6.9}$$

which behaves quadratically with the skew quad strength. However being the quadratic term proportional to σ_{13} and having a linear term with σ_{11} (which is for a moderate beam tilt angle some orders of magnitude bigger than σ_{13}) and knowing that typical strength values are about $kL \approx 0.05m^{-1}$ a linear approximation of the whole dependence is not absurd.

It is possible then to track in simulation a realistic beam through the lattice for the 4 skew quads scanning different intensities, looking for the response (i.e. the coupling term) in the 4 OTRs and fitting linearly for each couple skew-OTR. A Response Matrix C is built, and each term (i, j) of it is then the linearly fitted coefficient that relates the skew j with the coupling term $\langle xy \rangle$ measured at OTR i, it means, the Response Matrix is a Jacobian matrix with elements $C_{ij} = (\frac{\partial \langle xy \rangle_i}{\partial I_j})$. Fig. 6.6 shows as an example one of the

[1] A more general case for the beam matrix elements, where instead of a drift space an arbitrary transport matrix is placed after the skew can be seen, for example, in [75].

linear fits used to build the matrix. For the algorithm to work, any number m of skews and any number n of OTRs can be used, and C will be in general an $n \times m$ matrix. However, as it is installed in the ATF Control Room the routine foresees all 4 skews working and a minimum of 3 of the 4 OTRs operating.

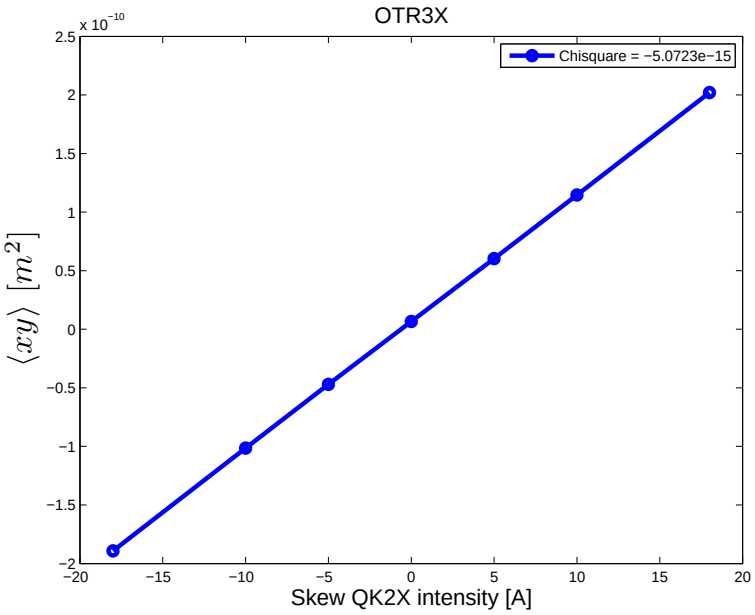

Figure 6.6: Linear fit used to build the Response Matrix. The $\langle xy \rangle$ term measured at $OTR3X$ is plotted as a function of the $QK2X$ intensity.

Once C has been built

$$\begin{pmatrix} \langle xy \rangle_{OTR0} \\ \langle xy \rangle_{OTR1} \\ \langle xy \rangle_{OTR2} \\ \langle xy \rangle_{OTR3} \end{pmatrix} = \begin{pmatrix} C_{11} & C_{12} & C_{13} & C_{14} \\ C_{21} & C_{22} & C_{23} & C_{24} \\ C_{31} & C_{32} & C_{33} & C_{34} \\ C_{41} & C_{42} & C_{43} & C_{44} \end{pmatrix} \cdot \begin{pmatrix} I_{skew1} \\ I_{skew2} \\ I_{skew3} \\ I_{skew4} \end{pmatrix}, \tag{6.10}$$

it is possible to obtain the intensity correction for a real coupled beam first by measuring the coupling terms with the OTRs and then using the pseudo-inverse of the C matrix

$$\begin{pmatrix} I_{skew1} \\ I_{skew2} \\ I_{skew3} \\ I_{skew4} \end{pmatrix} = pinv \begin{pmatrix} C_{11} & C_{12} & C_{13} & C_{14} \\ C_{21} & C_{22} & C_{23} & C_{24} \\ C_{31} & C_{32} & C_{33} & C_{34} \\ C_{41} & C_{42} & C_{43} & C_{44} \end{pmatrix} \cdot \begin{pmatrix} \langle xy \rangle_{OTR0} \\ \langle xy \rangle_{OTR1} \\ \langle xy \rangle_{OTR2} \\ \langle xy \rangle_{OTR3} \end{pmatrix}. \tag{6.11}$$

This technique permits several iterations in order to make it converge. The algorithm, as it stands, cancels the $\langle xy \rangle$ terms in the OTRs but as is shown in Fig. 6.3 the phase advance between the OTRs is not optimized because their location was forced by the

available physical space in the beam line and it does not have the same structure as the phase advance in the skew quadrupole region (i.e. each OTR is not in a different phase corresponding to $\langle xy \rangle$, $\langle x'y' \rangle$, $\langle x'y \rangle$ and $\langle xy' \rangle$) so, in principle, it is possible to have a residual coupling after the OTRs region. A different and optimal location in this sense for each single OTR could be found.

Solve transport matrix method

As explained in section 5.1 the Multi-OTR system allows a reconstruction of the full beam matrix Σ at some position assuming a non-coupling lattice between this point and the OTR region. If the skew quadrupoles are switched off (no intensity through them) the beam matrix can be reconstructed upstream and then it can be propagated mathematically downstream to the OTRs using the ideal lattice

$$\Sigma^d = R_{u\to d} \cdot \Sigma^u \cdot R_{u\to d}^T, \tag{6.12}$$

where the indexes u and d mean *upstream* and *downstream*. The transport matrix $R_{u\to d}$ is built as an explicit function of the skew quad strengths

$$R_{u\to d} = (R_{4\to d} \cdot R_{skew4} \cdot R_{3\to 4} \cdot R_{skew3} \cdot R_{2\to 3} \cdot R_{skew2} \cdot R_{1\to 2} \cdot R_{skew1} \cdot R_{0\to d}). \tag{6.13}$$

The result will be a downstream beam matrix with elements function of the 4 skew strengths.

$$\Sigma^d = \begin{pmatrix} \sigma_{11}^d & \sigma_{12}^d & \sigma_{13}^d & \sigma_{14}^d \\ \sigma_{12}^d & \sigma_{22}^d & \sigma_{23}^d & \sigma_{24}^d \\ \sigma_{13}^d & \sigma_{23}^d & \sigma_{33}^d & \sigma_{34}^d \\ \sigma_{14}^d & \sigma_{24}^d & \sigma_{34}^d & \sigma_{44}^d \end{pmatrix}. \tag{6.14}$$

Our interest is to constrain the four coupling terms of the beam matrix σ_{13}^d, σ_{14}^d, σ_{23}^d and σ_{24}^d to be zero. It is possible then to solve the 4 equation system obtaining 4 skew strengths that fulfill the non coupling condition.

$$\sigma_{ij}^d = f(kL_1, kL_2, kL_3, kL_4) = 0 \quad \text{for} \quad \begin{matrix} i = \{1,2\} \\ j = \{3,4\} \end{matrix}. \tag{6.15}$$

The Matlab function *solve* is used for this calculations, allowing to constrain an output within the skew strength limits. Since initially the algorithm assumes no intensity in the skews this is not an iterative procedure, thus no convergence can be found step by step. This added to the fact that it uses for calculation the nominal optics could lower the robustness of the method.

Other proposals

Other ideas have been proposed in order to correct the coupling. One of them uses a non-linear solver function (lsqnonlin in Matlab) in order to create a Lucretia beam that

reproduces the measurements at the OTR positions. Once one has the model beam and using the same non-linear solver the optimal skew quadrupole intensities are obtained. This method can take some minutes while performing the calculations and has demonstrated a good performance in simulations. It has not yet been used in ATF2.

6.1.4 Simulation comparison

Simulations comparing the three methods presented were carried out. The coupling at the entrance of the EXT line was introduced by slightly tilting the last quadrupole of the DR, called $QM5R1$. The coupling could be introduced directly when populating the beam or rotating and mixing the spatial and angular components but tilting a quadrupole is a simple way to introduce realistic coupling. Figure 6.7 shows the spatial tilt angle of the beam at the entrance of the EXT line (IEX marker), at the $OTR0$ and at $MSPIP$, the screen profile monitor just after the IP, as a function of the $QM5R1$ tilt angle.

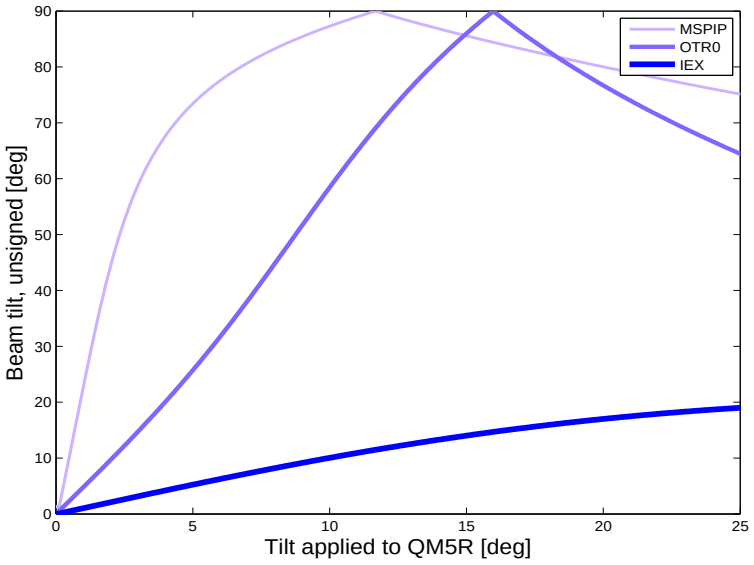

Figure 6.7: Coupling generation for simulations. Beam tilt in different positions as a function of $QM5R1$ quadrupole angle.

Figure 6.8 shows the results of the coupling correction algorithm comparison simulations. The transverse beam tilt at $MSPIP$ is plotted against the beam tilt at the entrance of the EXT line. The thick black line corresponds to the case when no correction is applied, while the thick colored lines correspond to the three coupling correction methods, neglecting in these cases any measurement error. It is to be noted that here, the response matrix algorithm has been programmed to make only one iteration, but in a real case the performance would be better increasing the number of iterations.

The crosses with error bars are the results of the simulation when measurement errors are included. There have been considered two sources of errors: one is a size measurement error which has been set to be gaussian with standard deviation 2% of the beam size and the other is a tilt in the reference system simulating a tilt in the OTR optics and the CCD camera which has been assumed to be uniformly distributed in the range $[-1°, 1°]$. The different methods for coupling correction with errors have been simulated 100 times and the crosses show the mean values of the angle at $MSPIP$ being the error bars their standard deviation (in order to clarify the plot, these bar have been shifted a little and separated one from the other). The input tilt angle has been limited to 1°, being this a realistic value for the extraction from the DR. It is to be noted that only measurement errors have been included, while no errors in the lattice are present. It means that, while the plot is illustrative to see the performance of each algorithm it doesn't show the model-dependence of the two last methods.

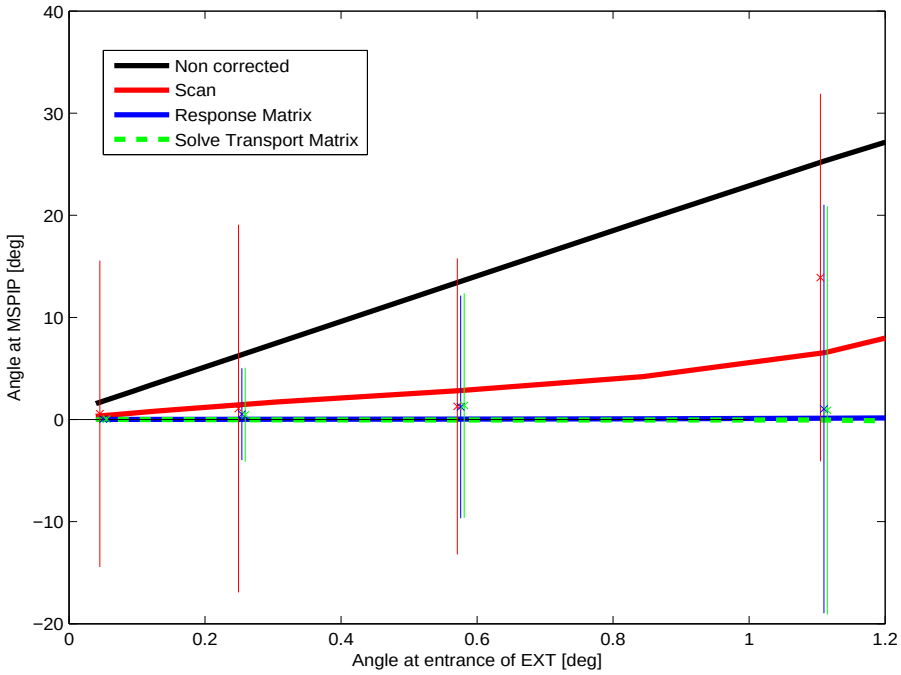

Figure 6.8: Simulation of the coupling correction with three different methods.

In simulation, the model-dependent algorithms show better behavior than the scan method, and the coupling is practically canceled at $MSPIP$. When measurement errors are included, the result is still consistent but the standard deviation is rather high for high angles. The behavior of the response matrix and the solve transport matrix method for higher angles are shown in figures 6.9 and 6.10. The angle windows for an acceptable correction are around $[-5°, 5°]$ for the response method and around $[-1.5°, 1.5°]$ for the solve transport matrix method, when no measurement error is taken in account. The Table

6.1 shows the transverse beam profiles and their corrections with the response matrix method for three different input angles at the entrance of the EXT line. The first column is just an index for the input angle, the second column states whether the profiles are coupling corrected or not, the third, fourth and fifth column shows the beam plots in the entrance of the EXT line, in OTR0X location and in the $MSPIP$ monitor respectively, and below them the tilt angle in degrees.

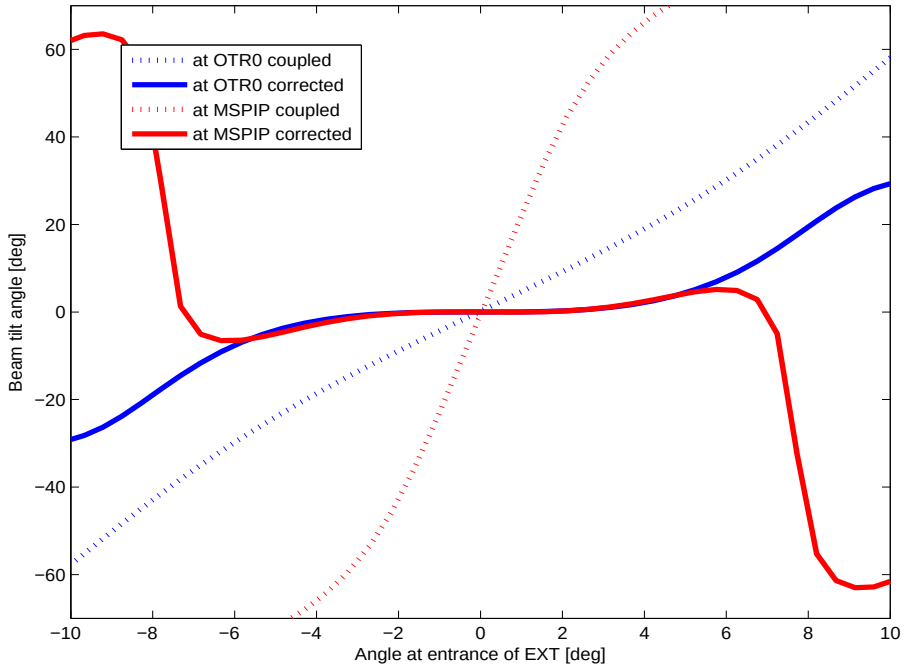

Figure 6.9: Simulation of coupling correction with the response matrix method.

6.1.5 Measurement comparison

Scan method

The scan method has been used since 2011 and has become a part of the routine for normal operation beam tuning. As it was explained it consist of scanning each single skew quadrupole sequentially. Plotting the vertical emittance versus the intensity will produce a parabola where the optimal intensity is the one which minimizes the emittance. In order to speed up the process, the coupling can be corrected by looking not at the vertical emittance but just at the vertical beam size in only one OTR, preferably the one with bigger size and more sensible to changes.

When a beam is extracted from a DR and injected into a transport line such as ATF2, any mismatch in the Twiss parameters between the extraction and the transport line can cause filamentation of the beam and this will increase the emittance until it reaches its last

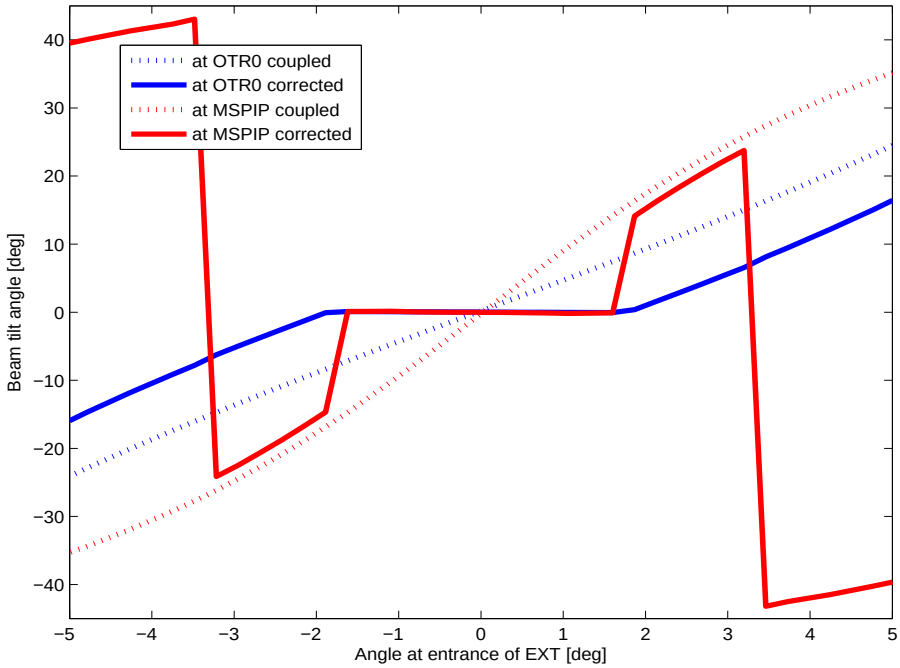

Figure 6.10: Simulation of the coupling correction with the solve transport matrix method.

value $\epsilon_{filamented} = \epsilon_D \cdot B_{mag}$. The B_{mag} parameter is the so called *mismatch parameter* ([76] and Section 4.2 in [77]) and it is a measure of how well the optics in the transport line are matched with the out-coming beam. It can be calculated by measuring the Twiss parameters and comparing them with the design ones (here written with the sub-index D)

$$B_{mag} = \frac{1}{2}(\beta\gamma_D - 2\alpha\alpha_D + \beta_D\gamma). \tag{6.16}$$

The identity $\epsilon_{filamented} = \epsilon_D \cdot B_{mag}$ only holds for perfect measurements and the only source of emittance growth coming from beta mismatch and then for a perfect matched beam the mismatch parameter would be 1. However the existence of non-gaussian elements of the beam and measurement errors and other aberrations etc causes this not to be so. Sometimes in the measurements the vertical emittance parabola against the intensity is not very clear in order to be fitted and thus the parameter to tune on is normally the product $\epsilon_{y_{measured}} * B_{mag}$ which shows a parabolic behavior better for a fit [82].

A set of measurements for a coupling correction using 3 OTRs was made on November, 6th 2011 shift. First of all the skew quadrupole intensities were set to 0 A, then $QK1X$ was scanned in intensities measuring $\epsilon_y \cdot B_{mag}$ for each point, the resulting parabola was fitted and the optimal intensity was found. This procedure was repeated for the remaining 3 skews in order leading to the parabolas in figure 6.11 and to the intensities shown in Table 6.2. One can see that for the first skew the parabola fits an intensity beyond the

Input	Correction	EXT begin	OTR0X	MSPIP
1	Off	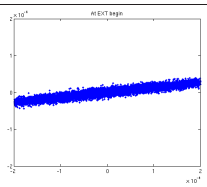	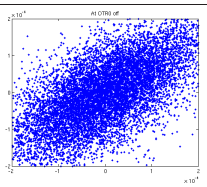	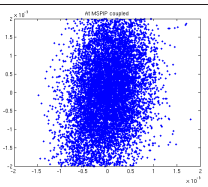
		7.73	41.46	82.05
	On		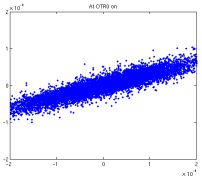	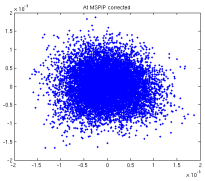
			17.63	-32.46
2	Off	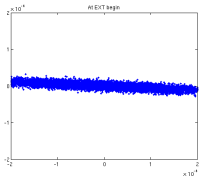	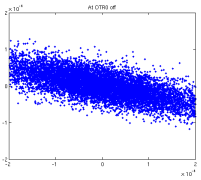	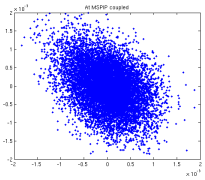
		-3.24	-14.79	-59.50
	On		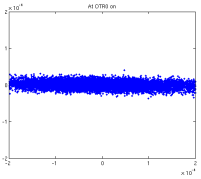	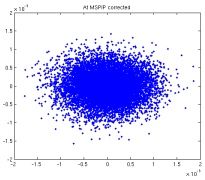
			-1.04	-1.53
3	Off	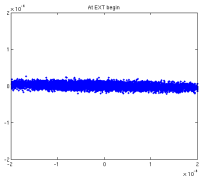	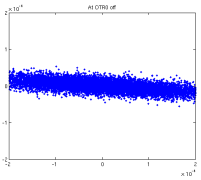	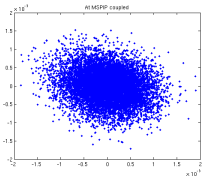
		-1.11	-4.82	-25.34
	On		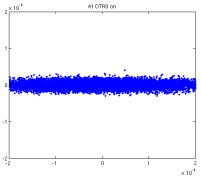	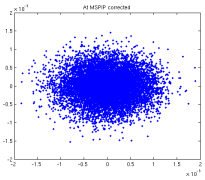
			-0.03	-0.03
		[deg]	[deg]	[deg]

Table 6.1: Coupling correction with the response matrix method.

± 20 *A* limits, in fact being this method sequentially, it does not obtain a pondered solution having in account the 4 skews globally but instead of that if the coupling is considerable

it tends to push the first scanned skew to its limit harder than the consecutive ones.

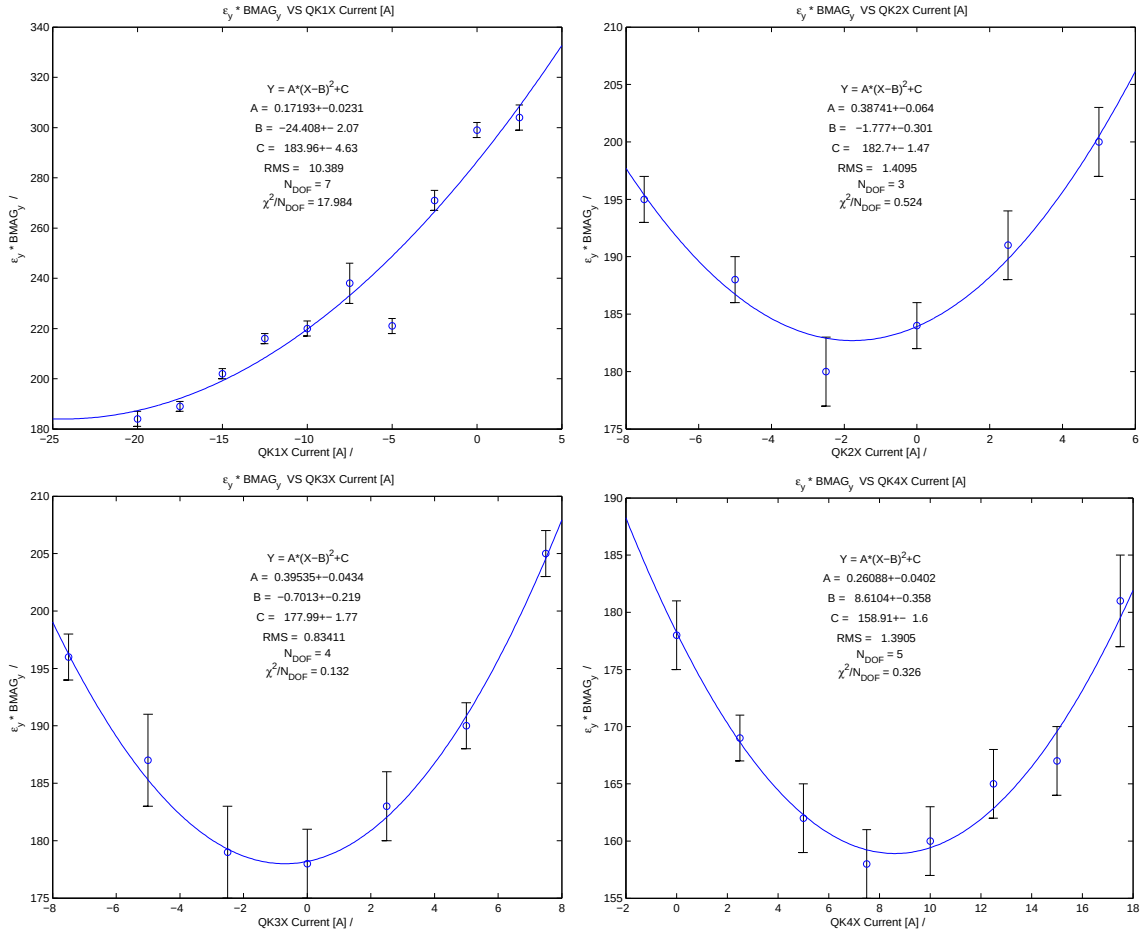

Figure 6.11: Fitted parabolas during a scan coupling correction on November, 6th 2011. The optimal intensity at the minimum of the emittance is given by the B parameter of the fit.

The correction takes typically from half to one hour to be completed. After that, in our example, the emittance lowered from $\epsilon_y = 100\ pm \cdot rad$ to $\epsilon_y = 62\ pm \cdot rad$. Table 6.3 shows the emittances and mismatch parameters before and after the correction.

Another correction done in January 2012 can be seen in figure 6.12 where by setting the skew intensities to -20 A, 8.0 A, 4.5 A and 5.2 A the vertical emittance was reduced from 130 $pm \cdot rad$ to 65 $pm \cdot rad$.

Since the algorithm does not make use of any design or ideal model to predict the correction but uses the real beam-line it is rather robust and it finds an acceptable solution provided that it is within the skew intensity limits. It is nonetheless the slower of all

	I_{QK1X} [A]	I_{QK2X} [A]	I_{QK3X} [A]	I_{QK4X} [A]
Before	0	0	0	0
After	-20	-1.8	-0.7	8.6

Table 6.2: Skew quadrupole intensities before and after a scan coupling correction on November, 6th 2011.

	ϵ_y $[pm \cdot rad]$	B_{mag_y}	ϵ_x $[nm \cdot rad]$	B_{mag_x}
Before	100 ± 1	1.19 ± 0.01	1.41 ± 0.01	1.06 ± 0.02
After	62 ± 2	1.01 ± 0.01	1.34 ± 0.03	1.16 ± 0.01

Table 6.3: Emittances before and after a scan coupling correction on November, 6th 2011.

methods presented because of the amount of emittance measurements needed to get an acceptable parabola fit.

Figure 6.13 shows an example of this correction method as seen in $OTR0X$. The first screen-shot corresponds to the beam just after finding. An automated dispersion correction is then made with the Flight Simulator tool and the result can be seen in the second screen-shot. Note the lowering of the beam size when minimizing the dispersion contribution. The third screen-shot shows the decoupled beam after a manual scan method.

Response matrix method

This method was installed in ATF Control Room on December 2011 and measurements were made to test it. As it is programmed, the method is integrated in the emittance measurement panel (figure 6.14) and thus connected to the FS, where it looks the name of the nominal optics and finds if the response matrix was already built for this lattice. If the answer is positive it loads the matrix, while if the matrix doesn't exist yet it builds it in some minutes by tracking as explained before and stores it. Once the response matrix is known it loads the last measurements stored by the emittance reconstruction algorithm, so it is necessary to make an emittance measurement before correcting the coupling. From the response matrix and the measurements loaded the strength for the skews is calculated by least squares.

Table 6.4 shows the results of an automatic coupling correction performed on 30th November 2012. The algorithm reduced the emittance in a factor 1/3 within seconds. The values of the beam matrix spatial coupling terms are shown before and after correction to illustrate it.

The advantages of this method are clear. Operationally, the tracking is made only once for each nominal lattice, so, if the response matrix is already saved for a given nominal lattice it just loads it, and it is only necessary to make a measurement with the Multi-OTR. It is then far more fast than the manual scan method. It is an iterative method and converges in a few iterations, being just one minute per iteration, and thus it saves a lot

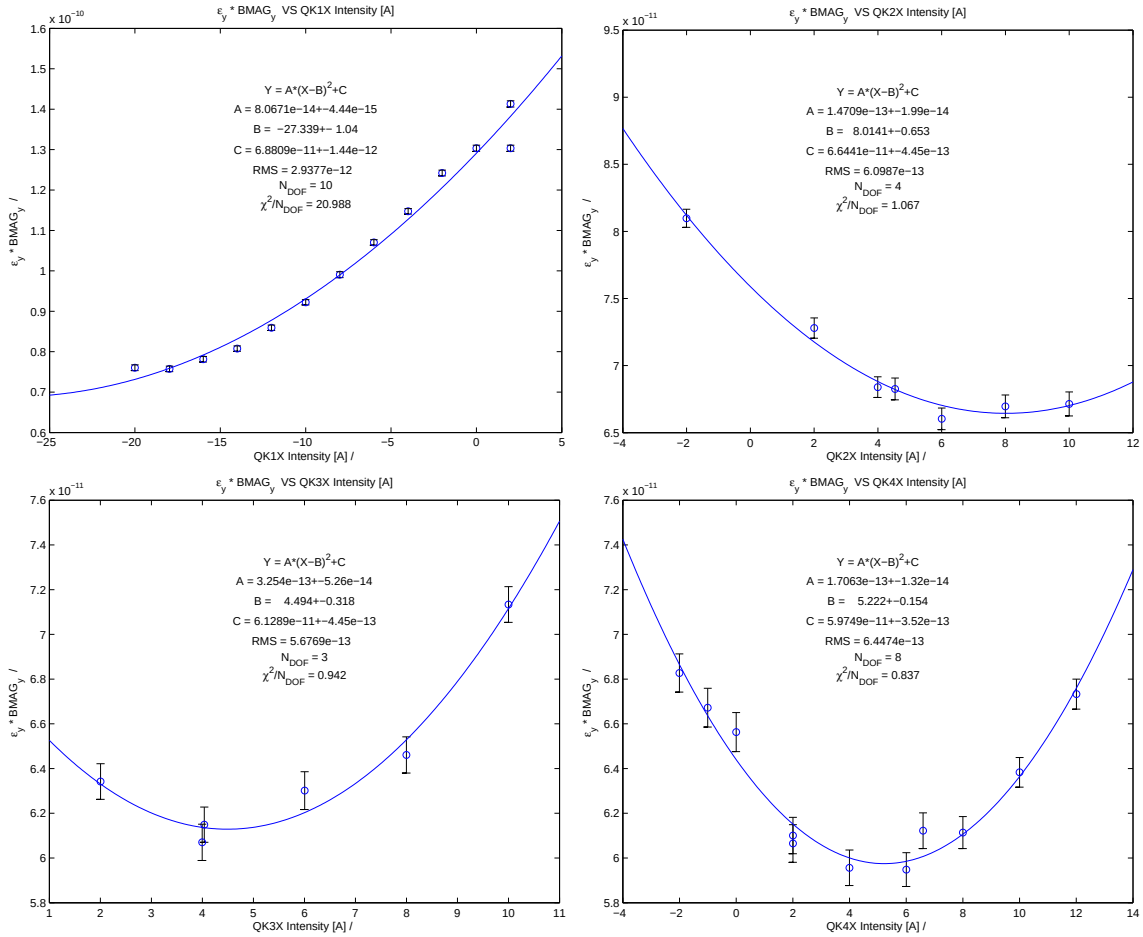

Figure 6.12: Another set of fitted parabolas during a scan coupling correction on January, 20th 2012.

of time with respect to the manual scanning one which needs no less than five emittance measurements per four skew quadrupoles. One would find it robust, in the sense that sometimes with the skew scanning method the parabola forced to set the strength at his limit value while other skews were set near to zero and with this method the intensities seem to be more well distributed. However there are some facts that can make this procedure somehow unstable. First of all the discussion about the fact that the phase advance between OTRs is not optimized and the Multi-OTR does not look at the same phases that the skew quadrupoles are able to cancel is making possible to have a residual coupling after the Multi-OTR. In fact a big coupling was seen in $MSPIP$ in December 2011 after some correction. Second the fact that the procedure is model-based and uses a response matrix derived from the nominal lattice being more sensitive to mismatches and other lattice errors. When the measured B_{mag} is high the method has been found to be not corrective, leading to a wrong solution. Finally, it is to be noted that the fact that the

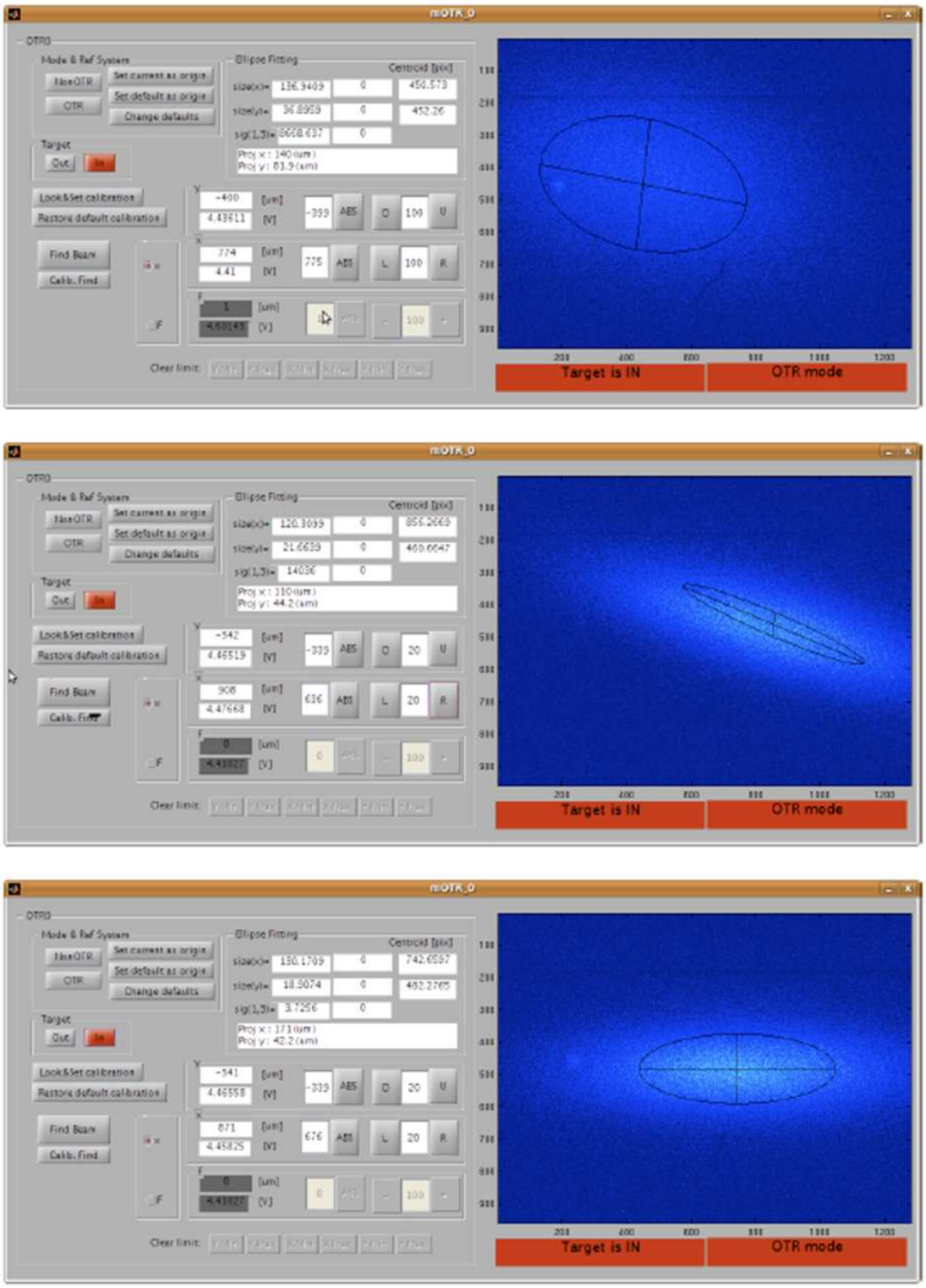

Figure 6.13: Effect of scan coupling correction in beam profile at $OTR0X$ location. First shot is as seen first time. Second shot is after automatically correcting the dispersion. Third shot is after a scan coupling correction. User interface is however not last version.

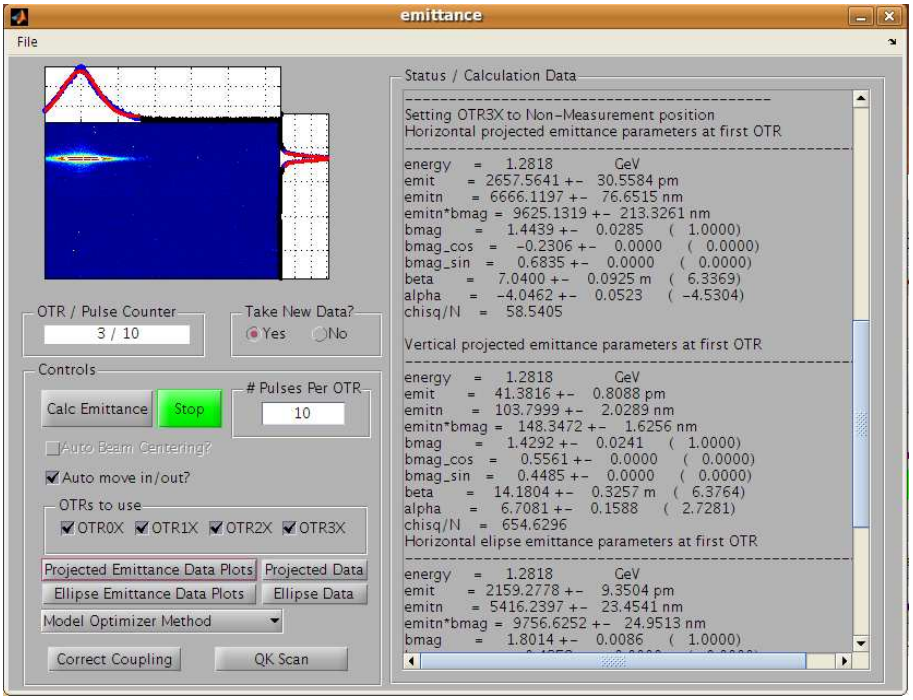

Figure 6.14: Emittance measurement panel. The coupling correction selector is in the bottom left part.

	Before	After
ϵ_y [pm·rad]	72.6 ± 0.06	48.2 ± 0.05
QK1X [A]	0	-9.8
QK2X [A]	0	2.4
QK3X [A]	0	4.6
QK4X [A]	0	4.4
$\langle xy \rangle_0$ [μm^2]	-840±20	-210±10
$\langle xy \rangle_1$ [μm^2]	-1120±20	-310±10
$\langle xy \rangle_2$ [μm^2]	-1360±10	-330±10
$\langle xy \rangle_3$ [μm^2]	-165±4	5±3

Table 6.4: Response matrix coupling correction made on 30th November 2012.

response matrix comes from a linear fit and we are neglecting quadratic behavior is not such a problem, because it is an iterative method so one could always, within the limits of resolution, improve the correction by a new iteration.

6.2 Energy spread measurement

In a linear accelerator one defines two kinds of energy spread: bunch to bunch and within a bunch. The first type is an effect of temperature drifts, variations in the amplitude, phase and frequency of the RF source, injection conditions and other limitations. This Section is centered in the second type, the energy spread within a bunch.

In a linac, the single particle energy is a sum of different contributions: the initial energy of the injected beam plus the energy gained during the acceleration plus the loss due to longitudinal wake-fields. However, due to the bunch length not all the particles within the bunch arrive in the same phase of the RF voltage and that leads to different energies when passing the acceleration structure. On the other hand, the wake-fields are generated in the head of the bunch and sensed in the tail, contributing to a widening of the energy distribution of the bunch. These facts altogether are the cause of a spread in the bunch energy. In some cases of high bunch current one must take profit of both sources of energy spread in order to cancel one with the other, i.e., cancel the energy variation along the bunch due to the slope in the RF field with the wake-field effect [77]. After the linac the beam is stored in the DR and there is cooled by SR to the limit of quantum fluctuations, minimizing this way the energy spread.

The energy spread of the beam is an important parameter that needs to be well known. For the low energy spread of the ATF beam, chromatic effects likely are not a problem except for at the focal point itself. In fact, it is responsible of a size growth in the IP which is approximately

$$\frac{\Delta\sigma^*_{x,y}}{\sigma^*_{x,y}} = W_{x,y}\frac{\sigma_E}{E}, \tag{6.17}$$

where W is the chromaticity and σ^* is the geometrical beam size at IP. The vertical chromaticity in ATF2 IP is around $W_y \sim 10^4$ and the energy spread is roughly $\frac{\sigma_E}{E} \sim 10^{-3}$ so the size can grow an order of magnitude due to chromaticity effects, in fact one of the ATF2 motivations is to test the Local Chromaticity Correction FF in order to minimize this effect [19].

The vertical position with respect to the reference orbit of a single particle along the lattice is determined by

$$y(s) = y_\beta(s) + D_y(s)\delta, \tag{6.18}$$

where y_β is the betatronic contribution due to oscillations around the reference orbit, D_y is the vertical dispersion in the location and $\delta = \frac{\Delta E}{E}$ is the relative error in the energy of the particle.

Considering a bunch of particles one can calculate the first and second moments of the distribution

$$\begin{aligned} \langle y \rangle &= \langle y_\beta \rangle + D_y\langle\delta\rangle = D_y\langle\delta\rangle \\ \langle y^2 \rangle &= \langle y_\beta^2 \rangle + D_y^2\langle\delta^2\rangle + 2\langle y_\beta\rangle D_y\langle\delta\rangle = \\ &= \langle y_\beta^2 \rangle + D_y^2\langle\delta^2\rangle \end{aligned}$$

where the term $\langle y_\beta \rangle$ is canceled because the betatron distribution is centered in 0. The first moment equation shows how the dispersion at some given point is measured, by scanning the frequency of the main DR and thus changing the energy and measuring the difference in the position of the centroid. The second moment equation relates linearly the square of the beam size with the square of the dispersion, being the slope $\langle\delta^2\rangle = \left(\frac{\sigma_E}{E}\right)^2$ the square of the relative energy spread, so it makes possible to calculate it by changing the dispersion and measuring the beam size.

Since the Multi-OTR is installed in a dispersion-free section it is necessary then to create it in order to perform this measurement. This is made in ATF2 by a pair of skew quadrupoles labeled $QS1X$ and $QS2X$. A sum multiknob with these skew quadrupoles which creates no horizontal dispersion nor coupling is used in order to correct vertical dispersion in the EXT line [83] but in principle they can be used to create it in the OTR locations.

Measurements of the energy spread were performed and one of these plots is shown in Figure 6.15. After a set of 3 measurements the final relative energy spread value was

$$\frac{\sigma_E}{E} = (8.4 \pm 1.2) \times 10^{-4}.$$

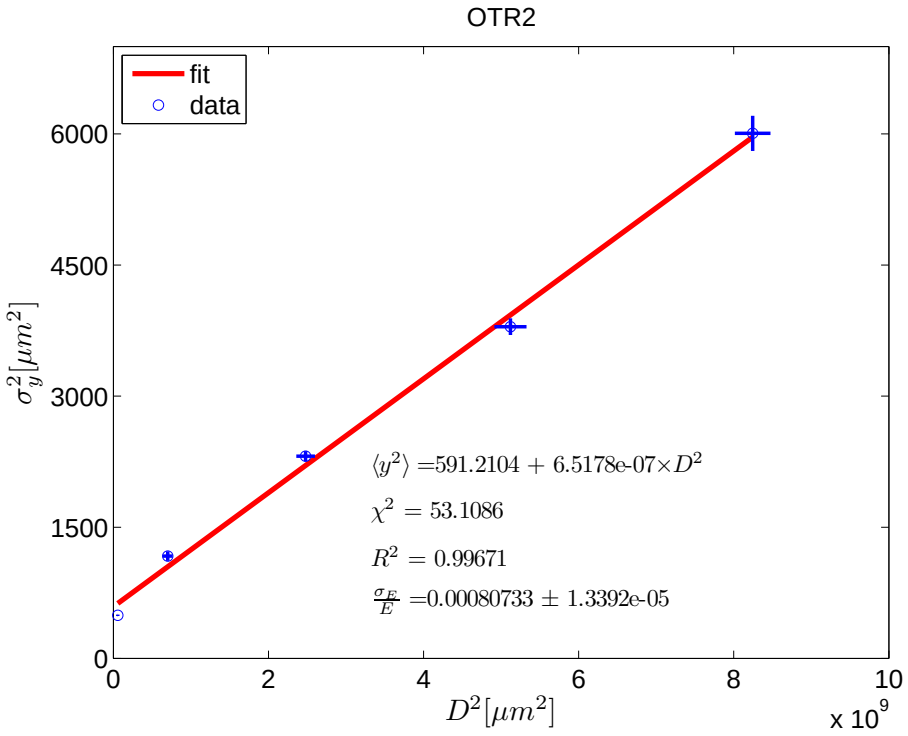

Figure 6.15: Energy spread measurements in OTR2X.

It is to be noted that the dispersion was measured using an automatic function of the Flight Simulator which uses a set of BPMs to measure and then estimate it in the locations in between. Therefore, the dispersion at the OTRs locations can be inaccurate and the result can be improved by measuring it directly with the OTR themselves. Moreover, during the measurements the intensity in the DR was rather variable. The final result can be improved as well by defining an intensity window and measuring the emittance only when the intensity value is within a certain range. This can be done with the Multi-OTR as presented in Section 3.3.2.

In the past, some energy spread measurements have been done to make impedance experiments in the ATF DR and to help in the understanding of the Intra-Beam Scattering (IBS) effects. In these cases in order to obtain the energy spread the beam width was measured using a screen monitor in a dispersive region after the extraction from the DR [3]. References of the measurements and studies can be found in [84, 85]. However, for regular studies the nominal value of the energy spread $\sigma_E = 0.8\%$ is used [19].

6.3 Intensity studies

Since the Multi-OTR is a beam size monitor system it is possible to perform correlation studies between the beam sizes and other beam parameters. For instance the dependency in the beam size and emittance with the bunch population.

On December 2011 a short test of the emittance value when changing the beam intensity was made. Figure 6.16 shows the result of this test. The energy was changed by means of the DR frequency and the emittance was measured with the Multi-OTR system. A similar study was done on 29th November 2012 and is shown in Figure 6.17.

This behaviour involves interaction between Intra Beam Scattering and impedance effects in the DR. Related studies were done in the past in ATF DR and can be seen in references [3, 84, 86].

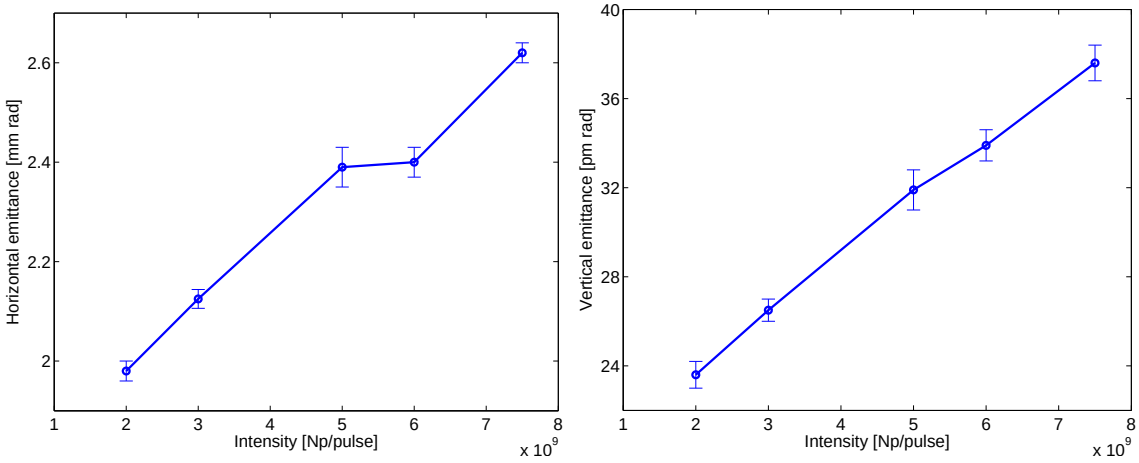

Figure 6.16: Emittance measurement against intensity. Horizontal on the left and vertical on the right. December 2011.

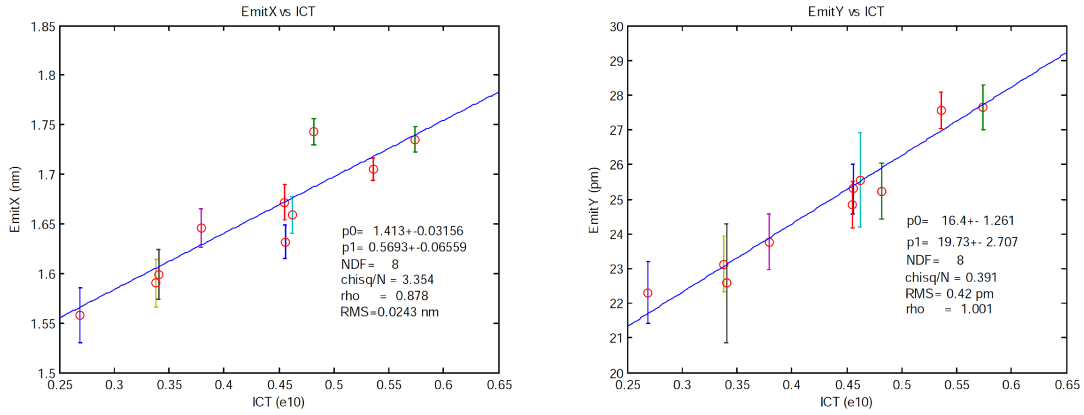

Figure 6.17: Emittance measurement against intensity. November 2012.

Chapter 7

Conclusions

Optical Transition Radiation (OTR) monitors are extensively used for beam diagnostics in a range of machines including high intensity proton beam facilities, Free Electron Lasers (FELs) and third generation Light Sources. In the framework of the prototypes for Future Linear Collider (FLC) at KEK (Japan) called ATF and ATF2, a system of four OTR monitors was projected with the aim of doing beam size measurements and emittance reconstruction after the DR. Furthermore it has been proved to be very useful in correcting coupling for beam tuning purposes.

The single OTR monitor has been designed based on an old existing monitor but with some improvements respect to this one. Four units have been built and assembled at IFIC and SLAC; and later installed in the ATF2 EXT line. The optical system has been characterized as well as the positioning system and the run limits for machine protection. The control software and the user interface have been programmed, installed and tested and now the controls are accessible from the ATF Control Room. The hardware design and the control software has been modified and improved during this period.

Analytical studies and realistic simulations regarding the emittance reconstruction algorithm have been done. Likewise, studies and simulations of different coupling correction algorithms have been concluded. In order to validate the results, comparisons with the results from existing Wire Scanners (WS) were made. WS and OTR measurements are in very good agreement.

The Multi-OTR system is being used to perform routine measurements since 2011. This measurements are done in less than a minute giving high statistics and working faster than other existing beam size monitor systems. Specifically the OTRs have been mainly used to infer the emittance and perform studies of its eventual growth and for the coupling correction during the tuning of ATF2. The system has been used to make beam energy spread measurements as well. On the 21th December 2012, during the runs in order to achieve the ATF2 Goal 1, a beam size of 72.8$\pm$5.4 nm was measured at the IP by means if the Shintake monitor, being this the smallest electron beam size ever mea-

sured. The previous record was obtained in 1995 by the Final Focus Test Beam (FFTB) at SLAC, with 77±7 nm [88]. ATF2 has overcome this record, which is a breakthrough towards the achivement of the necessary spot size for the required luminosity of the FLC. The Multi-OTR fast and reliable measurements have been crucial in order to obtain these successful results.

The Multi-OTR will be crucial on near future runs in order to achieve the two ATF2 Goals, specially the first one which is going to be addressed in Fall 2012 and Winter 2013.

The OTRs are completely functional, although some possible improvements have been envisaged and some of them will be implemented soon. The creation of wake-fields due to a simultaneous measurement will be avoided by the new designed target and target holders. The full 4D beam matrix reconstruction algorithm needs to be investigated in order to explain and fix the behavior in real measurements. Once this is done, the automatic coupling correction algorithm could be more robust even in non optimal conditions. The location of the OTRs could be revised depending mainly on the physical space in the beam line and the run constraints. Other functionalities such as the automatic beam finding using the information of the near BPMs or an auto-focusing routine could be possible improvements at mid term.

The Multi-OTR have other potential applications at ATF2 and also in the FLC. Being a single-shot device studies involving the beam position jitter as a parameter could be done. Possible material survivability experiments for the intensities and nominal beam sizes in single bunch mode could point the OTR as a good fast measurement device in start-up phases and commissioning of the machine, for instance in the Ring To Main Linac section of the future linear colliders, i.e. ILC and CLIC projects. In multi-bunch operation, due to the high number of bunches per train, the OTR targets would most likely be damaged. Studies in this direction to show the feasibility of the device can be carried out.

We conclude then that, within the survivability limits, the Multi-OTR is validated as a device to measure the beam size and reconstruct the emittance. Furthermore it is a very useful and reliable tool for cross-plane coupling correction, with potential application to certain transfer lines in future e^+e^- Linear Colliders and other machines such as FELs.

Appendix A

Beam dynamics and parameters: the emittance

In this appendix some basic concepts of beam dynamics are introduced in order to arrive at a definition of emittance which is important to understand the motivation of the Multi-OTR system. The discussion mainly follows the one in [89].

A.1 Transfer matrices

The 6-D canonical vector $\widehat{\boldsymbol{X}} = (\boldsymbol{x}, \boldsymbol{p})$ characterizes the movement of a particle in the accelerator in the canonical phase space. $\boldsymbol{x} = (x, y, s)$ being the spatial coordinates and $\boldsymbol{p} = (p_x, p_y, p_s)$ the momentum vector. The coordinates x and y are referred to transverse displacements with respect to the design orbit and the coordinate s is the one along the reference orbit.

Usually the so-called trace space is used instead of the canonical phase space, with the geometric coordinates $\boldsymbol{X}$ such that

$$\boldsymbol{X}(s) = \begin{pmatrix} x \\ x' \\ y \\ y' \\ l \\ \delta \end{pmatrix}, \tag{A.1}$$

with x and y referring to the displacement with respect to the reference orbit, l is the longitudinal displacement with respect to the reference particle, $x' = dx/ds$ and $y' = dy/ds$ the slopes with respect to the reference trajectory and $\delta = \Delta p/p$ the relative momentum deviation from the reference momentum. These coordinates are canonically conjugated only if the particle momentum is constant.

The particles along the accelerator are guided by the Lorentz force, which takes the form

$$\boldsymbol{F} = q(\boldsymbol{E} + \boldsymbol{v} \times \boldsymbol{B}), \tag{A.2}$$

being q the particle charge and $\boldsymbol{v}$ its velocity, $\boldsymbol{E}$ and $\boldsymbol{B}$ the electric and magnetic field vectors. By applying these forces to the particles it is possible to bend and define their trajectories.

In order to simplify we will focus in the cases in which the beam line consists in drift spaces, dipoles and quadrupoles, where the magnetic field depends linearly on the deviation of the particle with respect to the reference path. In this case the equations of the movement can be written as [9]

$$u''(s) = K_u(s)u(s) = \frac{\delta}{\rho_u(s)}, \tag{A.3}$$

which is the so called Hill's equation where $u(s)$ is for both $x(s)$ and $y(s)$, $\rho_u(s)$ represents the bending radius of the reference trajectory and $K_u(s)$ is defined as

$$\begin{array}{rcl} K_x(s) & = & -k(s) + \frac{1}{\rho_x^2(s)} \\ K_y(s) & = & k(s) + \frac{1}{\rho_x^2(s)} \end{array} \quad \text{where} \quad k(s) = \frac{q \cdot g(s)}{p}, \tag{A.4}$$

being $g(s)$ is the quadrupole magnetic field gradient. In a quadrupole the left term of the equation (A.3) is simplified to an harmonic oscillator form. The principal solutions of the homogeneous equation are

$$\left.\begin{array}{rcl} C_u(s) & = & cos(\sqrt{K_u}s) \\ S_u(s) & = & \frac{1}{\sqrt{K_u}} sin(\sqrt{K_u}s) \end{array}\right\} \quad \text{for} \quad K_u > 0$$

$$\left.\begin{array}{rcl} C_u(s) & = & cosh(\sqrt{K_u}s) \\ S_u(s) & = & \frac{1}{\sqrt{K_u}} sinh(\sqrt{K_u}s) \end{array}\right\} \quad \text{for} \quad K_u < 0 \tag{A.5}$$

When the particular solution for the inhomogeneous equation u_i is included the general solution of the Eq. (A.3) takes the form

$$\begin{array}{l} u(s) = u_0 C_u(s) + u_0' S_u(s) + \delta\eta_u(s) \\ u'(s) = u_0 C_u'(s) + u_0' S_u'(s) + \delta\eta_u'(s) \end{array} \quad \text{with} \quad \eta_u(s) = \frac{u_i}{\delta} \ , \tag{A.6}$$

the terms $\delta\eta_u(s)$ and $\delta\eta_u'(s)$ describe the part of the movement that depends of the momentum and the function $\eta_u(s)$ (sometimes $D(s)$) is called dispersion function. u_0 and u_0' are the initial parameters of the particle trajectory.

It can be shown that the longitudinal displacement l of an arbitrary particle with respect to the reference particle transforms as

$$\begin{aligned} l \;=\; & x_0 \underbrace{\int_{s_0}^{s} \frac{C_x(\tau)}{\rho_x(\tau)}\,\mathrm{d}\tau}_{R_{51}} + x_0' \underbrace{\int_{s_0}^{s} \frac{S_x(\tau)}{\rho_x(\tau)}\,\mathrm{d}\tau}_{R_{52}} + y_0 \underbrace{\int_{s_0}^{s} \frac{C_y(\tau)}{\rho_y(\tau)}\,\mathrm{d}\tau}_{R_{53}} + \dots \\ & \dots + y_0' \underbrace{\int_{s_0}^{s} \frac{S_y(\tau)}{\rho_y(\tau)}\,\mathrm{d}\tau}_{R_{54}} + \delta R_{56} + l_0 \end{aligned}, \tag{A.7}$$

with l_0 the initial longitudinal deviation from the reference particle. R_{56} is defined as the change in the length of the orbit ΔL divided by the particle's relative momentum deviation

$$R_{56} = \frac{\Delta L}{\delta} = \int_{s_0}^{s} \frac{\eta_x(\tau)}{\rho_x(\tau)}\,\mathrm{d}\tau + \int_{s_0}^{s} \frac{\eta_y(\tau)}{\rho_y(\tau)}\,\mathrm{d}\tau. \tag{A.8}$$

Eqs. (A.6) and (A.7) can be then combined in a matricial equation

$$\begin{pmatrix} x \\ x' \\ y \\ y' \\ l\delta \end{pmatrix} = \underbrace{\begin{pmatrix} R_{11} & R_{12} & R_{13} & R_{14} & R_{15} & R_{16} \\ R_{21} & R_{22} & R_{23} & R_{24} & R_{25} & R_{26} \\ R_{31} & R_{32} & R_{33} & R_{34} & R_{35} & R_{36} \\ R_{41} & R_{42} & R_{43} & R_{44} & R_{45} & R_{46} \\ R_{51} & R_{52} & R_{53} & R_{54} & R_{55} & R_{56} \\ R_{61} & R_{62} & R_{63} & R_{64} & R_{65} & R_{66} \end{pmatrix}}_{R} \begin{pmatrix} x_0 \\ x_0' \\ y_0 \\ y_0' \\ l_0\delta \end{pmatrix}, \tag{A.9}$$

where $\boldsymbol{R}$ is the transfer matrix

$$\boldsymbol{R} = \begin{pmatrix} C_x & S_x & 0 & 0 & 0 & R_{16} \\ C_x' & S_x' & 0 & 0 & 0 & R_{26} \\ 0 & 0 & C_y & S_y & 0 & R_{36} \\ 0 & 0 & C_y' & S_y' & 0 & R_{46} \\ R_{51} & R_{52} & R_{53} & R_{54} & R_{55} & R_{56} \\ 0 & 0 & 0 & 0 & 0 & 1 \end{pmatrix}. \tag{A.10}$$

The elements R_{16} and R_{36} characterize the dispersion and the elements R_{26} and R_{46} characterize the angular dispersion, both generated in the magnet described by the matrix $\boldsymbol{R}$ in the horizontal and vertical planes respectively.

By simply multiplying the transfer matrices corresponding to the different elements one can then calculate the transformation of the coordinates vector $\boldsymbol{X}$ along the whole beam line

$$\boldsymbol{X}_{end} = \boldsymbol{R}_n \cdot \boldsymbol{R}_{n-1} \cdot \dots \cdot \boldsymbol{R}_1 \cdot \boldsymbol{X}_{start}. \tag{A.11}$$

A.2 Liouville's theorem and phase space ellipse

So far we can track a single particle through the whole beam line by using Eq. (A.11), however, since the beams are very dense populated it is interesting to use some global parameter in order to describe the movement of the whole beam in the phase space.

Consider a complex system of N particles with the coordinates $(q_1(t), \ldots, q_N(t), p_1(t) \ldots p_N(t))$. If the system is conservative it is possible to be described by the Hamiltonian $H(q_1, \ldots, q_N, p_1 \ldots p_N, t)$ and the Hamilton equations will describe the evolution of the system [9]:

$$\dot{q}_i = \frac{\partial H}{\partial p_i} \qquad \dot{p}_i = -\frac{\partial H}{\partial q_i}. \tag{A.12}$$

Let $\Psi(q_1, \ldots, q_N, p_1 \ldots p_N, t)$ be the phase space density at a time t. The total derivative of Ψ with respect to the time is:

$$\begin{array}{rcccccl} \frac{d\Psi}{dt} & = & \frac{\partial \psi}{\partial t} & + & \sum_i \frac{\partial \Psi}{\partial q_i}\frac{\partial q_i}{\partial t} & + & \sum_i \frac{\partial \Psi}{\partial p_i}\frac{\partial p_i}{\partial t} = \\ & = & \frac{\partial \psi}{\partial t} & + & \sum_i \dot{q}_i \frac{\partial \Psi}{\partial q_i} & + & \sum_i \dot{p}_i \frac{\partial \Psi}{\partial p_i} \end{array}, \tag{A.13}$$

and using the equation of continuity

$$\frac{\partial \Psi}{\partial t} + \nabla(\Psi \boldsymbol{v}) = 0, \tag{A.14}$$

where $\boldsymbol{v} = (\dot{q}_1, \ldots, \dot{q}_N, \dot{p}_1 \ldots \dot{p}_N)$ it can be shown that

$$\begin{aligned} 0 &= \frac{\partial \Psi}{\partial t} + \nabla(\Psi \boldsymbol{v}) = \\ &= \frac{\partial \Psi}{\partial t} + \sum_i \dot{q}_i \frac{\partial \Psi}{\partial q_i} + \sum_i \dot{p}_i \frac{\partial \Psi}{\partial p_i} + \Psi \sum_i \left(\frac{\partial \dot{q}_i}{\partial q_i} + \frac{\partial \dot{p}_i}{\partial p_i} \right) = \\ &= \frac{\partial \Psi}{\partial t} + \sum_i \dot{q}_i \frac{\partial \Psi}{\partial q_i} + \sum_i \dot{p}_i \frac{\partial \Psi}{\partial p_i} + \Psi \sum_i \underbrace{\left(\frac{\partial}{\partial q_i}\frac{\partial H}{\partial p_i} - \frac{\partial}{\partial p_i}\frac{\partial H}{\partial q_i} \right)}_{=0} \end{aligned}, \tag{A.15}$$

which is the Liouville's theorem stating that under conservative forces the phase space density stays constant.

It can be shown [9] that a volume V of the phase space transforms as

$$V_{end} = \det \boldsymbol{R} \cdot V_{start}, \tag{A.16}$$

and therefore

$$\det \boldsymbol{R} = 1. \tag{A.17}$$

because the phase space density remains constant. This result has been obtained under some assumptions: using ordinates of Eq. (A.1) being canonically conjugated, i.e., the momentum of the particle is kept constant and assuming a conservative sytem.

In accelerators physics normally a phase space ellipse which encloses a given fraction of particles is defined.

For particles with $\delta = 0$, i.e. no momentum deviation, the movement Eq. (A.3) is simplified as

$$x''(s) + K_x(s)x(s) = 0. \tag{A.18}$$

The general solution for this equation is [9]

$$x(s) = a\sqrt{\beta_x(s)}\cos(\psi_x(s) - \psi_{x_0}), \tag{A.19}$$

with a and ψ_{x_0} constants, and the function $\psi_x(s)$ given by

$$\psi_x(s) = \sum_0^s \frac{\mathrm{d}\overline{s}}{\beta_x(\overline{s})}, \tag{A.20}$$

The $\beta_x(s)$ is the so called β-function and fulfills the differential equation

$$\frac{1}{2}\beta_x(s)\beta_x''(s) - \frac{1}{4}\beta_x'^2(s) + K_x(s)\beta_x^2(s) = 1. \tag{A.21}$$

Eq. A.19 and its derivative

$$x'(s) = \frac{a\beta_x'(s)}{2\sqrt{\beta_x(s)}}\cos(\psi_x(s) - \psi_{x_0}) - \frac{a}{\sqrt{\beta_x(s)}}\sin(\psi_x(s) - \psi_{x_0}), \tag{A.22}$$

can be combined to the invariant a^2

$$\left(\frac{1 + \frac{\beta_x'^2(s)}{4}}{\beta_x(s)}\right)x^2(s) - \beta_x'(s)x(s)x'(s) + \beta_x(s)x'^2(s) = a^2, \tag{A.23}$$

called the Courant-Snyder invariant, simplified to

$$\gamma_x(s)x^2(s) + 2\alpha_x(s)x(s)x'(s) + \beta_x(s)x'^2(s) = a^2, \tag{A.24}$$

by using the definitions

$$\alpha_x(s) = -\frac{1}{2}\beta_x'(s) \quad \text{and} \quad \gamma_x(s) = \frac{1 + \alpha_x^2(s)}{\beta_x(s)}. \tag{A.25}$$

This equation describes of an ellipse with parameters $\alpha_x(s)$,$\beta_x(s)$ and $\gamma_x(s)$ named Twiss parameters, which determine its shape and orientation. The movement of a particle described by Eq. (A.18) is called betatron motion and the area enclosed by the ellipse is given by πa^2.

It is then clear that betatron motion is around the perimeter of the ellipse described by Eq. A.25. The ellipse changes its shape along the beam line but its area stays constant.

We consider now a bunch of particles whose trajectories fill an area in the phase space x, x'. The area of the ellipse enclosing a given fraction of particles divided by π (there are other conventions) is called horizontal emittance ϵ_x

$$\epsilon_x = \frac{A}{\pi}. \tag{A.26}$$

and Equation (A.24) turns into

$$\gamma_x x^2 + 2\alpha_x x x'(s) + \beta_x x'^2 = \epsilon_x, \tag{A.27}$$

The same discussion can be made for vertical plane.

A.3 Beam Matrix

By introducing the bi-dimensional symmetric matrix σ called beam matrix one can express in another way the phase space ellipse equation

$$\begin{pmatrix} x & x' \end{pmatrix} \begin{pmatrix} \sigma_{11} & \sigma_{12} \\ \sigma_{21} & \sigma_{22} \end{pmatrix}^{-1} \begin{pmatrix} x \\ x' \end{pmatrix} = 1, \tag{A.28}$$

since $\sigma_{12} = \sigma_{21}$ that can be written as

$$\sigma_{22} x^2 - 2\sigma_{12} x x' + \sigma_{11} x'^2 = \det\sigma, \tag{A.29}$$

one relates the Twiss parameters and the beam matrix by comparing with A.27

$$\sigma = \begin{pmatrix} \sigma_{11} & \sigma_{12} \\ \sigma_{21} & \sigma_{22} \end{pmatrix} = \epsilon_x \begin{pmatrix} \beta_x & -\alpha_x \\ -\alpha_x & \gamma_x \end{pmatrix} \tag{A.30}$$

$$\epsilon_x = \sqrt{\det\sigma} = \sqrt{\sigma_{11}\sigma_{22} - \sigma_{12}^2}. \tag{A.31}$$

In order to know how the beam matrix is transformed from a position s_0 up to a position s we use the identity $I = R^{-1}R = R^T R^{T^{-1}}$ and starting from Eq. (A.28)

$$\begin{aligned} X_0^T R^T R^{T^{-1}} \sigma_0^{-1} R^{-1} R X_0 &= 1 \\ (RX_0)^T (R\sigma_0 R^T)^{-1} R X_0 &= 1 \ , \\ X^T (R\sigma_0 R^T)^{-1} R X &= 1 \end{aligned} \tag{A.32}$$

and then the beam matrix at the s position is

$$\sigma = R\sigma_0 R^T. \tag{A.33}$$

The definition of the beam matrix is somewhat arbitrary. For example, the ellipse which encloses the particles can contain all them or only a fraction. Using the second moments $\langle uv \rangle$ one can define the beam parameters in a statistical way. The second moments are defined by:

$$\langle uv\rangle = \frac{\sum_{-\infty}^{\infty}(u-\langle u\rangle)(v-\langle v\rangle)\ \Psi(x,x',y,y',l,\delta)\ \mathrm{d}x\ \mathrm{d}x'\ \mathrm{d}y\ \mathrm{d}y'\ \mathrm{d}l\ \mathrm{d}\delta}{\sum_{-\infty}^{\infty}\Psi(x,x',y,y',l,\delta)\ \mathrm{d}x\ \mathrm{d}x'\ \mathrm{d}y\ \mathrm{d}y'\ \mathrm{d}l\ \mathrm{d}\delta}, \tag{A.34}$$

where $\langle u\rangle$ is the first moment of the variable u

$$\langle u\rangle = \frac{\sum_{-\infty}^{\infty} u\ \Psi(x,x',y,y',l,\delta)\ \mathrm{d}x\ \mathrm{d}x'\ \mathrm{d}y\ \mathrm{d}y'\ \mathrm{d}l\ \mathrm{d}\delta}{\sum_{-\infty}^{\infty}\Psi(x,x',y,y',l,\delta)\ \mathrm{d}x\ \mathrm{d}x'\ \mathrm{d}y\ \mathrm{d}y'\ \mathrm{d}l\ \mathrm{d}\delta}. \tag{A.35}$$

Here u and v can stand for x, x', y, y', l, δ and Ψ represents the intensity distribution of the beam in six-dimensional space. The beam size is defined by the square root of the variances in the vertical and horizontal planes, i.e., the square root of the second moments $\langle x^2\rangle$ and $\langle y^2\rangle$ respectively).

With these second moments the six-dimensional beam matrix can be written

$$\sigma^{6D} = \begin{pmatrix} \langle x^2\rangle & \langle xx'\rangle & \langle xy\rangle & \langle xy'\rangle & \langle xl\rangle & \langle x\delta\rangle \\ \langle xx'\rangle & \langle x'^2\rangle & \langle x'y\rangle & \langle x'y'\rangle & \langle x'l\rangle & \langle x'\delta\rangle \\ \langle xy\rangle & \langle x'y\rangle & \langle y^2\rangle & \langle yy'\rangle & \langle yl\rangle & \langle y\delta\rangle \\ \langle xy'\rangle & \langle x'y'\rangle & \langle yy'\rangle & \langle y'^2\rangle & \langle y'l\rangle & \langle y'\delta\rangle \\ \langle xl\rangle & \langle x'l\rangle & \langle yl\rangle & \langle y'l\rangle & \langle l^2\rangle & \langle l\delta\rangle \\ \langle x\delta\rangle & \langle x'\delta\rangle & \langle y\delta\rangle & \langle y'\delta\rangle & \langle l\delta\rangle & \langle\delta^2\rangle \end{pmatrix}. \tag{A.36}$$

This is the representation mainly used in electron accelerators.

A.4 Transverse emittance

Assuming that one knows the 6D beam matrix, then $\epsilon_{rms}^{6D} = \sqrt{\det\sigma^{6D}}$ is the six-dimensional rms beam emittance. The projection of the six-dimensional ellipsoid over the transverse planes leads to the 4×4 beam matrix, which describes the dimensions of the projected beam in the transverse phase space.

$$\sigma^{4D} = \begin{pmatrix} \sigma_{xx} & \sigma_{xy} \\ \sigma_{xy}^T & \sigma_{yy} \end{pmatrix}. \tag{A.37}$$

When dispersion is present the second beam moments have two contributions, the purely betatronic and the one due to the dispersion. The matrix σ^{4D} can be then expressed as

$$\sigma^{4D} = \begin{pmatrix} \langle x_\beta^2\rangle + \eta_x^2\langle\delta^2\rangle & \langle x_\beta x'_\beta\rangle + \eta_x\eta'_x\langle\delta^2\rangle & \langle x_\beta y_\beta\rangle + \eta_x\eta_y\langle\delta^2\rangle & \langle x_\beta y'_\beta\rangle + \eta_x\eta'_y\langle\delta^2\rangle \\ \langle x_\beta x'_\beta\rangle + \eta_x\eta'_x\langle\delta^2\rangle & \langle {x'_\beta}^2\rangle + \eta_x'^2\langle\delta^2\rangle & \langle x'_\beta y_\beta\rangle + \eta'_x\eta_y\langle\delta^2\rangle & \langle x'_\beta y'_\beta\rangle + \eta'_x\eta'_y\langle\delta^2\rangle \\ \langle x_\beta y_\beta\rangle + \eta_x\eta_y\langle\delta^2\rangle & \langle x'_\beta y_\beta\rangle + \eta'_x\eta_y\langle\delta^2\rangle & \langle y_\beta^2\rangle + \eta_y^2\langle\delta^2\rangle & \langle y_\beta y'_\beta\rangle + \eta_y\eta'_y\langle\delta^2\rangle \\ \langle x_\beta y'_\beta\rangle + \eta_x\eta'_y\langle\delta^2\rangle & \langle x'_\beta y'_\beta\rangle + \eta'_x\eta'_y\langle\delta^2\rangle & \langle y_\beta y'_\beta\rangle + \eta_y\eta'_y\langle\delta^2\rangle & \langle {y'_\beta}^2\rangle + \eta_y'^2\langle\delta^2\rangle \end{pmatrix}, \tag{A.38}$$

where the dispersion functions are defined as

$$\begin{array}{rcl} \eta_x(s) & = & \frac{\langle x(s)\delta\rangle}{\langle\delta^2\rangle} \\ \eta'_x(s) & = & \frac{\langle x'(s)\delta\rangle}{\langle\delta^2\rangle} \end{array} , \tag{A.39}$$

and the equivalent for the vertical plane.

Eq. (A.38) shows the effective emittance. The betatronic emittance can be calculated subtracting the contribution of the dispersion to the beam matrix elements.

A part from the dispersion, a coupling between horizontal and vertical betatron oscillations is possible due to eventual tilt in the quadrupoles for instance. This is described by the matrix δ_{xy}. If all the elements of this matrix are zero then the beam is transversely uncoupled. In presence of coupling the projected (2D) emittances can be defined in the horizontal and vertical planes as

$$\begin{array}{l} \epsilon_{x,rms} = \sqrt{\det\sigma_{xx}} \\ \epsilon_{y,rms} = \sqrt{\det\sigma_{yy}} \end{array} . \tag{A.40}$$

The existing of eventual coupling between horizontal and vertical planes means that the axes of the (4D) hyper ellipsoid are rotated respect to the (x,x') and (y,y') planes. Using a symplectic transformation [68] it is possible to find a coordinate system in which the matrix is diagonal, as explained in 5.1.3 so that we obtain

$$\overline{\sigma}^{4D} = \begin{pmatrix} \epsilon_{1,rms} & 0 & 0 & 0 \\ 0 & \epsilon_{1,rms} & 0 & 0 \\ 0 & 0 & \epsilon_{2,rms} & 0 \\ 0 & 0 & 0 & \epsilon_{2,rms} \end{pmatrix} , \tag{A.41}$$

where $\epsilon_{1,rms}$ and $\epsilon_{2,rms}$ are the intrinsic rms emittances. It is possible to show that the product of the intrinsic emittances cannot be higher than the product of the projected ones

$$\epsilon^{4D}_{rms} = \epsilon_{1,rms}\epsilon_{2,rms} \leq \epsilon_{x,rms}\epsilon_{y,rms}. \tag{A.42}$$

If the beam energy changes the transverse coordinates (x, x') and (y, y') are not canonically conjugated anymore. In any case, the phase space density will be preserved for the canonical coordinates (x, p_x) and (y, p_y) as the Liouville theorem predicts. During the acceleration only the longitudinal momentum p_s grows while the transverse p_x and p_y stay constant. The slopes $x' = p_x/p_s$ and $y' = p_y/p_s$ decrease proportional to $1/p$ where p is the momentum of the beam. This lowering of the geometric emittance when the energy grows is called adiabatic damping. If we multiply the geometric emittance by the factor p/m_0c we have a quantity called normalized emittance

$$\epsilon_N = \frac{p}{m_0c}\epsilon. \tag{A.43}$$

The normalized emittance stays constant during acceleration.

Appendix B

Emittance reconstruction details

In this Appendix are presented some numerical rules related to the condition number of the matrices involved in the resolution of the emittance reconstruction [70].

B.1 Beam Matrix elements

The beam matrix elements between in term of the Twiss parameters the initial location (0) and the measurement location (i) could be expressed in the uncoupled case as:

$$R = R_{i,0} = \begin{pmatrix} R_{11} & R_{12} & 0 & 0 \\ R_{21} & R_{22} & 0 & 0 \\ 0 & 0 & R_{33} & R_{34} \\ 0 & 0 & R_{43} & R_{44} \end{pmatrix}, \tag{B.1}$$

with:

$$\begin{aligned}
R_{11} &= \sqrt{\frac{\beta_x^{(i)}}{\beta_x^{(0)}}}(\cos\phi_x^{(i0)} + \alpha_x^{(0)}\sin\phi_x^{(i0)}) \\
R_{12} &= \sqrt{\beta_x^{(i)}\beta_x^{(0)}}\sin\phi_x^{(i0)} \\
R_{21} &= -\frac{(1+\alpha_x^{(0)}\alpha_x^{(i)})}{\sqrt{\beta_x^{(i)}\beta_x^{(0)}}}\sin\phi_x^{(i0)} - \frac{(\alpha_x^{(i)}-\alpha_x^{(0)})}{\sqrt{\beta_x^{(i)}\beta_x^{(0)}}}\cos\phi_x^{(i0)} \\
R_{22} &= \sqrt{\frac{\beta_x^{(0)}}{\beta_x^{(i)}}}(\cos\phi_x^{(i0)} - \alpha_x^{(i)}\sin\phi_x^{(i0)}) \\
R_{33} &= \sqrt{\frac{\beta_y^{(i)}}{\beta_y^{(0)}}}(\cos\phi_y^{(i0)} + \alpha_y^{(0)}\sin\phi_y^{(i0)}) \\
R_{34} &= \sqrt{\beta_y^{(i)}\beta_y^{(0)}}\sin\phi_y^{(i0)} \\
R_{43} &= -\frac{(1+\alpha_y^{(0)}\alpha_y^{(i)})}{\sqrt{\beta_{y,i}^{(i)}\beta_y^{(0)}}}\sin\phi_y^{(i0)} + \frac{(\alpha_y^{(i)}-\alpha_y^{(0)})}{\sqrt{\beta_y^{(i)}\beta_y^{(0)}}}\cos\phi_y^{(i0)} \\
R_{44} &= \sqrt{\frac{\beta_y^{(0)}}{\beta_y^{(i)}}}(\cos\phi_y^{(i0)} - \alpha_y^{(i)}\sin\phi_y^{(i0)})
\end{aligned}, \tag{B.2}$$

with $\phi^{(i0)} = \phi^{(i)} - \phi^{(0)}$.

B.2 2D Emittance: Four or more measurements stations

- Minors of order 4 of M_X^*
  - row combination (1, 2, 3, 4)

$$l_1^* = \begin{vmatrix} R_{11}^{2(1)} & 2R_{11}^{(1)}R_{12}^{(1)} & R_{12}^{2(1)} & \hat{\sigma}_1^{(1)} \\ R_{11}^{2(2)} & 2R_{11}^{(2)}R_{12}^{(2)} & R_{12}^{2(2)} & \hat{\sigma}_1^{(2)} \\ R_{11}^{2(3)} & 2R_{11}^{(3)}R_{12}^{(3)} & R_{12}^{2(3)} & \hat{\sigma}_1^{(3)} \\ R_{11}^{2(4)} & 2R_{11}^{(4)}R_{12}^{(4)} & R_{12}^{2(4)} & \hat{\sigma}_1^{(4)} \end{vmatrix} =$$

$$\begin{aligned} &-\tfrac{1}{2}\{\beta_x^{(1)}\beta_x^{(2)}(\hat{\sigma}_1^{(3)}\beta_x^{(4)} - \hat{\sigma}_1^{(4)}\beta_x^{(3)})\sin 2\phi_x^{(21)} + \beta_x^{(1)}\beta_x^{(3)}(\hat{\sigma}_1^{(4)}\beta_x^{(2)} - \hat{\sigma}_1^{(2)}\beta_x^{(4)})\sin 2\phi_x^{(31)} + \\ &\beta_x^{(1)}\beta_x^{(4)}(\hat{\sigma}_1^{(2)}\beta_x^{(3)} - \hat{\sigma}_1^{(3)}\beta_x^{(2)})\sin 2\phi_x^{(41)} + \beta_x^{(2)}\beta_x^{(3)}(\hat{\sigma}_1^{(1)}\beta_x^{(4)} - \hat{\sigma}_1^{(4)}\beta_x^{(1)})\sin 2\phi_x^{(32)} + \\ &\beta_x^{(2)}\beta_x^{(4)}(\hat{\sigma}_1^{(3)}\beta_x^{(1)} - \hat{\sigma}_1^{(1)}\beta_x^{(3)})\sin 2\phi_x^{(42)} + \beta_x^{(3)}\beta_x^{(4)}(\hat{\sigma}_1^{(1)}\beta_x^{(2)} - \hat{\sigma}_1^{(2)}\beta_x^{(1)})\sin 2\phi_x^{(43)}\} \\ &= -\tfrac{1}{2}\{\beta_x^{(1)}\beta_x^{(2)}(\hat{\sigma}_1^{(3)}\beta_x^{(4)} - \hat{\sigma}_1^{(4)}\beta_x^{(3)})\sin\Phi_{x,1}\cos\Phi_{x,1} + \\ &\beta_x^{(1)}\beta_x^{(3)}(\hat{\sigma}_1^{(4)}\beta_x^{(2)} - \hat{\sigma}_1^{(2)}\beta_x^{(4)})\sin\Phi_{x,2}\cos\Phi_{x,2} + \\ &\beta_x^{(1)}\beta_x^{(4)}(\hat{\sigma}_1^{(2)}\beta_x^{(3)} - \hat{\sigma}_1^{(3)}\beta_x^{(2)})\sin\Phi_{x,3}\cos\Phi_{x,3} + \\ &\beta_x^{(2)}\beta_x^{(3)}(\hat{\sigma}_1^{(1)}\beta_x^{(4)} - \hat{\sigma}_1^{(4)}\beta_x^{(1)})\sin(\Phi_{x,2} - \Phi_{x,1})\cos(\Phi_{x,2} - \Phi_{x,1}) + \\ &\beta_x^{(2)}\beta_x^{(4)}(\hat{\sigma}_1^{(3)}\beta_x^{(1)} - \hat{\sigma}_1^{(1)}\beta_x^{(3)})\sin(\Phi_{x,3} - \Phi_{x,1})\cos(\Phi_{x,3} - \Phi_{x,1}) + \\ &\beta_x^{(3)}\beta_x^{(4)}(\hat{\sigma}_1^{(1)}\beta_x^{(2)} - \hat{\sigma}_1^{(2)}\beta_x^{(1)})\sin(\Phi_{x,3} - \Phi_{x,2})\cos(\Phi_{x,3} - \Phi_{x,2})\} \end{aligned} \quad , \tag{B.3}$$

    taking the expressions for the different matrix elements in terms of Twiss parameters (see Section B.1) and with $\phi_x^{(ij)} = (\phi_x^{(i)} - \phi_x^{(j)})$ with $ij = 1, 2, 3, 4$ being $\phi_x^{(32)} = \phi_x^{(31)} - \phi_x^{(21)}$ $\phi_x^{(42)} = \phi_x^{(41)} - \phi_x^{(21)}$ and $\phi_x^{(43)} = \phi_x^{(41)} - \phi_x^{(31)}$. These means that there are only three independent difference phase advances that we renamed as: $\phi_x^{(21)} = \Phi_{x,1}$, $\phi_x^{(31)} = \Phi_{x,2}$ and $\phi_x^{(41)} = \Phi_{x,3}$.
  - same expression with all the other rows combinations: (2, 3, 4, 5),... (N-3, N-2, N-1; N).

- Minors of order 3 of M_X^*
  - columns (1, 2 ,3) rows (1, 2, 3) combinations

$$\begin{aligned} m_1^* &= \begin{vmatrix} R_{11}^{2(1)} & 2R_{11}^{(1)}R_{12}^{(1)} & R_{12}^{2(1)} \\ R_{11}^{2(2)} & 2R_{11}^{(2)}R_{12}^{(2)} & R_{12}^{2(2)} \\ R_{11}^{2(3)} & 2R_{11}^{(3)}R_{12}^{(3)} & R_{12}^{2(3)} \end{vmatrix} \\ &= 2\beta_x^{(1)}\beta_x^{(2)}\beta_x^{(3)}\sin\phi_x^{(21)}\sin\phi_x^{(31)}\sin\phi_x^{(32)} \\ &= 2\beta_x^{(1)}\beta_x^{(2)}\beta_x^{(3)}\sin\Phi_{x,1}\sin\Phi_{x,2}\sin(\Phi_{x,2} - \Phi_{x,1}) \end{aligned} \quad , \tag{B.4}$$

    that is the equivalent to (5.15).

– same expression for columns (1, 2, 3) and all rows (1, 2, 4)...(N-2, N-1, N) combinations

– columns (1, 2 ,4) rows (1, 2, 3) combinations

$$m_2^* = \begin{vmatrix} R_{11}^{2(1)} & 2R_{11}^{(1)}R_{12}^{(1)} & \hat{\sigma}_1^{(1)} \\ R_{11}^{2(2)} & 2R_{11}^{(2)}R_{12}^{(2)} & \hat{\sigma}_1^{(2)} \\ R_{11}^{2(3)} & 2R_{11}^{(3)}R_{12}^{(3)} & \hat{\sigma}_1^{(3)} \end{vmatrix} =$$

$$\begin{aligned}
&\tfrac{1}{2\beta_x^{(0)}}\{2\alpha_x^{(0)}\{\cos 2\phi_x^{(10)}\beta_x^{(1)}(\beta_x^{(2)}\hat{\sigma}_1^{(3)} - \beta_x^{(3)}\hat{\sigma}_1^{(2)}) + \cos 2\phi_x^{(20)}\beta_x^{(2)}(\beta_x^{(3)}\hat{\sigma}_1^{(1)} - \beta_x^{(1)}\hat{\sigma}_1^{(3)}) + \\
&\cos 2\phi_x^{(30)}\beta_x^{(3)}(\beta_x^{(2)}\hat{\sigma}_1^{(1)} - \beta_x^{(2)}\hat{\sigma}_1^{(1)})\} + (\alpha_x^{(0)2} - 1)\{\sin 2\phi_x^{(10)}\beta_x^{(1)}(\beta_x^{(2)}\hat{\sigma}_1^{(3)} - \beta_x^{(3)}\hat{\sigma}_1^{(2)}) + \\
&\sin 2\phi_x^{(20)}\beta_x^{(2)}(\beta_x^{(1)}\hat{\sigma}_1^{(3)} - \beta_x^{(3)}\hat{\sigma}_1^{(1)}) + \sin 2\phi_x^{(30)}\beta_x^{(3)}(\beta_x^{(1)}\hat{\sigma}_1^{(2)} - \beta_x^{(2)}\hat{\sigma}_1^{(1)}) + \\
&\sin 2\phi_x^{(12)}\beta_x^{(1)}\beta_x^{(2)}\hat{\sigma}_1^{(3)} + \sin 2\phi_x^{(23)}\beta_x^{(2)}\beta_x^{(3)}\hat{\sigma}_1^{(1)}\}\} \\
&= \tfrac{1}{2\beta_x^{(0)}}\{2\alpha_x^{(0)}\{\cos 2\phi_x^{(10)}\beta_x^{(1)}(\beta_x^{(2)}\hat{\sigma}_1^{(3)} - \beta_x^{(3)}\hat{\sigma}_1^{(2)}) \\
&+ \cos 2(\Phi_{x,1} + \phi_x^{(10)})\beta_x^{(2)}(\beta_x^{(3)}\hat{\sigma}_1^{(1)} - \beta_x^{(1)}\hat{\sigma}_1^{(3)}) + \\
&\cos 2(\Phi_{x,2} + \phi_x^{(10)})\beta_x^{(3)}(\beta_x^{(2)}\hat{\sigma}_1^{(1)} - \beta_x^{(2)}\hat{\sigma}_1^{(1)})\} \\
&+ (\alpha_x^{(0)2} - 1)\{\sin 2\phi_x^{(10)}\beta_x^{(1)}(\beta_x^{(2)}\hat{\sigma}_1^{(3)} - \beta_x^{(3)}\hat{\sigma}_1^{(2)}) + \\
&\sin 2(\Phi_{x,1} + \phi_x^{(10)})\beta_x^{(2)}(\beta_x^{(1)}\hat{\sigma}_1^{(3)} - \beta_x^{(3)}\hat{\sigma}_1^{(1)}) + \\
&\sin 2(\Phi_{x,2} + \phi_x^{(10)})\beta_x^{(3)}(\beta_x^{(1)}\hat{\sigma}_1^{(2)} - \beta_x^{(2)}\hat{\sigma}_1^{(1)}) \\
&- \sin 2\Phi_{x,1}\beta_x^{(1)}\beta_x^{(2)}\hat{\sigma}_1^{(3)} - \sin 2(\Phi_{x,2} - \Phi_{x,1})\beta_x^{(2)}\beta_x^{(3)}\hat{\sigma}_1^{(1)}\}\}
\end{aligned} \tag{B.5}$$

– Same expression for columns (1, 2, 4) and all rows (1, 2, 4)...(N-2, N-1, N) combinations.

– Columns (1, 3 ,4) rows (1, 2, 3) combinations.

$$m_3^* = \begin{vmatrix} R_{11}^{2(1)} & R_{12}^{2(1)} & \hat{\sigma}_1^{(1)} \\ R_{11}^{2(2)} & R_{12}^{2(2)} & \hat{\sigma}_1^{(2)} \\ R_{11}^{2(3)} & R_{12}^{2(3)} & \hat{\sigma}_1^{(3)} \end{vmatrix} =$$

$$\begin{aligned}
&\tfrac{1}{2}\{\beta_x^{(1)}(\beta_x^{(2)}\hat{\sigma}_1^{(3)} - \beta_x^{(3)}\hat{\sigma}_1^{(2)})(\cos 2\phi_x^{(10)} - \alpha_x^{(0)}\sin 2\phi_x^{(10)}) + \\
&\beta_x^{(2)}(\beta_x^{(3)}\hat{\sigma}_1^{(1)} - \beta_x^{(1)}\hat{\sigma}_1^{(3)})(\cos 2\phi_x^{(20)} - \alpha_x^{(0)}\sin 2\phi_x^{(20)}) + \\
&\beta_x^{(3)}(\beta_x^{(1)}\hat{\sigma}_1^{(2)} - \beta_x^{(2)}\hat{\sigma}_1^{(1)})(\cos 2\phi_x^{(30)} - \alpha_x^{(0)}\sin 2\phi_x^{(30)}) + \\
&\alpha_x^{(0)}\beta_x^{(1)}\beta_x^{(2)}\hat{\sigma}_1^{(3)}\sin 2\phi_x^{(12)} + \alpha_x^{(0)}\beta_x^{(1)}\beta_x^{(3)}\hat{\sigma}_1^{(2)}\sin 2\phi_x^{(13)} + \alpha_x^{(0)}\beta_x^{(2)}\beta_x^{(3)}\hat{\sigma}_1^{(1)}\sin 2\phi_x^{(23)}\} \\
&= \tfrac{1}{2}\{\beta_x^{(1)}(\beta_x^{(2)}\hat{\sigma}_1^{(3)} - \beta_x^{(3)}\hat{\sigma}_1^{(2)})(\cos 2\phi_x^{(10)} - \alpha_x^{(0)}\sin 2\phi_x^{(10)}) + \\
&\beta_x^{(2)}(\beta_x^{(3)}\hat{\sigma}_1^{(1)} - \beta_x^{(1)}\hat{\sigma}_1^{(3)})(\cos 2(\Phi_{x,1} + \phi_x^{(10)}) - \alpha_x^{(0)}\sin 2(\Phi_{x,1} + \phi_x^{(10)})) + \\
&\beta_x^{(3)}(\beta_x^{(1)}\hat{\sigma}_1^{(2)} - \beta_x^{(2)}\hat{\sigma}_1^{(1)})(\cos 2(\Phi_{x,2} + \phi_x^{(10)}) - \alpha_x^{(0)}\sin 2(\Phi_{x,2} + \phi_x^{(10)})) \\
&-\alpha_x^{(0)}\beta_x^{(1)}\beta_x^{(2)}\hat{\sigma}_1^{(3)}\sin 2\Phi_{x,1} - \alpha_x^{(0)}\beta_x^{(1)}\beta_x^{(3)}\hat{\sigma}_1^{(2)}\sin 2\Phi_{x,2} \\
&-\alpha_x^{(0)}\beta_x^{(2)}\beta_x^{(3)}\hat{\sigma}_1^{(1)}\sin 2(\Phi_{x,2} - \Phi_{x,1})\}
\end{aligned} \tag{B.6}$$

– Same expression for columns (1, 3, 4) and all rows (1, 2, 4)... (N-2, N-1, N) combinations.

– Columns (2, 3 ,4) rows (1, 2, 3) combinations.

$$m_4^* = \begin{vmatrix} 2R_{11}^{(1)}R_{12}^{(1)} & R_{12}^{2(1)} & \hat{\sigma}_1^{(1)} \\ 2R_{11}^{(2)}R_{12}^{(2)} & R_{12}^{2(2)} & \hat{\sigma}_1^{(2)} \\ 2R_{11}^{(3)}R_{12}^{(3)} & R_{12}^{2(3)} & \hat{\sigma}_1^{(3)} \end{vmatrix} =$$

$$\begin{aligned} &\tfrac{\beta_x^{(0)}}{2}\{\beta_x^{(1)}(\beta_x^{(2)}\hat{\sigma}_1^{(3)} - \beta_x^{(3)}\hat{\sigma}_1^{(2)})\sin 2\phi_x^{(10)} + \beta_x^{(2)}(\beta_x^{(3)}\hat{\sigma}_1^{(1)} - \beta_x^{(1)}\hat{\sigma}_1^{(3)})\sin 2\phi_x^{(20)} + \\ &\beta_x^{(3)}(\beta_x^{(1)}\hat{\sigma}_1^{(2)} - \beta_x^{(2)}\hat{\sigma}_1^{(1)})\sin 2\phi_x^{(30)} - \beta_x^{(1)}\beta_x^{(2)}\hat{\sigma}_1^{(3)}\sin 2\Phi_x^{(12)} + \beta_x^{(1)}\beta_x^{(3)}\hat{\sigma}_1^{(2)}\sin 2\phi_x^{(13)} - \\ &\beta_x^{(2)}\beta_x^{(3)}\hat{\sigma}_1^{(1)}\sin 2\phi_x^{(23)}\} \\ &= \tfrac{\beta_x^{(0)}}{2}\{\beta_x^{(1)}(\beta_x^{(2)}\hat{\sigma}_1^{(3)} - \beta_x^{(3)}\hat{\sigma}_1^{(2)})\sin 2\phi_x^{(10)} + \beta_x^{(2)}(\beta_x^{(3)}\hat{\sigma}_1^{(1)} - \beta_x^{(1)}\hat{\sigma}_1^{(3)})\sin 2(\Phi_{x,1} + \phi_x^{(10)}) + \\ &\beta_x^{(3)}(\beta_x^{(1)}\hat{\sigma}_1^{(2)} - \beta_x^{(2)}\hat{\sigma}_1^{(1)})\sin 2(\Phi_{x,2} + \phi_x^{(10)}) + \beta_x^{(1)}\beta_x^{(2)}\hat{\sigma}_1^{(3)}\sin 2\Phi_{x,1} - \beta_x^{(1)}\beta_x^{(3)}\hat{\sigma}_1^{(2)}\sin 2\Phi_{x,2} \\ &+\beta_x^{(2)}\beta_x^{(3)}\hat{\sigma}_1^{(1)}\sin 2(\Phi_{x,2} - \Phi_{x,1})\} \end{aligned} \tag{B.7}$$

– Same expression for columns (2, 3, 4) and all rows (1, 2, 4)... (N-2, N-1, N) combinations . The same is valid for the vertical plane.

- Minors of order 2 of M_X^*

– columns (1, 2) rows (1, 2) combinations

$$n_{1,1}^* = \begin{vmatrix} R_{11}^{2(1)} & 2R_{11}^{(1)}R_{12}^{(1)} \\ R_{11}^{2(2)} & 2R_{11}^{(2)}R_{12}^{(2)} \end{vmatrix} =$$

$$\begin{aligned} &-\tfrac{2\beta_x^{(1)}\beta_x^{(2)}}{\beta_x^{(0)}}\sin\phi_x^{(12)}(\cos\phi_x^{(10)} + \alpha_x^{(0)}\sin\phi_x^{(10)})(\cos\phi_x^{(20)} + \alpha_x^{(0)}\sin\phi_x^{(20)}) \cdot \\ &= -\tfrac{2\beta_x^{(1)}\beta_x^{(2)}}{\beta_x^{(0)}}\sin\Phi_{x,1}(\cos\phi_x^{(10)} + \alpha_x^{(0)}\sin\phi_x^{(10)}) \\ &(\cos(\Phi_{x,1} + \phi_x^{(10)}) + \alpha_x^{(0)}\sin(\Phi_{x,1} + \phi_x^{(10)})) \end{aligned} \tag{B.8}$$

– Same expression for columns (1,2) and all rows (1, 3)... (N-1, N) combinations.

– Columns (1, 3) rows (1, 2) combinations.

$$n_{1,2}^* = \begin{vmatrix} R_{11}^{2(1)} & R_{12}^{2(1)} \\ R_{11}^{2(2)} & R_{12}^{2(2)} \end{vmatrix} =$$

$$\begin{aligned} &-\beta_x^{(1)}\beta_x^{(2)}\sin\phi_x^{(12)}(\cos\phi_x^{(20)}\sin\phi_x^{(10)} + \sin\phi_x^{(20)}(\cos\phi_x^{(10)} + 2\alpha_x^{(0)}\sin\phi_x^{(10)}) \cdot \\ &= -\beta_x^{(1)}\beta_x^{(2)}\sin\Phi_{x,1}(\cos(\Phi_{x,1} + \phi_x^{(10)})\sin\phi_x^{(10)} \\ &+\sin(\Phi_{x,1} + \phi_x^{(10)})(\cos\phi_x^{(10)} + 2\alpha_x^{(0)}\sin\phi_x^{(10)}) \end{aligned} \tag{B.9}$$

– Same expression for columns (1, 3) and all rows (1, 3)... (N-1, N) combinations.

– Columns (2, 3) rows (1, 2) combinations.

$$n^*_{1,3} = \begin{vmatrix} 2R^{(1)}_{11}R^{(1)}_{12} & R^{2(1)}_{12} \\ 2R^{(2)}_{11}R^{(2)}_{12} & R^{2(2)}_{12} \end{vmatrix} = \quad .$$
$$-2\beta^{(0)}_x\beta^{(1)}_x\beta^{(2)}_x \sin\phi^{(10)}_x \sin\phi^{(20)}_x \sin\phi^{(12)}_x \tag{B.10}$$
$$= -2\beta^{(0)}_x\beta^{(1)}_x\beta^{(2)}_x \sin\phi^{(10)}_x \sin(\Phi_{x,1}+\phi^{(10)}_x)\sin\Phi_{x,1}$$

– Same expression for columns (2, 3) and all rows (1, 3)... (N-1, N) combinations.

– Columns (1, 4) rows (1, 2) combinations.

$$n^*_{2,1} = \begin{vmatrix} R^{2(1)}_{11} & \hat\sigma^{(1)}_1 \\ R^{2(2)}_{11} & \hat\sigma^{(2)}_1 \end{vmatrix} =$$

$$-\tfrac{1}{2\beta^{(0)}_x}\{(1+\alpha^{2(0)}_x)(\beta^{(1)}_x\hat\sigma^{(2)}_1 - \beta^{(2)}_x\hat\sigma^{(1)}_1)+$$
$$(\alpha^{2(0)}_x - 1)(\beta^{(2)}_x\hat\sigma^{(1)}_1\cos 2\phi^{(20)}_x - \beta^{(1)}_x\hat\sigma^{(2)}_1\cos 2\phi^{(10)}_x)+ \quad . \tag{B.11}$$
$$2\alpha^{(0)}_x(\beta^{(1)}_x\hat\sigma^{(2)}_1\sin 2\phi^{(10)}_x - \beta^{(2)}_x\hat\sigma^{(1)}_1\sin 2\phi^{(20)}_x)\}$$
$$= -\tfrac{1}{2\beta^{(0)}_x}\{(1+\alpha^{2(0)}_x)(\beta^{(1)}_x\hat\sigma^{(2)}_1 - \beta^{(2)}_x\hat\sigma^{(1)}_1)+$$
$$(\alpha^{2(0)}_x - 1)(\beta^{(2)}_x\hat\sigma^{(1)}_1\cos 2(\Phi_{x,1}+\phi^{(10)}_x) - \beta^{(1)}_x\hat\sigma^{(2)}_1\cos 2\phi^{(10)}_x)+$$
$$2\alpha^{(0)}_x(\beta^{(1)}_x\hat\sigma^{(2)}_1\sin 2\phi^{(10)}_x - \beta^{(2)}_x\hat\sigma^{(1)}_1\sin 2(\Phi_{x,1}+\phi^{(10)}_x))\}$$

– Same expression for columns (1, 4) and all rows (1, 3)... (N-1, N) combinations.

– Columns (2, 4) rows (1, 2) combinations.

$$n^*_{2,2} = \begin{vmatrix} 2R^{(1)}_{11}R^{(1)}_{12} & \hat\sigma^{(1)}_1 \\ 2R^{(2)}_{11}R^{(2)}_{12} & \hat\sigma^{(2)}_1 \end{vmatrix} =$$

$$\alpha^{(0)}_x\{(\beta^{(1)}_x\hat\sigma^{(2)}_1 - \beta^{(2)}_x\hat\sigma^{(1)}_1) - \beta^{(1)}_x\hat\sigma^{(2)}_1\cos 2\phi^{(10)}_x + \beta^{(2)}_x\hat\sigma^{(1)}_1\cos 2\phi^{(20)}_x\}$$
$$+\beta^{(1)}_x\hat\sigma^{(2)}_1\sin 2\phi^{(10)}_x - \beta^{(2)}_x\hat\sigma^{(1)}_1\sin 2\phi^{(20)}_x \quad .$$
$$= \alpha^{(0)}_x\{(\beta^{(1)}_x\hat\sigma^{(2)}_1 - \beta^{(2)}_x\hat\sigma^{(1)}_1) - \beta^{(1)}_x\hat\sigma^{(2)}_1\cos 2\phi^{(10)}_x + \beta^{(2)}_x\hat\sigma^{(1)}_1\cos 2(\Phi_{x,1}+\phi^{(10)}_x)\}$$
$$+\beta^{(1)}_x\hat\sigma^{(2)}_1\sin 2\phi^{(10)}_x - \beta^{(2)}_x\hat\sigma^{(1)}_1\sin 2(\Phi_{x,1}+\phi^{(10)}_x)$$

(B.12)

– Same expression for columns (2, 4) and all rows (1, 3)... (N-1, N) combinations.

– Columns (3, 4) rows (1, 2) combinations.

$$n^*_{3,1} = \begin{vmatrix} R^{2(1)}_{12} & \hat\sigma^{(1)}_1 \\ R^{2(2)}_{12} & \hat\sigma^{(2)}_1 \end{vmatrix} =$$

$$\tfrac{1}{2}\beta^{(0)}_x\{(\beta^{(1)}_x\hat\sigma^{(2)}_1 - \beta^{(2)}_x\hat\sigma^{(1)}_1) - \beta^{(1)}_x\hat\sigma^{(2)}_1\cos 2\phi^{(10)}_x + \beta^{(2)}_x\hat\sigma^{(1)}_1\cos 2\phi^{(20)}_x\}$$
$$= \tfrac{1}{2}\beta^{(0)}_x\{(\beta^{(1)}_x\hat\sigma^{(2)}_1 - \beta^{(2)}_x\hat\sigma^{(1)}_1) - \beta^{(1)}_x\hat\sigma^{(2)}_1\cos 2\phi^{(10)}_x + \beta^{(2)}_x\hat\sigma^{(1)}_1\cos 2(\Phi_{x,1}+\phi^{(10)}_x)\}$$

(B.13)

– Same expression for columns (3, 4) and all rows (1, 3)... (N-1, N) combinations.

- Minors of order 3 of M_X

  – columns (1, 2 ,3) rows (1, 2, 3) combinations

$$\begin{aligned} m_1 = m_1^* &= \begin{vmatrix} R_{11}^{2(1)} & 2R_{11}^{(1)}R_{12}^{(1)} & R_{12}^{2(1)} \\ R_{11}^{2(2)} & 2R_{11}^{(2)}R_{12}^{(2)} & R_{12}^{2(2)} \\ R_{11}^{2(3)} & 2R_{11}^{(3)}R_{12}^{(3)} & R_{12}^{2(3)} \end{vmatrix} \\ &= 2\beta_x^{(1)}\beta_x^{(2)}\beta_x^{(3)}\sin\phi_x^{(21)}\sin\phi_x^{(31)}\sin\phi_x^{(32)} \\ &= 2\beta_x^{(1)}\beta_x^{(2)}\beta_x^{(3)}\sin\Phi_{x,1}\sin\Phi_{x,2}\sin(\Phi_{x,2}-\Phi_{x,1}) \end{aligned} \quad , \tag{B.14}$$

  that is the equivalent to (5.15).

  – Same expression for columns (1, 2, 3) and all rows (1, 2, 4)... (N-2, N-1, N) combinations.

- Minors of order 2 of M_X

  – columns (1, 2) rows (1, 2) combinations

$$n_{1,1} = n_{1,1}^* = \begin{vmatrix} R_{11}^{2(1)} & 2R_{11}^{(1)}R_{12}^{(1)} \\ R_{11}^{2(2)} & 2R_{11}^{(2)}R_{12}^{(2)} \end{vmatrix} =$$

$$\begin{aligned} &-\tfrac{2\beta_x^{(1)}\beta_x^{(2)}}{\beta_x^{(0)}}\sin\phi_x^{(12)}(\cos\phi_x^{(10)}+\alpha_x^{(0)}\sin\phi_x^{(10)})(\cos\phi_x^{(20)}+\alpha_x^{(0)}\sin\phi_x^{(20)}) \\ &= -\tfrac{2\beta_x^{(1)}\beta_x^{(2)}}{\beta_x^{(0)}}\sin\Phi_{x,1}(\cos\phi_x^{(10)}+\alpha_x^{(0)}\sin\phi_x^{(10)}) \\ &(\cos(\Phi_{x,1}+\phi_x^{(10)})+\alpha_x^{(0)}\sin(\Phi_{x,1}+\phi_x^{(10)})) \end{aligned} \quad . \tag{B.15}$$

  – Same expression for columns (1,2) and all rows (1, 3)... (N-1, N) combinations.

  – Columns (1, 3) rows (1, 2) combinations.

$$n_{1,2} = n_{1,2}^* = \begin{vmatrix} R_{11}^{2(1)} & R_{12}^{2(1)} \\ R_{11}^{2(2)} & R_{12}^{2(2)} \end{vmatrix} =$$

$$\begin{aligned} &-\beta_x^{(1)}\beta_x^{(2)}\sin\phi_x^{(12)}(\cos\phi_x^{(20)}\sin\phi_x^{(10)}+\sin\phi_x^{(20)}(\cos\phi_x^{(10)}+2\alpha_x^{(0)}\sin\phi_x^{(10)}) \\ &= -\beta_x^{(1)}\beta_x^{(2)}\sin\Phi_{x,1}(\cos(\Phi_{x,1}+\phi_x^{(10)})\sin\phi_x^{(10)} \\ &+\sin(\Phi_{x,1}+\phi_x^{(10)})(\cos\phi_x^{(10)}+2\alpha_x^{(0)}\sin\phi_x^{(10)}) \end{aligned} \quad . \tag{B.16}$$

  – Same expression for columns (1, 3) and all rows (1, 3)... (N-1, N) combinations.

– Columns (2, 3) rows (1, 2) combinations.

$$
\begin{aligned}
n^*_{1,3} = n_{1,3} = \begin{vmatrix} 2R^{(1)}_{11}R^{(1)}_{12} & R^{2(1)}_{12} \\ 2R^{(2)}_{11}R^{(2)}_{12} & R^{2(2)}_{12} \end{vmatrix} = \\
-2\beta^{(0)}_x\beta^{(1)}_x\beta^{(2)}_x \sin\phi^{(10)}_x \sin\phi^{(20)}_x \sin\phi^{(12)}_x \\
= -2\beta^{(0)}_x\beta^{(1)}_x\beta^{(2)}_x \sin\phi^{(10)}_x \sin(\Phi_{x,1} + \phi^{(10)}_x) \sin\Phi_{x,1}
\end{aligned}
\quad . \tag{B.17}
$$

– Same expression for columns (2, 3) and all rows (1, 3)... (N-1, N) combinations.

B.3 Full beam matrix diagonalization

Demonstration of Eq. (5.21): $det(\overline{\sigma}) = det(\sigma) = (\epsilon_1^2\epsilon_2^2)$

$$
\begin{aligned}
&det(\overline{\sigma}) = (\epsilon_1^2\epsilon_2^2) \\
&det(\overline{\sigma}) = det(\bar{R}\sigma\bar{R}^t) = det(\bar{R})det(\sigma)det(\bar{R}^t) = det(\sigma)
\end{aligned}
\quad , \tag{B.18}
$$

given that being $\bar{R}$ a symplectic a transformation the $det(\bar{R}) = 1$.

Demonstration of Eq. (5.22): $Tr(J\overline{\sigma})^2 = Tr(J\sigma)^2 = -2(\epsilon_1^2 + \epsilon_2^2)$

$$
\begin{aligned}
&Tr(J\overline{\sigma})^2 = -2(\epsilon_1^2 + \epsilon_2^2) \\
&Tr(J\overline{\sigma})^2 = Tr(J\bar{R}\sigma^t\bar{R})^2 = Tr(J\bar{R}\sigma^t\bar{R}\ J\bar{R}\sigma^t\bar{R}) = \\
&Tr(J\bar{R}\sigma^t\ J\ \sigma^t\bar{R}) = Tr(J\sigma^t\ J\sigma^t) = Tr(J\sigma)^2
\end{aligned}
\quad , \tag{B.19}
$$

being $\bar{R}J\bar{R} = J$.

Bibliography

[1] 4th July Press Conference at the CERN web: *http://cdsweb.cern.ch/record/1459604*.

[2] Y. Honda et al., *Achievement of Ultralow Emittance Beam in the Accelerator Test Facility Damping Ring*, Phys. Rev. Lett. 92 054802 (February, 2004)

[3] K. Kubo et al., *Extremely Low Vertical-Emittance Beam in the Accelerator Test Facility at KEK*, Phys. Rev. Lett. 88 194801 (May, 2002)

[4] M. Böge et al., *Utra-Low Vertical Emittance at the SLS*, PAC09, Vancouver, WE5RFP008 (2009)

[5] P. Raimondi and A. Seryi, *Novel Final Focus Design for Future Linear Colliders*, Phys. Rev. Lett. 86, 3779–3782 (2001)

[6] A. De Roeck et al., *From the LHC to Future Colliders*, arXiv:0909.3240 [hep-ph], (September, 2009)

[7] LHC Design Report, CERN-2004-003 (2004).

[8] ILC Global Design Effort Collaboration, *International Linear Collider Reference Design Report, Volume 2: Physics at the ILC*, http://www.linearcollider.org, (August, 2007)

[9] H. Wiedemann, *Particle Accelerator Physics*, Springer Verlag, 1993

[10] E. Wilson, *An introduction to particle accelerators*, Oxford University Press, 2001

[11] A. Chao and M. Tigner, *Handbook of Accelerator Physics and Engineering*, World Scientific, 1999

[12] ILC Global Design Effort Collaboration, *International Linear Collider Reference Design Report, Volume 3: Accelerator*, http://www.linearcollider.org, (August, 2007)

[13] ILC Global Design Effort Collaboration, *International Linear Collider Reference Design Report, Volume 1: Executive Summary*, http://www.linearcollider.org, (August, 2007)

[14] TESLA Technical Design Report (2001) *http://tesla.desy.de/new pages/TDR CD/start.html*

[15] CERN, *A Multi-TeV Linear Collider Based On CLIC Technology, CLIC Conceptual Design Report, Volume 1*, Draft from http://project-clic-cdr.web.cern.ch/project-CLIC-CDR/, 2012

[16] CLIC study team, *A 3 TeV e^+e^- Linear Collider Based on CLIC Technology*, CERN 2000-008, (July, 2000)

[17] H. Braun et al., *CLIC 2008 Parameters*, CLIC-Note-764, (October, 2008)

[18] ILC Global Design Effort, *ILC Research and Development Plan for the Technical Design Phase. Release 3*, Available at http://www.linearcollider.org/GDE/Project-Managers, (August, 2010)

[19] ATF2 Group, *ATF2 Proposal Vol.1*, CERN-AB-2005-035, (August 11, 2005)

[20] V. Ayvazyan et al., *LLRF Control System Upgrade at FLASH*, PCaPAC,10, THPL0125, (2010)

[21] T. Imai et al., *Double Kicker system in ATF*, arXiv:physics/0008133v1 [physics.acc-ph] (August, 200)

[22] T. Naito, *Multibunch beam extraction using the strip-line kicker at the KEK Accelerator Test Facility* Phys. Rev. Special Topics - Accelerators and Beams 14, 051002 (2011)

[23] S. Guiducci, *Chromaticity*, CAS CERN Accelerator School, CERN-91-04 (1991)

[24] S. Araki et al., *Recent Studies in ATF Damping Ring*, ICFA Beam Dynamics Newsletter No. 54 (April, 2011)

[25] ATF Collaboration, *ATF2 Summary and Status*, ICFA Beam Dynamics Newsletter No. 54 (April, 2011)

[26] P. Bambade et al., *Present status and first results of the final focus beam line at the KEK Accelerator Test Facility*, Phys. Rev. Special Topics - Accelerators and Beams 13, 042801, (2010)

[27] P. Emma et al., *Skew Quadrupoles for Dispersion Control in the ATF Extraction Line*, ATF Internal Report, ATF-99-03 (March 1999)

[28] B. Parker et al., *A superconducting Magnet Upgrade of the ATF2 Final Focus*, IPAC'10, Kyoto, WEPE041 (2010)

[29] Y. Iwashita et al., *Beam Test Plan of Permanent Magnet Quadrupole Lens at ATF2*, IPAC'10, Kyoto, WEPE017 (2010)

[30] R. Apsimon, *The Development and Implementation of a Beam Position Monitoring System for use in the FONT Feedback System at ATF2*, PhD Thesis, Oxford (2011)

[31] N. Terunuma et al., *Instrumentation for the ATF2 Facility*, IPAC'10, Kyoto, WEZMH02 (2010)

[32] G.B. Christian et al., *Latest Performance Results from the FONT4 Intra-train Position and Angle Feedback System at ATF2*, IPAC'11, San Sebastián, MOPO017, (September, 2011)

[33] S. Boogert et al., *Cavity Beam Position Monitor System for ATF2*, IPAC'11, San Sebastián, TUPC161 (2011)

[34] T. Tamanaka et al., *Shintake Monitor in ATF2: Present Status*, arXiv:1006.3625v1 [physics.ins-det], (June, 2010)

[35] J. Yan et al., *Measurement of Nanometer Scale Beam Size by Shintake Monitor*, ICFA Beam Dynamics Newsletter No. 54 (April, 2011)

[36] L.J. Nevay et al., *Micron-scale Laser-wire at the ATF2 at KEK Commissioning and Results*, IPAC'11, San Sebastián, TUPC158 (2011)

[37] E. Bravin, *Transverse Beam Profiles*, Lectures from Cern Accelerator School CAS (2008)

[38] H.Hayano et al., *Wire Scanners for Small Emittance Beam Measurements in ATF*, XX International Linac Conference, Monterey (2000)

[39] S. Bai et al., *First Beam Waist Measurements in the Final Focus Beam Line at the KEK Accelerator Test Facility*, Phys. Rev. Special Topics - Accelerators and Beams 13, 092804, (2010)

[40] I. M. Frank, *Transition Radiation and Optical Properties of Matter* Sov. Phys. Usp. 8 729, (1966)

[41] V. L. Ginzburg, *Radiation by uniformly moving sources*, Physics-Uspekhi (10) 973-982, (1996)

[42] J. D. Jackson, *Classical Electrodynamics. 3d Edition*, Wiley, New York (1998), 685-6

[43] B. Gitter, *Optical Transition Radiation*, CAA-TECH-NOTE-internal-# 24

[44] L. Wartski et al., *Interference Phenomenon in Optical Transition Radiation and its Application to Particle Beam Diagnostics and Multiple-scattering Measurements*, J. Appl. Phys. 46, 3644, (1975)

[45] J. Bosser et al., *Optical Transition Radiation Proton Beam Profile Monitor*, Nucl. Inst. Meth., A238 (1985) 45-52

[46] H. Koziol, *Beam Diagnostics for Accelerators*, Lectures from Cern Accelerator School CAS 2000, CERN 2005-004 (2005)

[47] P. Forck, *Lecture Notes on Beam Instrumentation and Diagnostics*, Joint Universities Accelerator School (2009)

[48] M. Olvegaard, *Performance of Parabolic and Diffusive OTR Screens at the CLIC Test Facility 3*, DIPAC'11, Hamburg, TUPD49 (2011)

[49] DESY XFEL Project Group, *The European X-Ray Free-Electron Laser: Technical design report*, DESY 2006-097, (July, 2007)

[50] S. Bhadra et al., *Optical Transition Radiation Monitor for the T2K Experiment*, arXiv:1201.1922 [physics.ins-det], (January 2012)

[51] Marc Ross et al., *A Very High Resolution Optical Transition Radiation Beam Profile Monitor*, SLAC-PUB-9280, (July, 2002)

[52] Douglas McCormick, private communication.

[53] S. Fartoukh et al., *Heat deposition by transient beam passage in spoilers*, CERN-SL-2001-012 AP, CLIC Note 477, 2001.

[54] Particle Data Group, *http://pdg.lbl.gov/2012/AtomicNuclearProperties/index.html*

[55] Matweb, *http://www.matweb.com*

[56] M. Alabau Pons et al., *Experimental Studies and Analysis of the Vertical Emittance Growth in the ATF Extraction Line in 2007-2008*, ATF Report: ATF–08–15, (March 03, 2009)

[57] *http://www.matweb.com*, a website widely used by the material engineering community that provides a very reputable source of material properties.

[58] S. M. Seltzer and M. J. Berger, *Improved Procedure for Calculating the Collision Stopping Power of Elements and Compounds for Electrons and Positrons*, Int. J. Appl. Radiat. Isot. Vol. 35, No, 7, pp. 665-676. 1984

[59] N. Delerue et al., *Single Shot Emittance Measurement Using Optical Transition Radiation*, arXiv:1005.2417v1 [physics.acc-ph], (November, 2008)

[60] EPICS control software: http://www.aps.anl.gov/epics/

[61] Lucretia simulation code: http://www.slac.stanford.edu/accel/ilc/... .../codes/Lucretia/web/overview.html

[62] P. Catravas et al., *Beam Profile Measurement at 30 GeV Using Optical Transition Radiation*, Proceedings of the Particle Accelerator Conference, (1999)

[63] X. Artru et al., *Experimental Investigations on Geometrical Resolution of Optical Transition Radiation (OTR)*, Nucl. Instr. and Meth. in Phys. Res. A 410 (1998) 148-158

[64] X. Artru et al., *Experimental investigations on geometrical resolution of electron beam profiles given by OTR in the GeV energy range*, Proc 5th European Particle Accelerator Conf., (June, 1996) p. 1686

[65] J.W. Flanagan, *Diagnostics for Ultra-Low Emittance Beams*, IPAC'11, San Sebastian, WEYB01, (2011)

[66] T. Naito et al., *Emittance Measurement Using X-Ray Beam Profile Monitor at KEK-ATF*, IBIC'12, Tsukuba, MOPB63 (2012)

[67] J. Turner et al., *Summary of Accelerator Physics Studies at KEK/ATF Nov.17-Nov.27,1998*, ATF-Report: ATF-99-17, (1999)

[68] K. Kubo, *How to calculate intrinsic emittances from 4-dimensional beam matrix*, ATF Internal Report, ATF-99-02 (March 1999)

[69] C. Rimbault et al., *4D Emittance Measurements Using Multiple Wire and Waist Scan Methods in the ATF Extraction Line*, EPAC'08, Genoa, TUPC087 (2008)

[70] A. Faus-Golfe, J. Navarro-Faus, *Emittance reconstruction from measured beam sizes*, to be published.

[71] S. Fartoukh, Private communication.

[72] G. White, *ATF2 Emittance Correction Study*, Talk in the 13th ATF2 Project Meeting, Tsukuba (January, 2012)

[73] Jeffrey C. Smith, *Coupling Correction in the ILC Ring To Main Linac*, LEPP, Cornell University, Ithaca, NY, (March 22, 2007)

[74] Glen White, *Final Focus Systems for Nanobeams: Design & Operation Challenges + Lessons to be Learnt from ATF*, KEK seminar, (December 6, 2011)

[75] John Rees and Lenny Rivkin, *On Measuring Emittances and Sigma Matrices*, SLAC-PUB 2305, SLAC/AP-18, (March, 1984)

[76] Matthew Sands, *A Beta Mismatch Parameter*, SLAC-AP-85, (April, 1991)

[77] M. Minty and F. Zimmermann, *Measurements and control of charged particle beams*, Springer, (2003)

[78] G. White et al., *A flight simulator for ATF2: A mechanism for international collaboration in the writing and deployment of online beam dynamics algorithms*, EPAC'08, Genoa, TUPP016, (2002)

[79] G. White et al., *Operational Experiences Tuning the ATF2 Final Focus Optics Towards Obtaining a 37 Nano-meter Electron Beam IP Spot Size*, IPAC'10, Kyoto, WEOBMH01, (2010)

[80] C. Rimbault et al., *Coupling Correction in ATF2 Extraction Line*, PAC'09, Vancouver, FR5PFP005, (2009)

[81] C. Rimbault et al., *Coupling Measurements in ATF2 Extraction Line*, IPAC'10, Kyoto, THPD080, (2010)

[82] G. White, *Private communication.*

[83] G. White et al., *Beam-based alignment, tuning and beam dynamics studies for the ATF2 extraction line and final focus system*, EPAC'08, Genoa, MOPP039, (2002)

[84] K.L.F. Bane et al., *Bunch Length Measurements at the ATF Damping Ring in April 2000*, SLAC-AAS-97, KEK-ATF-11 (October, 2000)

[85] K.L.F. Bane et al., *Impedance Analysis of Bunch Length Measurements at the ATF Damping Ring*, SLAC-PUB-8846, (May, 2001)

[86] K.L.F. Bane et al., *Intrabeam Scattering Analysis of ATF Beam Data Taken in April 2000*, SLAC-AP-135, ATF-00-14, (December, 2000)

[87] *Zeroth Order Design Report for the Next Linear Collider*, Available at *http://www-project.slac.stanford.edu/lc/ZDR/Zeroth.html*

[88] P. Tenenbaum, *Expanded Studies of Linear Collider Final Focus Systems at the Final Focus Test Beam*, PhD Thesis and SLAC-REPORT-95-475, (1995)

[89] F. Löhl, *Measurements of the transverse emittance at the VUV-FEL*, TESLA-FEL 2005-03, (2005)

Aknowledgements

First of all I would like to express my gratitude to Dr. Ángeles Faus-Golfe for introducing me in the field and giving me this opportunity and to Dr. Javier Resta-López for joining the supervision. Without their knowledge and wide experience this thesis would not have seen the light. They deserve the most of the aknowledgements.

Apart from supervisors there is another crucial condition for a thesis to be written. I would like to thank the financial support given by the Instituto de Física Corpuscular (IFIC) and by eventual other sources through IFIC.
I would like to thank also the Accelerator Physics Group for sharing knowledge, advise and help. César Blanch is specially aknowledged for his work in the mechanical design. Sincere aknowledgements as well to Jesús Navarro for his valuable contribution in the analytic emittance reconstruction studies.

Likewise, I am thankful to the SLAC Multi-OTR collaboration, specially to Dr. Glen White and Mark Woodley for their expertise and availability and Doug McCormick for his labour in the hardware aspect. This project would not have been possible without their work.
Thanks to the whole ATF/ATF2 collaboration at KEK for many different reasons: The organization for providing the infrastructures and the conditions to develop this project. I am grateful to the ATF staff members for sharing their knowledge of the machine and being available whenever issues regarding to it arose. To all the overseas crew not only for science but also for creating a familiar environment in a so distant and different (yet interesting!) place. In this sense Dr. Javier Resta-López receives again my gratitude for his unvaluable friendliness.

He d'agraïr, en la meua llengua, a tots aquells companys i amics que han estat presents durant este camí, relacionats o no amb ell. Menció especial al grup del dinar-i-xarradeta de l'IFIC. Als meus amics propers pel suport incondicional. A la meua família, la de sang i la nova, qualsevol agraïment se'ls queda curt.